N° d'ordre: 42033

# THÈSE

**Université de Lille 1 Sciences et Technologies**
École doctorale Sciences de la Matière, du Rayonnement et de l'Environnement

# MODELLING THE PLASTICITY OF WADSLEYITE AND RINGWOODITE:

## On the motion of dislocations in the Earth's transition zone

par

**Sebastian RITTERBEX**

Pour obtenir le grade de

**Docteur de l'Université**

Specialité: Sciences des Matériaux

Soutenue le 3 Juin 2016
devant le jury composé de

| | |
|---|---|
| Prof. B. Romanowicz | Président |
| Prof. S. Jahn | Rapporteur |
| Dr. D. Mainprice | Rapporteur |
| Dr. B. Schuberth | Examinateur |
| Dr. A. Walker | Examinateur |
| Prof. Ph. Carrez | Co-directeur de thèse |
| Prof. P. Cordier | Directeur de thèse |

*Ob nicht Natur zuletzt sich doch ergründe?*

Goethe.

*Fecisti nos ad te*
*et*
*inquietum est cor nostrum donec requiescat in te.*

St. Augustine of Hippo.
(Confessions)

# Acknowledgements

First of all, I would like to thank Barbara Romanowicz for examining this PhD thesis and for presiding the defence committee. I would like to thank warmly David Mainprice and Sandro Jahn for their careful review of this work and also Bernhard Schuberth and Andrew Walker for having accepted to examine this thesis manuscript, being part of the defence committee and for all their constructive comments.

More than grateful I am of having Patrick Cordier as my PhD supervisor, who I would like to thank heartily, first of all for having given me the opportunity to start my PhD, as one of the first, in the RheoMan project and for his confidence in my capabilities. Also I would like to thank Patrick for guiding me thoroughly through this PhD, for his advice, for all our discussions and for broadening my knowledge, my view and the insights I gained in the field of plastic deformation of minerals over the last years.
At the same time, I also would like to thank gratefully my co-supervisor, Philippe Carrez, who introduced me to the beauty of plastic deformation from the atomic to the macroscopic scale. I thank you warmly for guiding me through this PhD, for all our discussions, your ability to tackle difficult scientific questions from different angles, your help and the pleasant way in which we have been working together over the last years.

I was fortunate to do my PhD in the RheoMan group and among the other members of the UMET.

From RheoMan, I would like to say many thanks to Karine Gouriet, who kindly helped me to start-up my PhD and for all her advice. Many thanks I would also like to say to Pierre Hirel, for his kindness and support, all his help, our discussions and the knowledge he taught me in the field of computational materials science. Further I would like to say thanks to Antoine Kraych together with whom I started my PhD. I enjoyed our time together, all conferences we visited and especially I liked our sometimes long discussions about n'importe quoi.
In that sense, I would like to say many thanks to those who helped me, gave me some advice and for their kind presence during all those years: Francesca, Xiaoyu, Sasha, Sébastien, Nadège, Paul, Jannick, Alex, Riccardo, Srinivasan, Nils, Ahmed, Damien and Alexandre Legris. Merci!

Finally, I would like to thank my family and especially both of my parents, who gave me the opportunity to study and to develop myself to the best of my abilities and under the best of circumstances.

In one way or another, all of you participated to the success of this PhD thesis. En ce sens, merci à tous.

# Abstract

The transition zone is the region in the Earth's mantle between 410 and 660 km depth that separates the upper from the lower mantle. In spite of its small volume, it may play a role in constraining the style, vigour and scale of global mantle convection through, for instance, the fate of subducting slabs. Mantle convection is governed by plastic flow that occurs through the motion of crystal defects. Line defects or dislocations are considered to be one of the most efficient defects contributing to intracrystalline deformation. That is why in this work, we concentrate on the motion of dislocations in relation to the major phases of the mantle transition zone: wadsleyite and ringwoodite.

A theoretical mineral physics approach is used to model thermally activated glide motion of dislocations at appropriate pressure conditions by means of kink-pair nucleation on dissociated dislocations as they exist in both high-pressure polymorphs of olivine. The intrinsic properties of dislocation core structures are modelled with a generalized Peierls-Nabarro model and parametrized by atomic scale calculations to take into account the effect of pressure on atomic bonding. Plastic deformation is finally described in terms of steady-state conditions, by taking into account the instrinsic strain rate dependence on the mobility of the defects.

Since plastic deformation by the motion of dislocations is associated with creep, we use the above results and a climb mobility law combined with experimental data to address the effective creep process in wadsleyite and ringwoodite under natural conditions. We show the inefficiency of dislocation glide as a strain producing deformation mechanism in wadsleyite and ringwoodite under natural conditions and suggest the potential importance of pure climb creep in the main minerals constituting the Earth's transition zone. This would imply the mantle transition zone to be rheologically distinct from the upper mantle.

# Résumé

## Modélisation de la plasticité dans la wadsleyite et la ringwoodite:

*sur la dynamique des dislocations dans la zone de transition du manteau terrestre*

La zone de transition est située entre, environ, 410 et 660 km de profondeur dans le manteau terrestre. Elle sépare le manteau supérieur du manteau inférieur. Bien qu'il s'agisse d'une zone assez petite en volume du manteau terrestre, son rôle peut être important pour déterminer le mode, la vigueur et l'échelle de la convection globale, par exemple par le devenir de la subduction des plaques lithospheriques. Cette convection résulte de la déformation plastique des minéraux qui constituent le manteau, qui elle-même résulte du mouvement des défauts cristallins. Parmi ces défauts, les dislocations sont souvent considérées comme les agents les plus efficaces de la plasticité intracristalline. C'est pourquoi nous proposons d'étudier les mouvements des dislocations dans les principales phases de la zone de transition: la wadsleyite et la ringwoodite.

Par une approche de modélisation numérique de la physique des minéraux, nous avons déterminée la mobilité thermiquement activée du glissement des dislocations dissociées comme celles que l'on trouve dans les polymorphes haute-pression de l'olivine. A partir de l'échelle atomique, pour bien prendre en compte l'effet de pression sur les liaisons atomiques, nous avons modélisé les propriétés de coeur des dislocations en utilisant la théorie de Peierls-Nabarro généralisée. La déformation plastique est formulée en conditions stationnaire en rendant compte de la dependence intrinsèque du taux de déformation sur la mobilité des dislocations.

La déformation plastique par mouvement des dislocations dans les roches mantelliques résulte du fluage. Pour mieux comprendre les mécanismes de fluage dans la wadsleyite et la ringwoodite en conditions naturelles, on a utilisé les résultats précédemment définis sur le glissement que l'on a combiné avec la mobilité des dislocations en montée, paramétrée par des données expérimentales. Les résultats montrent que le glissement des dislocations est inefficace par rapport au fluage par montée dans des minéraux majeurs de la zone de transition. Cela suggère l'importance potentielle du fluage par montée, ce qui rendrait la zone de transition rhéologiquement distincte du manteau supérieur.

# Contents

# 1 Introduction

---

> *It will become clear that the simplicity of the inner*
>
> *Earth is only apparent ... we may perhaps expect that*
>
> *someday "physics of the interior of the Earth" will*
>
> *make as little sense as "physics of the crust".*
>
> Jean-Paul Poirier.
>
> (*Introduction to the Physics of the Earth's Interior, Cambridge University Press 1991.*)

---

The very nature of the dynamics of the solid Earth lies in the flow of thermal energy out the Earth's interior. The Earth can be considered as a "working" body that transforms heat into mechanical work for which the consequences are manifested at the Earth's surface by mountain belts, volcanoes and earthquakes and indirectly by processes captured in the geological record. The latest estimate of the global heat-ouput of the Earth is $46 \times 10^{12}$ W (Jaupart *et al.* 2007) that for the largest part consist of heat involved in the cooling of oceanic plates which are continuously formed at mid-oceanic ridges. There are three main heat sources that contribute to the Earth's global heat flow. The most important (in its present day state) contributions are the premordial heat due to the formation of the Earth and the radiogenic heat production as a consequence of the decay of radioactive isotopes such as $^{235}U$, $^{238}U$, $^{232}Th$ and $^{40}K$ in the mantle, and to a lesser extent followed by the latent heat as a result of phase transitions, mainly in form of the contribution of the crystallization of the inner core.

Heat from the Earth's interior is for the largest part transferred to the surface by solid-state convection within the mantle: this is the Earth's outer region down to about 2900 km depth and below which we can find the Earth's core. Counterintuitive to what one might think, thermal convection is a much more effective mechanism to transport heat out of the Earth's hot interior than through heat conduction. This is because the mantle is mainly composed of poor heat conductive solid silicate material to which we will come back.

Solid-state convection is directly related to the concept of continental drift that was first proposed by the German meteorologist Alfred Wegener. His idea became widely accepted in the sixties of the twentieth century when paleomagnetic observations of the ocean floor supported the concept of plate-tectonics, which turned out to be nothing more than the relative motion of the about twelve lithospheric plates, that form the outermost portion of the Earth as being part of global solid-state convection. In the current state of the Earth's evolution, these lithospheric plates are created at mid-oceanic ridges (oceanic lithosphere), transformed into orogens as a result of plate collisions (continental lithosphere) or disappear again after becoming gravitionally unstable when cooled down and being forced to penetrate (oceanic lithosphere) at plate boundaries into the Earth's interior.

## 1.1 State-of-the-Art

The physical description of the dynamics of the Earth's interior requires first of all knowledge of the radial distribution of the composition, pressure and temperature of the Earth's interior. These questions have been adressed in the fields of seismology, mineral physics and geochemistry for which we intend to give a brief overview of the main con-

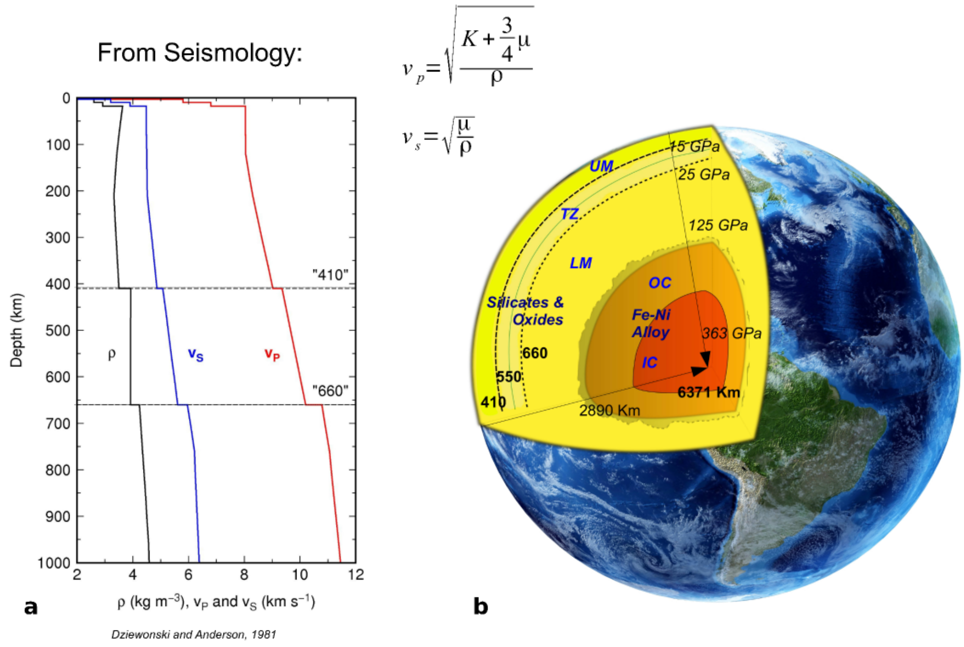

Figure 1.1: *a) Radial seismic body wave velocities* $v_p$ *and* $v_s$ *and density distribution as proposed by the preliminary Earth reference model (PREM) (Dziewonski and Anderson 1981). b) A schematic illustration is shown of the compositional layering of the Earth's interior as a function of depth, pressure and temperature.*

tributions of the respective fields with their results.

The development in seismological studies and related techniques during the last half of the twentieth century made it possible to gain a fortunate amount of information about the inaccessible interior of the Earth earned from the collection and analysis of normal modes and arrival times of seimic waves that travel through the Earth or along the Earth's subsurface after the occurrence of (major) Earthquakes. The collection of seismic body waves, which are dependent on the elastic properties of the material through which the waves travel, revealed that the Earth's interior is principally divided into a mainly solid mantle of 2900 km thick and a core with a radius of about 3480 km, subdivided into a liquid outer and a solid inner core. This has been characterized by the registration of the presence or absence of seismic body waves collected at seismic stations all over the world together with the identification of abrupt major changes in seismic velocities with depth. Abrupt variations in seismic body wave velocities are the primary indicators of changes in (radial) structure or composition of the Earth's interior which relates these seismic observations indirectly to either solid-solid or solid-liquid phase transitions, that could be chemical or structural (polymorphism) in nature (Fig. 1.1). In addition, in the late seventies of the twentieth century, the inversion of traveltime data with the use of spectral analysis of the Earth's normal modes or eigenvibrations made it possible to constrain the radial density and hence the directly related pressure distribution of the Earth's interior. The physical results of both achievements, as mentioned, in the field of seismology, together with the analysis of surface wave dispersion has been captured into a model that is known as the preliminary reference Earth model (PREM) proposed by Dziewonski and Anderson in 1981 (Fig. 1.1). The model confirmed in a more accurate way (as it includes wave attenuation and anisotropy for the first time) earlier studies of the structure of the Earth's mantle: the Earth's mantle can be mainly divided into three parts, an upper mantle that extends to a depth of about 410 km, a lower mantle between 660-2900 km and a region which ranges from 410-660 km depth that is known as the transition zone. Around the end of the ninetees, another seismic discontinuity was found locally around 2600 km depth that had led to the definition of the innermost part of the Earth's mantle which extends to the core-mantle boundary (CMB)(Lay *et al.* 1998). This innermost part of the Earth's mantle is known as the D"-layer, that has been named by Bullen (1950) before the discontinuity was found. Below the mantle, the Earth's core then extends from about 2900-6379 km and can be subdivided into a low viscous liquid outer core (no propagation of S-waves) until a depth of 5150 km and a solid inner core.

The seismic discontinuities identified as a function of pressure are directly related to abrupt variations in the material properties as they influence the seismic wave velocities and their arrival times. On the other hand, density jumps are constrained through reflection coefficients. This knowledge has been used in relation to the study of phase transitions in candidate materials investigated under high pressure and temperature conditions in laboratory experiments and by using theoretical models to construct phase diagrams. The candidate materials have been defined on the basis of geological, geochemical and petrological observations on one hand and on cosmochemical considerations on the other. The chemical composition of chondritic meteorites is considered to be a good reference for undifferentiated material that condensed from the solar nebula. Together with the analysis of the composition of geological outcrops of xenoliths and ophiolites, which are good representatives of (differentiated) upper mantle material, it has been determined that the Earth is primary composed of the atomic species Si, O, Mg, Al, Ca, Ni and Fe that are condensed to crystalline solids, mainly in the form of silicates and oxides. This forms the bulk of the Earth's mantle. An Fe-Ni alloy is expected to form the bulk the Earth's core (Birch, 1952). This has led to the first model of the chemical composition of the Earth's upper mantle, known as the pyrolitic model, which was introduced by Ringwood (1962; 1975). The model refers to the mineral assemblage with respect to a peridotitic composition of the upper mantle of $(Mg,Fe)_2SiO_4$ olivine and $(Mg,Fe,Ca)SiO_3$ pyroxene and garnet. Since then, efforts in the field of high pressure and temperature research in mineral physics have elucidated the main mineral candidate constituents of the Earth's interior as a function of pressure and temperature. This is illustrated in a simplified radial distribution of the mineralogy for a pyrolitic composition of the Earth's mantle as shown in Fig. 1.2.

Finally, the radial temperature of the Earth, often referred to as the geotherm, has been constrained on the basis of the above studies. The main phase boundaries in the Earth's mantle as a function of pressure and temperature for the respective mate-

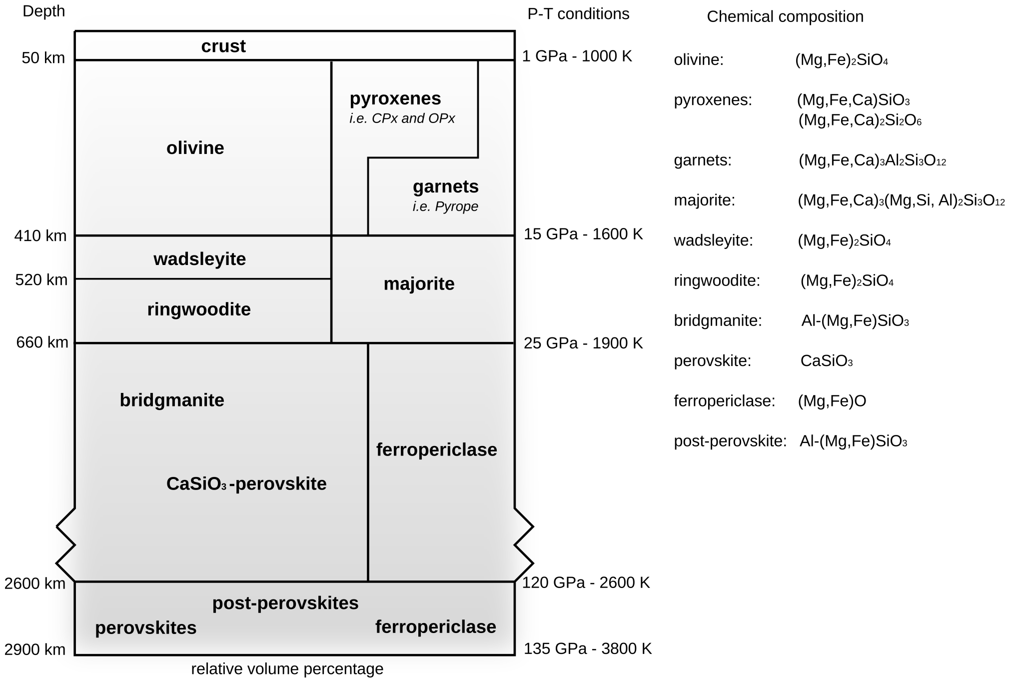

Figure 1.2: *Simplified radial distribution of the mineralogy for a pyrolitic composition of the Earth's mantle as a function of depth, volumetric mantle fraction, pressure and temperature.*

rials serve as anchor points for the geotherm. The P-T phase diagram for the relevant pressure range for a given mineral assemblage of the Earth's mantle can therefore be determined by mineral physics theory. Together with the revealed adiabaticity of the Earth's mantle, supported through the analysis of the Earth's radial eigenvibrations, it has been possible to model the Earth's geotherm (Anderson 1982; Ono 2008).

To summarize the main findings with respect to the radial composition of the Earth's mantle: the main constituent, which is estimated to form about 50-60% of the volume percentage of the upper mantle, is $(Mg,Fe)_2SiO_4$ olivine. This mineral has an orthorhombic crystal structure *Pbnm* that is no longer stable at the pressure and temperature conditions around a depth of 410 km and transforms into the closer packed $(Mg,Fe)_2SiO_4$ wadsleyite which defines the beginning of the transition zone, before it transforms into the even closer packed spinel $(Mg,Fe)_2SiO_4$ ringwoodite at 520 km depth. These phase transformations are purely polymorphic, which means that the phase transition of the material is characterized by a change in crystal structure with conservation of the chemical composition. Besides olivine, the upper mantle contains $(Mg,Fe,Ca)_2Si_2O_6$ pyroxenes and $(Mg,Fe,Ca)_3Al_2Si_3O_{12}$ garnets (*e.g.* pyrope). Apart from its main constituents wadsleyite and ringwoodite the transition zone is rich in majorite garnet. Then at 660 km depth, ringwoodite transforms in a mineral assemblage of Al-$(Mg,Fe)SiO_3$ bridgmanite (perovskite structure) together with minor percentages of $CaSiO_3$ perovskite and ferropericlase $(Mg,Fe)O$ (rock-salt structure). This region between 660-2600 km depth is known as the lower mantle. The bridgmanite is finally expected to transform at depths around 2600 km into its high-pressure polymorph post-perovskite in the Earth's lower mantle.

## 1.2 Plastic deformation in the transition zone

The evolution and dynamics of the Earth can be explained in terms of thermal solid-state convection of the Earth's silicate mantle, through which heat is transferred to the Earth's surface. The heterogeneous composition and structure of the Earth's interior governs the style of the overall convective pattern in the mantle. The region in the mantle between 410-660 km, known as the transition zone, plays an important role in the dynamics of the Earth's interior despite its relatively small volume in comparison to the upper but certainly to the lower mantle. Analysis from studies of isostatic post-glacial rebound has led to first order estimates of the radial distribution of the viscosity of the Earth's mantle, based on the initially proposed theory of Haskell (1935). Most models predict a gradual increase in viscosity from the upper into the lower mantle over the transition zone. The radial viscosity profile however is hardly constrained and uncertainties in the local variations may be as large as three to four orders of magnitude (Ricard and Wuming 1991; Mitrovica and Forte 2004). An other source of information comes from seismic tomography to determine the internal seismic wave speed structure of the Earth. This leads to imaging of the Earth's interior from the analysis that can be interpreted in terms of seismic wave speed differences as a consequence of thermal, chemical or structural anomalies or as a combination. Despite overall poor resolution, due to a sparse distribution of seismic sources and global record coverage, seismic tomography has revealed the subduction of slabs as being part of the convective system. Former studies report about the stagnation of slabs, as subducting lithosphere tends to flatten laterally, up to over a few thousand kilometers within the transition zone or just below (around 1000 km depth) (van der Hilst *et al.* 1991; van der Hilst *et al.* 1997; Tajima and Grand 1995; Grand *et al.* 1997; Fukao *et al.* 2001; Grand 2002; Zhao 2004; Fukao and Obayashi 2013). The same studies report, on the other hand, that at other places, slabs seem also to penetrate unhindered through the transition zone. So far, we dealt with information concerning the present-day-state of the Earth's interior. In addition, studies of forward numerical modelling on mantle convection, in particular the self-consistent thermo-chemical convection models (Tackley 2000) show that it is impossible to reproduce an Earth like convective system, *i.e.* with a plate-tectonic setting, without having a viscosity jump in one form or another, somewhere in the mid-mantle. These are all indications that the transition zone may play a vital role in the dynamics of the Earth's interior and as such we focus our study on this particular zone in the Earth's mantle.

Solid-state flow in the Earth's mantle is controlled by viscosity that varies with depth as function of the crystal chemistry, pressure and temperature. Plastic deformation of minerals is the fundamental underlying mechanism that determines the local viscosity in the Earth's mantle. The Earth's mantle mainly consists of crystalline solids: silicates and oxides. Besides their chemical composition these solids are characterized by an orderly arrangement of atoms into a crystalline lattice. It is specifically the motion of lattice defects, which are the carriers of solid-state deformation, that produces the strain responsible for plastic flow in extreme conditions of the deep Earth. There is a large number of defects that may exist in (poly)crystalline materials, *e.g.* starting from grain boudaries, lattice vacancies, intersticials, impurities, dislocations and disclinations. Line defects or dislocations are considered to be one of the most efficient defects contributing to intracrystalline deformation, on which we would like to concentrate in relation to the major phases of the transition zone: wadsleyite and ringwoodite. In the next section we intend to review what is already known about the minerals wadsleyite and ringwoodite and their plasticity due to deformation experiments and numerical modelling that have been developed. Special attention will be payed to (microstructural) studies of dislocations present in those materials.

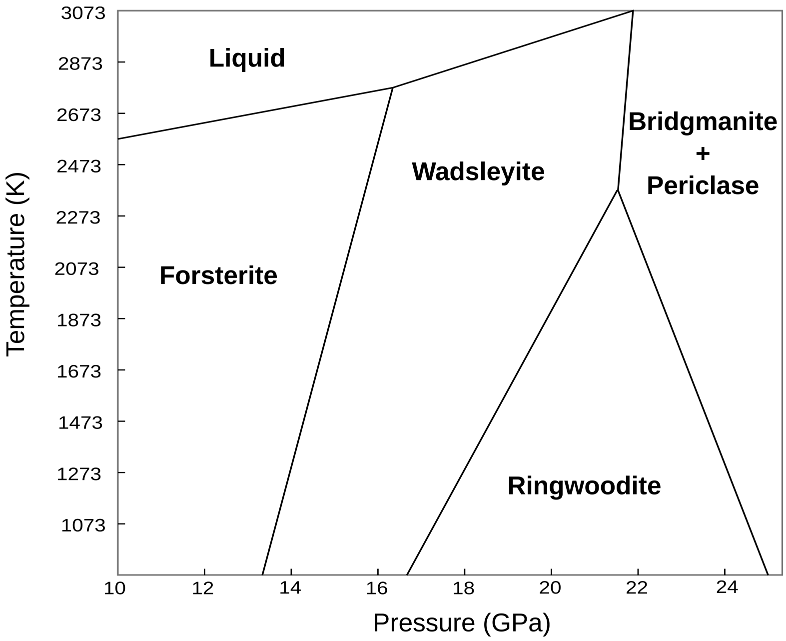

Figure 1.3: *Phase diagram of the $Mg_2SiO_4$ system. The illustration is based upon Fei* et al. *(1990).*

## 1.3 Wadsleyite

### 1.3.1 Crystal structure and natural occurrence

$(Fe,Mg)_2SiO_4$ wadsleyite is the major consituent of the upper transition zone that ranges from a depth of 410-520 km, at pressures ranging from $13-18$ GPa and temperatures between $1600-1800$ K. It is a high-pressure polymorph of and about 8% more dense than the most abundant upper mantle mineral $(Mg,Fe)_2SiO_4$ olivine (Agee 1998). The seismic discontuity that is globally found at 410 km depth is widely accepted to be the consequence of the phase transformation of olivine into its denser high pressure-polymorph wadsleyite. The seismic discontinuity is therefore due to the accompanying changes in physical properties between both polymorphs (Goldschmidt 1931; Ringwood and Major 1966; Akimoto and Sato 1968; Irifune and Ringwood 1987; Agee 1998). Wadsleyite is stable in the Earth's mantle until a depth of about 520 km for which the stability field with respect to $Mg_2SiO_4$ wadsleyite is illustrated in the phase diagram of the $Mg_2SiO_4$ system as shown in Fig. 1.3.

The crystal structure of wadsleyite consists of polyhedral $(SiO_4)^{4-}$ and $(MgO_6)^{10-}$ units where pairs of the $(SiO_4)^{4-}$ tetrahedra share a vertex to form isolated double tetrahedra groups of $(Si_2O_7)^{6-}$. Wadsleyite belongs as such to the sorosilicates as being part of the silicate minerals. Wadsleyite exhibits an orthorhombic crystal structure of space group *Imma*. The orthorhombic crystal structure may equally be understood as a distorted cubic close packed arrangement of the oxygen sublattice with the $Mg^{2+}$, $Fe^{2+}$ and $Si^{4+}$ cations placed at the octahedral and tetrahedral sites. The unit cell parameters of wadsleyite at 18.5 GPa have been determined experimentally by Horiuchi and Sawamato (1981) as $a = 5.70$ Å , $b = 11.44$ Å , and $c = 8.26$ Å . The unit cell of wadsleyite can be seen in Fig. 1.4 and 1.5.

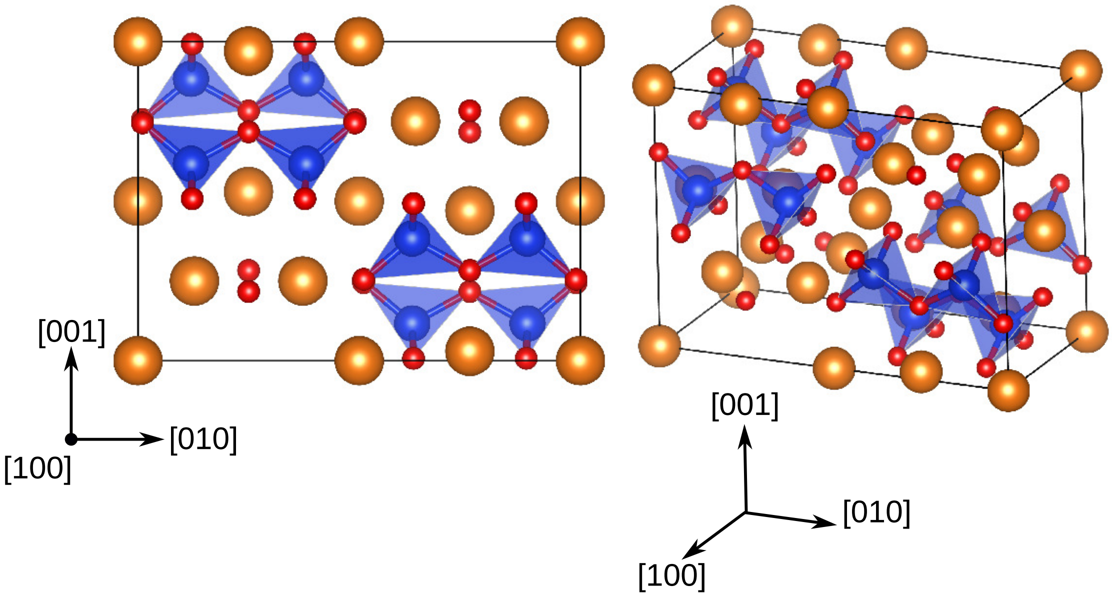

Figure 1.4: *Illustration of the unit cell of* $Mg_2SiO_4$ *wadsleyite that clearly shows the isolated* $(Si_2O_7)^{6-}$ *groups. The Mg, Si O atomic species are yellow, blue and red, respectively. The* $(SiO_4)^{4-}$ *tetrahedra are visualised in light blue.*

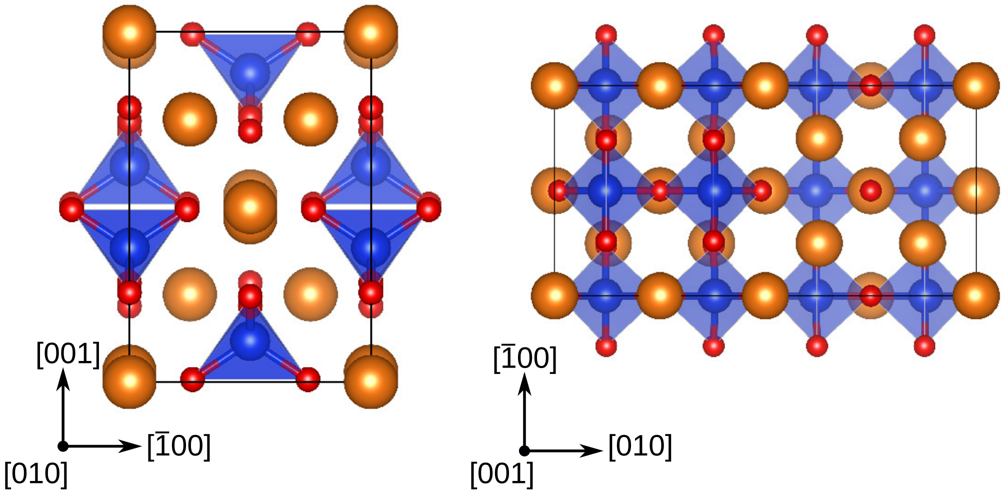

Figure 1.5: *Illustration of the unit cell of* $Mg_2SiO_4$ *wadsleyite with respect to the representation of the* $(SiO_4)^{4-}$ *tetrahedra colored in light blue. The Mg, Si O atomic species are yellow, blue and red, respectively.*

It was Ringwood and Major, in 1966, who first were able to synthesize wadsleyite which is not stable at ambient pressure and temperature conditions. However it was Putnis and Price in 1979 who discovered the natural occurrence of $(Mg,Fe)_2SiO_4$ wadsleyite in the Peace River meteorite (Price *et al.* 1983) that was eventually named after Dr. A. D. Wadsley.

### 1.3.2 Plasticity

The study of plastic deformation of wadsleyite has been started in the second half of the ninetees by experimental studies of so called stress-relaxation experiments. The experiments were performed by compressing powder samples (often San Carlos olivine) at ambient temperature after which the samples were heated and diffraction peak broadening could be monitored as a function of pressure, temperature and time, by X-ray diffraction (Weidner *et al.* 1992; Chen *et al.* 1998; Mosenfelder *et al.* 2000). These experimental data can be seen as a first order indicative measure of the strength of mineral phases which makes these experiments the pioneers of later work on effective plastic deformation that has been studied by the use of the multi-anvil apparatus and the rotational Drickamer apparatus (RDA) (Nishihara *et al.* 2008; Kawazoe *et al.* 2010; Kawazoe *et al.* 2013; Hustoft *et al.* 2013; Farla *et al.* 2015). The difficulties of conducting experiments on the plastic deformation of wadsleyite is its stability field at pressure and temperature conditions equal to those of the upper transition zone, depending on the type and amount of impurities it contains. A summary of the data available from experimental deformation on wadsleyite is shown in Fig. 1.6 as the applied stress or engineering stress as a function of temperature under steady state conditions.

The most remarkable of the experimental results in terms of plastic deformation is the relatively large effective flow stresses determined during deformation in the RDA in comparison to what has been found on olivine under upper mantle conditions $\sim \sigma \simeq 1.5$ GPa (Kawazoe *et al.* 2009; Nishihara *et al.* 2008).

The first who used the multi-anvil cell to deform wadsleyite, starting with monocrys-

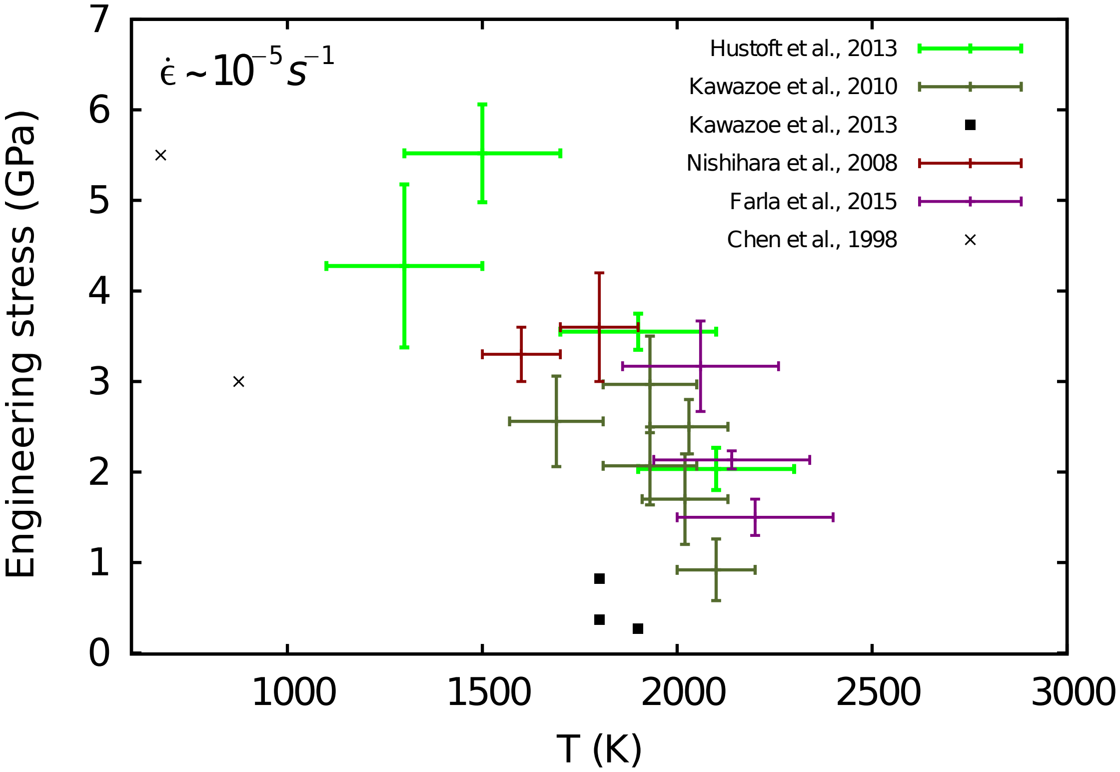

Figure 1.6: *Assemblage of the data gathered by the experimental deformation experiments on wadsleyite.*

talline San Carlos olivine to be transformed into wadsleyite at 16 GPa and ∼ 1900 K, was Sharp *et al.* (1994) and Dupas *et al.* (1994), but starting with synthetic harzburgite to be transformed into wadsleyite at 14 GPa and ∼ 1700 K. From these studies, dislocations with Burgers vector [100] have been identified, as well as the existence of the (010) stacking faults as observed in wadsleyite samples of the Peace River meteorite. It also resulted in the first observations of individual partial dislocations with Burgers vector $1/2\langle 111\rangle$. These findings were confirmed and extended by Dupas-Bruzek *et al.* (1998) and the experimental studies performed by Thurel and Cordier (2003), Thurel *et al.* (2003) and Thurel, Douin and Cordier (2003). In the latter three studies, deformation experiments were performed on recovered wadsleyite samples, synthesized from synthetic forsterite powder which has been transformed into wadsleyite, both supported by compression and shear in separate experimental runs using a multi-anvil cell device, after which the following nine slip systems were identified by transmission electron microscopy (TEM):

- [100](010)
- [100](001)
- [100]{011}
- [100]{021}
- $1/2\langle 111\rangle \{101\}$
- [010](001)
- [010]{101}
- [001](010)
- $\langle 101\rangle$ (010)

Thurel (2001) estimates that the glide systems most probable to operate under transition zone conditions in order of likelihood can be listed as follows:

- $1/2\langle 111\rangle \{101\}$
- [100](010)
- [100](001)
- [100]{011}
- [100]{021}

Dupras-Bruzek *et al.* (1998) conclude from microstructural analysis that dislocation climb appears to be very active at temperatures above 1200 K. These findings are supported by Mosenfelder et al. (2000) who interpreted the observation of the formation of subgrains (polygonization) in terms of climb activity. Thurel, Douin and Cordier (2003), on the other hand, do not find strong evidence of the dislocation climb after microstructural analysis and argues that the microstructures observed in studies of Dupras-Bruzek *et al.* (1998) and Mosenfelder *et al.* (2000) could as well be explained in terms of the olivine-wadsleyite phase transformation.

Finally, two main studies in the field of computational mineral physics with respect to intracrystalline plasticity of wadsleyite have to be addressed. In 2010, Walker calculated the core structure and energies of the [100] and [001] screw dislocations based on a cluster-based elastic-atomistic method using the *THB1* empirical potential. He concluded that the movement of the [001] screw dislocation will be inhibited by the necessity to destroy strong Si-O bonds contrary to the motion of the [100]-screw dislocations. This may give an explanation of the relatively large presence of dislocations with [100] Burgers vector in contrast to those with [001] Burgers vector as observed in experiments.

Metsue *et al.* (2010) used a Peierls-Nabarro based finite-element method to calculate the dislocation core structures and their potential activity through calculations of the Peierls stress that can be seen as the critical resolved shear stress ($CRSS$) at 0 K. They have taken into account the following slip systems: [100](010), [100](001), [010](100), [010](001), [001](010), $1/2\langle 111\rangle\{101\}$, for both the screw and edge dislocations. The calculations relied on the $\gamma$-surfaces of the potential slip planes, which were calculated by the use of the *THB1* empirical potential. The easiest slip systems were found to be the $1/2\langle 111\rangle\{101\}$ and [100](010) which is supported by the experimental observations as given above. Both screw and edge dislocations belonging to the $1/2\langle 111\rangle\{101\}$ and

[100](010) slip systems are characterized by a dissociation into collinear partials, separated by a stacking fault: $1/2\langle111\rangle \rightarrow 2/10\langle111\rangle+3/10\langle111\rangle$ and $[100] \rightarrow 1/2[100]+1/2[100]$.

## 1.4 Ringwoodite

### 1.4.1 Crystal structure and natural occurrence

$(Fe,Mg)_2SiO_4$ ringwoodite is the major consituent of the lower transition zone that ranges from a depth of 520-660 km, at pressures ranging form $18-25$ GPa and temperatures between $1700-1900$ K. It is about 4% more dense than its lower high-pressure polymorph wadsleyite and associated with the seismic discontinuity that is found at 520 km depth as the consequence of the phase transformation of wadsleyite into its denser higher pressure-polymorph ringwoodite. Ringwoodite is stable in the Earth's mantle until a depth of about 660 km for which the stability field with respect to $Mg_2SiO_4$ wadsleyite is illustrated in a the phase diagram of the $Mg_2SiO_4$ system as shown in Fig. 1.3.

Ringwoodite exhibits a spinel structure of space group *Fd3m* due to the cubic-close packing of the oxygen sublattice, where the $Mg^{2+}$ and $Fe^{2+}$ cations are embedded at the octahedral and the $Si^{4+}$ cations at the tetrahedral interstices respectively, in such a way that the $(SiO_4)^{4-}$ units form isolated tetrehedra. The unit cell parameter of ringwoodite as determined by Ringwood and Major (1970) and Meng *et al.* (1994) at ambient pressure and temperature conditions is equal to $a$=8.071 Å . Figures 1.7 and 1.8 show the unit cell and the crystal symmetry of ringwoodite.

Ringwoodite was first observed and identified in the Tenham meteorite by Binns *et al.* in 1969 and later in other shocked meteorites as the Peace River meteorite (Price *et al.* 1982), for which both samples were characterized and analyzed by TEM. However, after the work of Goldschmidt (1931) on $Mg_2GeO_4$ analogues, it was already Bernal who

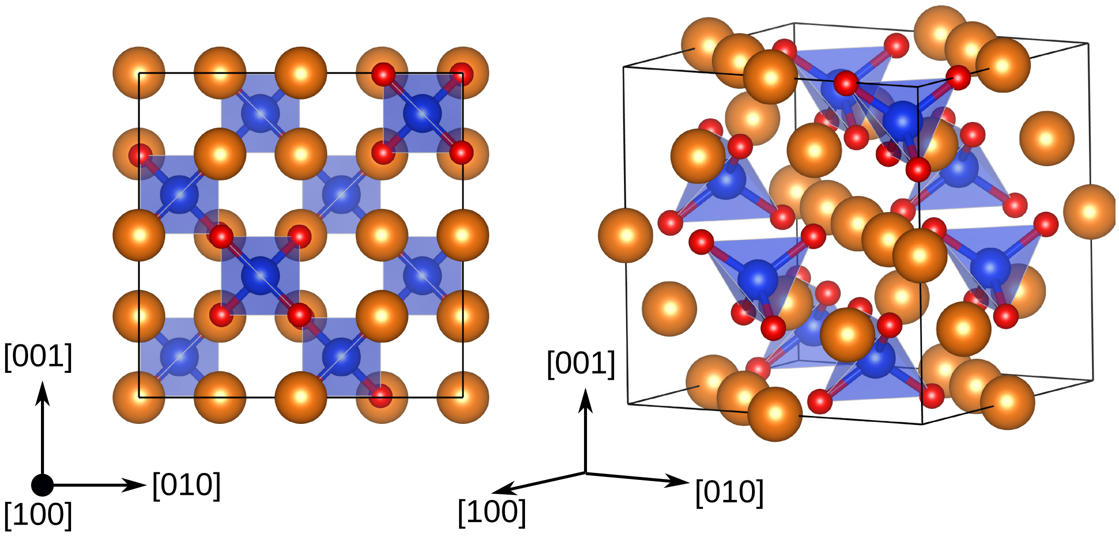

Figure 1.7: *Illustration of the unit cell of $Mg_2SiO_4$ ringwoodite that shows the isolated $(SiO_4)^{4-}$ groups. The Mg, Si O atomic species are yellow, blue and red, respectively. The $(SiO_4)^{4-}$ tetrahedra are visualised in light blue.*

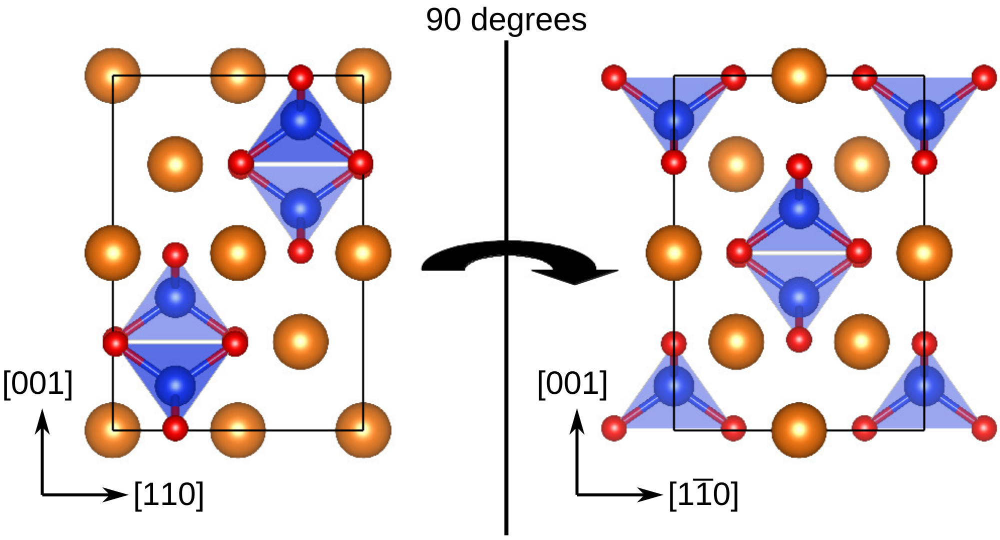

Figure 1.8: *Illustration of the unit cell of $Mg_2SiO_4$ ringwoodite with respect to the representation of the $(SiO_4)^{4-}$ tetrahedra colored in light blue. The Mg, Si O atomic species are yellow, blue and red, respectively.*

in 1936 proposed a high-pressure polymorph of olivine to exist with a more compact spinel crystal structure. Finally, $(Mg,Fe)_2SiO_4$ ringwoodite was named after Prof. A. E. Ringwood. Later it has been observed that ringwoodite crystals in the aforementioned meteorite samples contain lots of stacking faults. It was Madon and Poirier in 1980 who first observed the existence of dislocations within $(Mg,Fe)_2SiO_4$ spinel grains of the meteoritic samples.

### 1.4.2 Plasticity

The first techniques used to estimate the strength of ringwoodite, as in the case of wadsleyite, were stress relaxation experiments performed by monitoring diffraction peak broading with the use of X-ray diffraction techniques (Chen *et al.*, 1998; Xu *et al.*, 2003). It was Karato *et al.* in 1998 who performed the first deformation experiment on $(Mg,Fe)_2SiO_4$ ringwoodite at 16 GPa and 1600 K using a multi-anvil apparatus. The starting material was a synthetic olivine that has been compressed and heated until the phase transformation into ringwoodite after which it has undergone shear deformation during the same run. After TEM analysis of the recovered samples, they identified dislocations belonging the $1/2\langle 110\rangle\{111\}$ and $1/2\langle 110\rangle\{001\}$ slip systems. A study of Thurel (2001) shows presence of slip of the $1/2\langle 110\rangle$ dislocations in the $\{111\}$ and $\{110\}$ planes by using a multi-anvil apparatus. After being synthesized, the ringwoodite samples were deformed by compression and shear deformation and analysed by TEM studies. The principal slip direction in $(Mg,Fe)_2SiO_4$ ringwoodite is always observed to be parallel to the $\langle 110\rangle$ direction. The $1/2\langle 110\rangle$ is the shortest perfect and therefore unique Burgers vector in ringwoodite and in fact in minerals having the spinel structure. These $1/2\langle 110\rangle$ dislocations glide mainly in the $\{110\}$, $\{111\}$ and $\{001\}$ as observed. Earlier studies (Duclos 1981; Mitchell 1999; Welsch *et al.* 1974; Mitchell *et al.* 1976) on spinel analogues as $MgAl_2O_4$ and $MgO{\cdot}nAl_2O_3$ support that the Burgers vector direction of dislocations in spinels are always found to be equal to $1/2\langle 110\rangle$ which glide primarily in the $\{110\}$, $\{111\}$ as well as in the $\{001\}$ planes. The latter studies often report on the dissociation into partials separated by a stacking fault, something that was not yet observed in $(Mg,Fe)_2SiO_4$ ringwoodite by TEM studies conducted. However, stacking faults of the type $^1/_4\langle 110\rangle\{011\}$ were both observed in studies of ringwoodite grains in samples of the Tenham meteorite and in $Mg_2GeO_4$ analogues studied by Vaughan and Kohlstedt (1981). A study of Mitchell (1999) on $MgO{\cdot}nAl_2O_3$ spinel shows that dislocation networks are commonly observed with nodes extended by climb or glide into $^1/_4\langle 110\rangle$ partial dislocations. Microstructures associated with climb appear to become more important in the deformed samples at higher temperatures.

Besides the deformation experiment on ringwoodite by Karato *et al.* (1998), other deformation experiments were undertaken using the diamond avil cell (DAC) (Meade and Jeanloz 1990; Kavner and Duffy 2001; Wenk *et al.* 2004) and the D-DIA (multi-anvil apparatus) (Nishihara *et al.* 2005; Wenk *et al.* 2005) for deformation at ambient temperature and recently by deforming ringwoodite in the RDA at pressure and temperature conditions equivalent to the transition zone (Hustoft *et al.* 2013; Miyagi *et al.* 2014). A summary of the data available from experimental deformation on ringwoodite is shown in Fig. 1.9 for the engineering stress as a function of temperature under steady state conditions.

As for wadsleyite, we would like to note that the stresses determined by the deformation experiments using the RDA are relatively elevated in comparison to what has been found on olivine under upper mantle conditions ($\sigma \simeq 1.5$ GPa) by Kawazoe *et al.* (2009) and Nishihara *et al.* (2008).

Finally, one extensive theoretical study of Carrez *et al.* (2006) on the intracrystalline plasticity of $Mg_2SiO_4$ ringwoodite has been undertaken so far. They have used a 1-D Peierls-Nabarro model to calculate the dislocation core structures and their potential activity through calculations of the Peierls stress. They have taken into account the following slip systems: $^1/_2\langle 110\rangle\{001\}$, $^1/_2\langle 110\rangle\{110\}$ and $^1/_2\langle 110\rangle\{111\}$ by modeling both

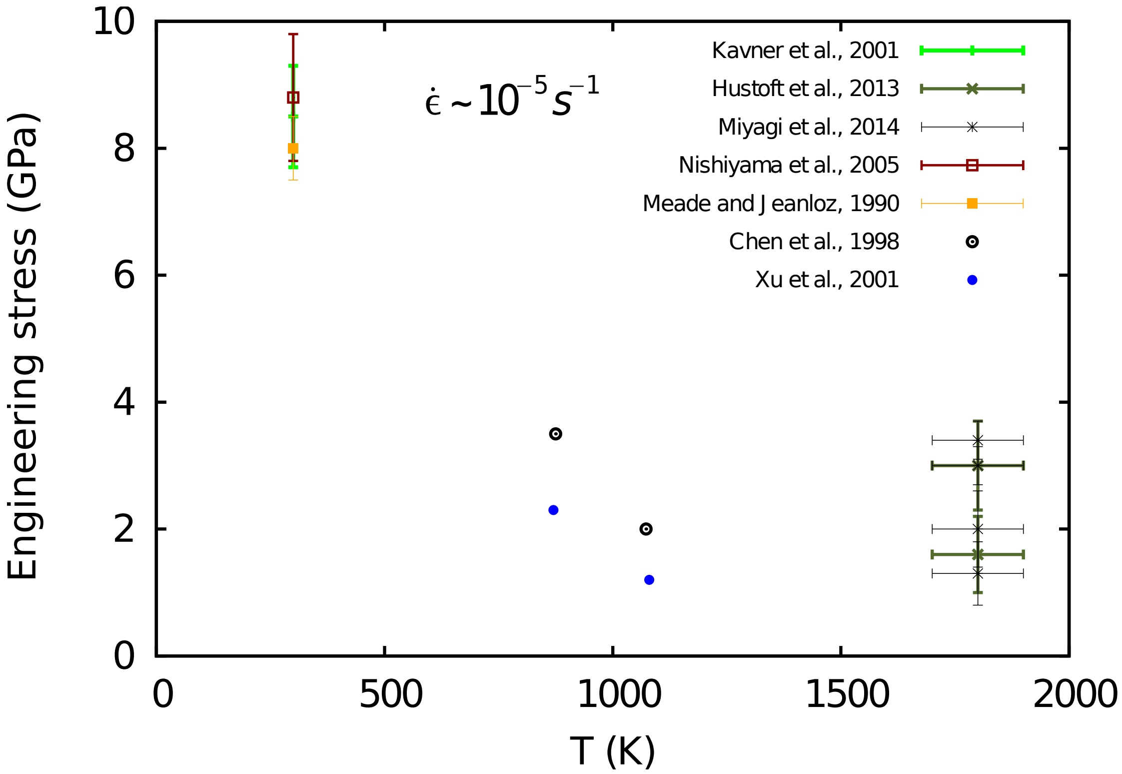

Figure 1.9: *Assemblage of the data gathered by the experimental deformation experiments on ringwoodite.*

the screw and edge dislocations. The calculations relied on the $\gamma$-surfaces of the potential slip planes, which were calculated using *ab initio* based density functional theory (DFT) calculations. This revealed that all core structures of the respective $1/2\langle 110\rangle$ screw and edge dislocations are extended with Burgers vector reactions that split the $1/2\langle 110\rangle$ Burgers vector into two partials dislocations separated by a stacking fault. Further viscoplastic self-constistent modeling (VPSC) was undertaken that was parametrized by the former Peierls stress analysis. The results emphasized that glide of the $1/2\langle 110\rangle\{111\}$ is likely to dominate the deformation followed by $1/2\langle 110\rangle\{110\}$ at low temperature conditions, which is supported by microstructural studies of preferred orientations in ringwoodite by Miyagi *et al.* (2014), Wenk *et al.* (2004) and Wenk *et al.* (2005).

## 1.5 Modelling dislocation glide in the transition zone

Mineral physics plays a central role in studying the dynamics of the Earth's interior as it provides relations between the intensive (crystal chemistry, stress, viscosity, pressure, temperature, *etc.*) and extensive variables (strain rate, free enthalpy, momentum, length, volume, mass, *etc.*) through constitutive equations, describing the rheology intrinsic to solid-state deformation.

A lot of effort has been dedicated over the last decades to deformation experiments at high pressure and temperature conditions of the deep Earth's interior in the field of mineral physics, *i.e.* multi-anvil appartus (Cordier and Rubie 2001) and D-DIA (Wang *et al.* 2003), diamond anvil cell and rotational Drickamer apparatus (Yamazaki and Karato 2001). It however still remains difficult to conduct experimental deformation at high pressure ($\sim$ 18 GPa) and high temperature ($\sim$ 1700 K) conditions of the transition zone. Furthermore, the rheological flow laws as constitutive equations deduced from experiments at typical laboratory strain rates of $10^{-5}$ $s^{-1}$ or larger, need to be extrapolated to the extremely low strain rate conditions of $10^{-16}$ $s^{-1}$ in the Earth's mantle. Finally, it has to be mentioned as well that the deformation mechanisms responsible for plastic deformation at laboratory strain rates may be different than under conditions of the deep Earth.

Computational mineral physics, however, provides alternative approaches to study plastic deformation of the high-pressure phases of the Earth's interior. In the present study, we would like to focus on the intracrystalline plasticity of the end-member phases $Mg_2SiO_4$ wadsleyite and ringwoodite at the typical pressure conditions of 15 GPa and 20 GPa, respectively. In particular, the aim is to determine the glide mobility of the rate controlling dislocations as a function of stress and temperature in order to derive the constitutive equations corresponding to glide. The research finds its foundation in the multiscale modelling approach of monocrystalline MgO (Amodeo *et al.* 2011; Amodeo *et al.* 2012; Cordier *et al.* 2012).

The description of intracrystalline plasticity, in our modelling, will be based on the mobility of dislocations that glide on specific crystallographic planes. To be able to glide, dislocations must overcome their intrinsic lattice friction which occurs through stress-assisted thermally-activated processes. This glide process is controlled by lattice friction if the temperature is lower than a critical temperature (commonly referred to as the athermal temperature $T_a$), when the critical resolved shear stress (CRSS) is temperature dependent. Dislocations can be subdived into two end-member characters: screw and edge dislocations. If a dislocation bows out under the action of resolved shear stress, in materials with high lattice friction, segments with the faster moving characters will produce a small amount of strain and leave behind long segments of the slow moving characters which will account for most of the plastic deformation produced. By using this approach, the model is also able to forecast the temperature threshold above which dislocation-dislocation interactions become essentially important to determine the dislocation mobility. The kinematics of glide below $\mathrm{T}_a$ depend strongly on the specific atomic arrangements that build the dislocation cores. The core structures of the potential dislocations will be calculated using the Peierls-Nabarro-Galerkin (PNG) method, a generalization of the Peierls-Nabarro (PN) model (Peierls 1940; Nabarro 1947). These calculations, once more, rely on first principle simulations of generalized stacking fault surfaces (or $\gamma$-surfaces). The latter allow us to address the effect of pressure on atomic bonding accurately. Lattice friction experienced by the dislocations belonging to the potential slip systems, is then calculated and quantified by the Peierls potential and its derivative, the Peierls stress. Finally, the glide mobility will be derived that results from thermally-activated motion of dislocations over their Peierls barriers by nucleation and propagation of unstable kink-pairs. We propose to describe this process through an elastic interaction model, initially proposed by Koizumi *et al.* (1993) and applied by Amodeo *et al.* (2011) on MgO. In the present work, this approach is extended to dissociated dislocations as they occur in wadsleyite and ringwoodite, which will be elucidated by our results of the dislocation core structures. The elastic interaction model will as such be adapted to handle kink-pair nucleation on partial dislocations. It is the core extension of the dissociated dislocations and the presence of the stacking faults that is finally determining the motion of the dislocation below the athermal temperature $T_a$. Dislocation mobilities are determined from the stress dependence on the nucleation rate of kink-pairs. The collective behaviour of dislocations, which finally determines the overall rate of deformation, will be obtained by linking the macroscopic strain rate to the plastic flow through the dislocation mobility under conditions both relevant to experiments and to the Earth's mantle.

The constitutive equations associated to pure single slip dislocation glide are compared to the data of experimentally deformed wadsleyite and ringwoodite. This enables us to address the potential contribution of dislocation glide during plastic deformation of both minerals under pressure, temperature and strain rate conditions of the transition zone. Implications for the rheology of the transition zone and the possible consequences for geodynamics will be discussed at the end of chapter three and in chapter four.

# 2 Methods and models

The numerical multiscale modelling approach we present in this study, relies on multiphysics at different scales in space and time. In this chapter, we present and describe the three main steps upon which the theoretical study is based. In the first part of the first section, we start to describe the *ab initio* based density functional theory used to calculate so called generalized stacking fault surfaces ($\gamma$-surfaces). In the second part of the first section, we will deal with the concept of $\gamma$-surfaces and its relation to dislocations. This is a key stage of the model where the influence of pressure on the electronic structure of wadsleyite and ringwoodite, and hence on their crystal structure, is accurately taken into account through first-principles calculations. The $\gamma$-surfaces provide an efficient tool to search for the low energy cost shear paths in the crystal. As such, $\gamma$-surfaces are one of the key ingredients to model dislocation core structures with the PNG-model which will be dealt with in the second section of this chapter. Lattice friction, then is quantified by a classical evaluation of the Peierls potential in the framework of the PN model (Peierls 1940; Nabarro 1947). The third and last section of this chapter describes the thermally-actived mechanism by which a dislocation line overcomes its lattice friction. This is presented by an elastic interaction model which allows us to calculate the critical configuration that triggers elementary displacements of dislocations. It allows us to obtain the critical enthalpy associated to a critical dislocation bow-out by the extremum of the corresponding total energy variation. The dislocation mobility and subsequent single slip collective behaviour of dislocations will be determined by the above results. Finally, we end this chapter by presenting a benchmark study on the elastic interaction model applied to monocrystalline $SrTiO_3$ perovskite. We made our choice for $SrTiO_3$ perovskite, since it is, for the high pressure minerals that constitute the Earth's mantle, experimentally still impossible to obtain very accurate data of the $CRSS$ as a function of $T$ related to dislocations belonging to a given slip system in single crystals.

## 2.1 Ab initio calculations: $\gamma$-Surfaces and elastic constants

---

*We must be clear that when it comes to atoms,*

*language can be used only as in poetry.*

Niels Bohr.

(quoted by W. Heisenberg, translation A.J. Pomerans in *Physics and Beyond: Encounters and Conversations 1971.*)

---

The aim of this chapter is to describe the conceptual idea and the use of generalized stacking fault surfaces (hereafter called $\gamma$-surfaces) and the way in which they, together with the elastic constants, are calculated by taking into account the appropriate pressure conditions for which $Mg_2SiO_4$ wadsleyite and ringwoodite are stable in the transition zone.

To begin with, a $\gamma$-surface is an energy landscape describing the excess energy as a result of a discontinuous shear of the crystal structure along a given (slip) plane. Therefore, both the $\gamma$-surfaces and the elastic constants involve knowledge on the total energy change of a distorted system composed of one or at least a small number of primitive cells of the respective material. An atomistic approach is necessary in order to take into account the intrinsic properties of both olivine polymorphs as accurately as possible. Elementary quantum mechanics tells us that the wavefunction $\Psi$ describes the quantum state of a given system. *Ab initio* atomistic calculations are based on density functional theory (DFT) and rely on solving the Schrödinger equation of a (many-particle) system without the need of any adjustable parameters. DFT is restricted to the description of the electronic structure of atoms in the system through which the total energy of the system's ground state can be solved for through Schrödinger's equation. As such, this method is very suitable to incorporate the intrinsic pressure-induced variations in the electronic structure captured in the total energy of the system. Although, this is a first-principles and self-consistent method and as such the most accurate to use in atomic scale modelling, it is limited to study systems with a restricted number of atoms because of its otherwise too large computational costs. As such it would be impossible to perform *ab initio* calculations to study dislocation core structures in complex materials such as minerals with primitive cells already containing a large number of atoms. However, it is very suitable to use for systems containing a few hundred of atoms such as in case of the calculation of $\gamma$-surfaces of complex silicates and of their material properties as the elastic constants.

### 2.1.1 Ab initio calculations: Theory

*Ab initio* calculations are based on quantum mechanics and rely as such on solving the non-relativistic time-independent Schrödinger equation:

$$H\Psi(\mathbf{r}_1, \mathbf{r}_2, ..., \mathbf{r}_M, \mathbf{R}_1, \mathbf{R}_2, ..., \mathbf{R}_N) = E\Psi(\mathbf{r}_1, \mathbf{r}_2, ..., \mathbf{r}_M, \mathbf{R}_1, \mathbf{R}_2, ..., \mathbf{R}_N) \tag{2.1}$$

in order to to obtain the total energy $E$ of a system of $M$ electrons at positions $\boldsymbol{r_i}$ and $N$ nuclei at positions $\boldsymbol{R_i}$. The Hamiltonian operator $H$ of a many-particle system characterized by the wavefunction $\Psi$ is defined as:

$$H = T + V \tag{2.2}$$

and can be decomposed into the following operators $T$ and $V$:

1. ***The kinetic energy operator*** $T = T_E + T_N$, where $T_E$ and $T_N$ are related to the kinetic energy of the electrons and the nuclei, respectively.

2. ***The potential energy operator*** $V = V_{E,E} + V_{N,N} + V_{E,N}$, where $V_{E,E}$, $V_{N,N}$ and $V_{E,N}$ are related to the interaction energy between the electrons, the nuclei and between the electrons and nuclei respectively.

It is impossible to obtain the exact wavefunction $\Psi$ in Eq. 2.1 by solving the Schrödinger equation for a system containing more than two electrons let alone for a large number of particles, so that a series of approximations have to be made in order to solve Eq. 2.1.

#### 2.1.1.1 Born-Oppenheimer approximation

One of the basic assumptions on which DFT relies was first proposed by Born and Oppenheimer in 1927 and is known as the Born-Oppenheimer or adiabatic approximation. The approximation is based on the observation that electrons are much lighter particles than the nuclei and therefore exhibit higher velocities: the electrons move more rapidly than the heavier nuclei to which the electrons are bound. As a consequence, the kinetic energy of the nuclei is negligible with respect to those of the electrons $T_E \gg T_N \rightarrow T_E + T_N \simeq T_E$ so that the Hamiltonian (Eq. 2.2) reduces to:

$$H = T_E + V_{E,E} + V_{E,N} + E_{N,N} \tag{2.3}$$

The interaction energy $V_{N,N}$ between the approximately stationary positioned nuclei has therefore been replaced by a constant $E_{N,N}$. As a consequence, $E_{N,N}$ does not play a role in solving the Schrödinger equation and will consequently be eliminated in the Hamiltonian. The Schrödinger equation can be further simplified by describing the interactions between the nuclei and the electrons in the form of an external potential $V(\boldsymbol{r})$ acting on the electrons so that the wave function $\Psi$ in Eq. 2.1 only depends on the electronic coordinates. The Hamiltonian $H$ for a single electron moving in an external potential $\epsilon(\boldsymbol{r})$ that mimicks the interaction between the electron and the nucleus to which it is bound, can thus be described by:

$$H = T_E + V_{E,N} = -\frac{\hbar^2 \nabla^2}{2m} + \epsilon(\mathbf{r}) \tag{2.4}$$

with $\hbar$ and $m$ equal to the reduced Planck constant and the electron mass respectively. In the case of a many-particle problem, where more electrons are moving in a potential, for example due to a crystalline lattice, the Schrödinger equation becomes:

$$H\Psi(\mathbf{r}_1, \mathbf{r}_2, ..., \mathbf{r}_M) = E\Psi(\mathbf{r}_1, \mathbf{r}_2, ..., \mathbf{r}_M) \tag{2.5}$$

with a Hamiltonian given by:

$$H = T_E + \{V_{E,N} + V_{E,E}\} = \sum_{i}^{M} -\frac{\hbar^2 \nabla_i^2}{2m} + \{v(\mathbf{r})\} \tag{2.6}$$

where the potential functional $v(\mathbf{r})$ corresponds to:

$$v(\mathbf{r}) = \sum_{i}^{M} V(\mathbf{r}_i) + \sum_{i<j} \frac{q^2}{|\mathbf{r}_i - \mathbf{r}_j|} \tag{2.7}$$

The number of electrons is given by $M$. The first term on the right hand side of Eq. 2.7 describes the interactions between the electrons and the external potential, the second term is equal to the electron-electron interactions (Coulomb interaction) with $q$ being the electron charge. The interactions between the nuclei $E_{N,N}$ is left out as it is a constant. Different methods can be adopted to solve the above many-body problem in a self-consistent way. One of the methods is by using the Hartree Fock theory which is based on a simple approximation of the true many-body wavefunction. We however will use a more advanced approach proposed by density functional theory (DFT) for which the framework was constructed in 1965 by Hohenberg and Kohn.

#### 2.1.1.2 Density functional theory

The classical approach to tackle the Schrödinger equation is by first defining the external potential $V_{ext}(\boldsymbol{r})$ that determines the system (*e.g.* atom, molecule, crystal lattice, ...) and solve the wavefunction $\Psi$ which gives access to the observables of the systems through

$\langle\Psi^*|...|\Psi\rangle$. One of the observables that can be calculated is the electronic density $n(\boldsymbol{r})$:

$$n(\mathbf{r}) = M \int d^3r_2 \int d^3r_3 \int d^3r_M \Psi^*(\mathbf{r}, \mathbf{r}_2, ..., \mathbf{r}_M)\Psi(\mathbf{r}, \mathbf{r}_2, ..., \mathbf{r}_M) \tag{2.8}$$

Hohenberg and Kohn (1965) stated in their Hohenberg-Kohn (HK) theorem that Eq. 2.8 can be inverted for all ground states: a ground-state wave function $\Psi_0$ is a functional of the ground-state density $n_0$. This implies that all ground-state observables are functionals of $n_0$. It opens the opportunity to replace the many electron problem to which our quantum mechanical system has been reduced, by a one electron system that interacts with an external potential $V_{ext}$ through the formulation of the total energy of the system $E_t[n]$ as a function of the electronic density $n(\boldsymbol{r})$:

$$E_t[n] = T_s[n] + \int V_{ext}(\mathbf{r})n(\mathbf{r})d^3r + E_H[n] + E_{xc}[n] \tag{2.9}$$

where $T_s$ corresponds to the kinetic energy of an isolated electron and where $E_H$ is equal to the Coulomb self-interaction energy (Hartree energy). The latter describes the electrostatic self-interaction energy of the charge distribution $n(\mathbf{r})$ in terms of the electronic coordinates $\mathbf{r}$ and $\mathbf{r}'$:

$$E_H[n] = \frac{q^2}{2} \int d^3r \int d^3r' \frac{n(\mathbf{r})n(\mathbf{r}')}{|\mathbf{r} - \mathbf{r}'|} \tag{2.10}$$

The formulation of the total energy $E_t[n]$ of a system in terms of single-electron systems as in Eq 2.9 is the achievement of Kohn and Sham (1965). The approximation is based on the decomposition of the total energy of the system into a part that represents the energy of the non-interacting electrons (single electrons) and the residual part related to the interacting electrons. This is the way in which the kinetic energy functional $T_{kinetic}[n]$ and the Coulomb interaction functional $E_{coulomb}[n]$ are treated. The residual parts are described by the so called exchange-correlation functional $E_{xc}$ that contains the differences $T_{cor} = T_{kinetic} - T_s$ and $E_{cor+x} = E_{coulomb} - E_H$ for the kinetic and Coulomb functionals in which $T_{cor}$ contributes most to the correlation energy. $E_{cor+x}$ also contains the exchange functional $E_x$ which is due to corrections according to the Pauli exclusion principle. There is no general exact expression for the exchange-correlation functional $E_{xc}$ in terms of the electronic density so that it will depend on approximations that will be briefly described in the next sections.

The effective single electron approach as defined in the Kohn-Sham formulation of the total energy of the system allows us to determine the fundamental electronic ground state of the total system in a self consistent way. The essential problem lies in solving the density by minimization of the total energy $E_t[n]$ of the single electron system(s):

$$0 = \frac{\partial E_t[n]}{\partial n(\mathbf{r})} = \frac{\partial T_s[n]}{\partial n(\mathbf{r})} + V_s[n](\mathbf{r}) \tag{2.11}$$

so that the potential functional $V_s[n](\boldsymbol{r})$ in the Hamiltonian of the single-electron Schrödinger equation can be expressed as:

$$V_s[n](\boldsymbol{r}) = V[n](\boldsymbol{r}) + V_H[n](\boldsymbol{r}) + V_{xc}[n](\boldsymbol{r}) \tag{2.12}$$

where $V[n](\boldsymbol{r})$ corresponds to the external potential the electrons move in. Eq. 2.12 is known as the Kohn-Sham potential. Minimization of $E_t[n]$ can now be replaced by solving the Schrödinger-like Kohn-Sham equations of a single noninteracting electron system in the potential $V_s[n](\boldsymbol{r})$:

$$\left[-\frac{\hbar^2\nabla^2}{2m} + V_s[n](\mathbf{r})\right]\phi_i(\mathbf{r}) = \epsilon_i\phi_i \tag{2.13}$$

through which the density $n(\boldsymbol{r})$ of the original system can be obtained by the Kohn-Sham orbitals $\phi_i$:

$$n(\mathbf{r}) \equiv n_s(\mathbf{r}) = \sum_i^M f_i |\phi_i(\mathbf{r})|^2 \tag{2.14}$$

where $f_i$ corresponds the occupation of the $i$'th orbital. Note that there is a strong similarity between the insolvable Schrödinger equation of a many-particle system (Eq. 2.5) and the Kohn-Sham equations (KS) (Eq. 2.12 and 2.14).

The iterative scheme to solve the KS equations starts with an initial guess $n^0(\boldsymbol{r})$, so that the corresponding $V_s^0[n](\boldsymbol{r})$ can be calculated, through which the single-electron Schrödinger-like equation of the auxiliary system can be solved for the wavefunction $\phi_i^0$. A new density $n^1(\boldsymbol{r})$ can be calculated from the $\phi_i^0$ orbitals that allows to calculate again $V_s^1[n](\boldsymbol{r})$ to resolve the differential equation (Eq. 2.13). The iterative scheme is repeated until a predefined cutoff convergence criterion has been achieved. The solution of the KS-equations lead to the ground state electron charge density $n_0(\boldsymbol{r})$ and to the total ground state energy of the system for a fixed set of nuclei (Eq. 2.9). Finally, geometry optimization requires a second minimization scheme of the total energy of the system as a function of the atomic positions (*e.g.* relaxed crystal structure).

## 2.1.2 Ab initio calculations: Application

### 2.1.2.1 The exchange-correlation functionals

- **Local-density approximation**

  The most simple approach to define the exchange correlation functional is by assuming that both the exchange energy $E_x[n]$ and correlation energy $E_c[n]$ are local functionals of the electronic density:

$$E_{xc}^{LDA}[n] = \int n(\mathbf{r})\{E_x[n] + E_c[n]\} d^3r \tag{2.15}$$

where $E_x[n]$ and $E_c[n]$ are energy functionals related to a uniform electron gas (UEG). Although analytic expressions can be found for the exchange energy of a UEG, quantum Monte Carlo (QMC) methods are often used to calculate the correlation energy of a UEG. The above approach is known as the local-density approximation or LDA and has been introduced by Kohn and Sham (1965).

- **Generalized-gradient approximation**

  The exchange-correlation functional $E_{xc}^{LDA}[n]$ does not account for local changes in the electronic density as it occurs in any system that is spatially inhomogeneous. The generalized-gradient approximation or GGA takes into account the gradient of electronic density variations on the exchange $E_x[n]$ and correlation $E_c[n]$ functionals:

$$E_{xc}^{GGA}[n] = \int n(\mathbf{r}) f[n, \nabla n]\{E_x[n] + E_c[n]\} d^3r \tag{2.16}$$

  There are several methods to calculate the functional term $f[n, \nabla n]$ including the density variation $\nabla n$, such as the one formulated by Perdew, Burke and Ernzerhof (1996) often referred to as the PBE formalism.

#### 2.1.2.2 Crystal structure and Bloch's theorem

To obtain the total energy of a system, in the framework of DFT, requires knowledge of the local electronic density at any point of the system. The system, in our case is defined by minerals where the atomic positions obey a certain motif: the crystal lattice, for which the smallest unit (in the Bravais lattice formalism) in reciprocal space is known as the first Brillouin zone. The electronic density and therefore the Kohn-Sham orbitals

$\phi_i$ of a mineral system will consequently have the same periodicity as the crystal lattice:

$$\phi_i = u_i(\mathbf{r})e^{ik\mathbf{r}} \tag{2.17}$$

where each KS-orbital $\phi_i$ is expressed by a set of plane wave functions for which $u_i(\boldsymbol{r})$ ought to be continuous and has to be calculated for an infinite number of $k$ spanning just the first Brillouin zone (Bloch's theorem). Monkhorst and Pack (1976) have developed a method which allows to sample the first Brillouin zone by constructing a mesh for a finite number of discretized $k$-points. Sampling of the number of $k$-points is dependent on the size of the system and has to be refined until convergence of the total ground state energy has been achieved. The energy cutoff $E_{\text{cutoff}}$ as defined in table 2.1 determines the number of basis functions that will be used.

| Atomic Species | Fundamental electronic configuration | Electronic configuration pseudopotential | Number of valence electrons | $E_{\text{cutoff}}$ (eV) |
|---|---|---|---|---|
| Mg (US) | [Ne]$3s^2$ | $p^6s^2$ | 8 | 365.887 |
| Mg (PAW) | [Ne]$3s^2$ | $s^2p^0$ | 2 | 210.083 |
| Si (US) | [Ne]$2s^22p^2$ | $s^2p^2$ | 4 | 300.0 |
| Si (PAW) | [Ne]$2s^22p^2$ | $s^2p^2$ | 4 | 245.435 |
| O (US) | [Ar]$2s^22p^4$ | $s^2p^4$ | 6 | 395.994 |
| O (PAW) | [Ar]$2s^22p^4$ | $s^2p^4$ | 6 | 400 |

Table 2.1: *Characteristics of the pseudopotentials related to the US-pseudopotentials and PAW-method regarding the atomic species in* $Mg_2SiO_4$ *wadsleyite and ringwoodite from the VASP-documentation. The energy cutoff* $E_{\text{cutoff}}$ *shown are the minimum cutoff values that should be used for the individual atoms.*

### 2.1.2.3 Pseudopotentials

The nuclei in DFT appear only in the form of a potential $V[n](\boldsymbol{r})$ acting on the electrons. The electronic degrees of freedom can be further reduced by replacing the isolated nuclei by effective ions: the nucleus plus the inner atomic electrons defined in a zone $r < r_c$. Often, *ab initio* calculations make use of potentials that replace the all-electron-potentials by the potential energy of the interactions between the effective ions and the remaining valence electrons which mainly determine the material properties. These potentials are known as pseudopotentials. The ultrasoft (US)-pseudopotentials (Vanderbilt 1990; Kresse and Hafner 1994) smoothen the pseudo wavefunctions of the inner core regions $r < r_c$, where the orbitals of the "real" electrons would undergo heavy oscillations. The projector augmented wave (PAW) method, on the other hand, accounts for the orbitals of the inner electrons as well by using a linear transformation of the total electron wavefunction into a pseudo wavefunction in the region $r < r_c$. This method is developed by Blöchl (1994). Apart from the all-electron-methods, the PAW is considered to be one of the most accurate method to handle the interactions between the nuclei and the electrons, whereas the US-potentials are not norm-conserving but also the least time consuming. See table 2.1 for the essential characteristics of the US-pseudopentials and PAW-method that have been used in this study. In our calculations, we have been using $E_{\mathrm{cutoff}}$=600 eV for all atoms and for both US and PAW.

#### 2.1.2.4 VASP: wadsleyite and ringwoodite

All *ab initio* based calculations are performed with the VASP code (Kresse and Hafner 1993; Kresse and Furthmüller 1996) using the GGA (PBE, Perdew *et al.* (1996)) and US pseudopotentials or the PAW method. The outermost core radii for the Mg, Si and O atoms are set to 1.058, 0.953 and 0.820 Å respectively. The first Brillouin-zone has been sampled using the Monkhorst-Pack grid adapted to each different simulation with an electronic density that is expanded on a plane wave basis set with a single energy cut-off value $E_{\mathrm{cutoff}}$ of 600 eV to impose a convergence better than $4\times10^{-5}$ eV per atom for the total energy. As an illustration, Fig. 2.1 shows the energy convergence test of the $k$-point sampling of the first Brillouin zone for a primitive cell of $Mg_2SiO_4$ ringwoodite

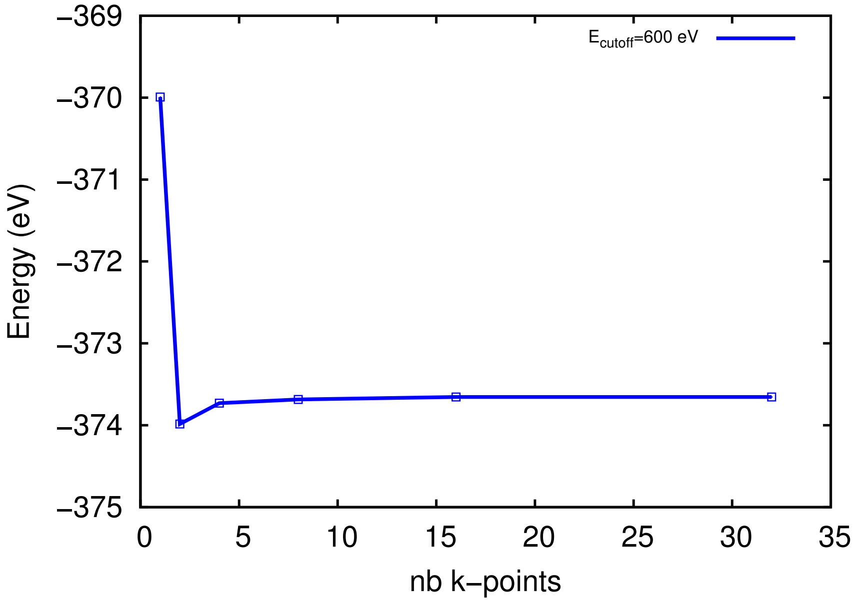

Figure 2.1: *Monkhorst & Pack sampling of the first Brillouin zone: ground state energy evolution as a function of the number of k-points in a unit cell of* $Mg_2SiO_4$ *ringwoodite at* 20 *GPa using* ab initio *calculations for an energy cutoff* $E_{\mathrm{cutoff}}$=600 *eV on the US-pseudopotentials.*

at 20 GPa. It can be seen that sampling with about 8 $k$-points is sufficient in this case, using the US-pseudopotentials.

Both the $\gamma$-surfaces and the elastic constants are calculated by *ab initio* atomistic simulations. The perfect crystal structures will be obtained by a full relaxation of the atomic positions and box volume $V_0$ of the unit cells at the appropriate pressure conditions. Any further system will be constructed upon those unit cells with fixed volume $V'$ and performed under ambient pressure conditions.

### 2.1.3 $\gamma$-Surface: generalized stacking fault energies

Generalized stacking fault surfaces ($\gamma$-surfaces) are based upon a purely theoretical concept. A $\gamma$-surface maps the energy landscape that corresponds to an excess energy $\gamma$ per unit area due to an imposed discontinuous shear in the crystal structure along a given crystallographic (slip) plane. This is achieved by calculating the energies corresponding to rigid displacements (shear) of the crystal half above with respect to the one below the stacking fault plane (Christian and Vítek 1970). As such, the concept relies on mapping the energies required to create any stacking fault that is possible for a given plane that is constrained to the smallest unit of the periodic crystalline lattice (see Fig. 2.2):

$$\gamma = \frac{E_{\text{stacked}} - E_{\text{perfect}}}{AB} \tag{2.18}$$

where $E_{\text{stacked}}$ is the total energy of the stacked crystal, $E_{\text{perfect}}$ is the total energy of the perfect crystal and $A$ and $B$ are the dimensions of the (slip) plane. Since a $\gamma$-surface is purely theoretical, there is no way to reproduce it experimentally. However, the method enables us to identify the existence of stacking faults in the material by the presence of metastable energy minima. An example is shown for the $\{001\}$ in ringwoodite at 20 GPa in Fig. 2.2. The metastable energy minimum along a $\frac{1}{2}\langle 110\rangle$ direction shows the existence of a stacking fault in this plane. The corresponding stacking fault is a planar defect and exhibits an energy equal to the $\gamma$-value. This, on the other hand, could be compared to experimental measurements on stacking faults in single crystals.

Besides, the $\gamma$-surfaces also form an essential tool to obtain the first order elementary characteristics of the potential manifestation of slip systems in a crystal. A dislocation is a line defect characterized by an elementary quantity of lattice shear: Burgers vector $\boldsymbol{b}$, that can be associated to the energy excess due to a discontinuous shear of a perfect crystal lattice. The lowest energy shear path along the direction with the shortest lattice periodicity with respect to different potential glide planes therefore allows us both to identify the best candidate of the Burgers vector on each potential plane and to indicate indirectly the slip system which potentially exhibits the lowest energy configuration. Besides this semi-qualitative information on the potential slip systems in the material, the $\gamma$-surfaces also form the key ingredient for modelling dislocation core structures with the Peierls-Nabarro(-Galerkin) method, which will be dealt with in the next section.

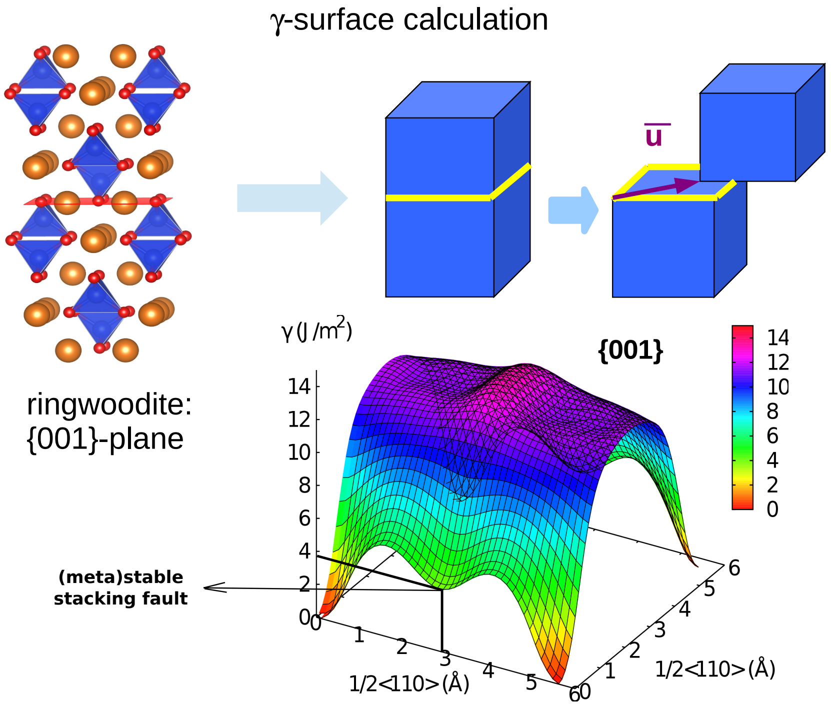

Figure 2.2: *Illustration of the supercell constructions built to calculate the corresponding $\gamma$-surface with respect to a given stacking fault plane (potential glide plane) indicated in red.*

All $\gamma$-surfaces are obtained by the use of *ab initio* calculations to explicitly incorporate the pressure-induced changes in the electronic structure. To calculate the $\gamma$-surfaces, supercells are built in a Cartesian frame of reference for each potential slip plane defined by its normal and shear directions. The $\gamma$-surface is calculated by imposing a shear displacement to the part above the stacking fault plane of the supercell. The crucial step consists in defining this stacking fault plane by choosing a cutting level in order to separate the upper half from the lower half of the supercell in such a way that a minimum number of valence electrons involved in the atomic bonding have to be destroyed in order

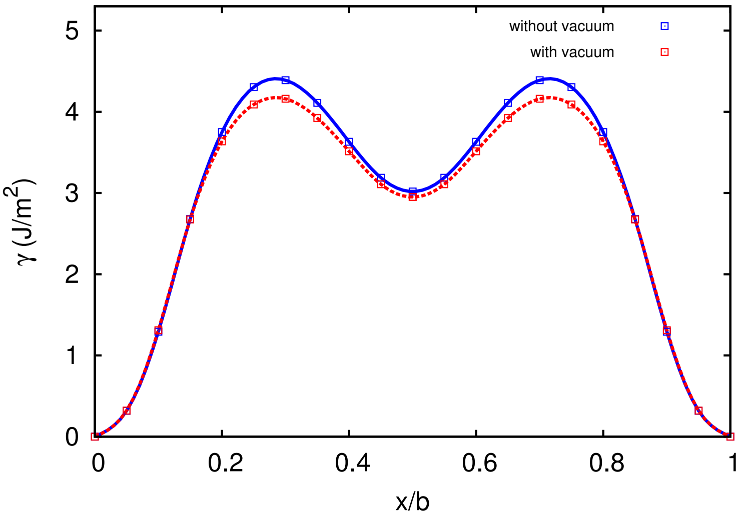

Figure 2.3: *The influence on the stacking fault energies of a supercell construction with and without a vacuum buffer (fully 3-D periodic boundary conditions). Both $\gamma$-lines shown correspond to the $\frac{1}{2}\langle 110\rangle$ direction of the $\{001\}$ in $Mg_2SiO_4$ ringwoodite at 0 GPa.*

to create the stacking faults. In both minerals, $Mg_2SiO_4$ wadsleyite and ringwoodite, it is possible to find a cutting level with respect to all the (stacking fault) planes considered in this study, in such a way that it avoids to cut the strong Si-O bonds. All atoms, except those located near the external boundary layers are allowed to relax perpendicular to the shear plane in order to minimize the energy of the $\gamma$-surfaces. Complete relaxation of the atoms in every direction would result in a disappearance of the stacking fault, since the perfect crystal structure exhibits the lowest energy configuration. Up to 16 atomic layers (depending on the supercell geometry) are used to be able to relax the crystal structure and to converge the total energy. An extra vacuum buffer of 6 Å has been added in the direction normal to the slip plane to reduce the number of atoms and to ensure the lack of interaction between stacking fault replicas as a result of the use of periodic boundary conditions. The disadvantage, however of the introduction of a vacuum buffer is that the free crystal surfaces that have been created in this way may carry a certain amount of charge which may interact with the stacking fault and influence the total energy of the calculations. Both approaches (with and without a vacuum buffer) have been investigated for which the $\gamma$-lines in the $1/2\langle 110\rangle$ direction of the $\{001\}$ in $Mg_2SiO_4$ ringwoodite at 0 GPa are shown in Fig. 2.3. The example shows that there are only minimal differences between both approaches for which the supercell construction with an extra vacuum buffer results in the lowest excess energy configuration. The excess energy values are found to be in good agreement at the metastable minima, which gives the energy of the stacking fault in that plane. We adopted the method with addition of the vacuum buffer (as it gives the lowest excess energies) in all the further calculations of $\gamma$-surfaces in this study. Finally, Fig. 2.2 gives an illustration of the supercell constructions in order to produce the $\gamma$-surfaces with respect to a given stacking fault plane (corresponding to a potential glide plane).

### 2.1.4 Elastic constants

The athermal elastic constants are calculated at the appropriate pressure conditions by imposing small (elastic) deformations between a maximum of $-3\% \leq \epsilon \leq +3\%$. The energy excess $\Delta E$ between strained and unstrained unitcells are obtained by using *ab initio* calculations. The applied strain is given in matrix notation with respect to the strain tensor components $\epsilon_{ij}$:

$$\begin{pmatrix} \epsilon_1 \\ \epsilon_2 \\ \epsilon_3 \\ \epsilon_4 \\ \epsilon_5 \\ \epsilon_6 \end{pmatrix} = \begin{pmatrix} \epsilon_{11} \\ \epsilon_{22} \\ \epsilon_{33} \\ 2\epsilon_{12} \\ 2\epsilon_{14} \\ 2\epsilon_{23} \end{pmatrix}$$

and the induced stress, according to elastic deformation, is equal to $\sigma_i = c_{ij}\epsilon_j$, where $c_{ij}$ corresponds to the stiffness tensor. The amount of elastic work $W$ performed can be expressed as:

$$W = \frac{1}{2}\sigma_i\epsilon_i = \frac{1}{2}c_{ij}\epsilon_j\epsilon_i \tag{2.19}$$

The confining pressure $p$, in case of applying $\epsilon_i$ with $i$=1,2,3, performs work as well, which has to be taken into account. In that case, the elastic constants constituting the stiffness tensor $c_{ij}$ can be obtained with the symmetric substitution tensor $c_{ijkl}$ for which $i$=$k$ and $j$=$l$, by a variation in the application of $\epsilon_1 = \epsilon_2 = \epsilon_3 = \epsilon$:

- Applying either $\epsilon_1$, $\epsilon_2$ or $\epsilon_3 \rightarrow (i{=}j)$

$$\frac{\Delta E}{V_0} = -p\epsilon_i + \frac{1}{2}c_{ijkl}\delta_{kl}\epsilon_j\epsilon_i \tag{2.20}$$

- Applying a combination of $\epsilon_i$ and $\epsilon_j \rightarrow (i \neq j)$

$$\frac{\Delta E}{V_0} = -p\left[\epsilon_i + \epsilon_j\right] + \frac{1}{2}\left[c_{ijkl}\delta_{jl} + c_{ijkl}\delta_{ik} + 2c_{ijkl}\delta_{kl} - 2p\right]\epsilon_j\epsilon_i \tag{2.21}$$

The pressure will not be involved in case of the application of either $\epsilon_4$, $\epsilon_5$ or $\epsilon_6 \rightarrow (i{=}j)$:

$$\frac{\Delta E}{V_0} = 2c_{ijkl}\delta_{kl}\epsilon_j\epsilon_i \tag{2.22}$$

In the above equations, $\delta_{\alpha\beta}$ corresponds to the Kronecker delta. All subscripts are written in the Einstein summation convention. The elastic constants are finally determined by fitting $\Delta E$ versus $\epsilon$ by a second order polynomial: $ax^2 + bx + c$, for which the curve related to $c_{44}$ in $Mg_2SiO_4$ ringwoodite at 20 GPa is shown in Fig. 2.4 as an example.

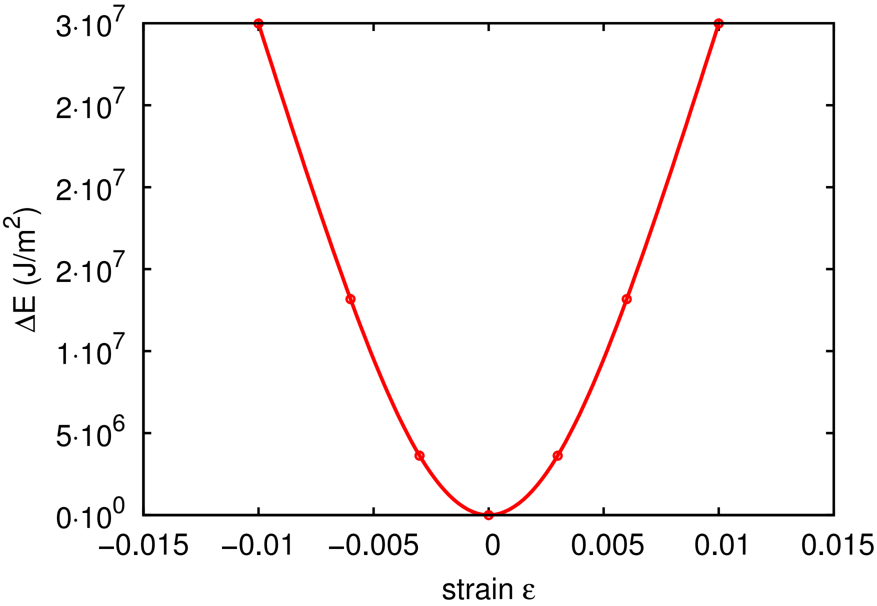

Figure 2.4: *The evolution of the energy excess* $\Delta E$ *with strain* $\epsilon_4 = \epsilon$ *in order to calculate* $c_{44}$ *in* $Mg_2SiO_4$ *at 20 GPa.*

## 2.2 Resistance to dislocation glide: continuum-atomistic approach

---

> *Là, tout n'est qu'ordre et beauté ...*
>
> Charles Baudelaire.
>
> (L'invitation au voyage, *Fleurs du Mal.*)

---

### 2.2.1 Introduction

A dislocation is a line defect characterized by an elementary quantity of lattice shear given by the Burgers vector $\boldsymbol{b}$. The local lattice distortions are caused by the atomic displacements within an arranged crystalline lattice. The distortions are the largest at the center of the defect. The spread of the Burgers vector in the glide plane mainly determines the core structure of the dislocation (Fig. 2.5). It was Sir Rudolf Ernst Peierls who first suggested in his 1940 paper: "The size of a dislocation" (Peierls 1940) that the glide motion of a dislocation under an external state of stress is dependent on the extension of the dislocation core in the glide plane. The size of a dislocation is described by the core extension that defines the non-linear atomic misfit displacements that build the defect. This core structure mainly determines the amount of lattice friction opposed to the motion of the defect. It is the lattice friction that represents the intrinsic resistance to the glide motion of dislocations. A description of the core structure of a dislocation is therefore essential to model its intrinsic glide mobility. The dislocation core structure is strongly dependent on the local non-linear atomic interactions around the dislocation line. The use of a fully atomistic approach would therefore be the most obvious choise to model dislocation core structures in crystalline materials. This can be done by using a first-principles approach or by the use of an empirical potential that reproduces the material properties at the atomic scale. Since first-principles based methods are less efficient as the simulation boxes require a large number of atoms to model dislocation core structures, the use of empirical potentials is the most conventional. Studies in which a fully atomistic approach is used to model dislocations in minerals include Woo and Püls (1977), Walker *et al.* (2004), [a]Walker *et al.* (2005), [b]Walker *et al.* (2005), Carrez *et al.* (2008) and Hirel *et al.* (2014). However, in the absence of a suitable appropriate empirical potential to model the core structure of line defects, a hybrid continuum-atomistic Peierls-Nabarro-Galerkin approach can be used which is based on the one-dimensional Peierls-Nabarro model (PN-model). Studies of dislocations in minerals using the Peierls-Nabarro theory include Miranda & Scandolo (2005), Carrez *et al.* (2006), Carrez *et al.* (2007), Carrez *et al.* (2009), Durinck *et al.* (2007), Ferré *et al.* (2007), Ferré *et al.* (2009), Metsue *et al.* (2010), [a]Metsue *et al* (2010) and Gouriet *et al.* (2014) on MgO periclase, $Mg_2SiO_4$ ringwoodite, $MgSiO_3$ post-perovskite, $Mg_2SiO_4$ wadsleyite, $CaMgSi_2O_6$ diopside, $Mg_2SiO_4$ forsterite, $CaSiO_3$ perovskite and $MgSiO_3$ perovskite, respectively.

In order to glide from one to the next stable position in the crystal structure, the dislocation core has to overcome an energy barrier as a consequence of friction exerted by the crystal lattice that is opposed to the motion of the dislocation. In absence of thermal activation at 0 K this barrier is called the Peierls potential. The maximum of the derivative of this potential, with respect to position of the dislocation, is proportional to the Peierls stress $\tau_p$ which can be seen as a pure mechanical measure of the lattice friction experienced by the dislocation. Lattice friction quantified by the Peierls potential can be calculated in the framework of the PN-model by making use of the relaxed core structure of the dislocation.

The aim of this chapter is to describe the methods used to obtain the core structures of dislocations in $Mg_2SiO_4$ wadsleyite and ringwoodite and the way in which lattice friction as opposed to the glide motion of dislocations is quantified in the framework of the Peierls-Nabarro theory. This chapter is divided into four sections. The first section briefly describes the main features of the 1D PN-model on which the PNG-method is based. The PNG-model itself is described in the second section. The following two sections are dedicated to the description of the core structure (section 2.2.3) and the quantification of the lattice friction (section 2.2.4) with respect to the glide of dislocations.

### 2.2.2 Peierls-Nabarro model in one dimension

The PN-model was first introduced by Peierls (1940) and later refined and completed by Nabarro (1947) and is based on both continuum elasticity theory and local atomic-scale information. In the PN-model (Fig. 2.5), the crystal is considered to be an elastic continuum which is divided into two elastic semi-infinite half crystals $A$ and $B$, separated by a misfit region $C$ of inelastic (atomic) displacements constrained into the glide plane in which the dislocation core spreads in the direction normal to the dislocation line.

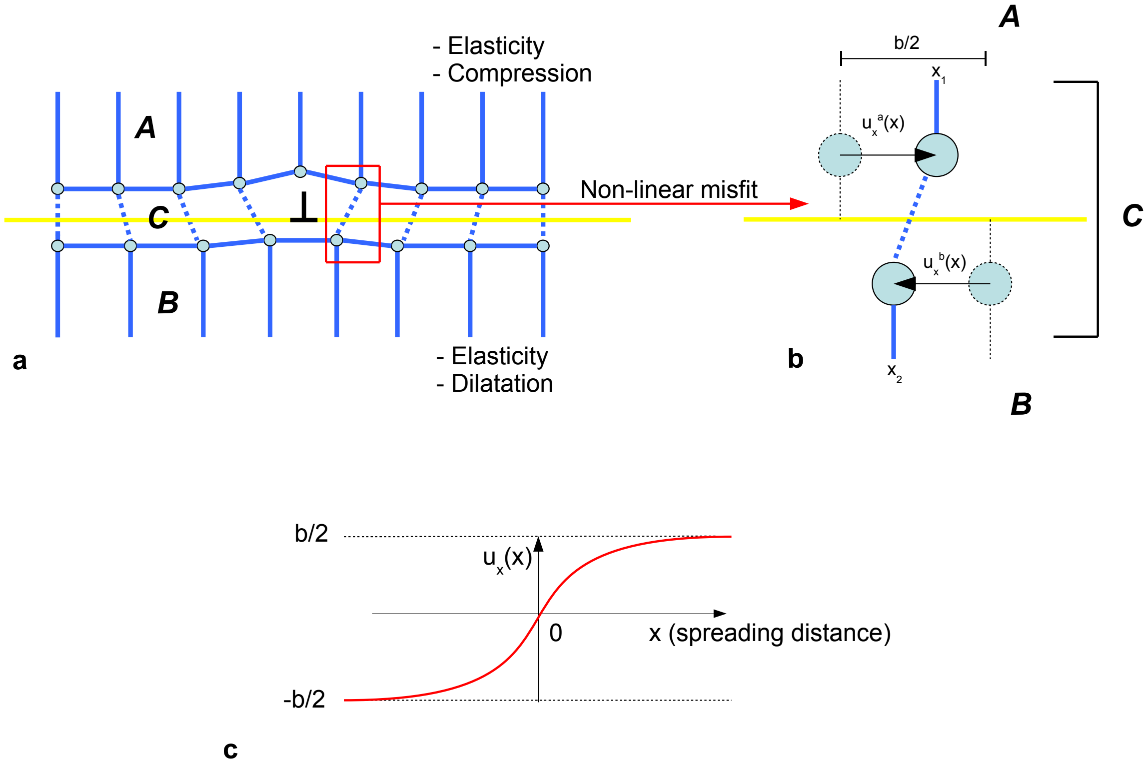

Figure 2.5: *Illustration of the conceptual idea of the Peierls-Nabarro model by making use of an edge dislocation. a) Edge dislocation illustrating the atomic misfit region in between two semi-infinite half crystals. The atomic misfit can be seen as an interplanar misfit between atomic planes perpendicular to the glide plane as a result of the elastic and non-elastic interaction forces between both half crystals. b) At equilibrium conditions, both forces balance each other which results in the local misfit displacements* $u_x$ *or the disregistry* $S(x)$. *c) The local misfit displacements* $u_x$ *is a function that evolves from* $-b/2$ *to* $b/2$ *and shows the spread of the dislocation core structure in the glide plane in the direction of glide.*

Figure 2.5 illustrates the case of an edge dislocation in the context of the PN-model. The same theory, however, is applicable independent of the character of the dislocation. The dislocation core in the PN-model is based on a continuous distribution of infinitesimal shear $S(x)$ across a given glide plane:

$$S(x) = u_x(x) + \frac{b}{2} \tag{2.23}$$

where $u_x(x)$ corresponds to the relative local atomic (misfit plane) displacements in the region $C$ between the halfcrystals $A$ and $B$: $u_x(x) = u_x^a(x) - u_x^b(x)$ (see Fig. 2.5). We will call $u_x$ from now on the local misfit displacement. The mismatch $S(x)$, which is a direct measure of the misfit displacement $u_x$, is called the disregistry function. The disregistry $S(x)$ therefore quantifies the spread of the dislocation core structure in the direction $x$ normal to the dislocation line in a given glide plane. The derivative of the disregistry $dS(x)/dx$ describes the continuous local Burgers vector density $\rho$ which is a measure of the localized lattice misfit produced by the dislocation core on the glide plane in the crystal structure. The local stress generated by the shear displacements $S(x)$ can thus be represented as a distribution of infinitesimal Burgers vectors $db$ which implies that $S(x)$ has to obey the following boundary conditions:

$$\begin{cases} \lim_{x\to-\infty} S(x) = 0 \\ \lim_{x\to+\infty} S(x) = b \end{cases} \tag{2.24}$$

so that summation of all displacements by the infinitesimal Burgers vectors $db$ along the direction of spread in the glide plane results in following normalisation condition (Eshelby 1949):

$$b = \int_{-\infty}^{+\infty} \left(\frac{dS(x)}{dx}\right)_{x=x'} dx' = \int_{-\infty}^{+\infty} \rho(x')dx' \tag{2.25}$$

The misfit displacements out of the glide plane are neglected in this approach.

*Two distinct types of forces are generated by the dislocation system*:

- **Elastic interaction forces** between the infinitesimal dislocation segments $db$ and the half crystals. The total elastic energy of the system is given by the summation of work performed by the elementary infinitesimal dislocation segments $db$:

$$E_{elastic} = 1/2 \int_{-\infty}^{+\infty} \sigma_{by}(x) S(x) dx \tag{2.26}$$

The stress $\sigma_{by}(x)$ induced by the local Burgers vector distribution at point $x'$ along the spreading the direction in the glide plane equals:

$$\sigma_{by}(x) = \frac{K}{2\pi} \int_{-\infty}^{+\infty} \frac{\rho(x')}{x - x'} dx' \tag{2.27}$$

where $K$ is the energy coefficient which in the isotropic case is equal to $K = \mu$ and $K = \mu/(1-\nu)$ for screw and edge dislocations respectively. The above stress $\sigma_{by}$ tends to keep the misfit aligned with the atomic planes in bulk of half crystals $A$ and $B$ by spreading out the shear $S(x)$. The resulting elastic energy becomes :

$$\begin{aligned} E_{elastic} &= \frac{K}{4\pi} \int_{-\infty}^{+\infty} \int_{-\infty}^{+\infty} \frac{\rho(x') S(x)}{x - x'} dx dx' \\ &= -\frac{K}{4\pi} \int_{-\infty}^{+\infty} \int_{-\infty}^{+\infty} \rho(x)\rho(x') log|x - x'| dx dx' \end{aligned} \tag{2.28}$$

- **Non-elastic restoring forces** between atoms of the misfit planes on either side $A$ and $B$ of the glide plane. This force tends to align the atoms across the glide plane by reducing the spread of the shear $S(x)$. The total energy $E_\gamma$ as a result of the work done by these forces across the glide plane is given by the sum of all stacking fault energies $\gamma$ as function of shear $S(x)$ along the spreading direction:

$$E_\gamma = \int_{-\infty}^{+\infty} \gamma(S(x)) dx \tag{2.29}$$

In the original PN-model, the inelastic stacking fault energy $\gamma(S(x))$ was considered to be a simple sinusoidal function due to the periodicity of the crystal lattice:

$$\gamma(S(x)) = \frac{Kb}{\pi}\left(1 - cos\left(\frac{2\pi S(x)}{b}\right)\right) \tag{2.30}$$

In 1994, Joos *et al.* already mentioned that the restoring forces $\nabla\gamma(S(x))$ in a real crystal may be significantly different from a sinusoidal function. In 1970, Christan and Vítek proposed that atomic scale generalized stacking fault energies (GSF) can be used to calculate the inelastic restoring forces. The $\gamma$-lines or $\gamma$-surfaces therefore, have to be calculated at the atomic scale as discussed in the section 2.1.3 (Vítek 1968; Christian and Vítek 1970).

If the system is in equilibrium, both elastic and inelastic forces balance each other.

The total classical Hamiltonian $H$ of the dislocated crystal system is given by:

$$H = \int_{-\infty}^{+\infty} \gamma(S(x))dx - \frac{K}{4\pi}\int_{-\infty}^{+\infty}\int_{-\infty}^{+\infty} \rho(x)\rho(x')log|x - x'|dxdx' \tag{2.31}$$

Minimization of the Hamiltoninan $H$ leads to the effective stable dislocation core structure $S(x)$. Eq. 2.31 can be reduced to an Euler-Lagrange equation by making use of the Lagrange multiplier $\lambda$:

$$H = \int_{-\infty}^{+\infty} \gamma(S(x))dx - \frac{K}{4\pi}\int_{-\infty}^{+\infty}\int_{-\infty}^{+\infty} \rho(x)\rho(x')\log|x - x'|dxdx' + \lambda\int_{-\infty}^{+\infty}\rho(x)dx \tag{2.32}$$

for which minimization leads to the well known Peierls-Nabarro equation (Peierls 1940; Nabarro 1947):

$$0 = \frac{K}{2\pi}\int_{-\infty}^{+\infty}\frac{\rho(x)dx'}{x-x'} + \frac{d\gamma(S(x))}{dx} \tag{2.33}$$

Let us now solve Eq. 2.33 in the most simple case for which the stacking fault energy $\gamma(S(x))$ is given by a pure sinusoidal function as in Eq. 2.30:

$$\frac{K}{2\pi}\int_{-\infty}^{+\infty}\frac{\rho(x)dx'}{x-x'} = 2K\sin\left(\frac{2\pi S(x)}{b}\right) = \tau_0\sin\left(\frac{2\pi S(x)}{b}\right) \tag{2.34}$$

where $\tau_0$ is the ideal shear stress ($ISS$). We will try a solution for the disregistry $S(x)$ and its derivative, the local Burgers vector density $\rho(x)$ as proposed by Peierls (1940):

1. The disregistry $S(x) = \frac{b}{2} + \frac{b}{\pi}\arctan\left(\frac{x}{\xi}\right)$
2. The local Burgers vector density $\rho = \frac{dS(x)}{dx} = \frac{b}{\pi}\frac{\xi}{x^2+\xi^2}$

$$\begin{aligned} -\frac{K}{2\pi}\frac{\xi b}{\pi}\int_{-\infty}^{+\infty}\frac{1}{x-x'}\frac{dx}{x'^2+\xi^2} &= \tau_0\sin\left(\pi + 2\arctan\left(\frac{x}{\xi}\right)\right) \\ &= -\tau_0 sin\left(2\arctan\left(\frac{x}{\xi}\right)\right) \end{aligned} \tag{2.35}$$

that can be reduced to

$$-\frac{K}{2\pi}\frac{\xi b}{\pi}\frac{\pi x}{(x^2+\xi^2)\,\xi} = -2\tau_0\frac{x\xi}{x^2+\xi^2} \tag{2.36}$$

which results in the condition that $\xi = Kb/4\pi\tau_0$, where $\xi$ is the halfwidth of the dislocation core structure. The half-width $\xi$ of a dislocation can be seen as the domain between half of the maximum of the Burgers vector density. The above demonstrates that the disregistry function $S(x)$ as a proposed solution is a function of the $\gamma$ through the $ISS$ $\tau_0$: $S(\xi(\gamma(\tau_0)))$.

The 1D PN-model however is based on strong a-priori assumptions, such as a planar core spreading, a 1D reconstruction of the dislocation core and the impossiblity of treating dislocations that exhibit both edge and screw components or dissociations into non-collinear partials. In other words, the model reduces a dislocation to a one dimensional structure in a 3-D crystal lattice. Another disadvantage are the strong limitations in modelling very confined core structures. The restrictions of the 1-D model as such has been discussed in Schoeck (2005) and Schoeck (2006). The assumptions finally, may be in some cases too oversimplified to model dislocation core structures in complex materials such as minerals. A good example of this is the inability of the PN-model to handle the non-planar core spreading of the [001] screw dislocations in $Mg_2SiO_4$ forsterite (Durinck *et al.* 2007; Carrez *et al.* 2008).

### 2.2.3 Peierls-Nabarro-Galerkin model

The dislocation core structures in $Mg_2SiO_4$ wadsleyite and ringwoodite (at the appropriate pressures) are calculated with the PNG model based code *Cod²ex* (Denoual 2004; Denoual 2007). This model is a generalization of the PN-model as described in the paragraph above, in the framework of the element-free Galerkin method. It allows for the introduction of multiple glide planes which makes it possible to describe the dislocation core structures in three dimensions, however constrained to the geometries of the introduced glide planes. Just as in the PN model, the configuration of the most stable core structure emerges naturally by minimization of the total energy of the system composed of the elastic strain energy and the inelastic stacking fault energy across the potential glide plane(s). The latter is given as an interplanar potential that mimicks all inelastic forces acting across the glide plane(s). The interplanar potential is directly derived from the $\gamma$-surfaces. Minimization of the energy occurs through a continuous field approximation. The introduction of a perfect Volterra dislocation on a slip plane $\Sigma$ within the crystal volume $V$ leads to the formation of two distinct fields:

1. A continuous three dimensional elastic field $\boldsymbol{u}(\boldsymbol{r})$ of the space contained by the volume $V$.
2. A discontinuous two-dimensional field $\boldsymbol{f}(\boldsymbol{r})$ expressed in the orthonormal basis that spans the plane(s) $\Sigma$.

Therefore $\boldsymbol{u}(\boldsymbol{r})$ gives a representation of the continuous deformation around the dislocation core, whereas $\boldsymbol{f}(\boldsymbol{r})$ describes the displacements by crossing the glide plane $\Sigma$. The total deformation of the crystal system containing a dislocation introduced into the plane $\Sigma$ is given by the homogeneous strain $\epsilon_{ij}^t$:

$$\epsilon_{ij}^t = \epsilon_{ij}^e + \epsilon_{ij}^f = \frac{1}{2}\left(u_{i,j} + u_{j,i}\right) \tag{2.37}$$

where $\boldsymbol{u}$ corresponds to the displacement field and where $\epsilon_{ij}^e$ are the pure elastic and $\epsilon_{ij}^f$ the pure inelastic parts of the components $\epsilon_{ij}^t$ of the total strain (tensor) generated. The PNG model is based on a description of the total Langrangian of the system, given by:

$$-L(\mathbf{u},\mathbf{f}) = \int_\Sigma E_{sf}(\mathbf{f}(\mathbf{r}))d\Sigma + \int_V \{E_e(\mathbf{u}(\mathbf{r}),\mathbf{f}(\mathbf{r})) - \frac{1}{2}\Omega\dot{\mathbf{u}}(\mathbf{r})^2\}dV \tag{2.38}$$

where $\Omega$ corresponds to the material density, $\dot{\boldsymbol{u}}$ is equal to the time derivative $d\boldsymbol{u}/dt$ of displacement field $\boldsymbol{u}(\boldsymbol{r})$ and $E_{sf}$ is equal to the inelastic stacking fault energy. The latter is given by the $\gamma$-surfaces produced through atomistic simulations, from which the purely elastic part has been extracted. Further, $E_e$ is equal to the total elastic strain energy:

$$E_e(u,f) = \frac{1}{2}\{\epsilon_{ij}^e C_{ijkl}\epsilon_{kl}^e\} \tag{2.39}$$

where $C_{ijkl}$ corresponds to the full stiffness tensor. Note that the Lagrangian of the system (Eq. 2.38) is very similar and strongly related to the Hamiltonian of the dislocation system in the PN-model (Eq. 2.31).

Minimizing the Lagrangian of Eq. 2.38 with respect to $\boldsymbol{u}(\boldsymbol{r})$ and $\boldsymbol{f}(\boldsymbol{r})$ leads to the relaxed dislocation core structure within volume $V$. The lowest energy configuration arising from the initial introduction of the dislocation can lead to a Burgers vector distribution within multiple glide planes. An element free Galerkin method is used to compute the evolution of $\boldsymbol{u}(\boldsymbol{r})$. Minimization of $\boldsymbol{f}(\boldsymbol{r})$ is achieved by using a time dependent Ginzburg-Landau (TDGL) type of viscous relaxation mechanism:

$$\dot{\mathbf{f}}(\mathbf{r}) = \frac{1}{\xi}\frac{\partial L(\mathbf{u},\mathbf{f})}{\partial \mathbf{f}(\mathbf{r})} \tag{2.40}$$

where $\xi$ is a kinetic parameter which corresponds to the "relaxation viscosity" of the glide plane.

Discretization within the element-free Galerkin method is achieved through a nodal structure on volume $V$ and surface $\Sigma$. The volume $V$ is equal to a simulation cell represented by the crystal on which the nodal mesh is constructed as a replica of the crystal structure by the introduction of the planes $\Sigma$ corresponding the generalized stacking fault energies (GSF) or $\gamma$-surfaces calculated (atomistically) on those planes in the crystal.

The three main ingredients to calculate the relaxed dislocation core structure therefore are:

1. Crystal structure of the material.
2. $\gamma$-surfaces of the potential glide planes (calculated atomistically).
3. Elastic constants of the full stiffness tensor.

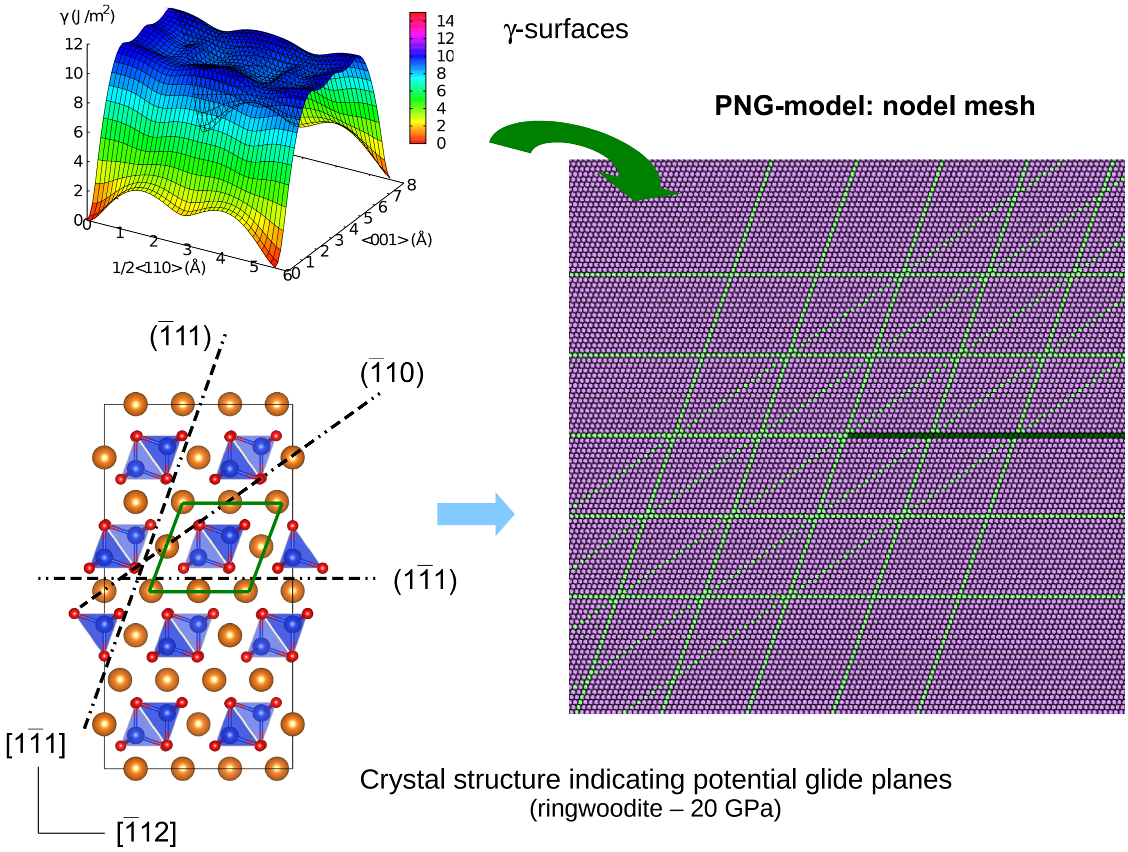

Figure 2.6: *Illustration of the conceptual idea of the Peierls-Nabarro-Galerkin model for the mesh construction suitable to determine the core spreading of the* $1/2\langle 110\rangle$ *screw dislocation in* $Mg_2SiO_4$ *ringwoodite. The crystal lattice of ringwoodite is reproduced by the* $\gamma$-*surfaces on a nodal mesh indicated in green. They are those planes in which the dislocation core structure is able to spread after the initial introduction of a Volterra dislocation (dark green nodes) where the* $[110]$-*direction points out of the paper. Linear elasticity is calculated on all purple nodes, which means all the nodes not belonging to the* $\gamma$-*surfaces.*

Fig. 2.6 gives an example of the nodal mesh used to calculate the core structure of the $1/2\langle 110\rangle$ screw dislocation in $Mg_2SiO_4$ ringwoodite. The $\gamma$-surfaces of the potential glide planes (green dots) reconstruct the crystal structure. A multiplicity of all potential glide planes is used to reproduce the periodic variation of the total dislocation core energy with respect to the crystal structure (Denoual 2007). The darkgreen nodes within the mesh in Fig. 2.6 represent the plane of introduction of the initial dislocation that creates a rigid step in the mesh in the direction and equal to the modulus of the Burgers vector. The dislocation is considered to be infinite in the direction of the line. Free boundary conditions are used in the simulation as the elastic field caused by the dislocation are imposed on the boundaries of the simulation cell. A value of the kinetic parameter $\xi^{-1}$=$10^{-6}$ m/(Pa s), for all simulation cells constructed in this study, is found to be sufficient to guarantee complete convergence of the calculations.

#### 2.2.3.1 Dislocation core structures

The principal outcome of the PNG model are the final displacement fields $\boldsymbol{u}(\boldsymbol{r})$ and $\boldsymbol{f}(\boldsymbol{r})$ for a relaxed dislocation core structure. The final core structure is described as the spread of the Burgers vector distribution in the potential glide planes $\Sigma$, in the direction $x$ perpendicular to the line, by the inelastic displacement field $f_\Sigma(x)$. The function $f_\Sigma(x)$ therefore can be represented as the distregistry $S_\Sigma(x)$ in the plane $\Sigma$ as formulated in the framework of the PN-model (chapter 1.2). Following Joos *et al.* (1994), the disregistry $S_\Sigma(x)$ of the dislocation core in plane $\Sigma$ has to satisfy the general solution of the Peierls-Nabarro equation:

$$S_\Sigma(x) = \frac{b_\Sigma}{2} + \frac{b_\Sigma}{\pi} \sum_{i=1}^{N} \alpha_i \arctan\left(\frac{x - x_i}{\xi_i}\right) \tag{2.41}$$

where $b_\Sigma$ is equal to the Burgers vector distribution in the plane $\Sigma$

$$b_\Sigma = \int_{-\infty}^{+\infty} \rho_\Sigma(x) dx \tag{2.42}$$

and where $\rho_\Sigma(x)$ is equal to the local Burgers vector density:

$$\rho_\Sigma(x) = \frac{dS_\Sigma}{dx} = \frac{b_\Sigma}{\pi} \sum_{i=1}^{N} \alpha_i \frac{\xi_i}{(x - x_i)^2 + \xi_i^2} \tag{2.43}$$

where $\alpha_i$, $\xi_i$ and $x_i$ are variational constants which can be obtained using a least squares minimization by fitting $f_\Sigma(x)$ with the function given by Eq. 2.41. Both $S_\Sigma(x)$ and $\rho_\Sigma(x)$ have to obey to the normalisation condition of Eq. 2.25 which requires that $\sum_{i=1}^{N} \alpha_i = 1$.

Since edge dislocations are confined to their plane of introduction, the complete Burgers vector distribution for the edge character(s) after relaxation will be established in the plane of initial introduction. For the simple case of a pure edge dislocation, the PN and the PNG-model will give the same result according to Eq. 2.41, constrained to the plane of introduction $\Sigma$. The Burgers vector for screw dislocations, on the other hand, can be distributed in all potential glide planes.

Once the relaxed core structure of the dislocation is known, the Peierls potential $V_p$ and its derivative with respect to the dislocation position, the Peierls stress $\tau_p$, can be quantified since it is principally the core structure of a dislocation that determines the amount of lattice friction which is opposed to the glide motion of the dislocation in the crystal lattice.

### 2.2.4 Lattice friction

The intrinsic lattice resistance to the glide motion of a dislocation can be quantified in terms of energy by the Peierls potential $V_p$. The potential $V_p$ describes the energy along the gliding direction which the dislocation has to face in order to move from one to the following stable position in the crystal lattice. Under equilibrium conditions in the absence of an external state of stress, the dislocation is placed in the valley(s) of the Peierls potential. The Peierls valleys are separated by the shortest lattice periodicity in the direction of glide: the Peierls periodicity $a'$. The maximum of the derivative of $V_p$ is equal to the Peierls stress which is a pure mechanical measure of the lattice friction opposed to dislocation motion. The Peierls stress $\tau_p$ is therefore defined as the resolved shear stress at 0 K (*i.e.* the stress to be applied on the dislocation, in the absence of thermal activation, to make it cross the Peierls barrier).

The core structure of a dislocation, in the scheme of the PN-model, is described by a continuous distribution of shear across the glide plane, given the local misfit displacement $u_x(x)$ or in terms of the disregistry $S(x)$. Lattice discretisation of the atomic structure has to be reintroduced to be able to describe the lattice friction opposed to dislocation glide. This can be achieved by calculating the Peierls potential $V_p$ as the total energy cost of displacing the dislocation rigidly form one to the next Peierls valley. The potential is obtained by a summation of the energy cost relative to the dislocation core displacement $\chi$ in the crystal structure. The Peierls potential is the result of two main energy constributions as a function of the core displacement $\chi$:

1. summation of the misfit energy between pairs of crystal planes (Christian and Vítek 1970; Joós *et al.* 1994)
2. summation of the elastic strain energy caused by the misfit between pairs of crystal plains (Wang 2006)

The potential $V_p$ is obtained by summing the misfit and elastic strain energy between $x$ pairs of crystal planes, normal to the glide plane, by moving the dislocation core rigidly through the crystal structure by $a'$:

$$V_p(\chi) = \sum_{x=-\infty}^{+\infty} \gamma(u_x)a' + \frac{a'}{2}\left[\sum_{x=-\infty}^{+\infty} F^a(u_x)u_x^a + F^b(u_x)u_x^b\right] \tag{2.44}$$

where the local misfit displacement $u_x$ is a function of the core displacement $\chi$:

$$u_x(\chi) = u_x(xa' - \chi) \tag{2.45}$$

for which the core displacement $\chi \to [0 : a']$. The first term on the right hand side of Eq. 2.44 corresponds to the misfit interaction energy $\gamma$ and is equal to the stacking fault energy per unit area of the primitive cell of the glide plane. The second term on the right hand side of Eq. 2.44 describes the total elastic strain energy in the misfit region $C$ of Fig. 2.5, in which the elastic restoring force is given by:

$$F^{a,b}(u_x) = -\left[\frac{\partial\gamma}{u_x}(u_x)\right]^{a,b} \tag{2.46}$$

As already mentioned in section 2.2.2, $u_x(x)$ corresponds to the relative local atomic (misfit plane) displacements in the region $C$ between the half crystals $A$ and $B$: $u_x(x) = u_x^a(x) - u_x^b(x)$. The superscripts $a$ and $b$ are used to indicate a crystal half plane belonging to half crystal $A$ or $B$ respectively.

The stress necessary to overcome the Peierls barrier at any point along the glide direction $\chi$ without thermal activation is defined as the Peierls force $\Sigma(\chi)$:

$$\Sigma(\chi) = \frac{1}{b}\frac{\partial V_p(\chi)}{\partial\chi} = \frac{1}{b}\nabla V_p(\chi) \tag{2.47}$$

where $b$ is equal to the modulus of the Burgers vector. The maximum of $\Sigma(\chi)$ is equivalent to the Peierls stress $\tau_p$:

$$\tau_p = max\{\frac{1}{b}\nabla V_p(\chi)\} \tag{2.48}$$

Classically, as done in Peierls (1940), the Peierls potential $V_p$ is estimated through the misfit term only (Joós *et al.* 1994; Schoeck 1999). The stable configuration of a dislocation core, in this case, exhibits a maximum instead of a minimum energy. However, it is also the elastic strain energy, as a consequence of the misfit between the atomic planes, that varies by displacing the dislocation core structure rigidly through the crystal lattice (Wang 2006). Both misfit and elastic strain energy contributions are strictly opposite in sign. The addition of both energy contributions as a function of the direction of motion on the glide plane results in the effective Peierls potential with a minimum energy at the stable lattice configurations. Adding the contribution of the elastic strain energy to the

Peierls potential consequently leads to an overall lower Peierls barrier than a potential which is purely defined by the misfit energy.

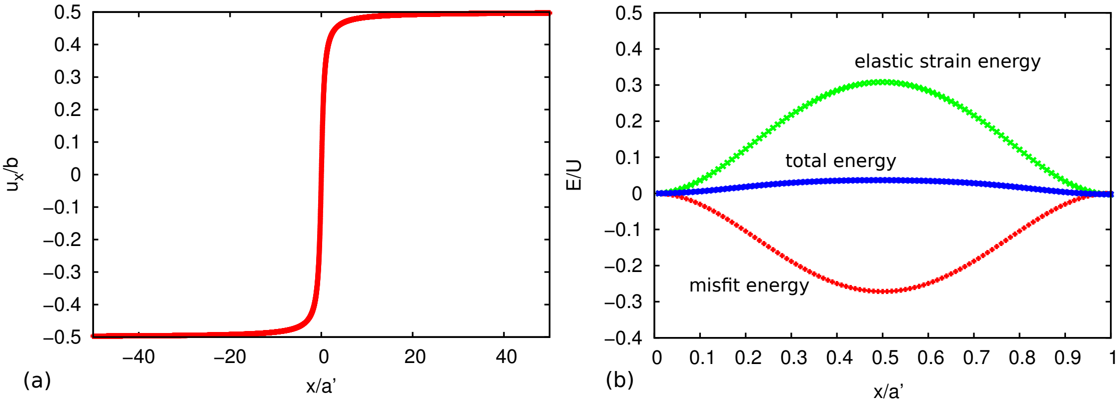

Figure 2.7: *Example of the core structure and associated Peierls potential with Peierls periodicity $a'$ for a compact screw dislocation core in a simple cubic lattice. a) The local misfit displacement $u_x$ associated to the disregistry $S(x)$ which describes the spread of the dislocation core. b) Calculation of the contribution of the misfit and the elastic strain energy to the total energy given by the Peierls potential for a screw core in a simple cubic lattice. Both misfit and elastic strain energy have opposite signs which leads to an effective potential. It is clear that by calculating the potential as the misfit energy between pairs of atomic plains leads to a situation where the dislocation exhibits the maximum instead of the miminum energy configuration at equilibrium position.*

The effect of the contribution of both misfit and elastic strain energy to the Peierls potential is illustrated in the scholastic example of a screw dislocation in a simple cubic lattice, with a lattice constant $d$, Burgers vector modulus $b$, Peierls periodicity $a'$, such that $d = b = a' = 1$ Å. Taking the assumption of a pure *sine*-like force field $F_r$ in the glide plane leads to the following formulation of the $\gamma$-line:

$$\gamma(u_x(x)) = \frac{U}{2}\left[1 - \cos\left(\frac{2\pi u_x(x)}{b}\right)\right] \rightarrow$$

$$F_r(x) = \frac{d\gamma}{du_x} = \frac{\pi U}{b}\sin\left(\frac{2\pi u_x}{b}\right) \quad (2.49)$$

for which $U = 2Kb/\pi$. The analytical solution (Eq. 2.41) of the PN equation in this simple case is given by:

$$u_x(x) = \frac{b}{\pi}\arctan\left(\frac{x}{\xi}\right) \tag{2.50}$$

where the half-width $\xi$ of the screw dislocation core is equal to $\xi = Kb/4\pi\tau_0$ by using the second derivative $\partial^2\gamma/\partial u_x^2 \to \mu = 2\pi\tau_0$. Having the misfit displacement $u_x$ and the $\gamma$-line, the Peierls potential can be obtained as described in Eq. 2.44. Figure 2.7 shows the separate contribution of the misfit and the elastic strain energy to the total energy defined as the Peierls potential $V_p$ as a function of the core displacements between $[0 : a']$. This simple example shows that there is a tendency to have lower Peierls potentials by taking into account both the contributions of the misfit and elastic strain energy to the potential instead of only the misfit energy. However, the exact contribution of both misfit and the elastic energy to the Peierls potential depend strongly on the complexity of shape and symmetry of the disregistry function.

## 2.3 Thermally activated glide of dissociated dislocations

> *It can scarcely be denied that the supreme goal of all theory is to make the irreducible basic elements as simple and as few as possible without having to surrender the adequate representation of a single datum of experience.*
>
> Albert Einstein.
>
> (*On the Method of Theoretical Physics*, 10 June 1933.)

### 2.3.1 Introduction

As we have seen in chapter 2.2, the Peierls potential $V_p$ describes the energy a dislocation has to face in order to move from one to the following stable position in the crystal lattice as a consequence of the interaction between the dislocation and the crystal lattice. Under equilibrium conditions, in the absence of an external state of stress, the dislocation is well placed in the valley(s) of the Peierls potential. The stress necessary to move a dislocation without any thermal activation, at 0 K, is maximal and equal to the Peierls stress $\tau_p$. However, at finite temperatures, the dislocation is able to move at $\tau < \tau_p$ since thermal activation allows segments of the dislocation line to bow out under an applied stress (Seeger and Schiller 1962; Dorn and Rajnak 1964; Guyot and Dorn 1967; Celli *et al.* 1963; Hirth and Lothe 1982). In case of the existence of a high Peierls potential, thermal activation is controlled by the nucleation and propagation of unstable kink-pairs that allow the dislocation line to slip through the crystal lattice from one Peierls valley to the next (Kubin 2013). Different models exist to describe this process, such as the line-tension model (Friedel 1964), pure kink-kink interaction model (Seeger 1981) and the elastic interaction model (Koizumi *et al.* 1994) suitable at the low stress regime, initially proposed by Koizumi *et al.* (1993) and applied by Amodeo *et al.* (2011) on MgO. In the latter cases, the elastic interaction model was applied to undissociated dislocations. In the present work, we will adopt the elastic interaction model and extend this approach to collinear dissociated dislocations as they occur in wasleyite and ringwoodite. Therefore, kink-pair nucleation must be handled on two partial dislocations. The model allows us to obtain the enthalpy variation associated with a critical dislocation bow-out over the Peierls potential by the extremum of the corresponding total energy variation. The latter depends on the dislocation core structures, the Peierls potential and the associated Peierls stresses. Dislocation mobilities can be finally determined from the stress dependence on the nucleation rate of kink-pairs. The rate of kink-pair nucleation is governed by the critical enthalpy variation as determined by the elastic interaction model.

Finally, the kink-pair model as adapted for dissociated dislocations will be benchmarked on $SrTiO_3$ perovskite for which there is activity of dissociated dislocations at ambient conditions as has been observed and measured accurately in experiments. Illustrations of both $Mg_2SiO_4$ ringwoodite and $SrTiO_3$ perovskite will be used throughout the entire section.

### 2.3.2 Kink-pair nucleation: elastic interaction model

The elastic interaction model (Koizumi *et al.* 1993) is used to calculate the energy of the saddle point $\Delta H^{crit}$ of $\Delta H$ with respect to the kink-pair geometry. This saddle point of the energy surface $\Delta H$ is dependent on the applied resolved shear stress $\tau$. For low and intermediate $\tau$, the kink-pair width is much larger than the spread of the kink shape along the dislocation line. In that case, a kink-pair can be assumed to have a rectangular geometry (Koizumi *et al.* 1994). Therefore, the model is based on the assumption that at low stresses, a metastable rectangular kink-pair bow-out exhibits a critical height $h^{crit}$ displacing a critical line width $w^{crit}$ on a dislocation segment. The change in energy between a straight and a kinked dislocation is dependent on the applied resolved shear stress and has to be calculated to describe the nucleation process. This is not as trivial for dissociated dislocations, as a kink-pair needs to be formed on both partials in order to move the complete dislocation (Fig. 2.8). Indeed, this can occur in several different ways (Möller 1978; Mitchell *et al.* 2003). Two kink-pairs may nucleate simultaneously (Fig. 2.8a) in such a way that they coincide along both partials (this is the so-called "correlated" nucleation). On the other hand, one kink-pair can first nucleate independently on the leading or on the trailing partial and only then on the second partial (hereafter called "uncorrelated" nucleation). Two end-member types of uncorrelated nucleation processes are possible: the outward motion of the leading partial as a first unit step, followed by the inward motion of the trailing partial (Fig. 2.8b) or the

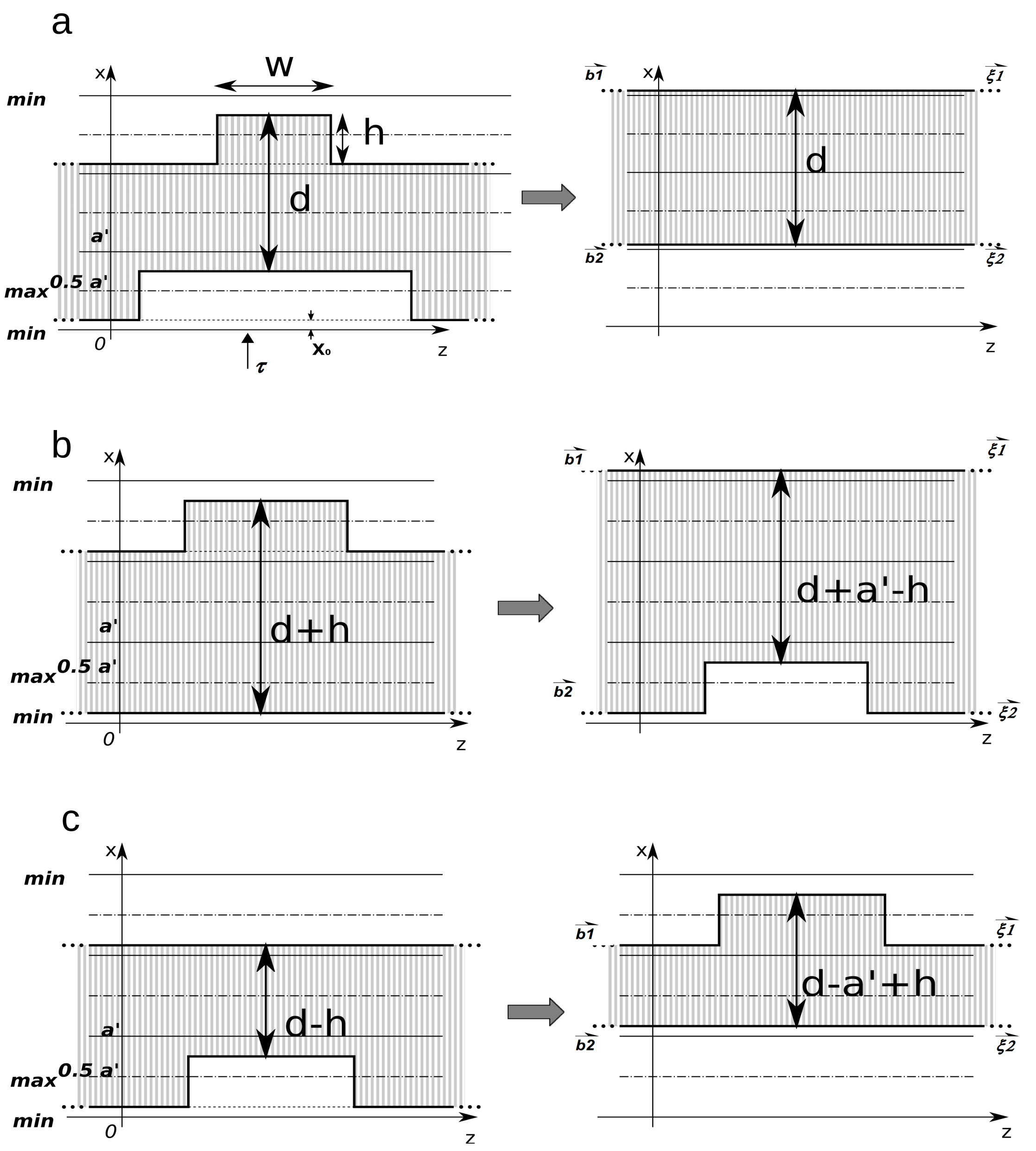

Figure 2.8: *Kink-pair nucleation on collinear dissociated dislocations with equilibrium stacking fault width d, Peierls periodicity $a'$ and kink-pair height h and width w. (a) Correlated nucleation process: coherently simultaneous kink-pair nucleation on partial dislocations. (b) Uncorrelated nucleation: kink-pair nucleation starting from the leading partial followed by a nucleation of the trailing partial. (c) Uncorrelated nucleation: kink-pair nucleation starting from the trailing partial followed by the nucleation of the leading partial.*

inward motion of the trailing partial as a first unitstep followed by the outward motion of the leading partial (Fig. 2.8c). The variation in enthalpy $\Delta H$ related to kink-pair nucleation on dissociated dislocations can be generally described as follows:

$$\Delta H = \Delta E_{elastic} + c_i \Delta P_p + \Delta W_{sf} + c_i W_p \tag{2.51}$$

where

$$\Delta E_{elastic} = \Delta E_{\xi_1} + \Delta E_{\xi_2} + \Delta E_{\xi_1,\xi_2} \tag{2.52}$$

$\Delta E_{elastic}$ is the change in elastic energy, $\Delta W_{sf} = \pm\gamma hw$ is the change in stacking fault energy due to the nucleation processes, where $\gamma$ is equal to the equilibrium stacking fault energy, $\Delta P_p$ is the variation in Peierls energy related to one partial, caused by the energy cost of segments that lie on the Peierls potential away from the valley, and finally $\Delta W_p = -\tau b_p hw$ is the plastic work under the action of the resolved shear stress $\tau$. In Eq. 2.51, $c_i = c_u = 1$ for uncorrelated and $c_i = c_c = 2$ for correlated kink-pair nucleation in which case $\Delta W_{sf}$ vanishes.

In the literature, the activation energy of Eq. 2.51 with the "work" term included is often referred to as either "the activation free enthalpy" or "Gibbs free energy of activation" (Gibbs 1965; Schoeck 1965). In case $\Delta H$ is interpreted in terms of "Gibbs" energy, Eq. 2.51 lacks an energy term $T\Delta S_k$ related to a variation in the entropy $\Delta S_k$ associated with kink-pair nucleation. This is in the first place due to the fact that there is little known about the quantification of the entropy variation as a consequence of kink-pair nucleation. However, Hirth and Lothe (1982) relate this variation in entropy $\Delta S_k$ to the entropy variation $\Delta S_{\omega_k}$ associated with the change in phonon vibration modes $\omega_k$ within the crystal. They suppose a vibrational frequency $\omega_p$ of the dislocation lying in the Peierls valley. Under the assumption of invariance of the total number of vibrational modes, the energy related to the entropy change in the high-temperature limit is given by:

$$T\Delta S_k = k_b T\left[\log\left(\frac{k_b T}{\hbar\omega_k}\right) - \log\left(\frac{k_b T}{\hbar\omega_p}\right)\right] = k_b T\log\left(\frac{\omega_p}{\omega_k}\right) \tag{2.53}$$

for which only the kink-vibrations are excited classically at high-temperature: $\hbar\omega_p >> k_b T >> \hbar\omega_k$, so that the energy related to the total entropy variation due to kink formation can be estimated to be equal to:

$$T\Delta S_k = k_b T\log\left(\frac{k_b T}{\hbar\omega_k}\right) = ck_b T\log\left(\frac{k_b T}{h\delta\nu}\right) \tag{2.54}$$

where $\omega_k = 2\pi\nu$ with $\nu$ equal to the vibrational frequency, typically in the order of the Debye frequency $\nu_D = 10^{13}$ s$^{-1}$. The constant $\delta$ determines the effective vibrational frequency and can be estimated to have values within the domain [$10^{-3}$:1]. For a temperature value of 1700 K, which reflects a typical temperature in the transition zone, this leads to the following estimates of the energy $T\Delta S_k$=0.2-1.2 eV. In chapter three, we will compare these values with respect to the energies associated with dislocation motion at high temperature.

In general, the screw dislocations belonging to a given slip system have more confined cores than the edge dislocations belonging to the same slip system. This means that the edge dislocations have the tendency to spread more out into the glide plane than the screw dislocations. This is the consequence of the Poisson ratio $\nu$ in the anisotropic energy coefficient $K$ (Eq. 2.27). As a consequence, lattice friction will be generally lower for the edge than for the screw dislocations. The screw dislocations will therefore account for most of the plastic strain produced during deformation. The kink-pair model is therefore based on initial dislocations lines that exhibit a pure screw character, nucleating kinks with a pure edge character, since the model describes the formation of rectangular kink-pairs. At low stress conditions, the kinks have to be widely separated in order not to collapse as a consequence of the mutual attractive kink-kink interaction. The larger the resolved shear stress applied in the direction of motion, the more the width between the kinks decreases as the applied stress works against the collapse of the kinks.

#### 2.3.2.1 Peierls energy

The formation of a kink-pair on a partial leads to a variation in the Peierls energy dependent on the Peierls potential $V_p$ (Eq. 2.44). The applied resolved shear stress $\tau$ will force the dislocation into a new quasi-equilibrium position $x_0$ within the crystal lattice. The dissociated dislocation is assumed to displace rigidly into the new position $x_0$, since both partials experience the same stress condition. This has to be calculated for every new applied resolved shear stress $\tau$:

$$\left.\frac{dV_p(x)}{dx}\right|_{x=x_0} = \tau b \tag{2.55}$$

Following Koizumi (1993), the total variation in Peierls energy can now be described as

$$\Delta P_p = \int_{x_0}^{x_0+h} V_p dx + \frac{w}{2}\left[V_p\left(x_0+h\right) - V_p\left(x_0\right)\right] \tag{2.56}$$

The underlying assumption is that in the case of two equivalent partial dislocations, each of them has to overcome half of the complete Peierls potential $V_p$. The first part on the right hand side of Eq. 2.56 describes the energy associated with kinks crossing the potential whereas the second term accounts for the energy related to the position $x_0$ of the nucleated line segment $w$ in the crystal. We like to mention that the deviation $x_0$ of the initial partial lines from the Peierls vallies is nevertheless very small.

To be able to handle the Peierls potential as obtained by Eq. 2.44 for any given dislocation, we choose to parametrize the latter by the following sinosoidal function $V_p(x)$ introduced by Koizumi (1993):

$$\begin{aligned} V_p(x) &= \frac{C}{2\pi} a' b \tau_p g(x) \\ g(x) &= 1 - \cos\left(\frac{2\phi}{a'}x\right) - \frac{\alpha}{2}\left(1 - \cos\left(\frac{2\phi}{a'}x\right)\right)^2, 0 \leq \alpha \leq 1, \\ C &= \sqrt{2}\frac{(1-\alpha)^2 + 4\alpha^2 + (1-\alpha)\sqrt{(1-\alpha)^2 + 8\alpha^2}}{\left\{(1-\alpha)^2 + 2\alpha^2 + (1-\alpha)\sqrt{(1-\alpha)^2 + 8\alpha^2}\right\}^{3/2}} \end{aligned} \tag{2.57}$$

The variational constant $\alpha$ can be obtained using a least squares minimization by fitting $V_p(x)$ with the potential calculated as given in Eq. 2.44. The variational constant $\alpha$ determines the amplitude of the potential which is purely sinusoidal in case $\alpha = 0$ and exhibits a camel hump shape for values of $\alpha > 0.5$.

We would like to note that in case each partial needs to overcome half of the complete potential: $V_p(x) \rightarrow \frac{1}{2}\frac{C}{2\pi}a'b\tau_p g(x) = \frac{C}{2\pi}a'b_p\tau_p g(x)$. As such, we consider that the Peierls stress to move the complete dislocation without thermal activation is independent of the type of kink-pair nucleation process in case both partials are strictly equivalent.

#### 2.3.2.2 Elastic energy

All variations in the elastic energy $\Delta E_{elastic}$ (Eq. 2.51), between two consecutive dislocation configurations divided into segments (as shown in Fig. 2.11), are calculated considering piecewise straight line segments within an isotropic elastic continuum by using the coplanar elastic interaction formalism formulated by Hirth and Lothe (1982). Here, the change in elastic interaction energy between the two partial dislocation lines is given by $\Delta E_{\xi_1,\xi_2}$ that is dependent on the specific type of nucleation process (which will be dealt with in next section). The overall variation in elastic energy $\Delta E_{\xi_n}$ of the partial (screw) lines (Eq. 2.51), is given by the total change in elastic interaction energy and the change in self-energy of the lines $\xi_1$ and $\xi_2$ and is given by:

$$\Delta E_{\xi_n}(h,w) = \frac{\mu b_p^2}{2\pi}\left(\sqrt{w^2+h^2} - w - h + w\log\frac{2w}{w+\sqrt{w^2+h^2}}\right.$$
$$\left. - \frac{1}{1-\nu}\left(w - \sqrt{w^2+h^2} + h\log\frac{h+\sqrt{w^2+h^2}}{w} - h\log\frac{h}{e\rho}\right)\right) \tag{2.58}$$

The above function $\Delta E_{\xi_n}$ depends on the height $h$ of and the width $w$ between kink-pairs, but also on the change in absolute self energy of the partial dislocations due to the creation of new kink-line segments. The latter is expressed in a fixed cutoff radius $\rho$ (Hirth and Lothe 1982; Koizumi et al. 1993). The cutoff radius $\rho$ is postulated as the distance below which dislocation segments are not supposed to interact to avoid energy divergence. The cutoff radius therefore strongly depends on the local inelastic distortion field of the dislocation core. In our case, the height of the kinks $h$ are comparable to the core spreading $\xi_n$ of the partials, which means that the self-energy of a kink is about equal to the energy of a core segment of length $h$. As such, we propose to parametrize $\rho$ by the spread of the core structure of the partial lines. However, there is no definite way to determine $\rho$ other than by the use of atomistics, which would be a complete study on its own. Nevertheless, there are ways to constrain $\rho$ within a restricted domain.

The expression of $\Delta E_{\xi_n}$ can be simplified by a Taylor development in $h/w$ (Hirth and Lothe 1982) which leads to the following result:

$$\Delta E_{\xi_n} = \frac{\mu b_p^2}{4\pi(1-\nu)}\left\{h\left[\log\left(\frac{h}{\rho}\right) - 2 + \nu\right] - \frac{h^2(1+\nu)}{2\pi w}\right\} \tag{2.59}$$

with $\mu$ and $\nu$ equal to the shear modulus and the Poisson ratio, respectively. The first term on the right hand side of Eq. 2.59 accounts for the self energies of both kinks on the partial lines and the second term describes the interaction between the kinks. The change in self-energy $U_k$ due to the nucleation of a single kink on a partial line can therefore be given by:

$$U_k = \frac{\mu b_p^2 h}{4\pi(1-\nu)} \left[ \log\left(\frac{h}{\rho}\right) - 2 + \nu \right] + \int_{x_0}^{x_0+h} \frac{1}{2} V_p dx \tag{2.60}$$

The self energy $U_k$ of the kink is due to the local change in core energy of the initial screw partial and is therefore directly related to the spread of the core in the glide plane and to the change in Peierls energy (in case identical partials are considered). The larger the initial spreading of the partial core (the larger $\rho$), the lower the variation in self-energy (the lower $U_k$) of the line due to the formation of a kink as can be seen in Eq. 2.60, since a larger volume of the crystal lattice has already been distorted by the partial line.

In previous works (Koizumi et al. 1993; Carrez et al. 2009; Amodeo et al. 2010), a cut-off radius of 5% of the core spreading was considered for undissociated dislocations ($\rho = 0.05\xi$) in order to introduce the dependency of the change in self energy on the choice of slip system. In this case we parametrize the cut-off radius by the width of a partial dislocation core $\xi_n$ as $\rho = 0.1\xi_n$. We explain why below.
As the self-energy of the kink can be associated with the core energy $W_k = \kappa\mu b_p^3$, with $\kappa \approx 0.1$, we are able to make a first order approximation with respect to the above assumption by:

$$W_k \approx \frac{\mu b_p^2 h}{4\pi(1-\nu)} \left[ \log\left(\frac{h}{\rho}\right) - 2 + \nu \right] + \int_{x_0}^{x_0+h} \frac{1}{2} V_p dx \tag{2.61}$$

for which $\rho$ can be solved. As the kink-pair model is valid in the low stress regime, the end-member case is used in Eq. 2.61: $\tau \rightarrow 0$ leads to $max\{h\} = a'$, where $a'$ is equal to the Peierls periodicity and $x_0$=0. In that case, it is confirmed that $\rho = (0.1 \pm 0.03)\xi_n$.

In order to investigate the sensitivity of the kink self-energy, directly related to $\Delta H$

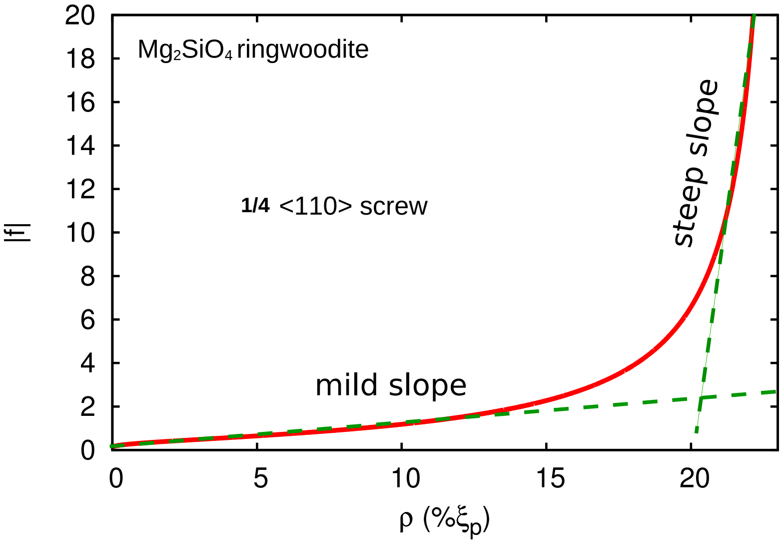

Figure 2.9: *Sensitivity of the cut-off radius $\rho$ on the function $|f|$ and therefore on the relative error in $\Delta H$ by the choise of $\rho$. The latter is parametrized by the core spreading of the partial dislocation lines.*

(Eq. 2.51), with the choise of $\rho$, we derived $\partial U_k/\partial\rho \rightarrow$

$$\frac{\partial U_k}{U_k} = f(\rho)\frac{\partial\rho}{\rho} \tag{2.62}$$

with

$$f(\rho) = \frac{1}{\log(\frac{h}{\rho}) - 2 + \nu} \tag{2.63}$$

An example for the $1/4\langle110\rangle\,\{110\}$ partial in ringwoodite can be seen in Fig. 2.9. Since we focus on the low stress regime, we look at the end-member case where $\tau \rightarrow 0$: $h \rightarrow a'$. We can observe that the absolute value of $f$ as a function of $\rho$ can be roughly divided into two regions: one where $f$, and hence $\Delta H$, is highly sensitive to a change in $\rho$ for values above $15-20\%$ of $\xi_n$. The relative error in $\Delta H$ is small for values of $\rho$ around 10% of the partial core spreading $\xi_n$. The latter seems the best choice for the cutoff radius $\rho$ as it is in agreement with the core energy based estimates. However, it has to be stressed that the self-energy of a kink cannot be known *a priori* and that the relative errors in our choise of $\rho$ affect the absolute values of the critical nucleation enthalpies. Nevertheless, it will not influence the relative difference with respect to different slip systems since the cutoff has been parametrized as a function of $\xi_n$ which explicitly depends on the dislocation considered.

#### 2.3.2.3 Model solution

An enthalpy variation $\Delta H$ (Eq. 2.51) is associated with the mechanism of each type of kink-pair nucleation. For a given stress $\tau$, the critical nucleation enthalphy $\Delta H^{crit}$ as a function of the critical kink-pair geometry can be found as the saddle point configuration of the respective total enthalpy variation $\Delta H$.

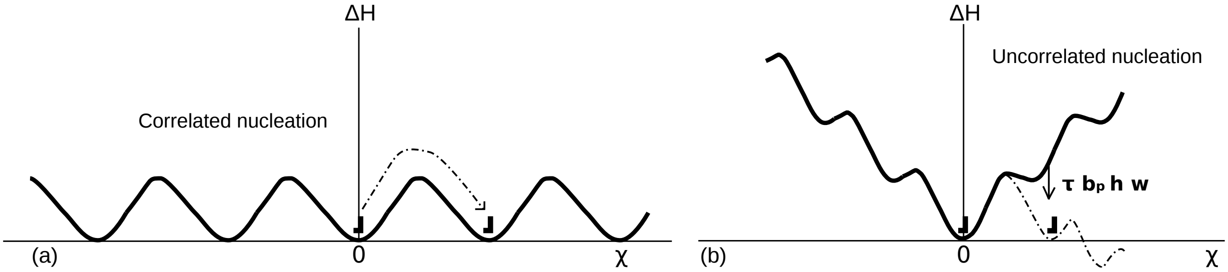

Figure 2.10: *Illustration of the enthalpy variation* $\Delta H(\tau = 0)$ *as a function of the position of a partial dislocation in the crystal lattice in case of (a) correlated nucleation of kink-pairs and (b) uncorrelated nucleation of kink-pairs. The latter implies that the work done by the applied stress needs to be sufficient to lower the energy level of the next Peierls valley. The consequence is that uncorrelated nucleation of kink-pairs can only take place at* $\tau \geq \tau_c$ *(critical stress).*

This makes it possible to calculate the critical nucleation enthalpy of kink-pair formation $\Delta H^{crit}$ for both correlated as well as for the two uncorrelated nucleation mechanisms. Both uncorrelated nucleation mechanisms involve two unit steps (Fig. 2.8). Uncorrelated nucleation requires a substantial change in stacking fault width $d$ which increases the absolute energy level of the next Peierls valley, associated with the inward or outward motion of one partial, after the first nucleation step with respect to the original valley (Fig. 2.10). This is the consequence of a significant change in equilibrium stacking fault width $d$ and the subsequent change in stacking fault energy and elastic interaction energy between both partials. This means that no saddle point exists for $\tau < \tau_c$ (critical stress), regarding independent nucleation of kink-pairs on the partials (Möller 1978; Takeuchi 1995; Mitchell *et al.* 2003). The critical stress is therefore fully determined by the properties of the dissociated dislocation core structure. However, the stacking fault width is more or less maintained in case of correlated kink-pair nucleation so that this process is possible at all stresses $0 < \tau \leq \tau_p$, as there is no decoupled motion of the partials that changes the absolute value of the Peierls valleys. It however becomes less favorable for $\tau \geq \tau_c$ due to the larger nucleation enthalpy compared to the uncorrelated processes (see Fig. 2.11).

Because of the restriction of the elastic interaction model to the low stress regime as mentioned by Caillard and Martin (2003), the critical nucleation enthalpy can be extrapolated up to the Peierls stress based on the classical formalism proposed by Kocks *et al.* (1975):

$$\Delta H^{crit}(\tau) = \Delta H_0 \left(1 - (\tau_{\mathit{eff}}/\tau_p)^p\right)^q \tag{2.64}$$

where $\tau_{\mathit{eff}}$ is the effective resolved shear stress. For correlated nucleation $\tau_{\mathit{eff}} = \tau$ and for uncorrelated nucleation $\tau_{\mathit{eff}} = \alpha\,(\tau - \tau_c)$, with $\alpha = \tau_p/\left(\tau_p - \tau_c\right) \approx 1$. $\tau_c$ is equal to the critical stress above which uncorrelated nucleation is able to occur. $\Delta H_0$ is equal to $\Delta H_c^{crit}(\tau = 0)$ and $\Delta H_u^{crit}(\tau = \tau_c)$ for the correlated and uncorrelated nucleation mechanisms respectively. The saddle point energies $\Delta H^{crit}$ (calculated at low stress) are used to fit the empirical parameters $p$ and $q$.

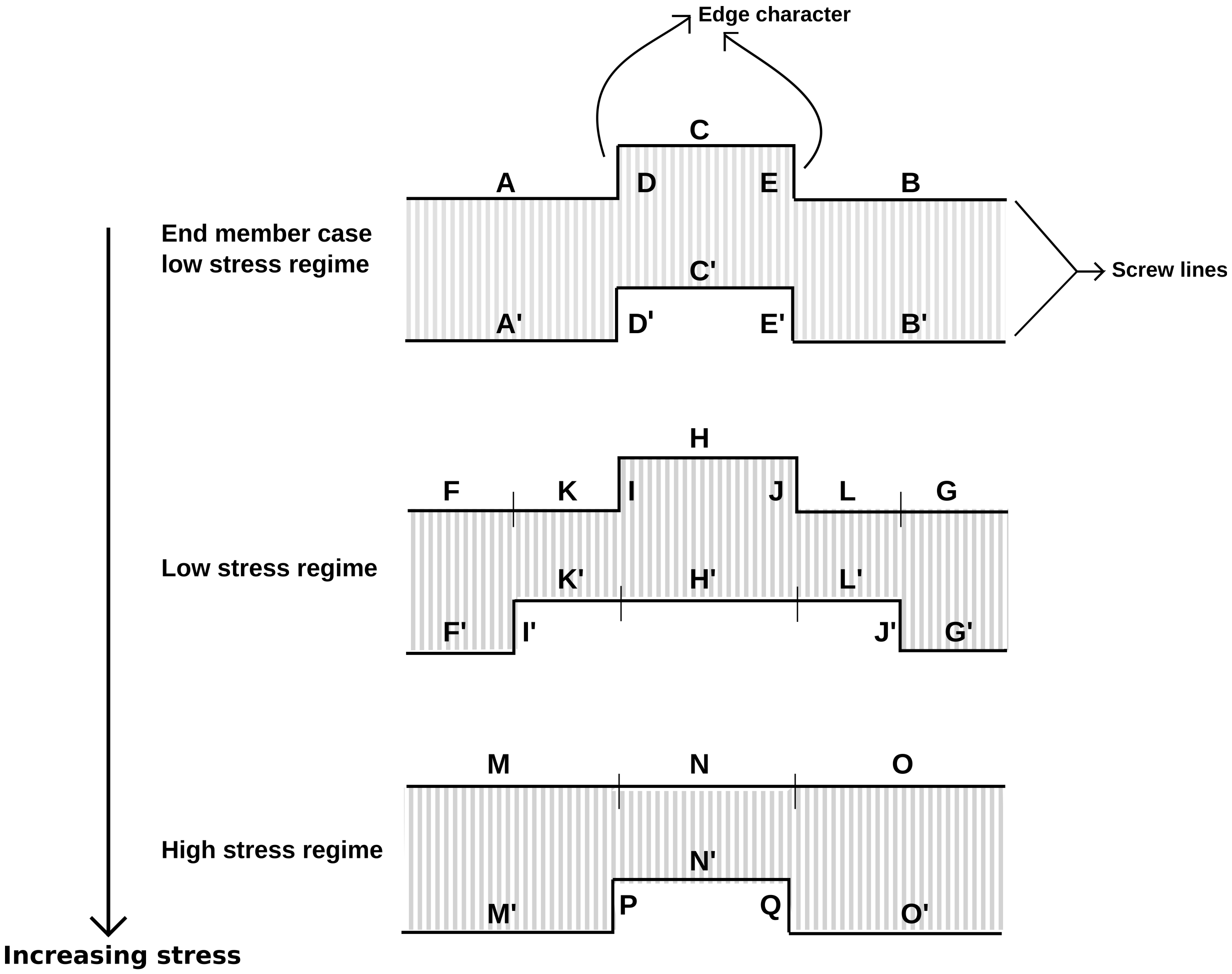

Figure 2.11: *Illustration of the kink-pair nucleation processes on dissociated screw dislocations as a function of the applied stress. Correlated nucleation of kink-pairs on both partials occurs under low stress conditions for which the end-member case implies conservation of the stacking fault d. If stress increases towards higher values, kink-pair nucleation will be gradually taken over by uncorrelated nucleation starting from the trailing partial.*

#### 2.3.2.4 Correlated versus uncorrelated nucleation

#### Correlated kink-pair nucleation: low stress regime

***End-member case in the low stress regime:*** $\tau \to 0$

Kink-pair nucleation in the end-member case $\tau \to 0$, relies on the nucleation of two strictly identical rectangular kink-pairs on both partial dislocations. The underlying reason is that the work performed by the resolved shear stress is insufficient to allow for the energy cost related to a change in the equilibrium stacking fault width $d$. This implies that all kinks exhibit an equivalent height $h$ and that both kink-pairs consist of two kinks separated by an equivalent width $w$ (Fig. 2.11). The change in stacking fault width $d$ associated with this type of kink-pair nucleation is negligible as can be seen in Fig. 2.11. The variation in enthalpy $\Delta H_c$ associated with correlated nucleation of two identical kink-pairs on both partials has been derived analytically and is equal to:

$$\Delta H_c = \Delta E_{\xi_1} + \Delta E_{\xi_2} + \Delta E_{\xi_1,\xi_2} + 2\Delta P_p + 2\Delta W_p \tag{2.65}$$

In the above equation, the plastic work performed by the resolved shear stress $\tau$ on one partial is equal to $\Delta W_p$ and the change in Peierls energy due to kink-pair formation on a partial is given by $\Delta P_p$. The change in elastic energy $\Delta E_{\xi_n}$ of a screw partial $\xi_n$ is given by Eq. 2.58. The height $h$ of the kinks and the width $w$ between a pair of kinks describe the geometry of the kink-pair(s).

The change in elastic interaction $\Delta E_{\xi_1,\xi_2}$ between the partial dislocations is due to the contributions of elastic interactions $W_{int}$ between the kinks of both lines (Fig. 2.11): $\Delta E_{\xi_1,\xi_2}$=$W_{int}(DD')$+$W_{int}(DE')$+$W_{int}(EE')$+$W_{int}(ED') \approx W_{int}(DD')$+$W_{int}(EE') = 2W_{int}(DD')$ at low stress conditions since the width between the kink-pairs (segments $C$ and $C'$) is large. At high stress the interactions $DE'$ and $ED'$ would lower the enthalpy variation of kink-pair formation since the egde lines are opposite in sign, however these second order contributions can be neglected since this mechanism governs the kink-pair nucleation in the low stress regime. The change in elastic interaction $\Delta E_{\xi_1,\xi_2}$ has been derived as:

$$\Delta E_{\xi_1,\xi_2} = \Delta E_k = \frac{\mu b_p^2}{2\pi\left(1-\nu\right)} h \log \frac{d}{d-h} \tag{2.66}$$

where $d$ is equal to the equilibrium stacking fault width.

By solving $\partial H/\partial h$=$\partial H/\partial w$=0, for a given stress $\tau$, the critical nucleation enthalphy $\Delta H_c^{crit}$ as a function of the critical kink-pair geometry, $h^{crit}$ and $w^{crit}$, can be found as the saddle point configuration of the respective total enthalpy variation $\Delta H_c$. Generally, the height $h$ of all kinks, in the end-member case where $\tau \to 0$, is equal to a full period $a'$ of the Peierls potential.

***Low stress regime:*** $\tau > 0$

Kink-pair nucleation in the end-member case at low stress conditions is based on the nucleation of two strictly identical kink-pairs on both partials. However, the work done by the applied resolved shear stress $\tau$ in the low stress regime can be sufficient to account for the energy variation related to small changes in the stacking fault, as illustrated in Fig. 2.11, by correlated formation of two geometrically different kink-pairs on both partials. Since we are still in the low stress regime, the critical height is taken to be fixed as $h^{crit} = a'$ for $\tau \to 0$ and the widths $w_1$ (H) and $w_2$ (K'+H'+L') between the kink-pairs on both partials 1 and 2 respectively are now taken to be the free geometrical variables (Fig. 2.11 and 2.8a). The critical nucleation enthalpy $\Delta H_{cc}$ associated with this nucleation processes is equal to:

$$\Delta H_{cc} = \Delta E_{\xi_1} + \Delta E_{\xi_2} + \Delta E^s_{\xi_1,\xi_2} + 2\Delta P_p + 2\Delta W_p \tag{2.67}$$

where the change in elastic energy $\Delta E_{\xi_n}$ of a screw partial $\xi_n$ is given by Eq. 2.58. The elastic interaction energy between the partials is equal to $\Delta E^s_{\xi_1,\xi_2} = \Delta E_{\xi_1,\xi_2} + \Delta W_s$.

The energy cost $\Delta W_s$ depends on two opposite contributions: 1) the energy variation due to the change in stacking fault energy $2\gamma a' w$ and 2) the along going variation in interaction energy between the partial lines (segments $KK'$ and $LL'$ in Fig. 2.11):

$$\Delta W_s = \frac{\mu b_p^2}{2\pi}\left(-2a' - 2\sqrt{w^2+(d-a')^2} - w\log\frac{\sqrt{w^2+(d-a')^2}-w}{\sqrt{w^2+(d-a')^2}+w}\right.$$
$$\left. +2\sqrt{w^2+d^2} + w\log\frac{\sqrt{w^2+d^2}-w}{\sqrt{w^2+d^2}+w}\right) - 2\gamma a' w \quad (2.68)$$

where $d$ is the equilibrium stacking fault width and $w{=}{}^1\!/{}_2(w_2 - w_1) > 0$ (equal to the length of the line segments $K = K' = L = L'$ in Fig. 2.11).

The change in elastic interaction $\Delta E_{\xi_1,\xi_2}$ between the partial dislocations is due to the contributions of elastic interactions $W_{int}$ between the kinks of both lines (Fig. 2.11): $\Delta E_{\xi_1,\xi_2} = W_{int}(II') + W_{int}(IJ') + W_{int}(JJ') + W_{int}(JI') \approx W_{int}(II') + W_{int}(JJ') = 2W_{int}(II')$ at low stress conditions since the width between the kink-pairs (segments $H$ and $H'$) is large. The change in elastic interaction $\Delta E_{\xi_1,\xi_2}$ in this case has been derived as:

$$\Delta E_{\xi_1,\xi_2} = \frac{\mu b_p^2}{2\pi(1-\nu)}\left(2\sqrt{w^2+d^2} - d\log\frac{\sqrt{w^2+d^2}+d}{\sqrt{w^2+d^2}-d}\right.$$
$$-\sqrt{w^2+(d+a')^2} + {}^1\!/{}_2(d+a')\log\frac{\sqrt{w^2+(d+a')^2}+(d+a')}{\sqrt{w^2+(d+a')^2}-(d+a')}$$
$$\left. -\sqrt{w^2+(d-a')^2} + {}^1\!/{}_2(d-a')\log\frac{\sqrt{w^2+(d-a')^2}+(d-a')}{\sqrt{w^2+(d-a')^2}-(d-a')}\right) \quad (2.69)$$

By solving $\partial H/\partial w_1{=}\partial H/\partial w_2{=}0$, for a given stress $\tau$, the critical nucleation enthalphy $\Delta H_{cc}^{crit}$ can be found as the saddle point configuration of the respective total enthalpy variation $\Delta H_{cc}$.

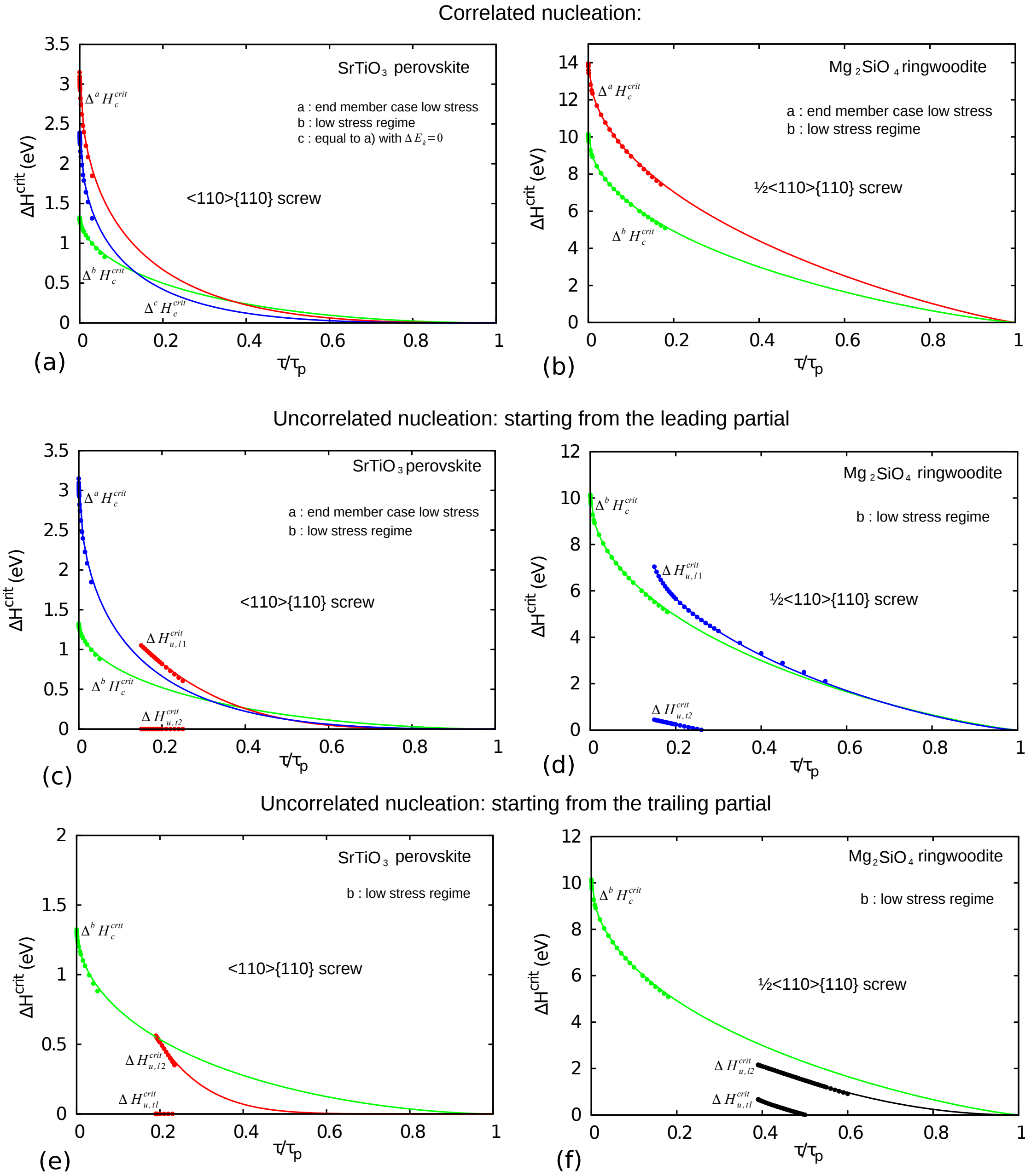

Figure 2.12: *Overview of the critical nucleation enthalpies associated with all nucleation mechanisms possible: correlated and both unit processes of uncorrelated kink-pair nucleation. The first column shows the results for $SrTiO_3$ perovskite at ambient pressure conditions and the second column for $Mg_2SiO_4$ ringwoodite at 20 GPa.*

### *Systems with small dissociation widths*

Here, we focus on dissociated dislocations with partials being strongly coupled together, *i.e.* each partial is significantly influenced by the elastic field of the other partial. This implies that the dissociated dislocation exhibits low to intermediate stacking fault widths of $\sim a' \leq d \leq 3a'$, or large stacking fault energies $\gamma$, which is for screw dislocations only dependent on the value of the shear modulus $\mu$ in case pure linear elasticity applies:

$$\gamma = \frac{\mu}{2\pi d}\left\{(\boldsymbol{b_1}\cdot\boldsymbol{\xi_1})(\boldsymbol{b_2}\cdot\boldsymbol{\xi_2}) + \frac{(\boldsymbol{b_1}\times\boldsymbol{\xi_1})\cdot(\boldsymbol{b_2}\times\boldsymbol{\xi_2})}{1-\nu}\right\} \tag{2.70}$$

The partial Burgers vectors and partial screw lines in Eq. 2.70 are given by $\boldsymbol{b_n}$ and $\boldsymbol{\xi_n}$, respectively. The critical nucleation enthalpies of these systems calculated at low stress conditions using Eq. 2.67 are equal to the critical nucleation enthalpies in the end member case at low stress using Eq. 2.65, on the condition that $\Delta E_k$=0 (Eq. 2.66). This implies that the use of linear elasticity overestimates the kink-kink interaction between the rectangular kink-pairs on both partials in the end-member case of the low stress regime, since small changes in the stacking fault are able to reduce the kink-kink interactions. As a consequence, the enthalpy variation associated with correlated kink-pair nucleation on dissociated dislocation with high stacking fault energy is finally taken to be equal to Eq. 2.65 with $\Delta E_{\xi_1,\xi_2}$=$E_k$=0 (Eq. 2.66).

An example is given in Fig. 2.12b of the $^1/_2\langle 110\rangle\,\{110\}$ screw dislocation in ringwoodite. The equilibrium stacking fault width is equal to $d$=8 Å (which is $2a'$) with an stacking fault energy of about 2 J/m$^{-2}$. The red curve is calculated using Eq. 2.65 and the green curve by the use of Eq. (2.67). The latter is equivalent to the use of Eq. 2.65 given that $\Delta E_k$=0 (Eq. 2.66).

***Systems with large dissociation widths***

The situation is different in the case of dissociated dislocations with partials being weakly coupled together, *i.e.* each partial is only marginally influenced by the elastic field of the other partial. In this case, dissociated dislocations exhibit large stacking fault widths of $d \geq 3a'$, or relatively low stacking fault energies $\gamma$. The difference with respect to systems with strongly coupled partials lies in the difference between $\Delta W_s$ (Eq. 2.67 and 2.68) in case small changes in the stacking fault $d$ are allowed at low stress. If the dissociation width $d$ is small, the change in stacking fault energy more or less compensates the associated variation in interaction energy between the partial lines. In case of weakly coupled partials, both terms have significant different weights: the change in stacking fault energy becomes more important than the variation in elastic interaction energy between the partials, despite the low stacking fault energies. This is due to the fact that the variation in interaction energy between widely separated partial lines is negligible, because of the large separation between the partials. It means that stacking fault changes in case of weakly coupled partials helps the nucleation process to occur by a decrease in the critical activation enthalpy at low stress. Therefore, the enthalpy variation associated with correlated kink-pair nucleation regarding weakly coupled partials is finally taken to be equal to Eq. 2.67 in order to caption the aforementioned role of the stacking fault.

An example is given in Fig. 2.12a of the $\langle 110 \rangle \{110\}$ screw dislocation in $SrTiO_3$ perovskite which is characterized by an equilibrium stacking fault width of about $d$=30 Å ($\sim 6a'$). The red curve is calculated using Eq. 2.65 and the green curve by the use of Eq. 2.67. The latter, in this case, results in different activation enthalpies than the use of Eq. 2.65 with $\Delta E_k$=0 (Eq. 2.66). The significant separation between the partials allows a decrease in stacking fault energy without a significant increase in the interaction between the partials (Fig. 2.11).

Figure 2.12a shows two typical features related to the enthalpy curves associated with weakly coupled partials. The first is the substantial reduction in nucleation enthalpy at low stresses with respect to the low stress end-member case. This is because of the stacking fault decrease that favors the nucleation process to occur. The second characteristic is that the gradient of the enthalpy evolution with stress in the low stress regime approximation (green curve) is smaller than the one of the low stress end member case (red curve) at low stresses. This is due to the fact that in both approximations the enthalpy curves are constrained by the Peierls stress in the high stress regime.

### Uncorrelated kink-pair nucleation: high stress regime

The alternative to glide of dissociated dislocations is the motion of the partials as a result of uncorrelated kink-pair nucleation. These processes typically govern kink-pair nucleation on dissociated dislocations in the high stress regime since this type of mechanism is characterized by an explicit change in the equilibrium stacking fault width which does not allow the isolated partials to move independently by kink-pair nucleation at low stress conditions. The kink-pair model in the high stress regime relies on the nucleation of a rectangular kink-pair of height $h$ and width $w$ on one partial dislocation at a time. The variation in enthalpy $\Delta H_{u_n}$ associated with one unit step of uncorrelated kink-pair nucleation can be described as follows:

$$\Delta H_{u_n} = \Delta E_{\xi_n} + \Delta E_{\xi_1,\xi_2} + \Delta W_{sf} + \Delta P_p + \Delta W_p \tag{2.71}$$

where the variation in interaction energy $\Delta E_{\xi_1,\xi_2}$ between the partials is described as the change in elastic interaction energy between both dislocation lines (segments $NN'$ in Fig. 2.11) as a consequence of the kink-pair formation on either the leading or the trailing partial:

$$\Delta E_{\xi_1,\xi_2} = \frac{\mu b_p^2}{4\pi}\left(\pm 2h - 2\sqrt{w^2+d_f^2} - w\log\frac{\sqrt{w^2+d_f^2}-w}{\sqrt{w^2+d_f^2}+w}\right.$$
$$\left. +2\sqrt{w^2+d_i^2} + w\log\frac{\sqrt{w^2+d_i^2}-w}{\sqrt{w^2+d_i^2}+w}\right) \qquad (2.72)$$

This expression is dependent on the precise mechanism of a unit step such that $d_i$ and $d_f$ correspond to the initial and final stacking fault width between both partial dislocations respectively during nucleation as shown in Fig. 2.8b and c. $\Delta W_{sf}$ is equal to the change in stacking fault energy $\pm\gamma hw$ and balances as such the variation in elastic interaction energy $\Delta E_{\xi_1,\xi_2}$.

#### 2.3.2.5 Critical nucleation enthalpies

The enthalpy evolution with stress according to kink-pair nucleation on dissociated dislocations can be described in a general way in the framework of the elastic interaction model. Correlated nucleation of kink-pairs is always captured by the single critical activation enthalphy [1] $\Delta H_c^{crit}$ (Fig. 2.12a and b). However, two independent uncorrelated nucleation processes can be distinguished (Fig. 2.8). The process where the leading partial first starts to move outwards, described by [2] $\Delta H_{u,l_1}^{crit}$, followed by the inward migration of the trailing partial, given by $\Delta H_{u,t_2}^{crit}$, is entirely governed by the first nucleation step: $\Delta H_{u,t_2}^{crit} \ll \Delta H_{u,l_1}^{crit} \approx \Delta H_c^{crit}$. This uncorrelated nucleation process is therefore equivalent to correlated nucleation since the first nucleation step governs the critical enthalpy change of the whole process and displays a similar critical enthalpy evolution

---

[1] The subscript ”c” refers to correlated nucleation processes occuring coherently at both partials whear-eas the subscript ”u” refers to uncorrelated nucleation of a kink-pair on the partial dislocation lines. These subscripts will be used in the same manner throughout the rest of the thesis.

[2] The subscripts ”l” and ”t” refer to the outward motion of leading partial and the inward motion of the trailing partial respectively as due to uncorrelated kink-pair nucleation. The subscripts ”1” and ”2” refer to the first and second unit step respectively of uncorrelated nucleation of kink-pairs.

as correlated nucleation. Examples of this processes are shown in Fig. 2.12c and d. For the second uncorrelated nucleation processes, the first step is described by $\Delta H_{u,t_1}^{crit}$ of the inward migration of the trailing partial followed by the outward motion of the leading partial described by $\Delta H_{u,l_2}^{crit}$ and is much larger than the first step: $\Delta H_{u,t_1}^{crit} \ll \Delta H_{u,l_2}^{crit}$. Examples are shown in Fig. 2.12e and f. Hence, uncorrelated nucleation of kink-pairs is therefore essentially determined by $\Delta H_{u,l_2}^{crit}$ to which we will simply refer as $\Delta H_u^{crit}$, on the condition that uncorrelated nucleation of kink-pairs starting from the trailing partial (Fig. 2.8c) is possible to occur.

In case the equilibrium dissociation width $d$ is equal to a single period $a'$ of the Peierls potential: kink-pair nucleation that starts from the trailing partial is impossible to occur since the change in interaction energy of the partials would diverge. The evolution of the critical nucleation enthalpy with stress would be entirely given by $\Delta H_c^{crit}$, since $\Delta H_{u,l_1}^{crit} \approx \Delta H_c^{crit}$.

### Model summary

As a small summary, Fig. 2.11 shows the characteristics of kink-pair nucleation as a function of applied stress that is brought together in the model. Starting from Fig. 2.11b at low stress conditions, kink-pair nucleation is forced to occur in a correlated manner at both partials. Only a small variation in equilibrium stacking fault width $d$ is allowed. This small variation in $d$, in case the partials are weakly coupled (*i.e.* partials are separated by a large equilibrium distance $d$), is able to reduce the saddle point configuration of the metastable system by lowering the stacking fault energy without any change in elastic interaction between the partials. Under these low stress conditions, the widths $w_1$ (partial 1) and $w_2$ (partial 2) between the kink-pairs are relatively equal. However, if stress increases, one of the kink-pairs tends to collapse and the kink-pair nucleation process becomes progressively decoupled: independent uncorrelated kink-pair nucleation on both partials (Fig. 2.11c) that is dominated by the second unitstep of a complete kink-pair nucelation process which starts from the trailing partial (Fig. 2.8c).

### 2.3.3 Dislocation mobility

Below the athermal temperature, dislocation motion is the result of the interaction between dislocations and the crystal lattice. The motion of a dissociated dislocation of length $L$ over an elementary lattice period $a'$ is characterized by the nucleation of a kink-pair on both partials. Therefore, the dislocation mobility depends on the waiting time for a complete nucleation process to occur, *i.e.* on the rate of the governing kink-pair nucleation process. The average dislocation velocity (Dorn and Rajnak 1964; Guyot and Dorn 1967; Möller 1978) under the action of a uniform resolved shear stress can be described as:

$$v\left(\tau, T\right) = \frac{a'}{t} = a'J \tag{2.73}$$

where $t$ is equal to the waiting time of the complete dislocation to move a unit distance $a'$ (Peierls periodicity). $J$ describes the kink-pair nucleation rate which for correlated kink-pair formation $J_c$ is given by:

$$J_c = \nu_0 \frac{b_p}{w^{crit}\left(\tau\right)} \frac{L}{2b_p} \exp\left(-\frac{\Delta H_c^{crit}\left(\tau\right)}{k_b T}\right) \tag{2.74}$$

where $b_p$ is the modulus of the Burgers vector of the partial dislocations. The nucleation rate $J$ (Eq. 2.74) is the product of three terms: $\exp\left(-\Delta H^{crit}\left(\tau\right)/k_b T\right)$ is equal to the probability distribution of kink-pair formation, $\nu_0 b_p / w^{crit}$ is the jump frequency with which the partials attack the energy barrier, with the Debye frequency $\nu_0 {=} \left(3N/4\pi V\right)^{1/3} v_p$ and $N/V$ being equal to the number density of the crystal and $v_p$ corresponding to the P-wave speed. Further, $L/c_i b_p$ is the number of sites at which nucleation might occur on the partial lines. For correlated nucleation $c_i {=} c_c {=} 2$, whereas for uncorrelated nucleation $c_i$=$c_u$=1. The number of potential nucleation sites is smaller for correlated than for uncorrelated kink-pair nucleation since only the resonance modes of the complete dislocation allow nucleation of kink-pairs on both partials (Takeuchi 1995). The average length of the dislocation lines is given by $L = 1/\sqrt{\rho_m}$. Here, $\rho_m$ corresponds to the dislocation density, taken to be $10^{12}$ m$^{-2}$ under experimental and $10^8$ m$^{-2}$ for mantle conditions to take into account the stress difference between both regimes. The pre-exponential factor in Eq. 2.74 may also, to some extent, depend on temperature, but it is negligible with respect to the exponential term.

The dislocation mobility for $\tau \leq \tau_c$ can therefore be described by:

$$v_c\left(\tau, T\right) = a' J_c\left(\Delta H_c^{crit}\right) \tag{2.75}$$

The dislocation velocity for $\tau \geq \tau_c$ is due to both correlated and uncorrelated kink-pair nucleation and is given, following Möller (1978), by:

$$v_{c+u}\left(\tau, T\right) = \frac{1}{2} a' \left[J_c\left(\Delta H_c^{crit}\right) + J_u\left(\Delta H_u^{crit}\right)\right] \tag{2.76}$$

where the nucleation rate corresponding to uncorrelated nucleation can be formulated as:

$$J_u = \left(t_{u,t_1} + t_{u,l_2}\right)^{-1} = \left(\frac{1}{J_{u,t_1}} + \frac{1}{J_{u,l_2}}\right)^{-1} \simeq J_{u,l_2} \tag{2.77}$$

where the $J_{u,t_1}$ and $J_{u,l_2}$ correspond to the nucleation rate associated with the inward motion of the trailing partial and the outward motion of the leading partial (characterized by $\Delta H_u^{crit}$) respectively. The nucleation rate of kink-pairs that corresponds to $J_u$ is defined as

$$J_u = \nu_0 \frac{b_p}{w^{crit}(\tau)} \frac{L}{b_p} \left( \frac{\tau - \tau_c}{\tau} \right) \exp \left( - \frac{\Delta H_u^{crit}(\tau)}{k_b T} \right) \tag{2.78}$$

The pre-exponential factor $(\tau - \tau_c)/\tau$ has been introduced to guarantee the continuity between both velocity solutions $v_c$ and $v_{c+u}$. It relies on the assumption that the dislocation velocity $v_{c+u}$ at $\tau = \tau_c$ has to be strictly equal to that of $v_c$ since the velocity below $\tau_c$ is only the result of correlated nucleation of kink-pairs on the partials.

In case the dissociation width is equal to a single period of the Peierls potential, kink-pair nucleation that starts from the trailing partial is impossible to occur as already mentionned before. In that case, uncorrelated nucleation will be entirely governed by the process where the leading partial starts to move outward followed by the inward motion of the trailing partial:

$$J_u = \left[ \left( \frac{1}{J_{u,l_1}} + \frac{1}{J_{u,t_2}} \right)^{-1} \right] \simeq J_{u,l_1} \simeq J_c \tag{2.79}$$

The partials are strongly coupled as a result of the minimum dissociation width and we can see that the dislocation mobility in the entire stress regime $0 < \tau \leq \tau_p$ will be essentially governed by correlated nucleation of kink-pairs along both partials. In this special case, the dissociated dislocation can be considered to have a compact core structure and the dislocation mobility can to first order be approximated by using the same method as in Amodeo *et al.* (2011).

### 2.3.4 Single slip constitutive equations

Below the athermal temperature, plastic flow is directly controlled by the mobility of dislocations. In this regime, the relation between the atomic scale behavior of individual dislocations and the average collective macroscopic behavior can be derived from

Orowan's equation:

$$\dot{\epsilon} = \rho_m b v = \dot{\epsilon}_0 \exp\left(\frac{-\Delta H^{crit}(\tau)}{k_b T}\right) \tag{2.80}$$

where $\rho_m$ corresponds to the mobile dislocation density, $b$ is the modulus of the Burgers vector, $v$ is the average dislocation velocity and $k_b$ is Boltzmann constant. For any given constant strain rate $\dot{\epsilon}$, Eq. 2.80 can be solved for the temperature as function of the shear stress $\tau$, which can be seen as the critical resolved shear stress $CRSS$.

By taking the natural logarithm of Eq. 2.80, the latter can be rewritten as:

$$\log\left(\dot{\epsilon}_0/\dot{\epsilon}\right) = \beta = \frac{\Delta H^{crit}(\tau)}{k_b T} \rightarrow \Delta H^{crit}(\tau)\Big|_{\tau=CRSS} = \beta k_b T \tag{2.81}$$

Physically, it shows the direct relation between the microscopic processes of kink-pair formation captured by the resolved shear stress dependence $\tau$ on the critical nucleation enthalpies $\Delta H^{crit}$ and the macroscopic temperature $T$ observable as function of the $CRSS$.

The physics that describes the dislocation mobility as a result of thermally activated kink-pair nucleation is strongly dependent on the intrinsic lattice friction (Peierls potential en Peierls stress) and therefore on the core structure of the dislocation considered. The evolution of the $CRSS$ with $T$ for a given dislocation is therefore largely determined by the material properties and the crystal chemistry at the appropriate physical conditions. Nevertheless, there is a number of general features to summarize with respect to the model. We illustrate that by considering three non-equivalent collinear dissociated dislocations each gliding in different planes in a fictive material. All dislocations exhibit the same Peierls stress (they experience the same intrinsic lattice friction) and the critical nucleation enthalpies $\Delta H^{crit}$ at $\tau \rightarrow 0$ are strictly equivalent as well. The main difference between them is the dissociation width and the corresponding stacking fault energies depending on the shear modulus $\mu$ with respect to each dislocation. One of the dissociated dislocations is considered to have strongly coupled partials, the next one intermediate coupled partials and the last one is finally characterized by weakly coupled partials. We suppose as well that the weakly coupled partials have more extended core structures in the glide plane than the strongly coupled partials that exhibits a small dissociation width. Figure 2.13 gives an illustration of the different evolutions of $\Delta H^{crit}$ to be expected as a function of $\tau$ for the three cases considered. In any case, there exists a critical stress $\tau_c$ below which only correlated kink-pair nucleation can take place and above which both uncorrelated and correlated nucleation operate in parallel. The critical stress $\tau_c$ is the lowest for the system having weakly coupled partials. In case the partials are strongly coupled, *e.g.* dissociation width is about equal to a single period of the Peierls potential, the mobility is completely governed by correlated nucleation.

The microscopic description of thermally activated dislocation glide can be converted into a constitutive equation as the $T$-dependence of the $CRSS$, as illustrated by Eq. 2.81. This conversion is shown in Fig. 2.13 for the three dissociated dislocations in our fictive material. The intrinsic lattice friction is equal in all cases, since all dislocations are assumed to have the same Peierls stress $\tau_p$. However, the evolution of the $CRSS$ with $T$ in the presence of thermal activation is significantly different for the three dislocations considered. The $CRSS$ for the system with weakly coupled partials decreases faster with $T$ than for the system with the strongly coupled partials: the evolution of the $CRSS$ as a function of $T$ for strongly coupled partials has the tendency to exhibit a more linear evolution than the case of weakly coupled partials with more extended core structures, for which the evolution is expected to be more exponential. This behaviour can be explained by two effects:

1) the effect of the large equilibrium stacking fault width that drastically lowers the change in interaction energy between both partials related to kink-pair nucleation.

2) the effect of the cutoff radius $\rho$ by its dependence on the core spreading of the partials.

We, nevertheless, want to strongly emphasize the uniqueness of the constitutive equations related to a particular dislocation belonging to a given system, which is strongly dependent on the intrinsic lattice friction that will be determined by the core structure of the dislocation. The latter is dependent on the material properties and the crystal chemistry.

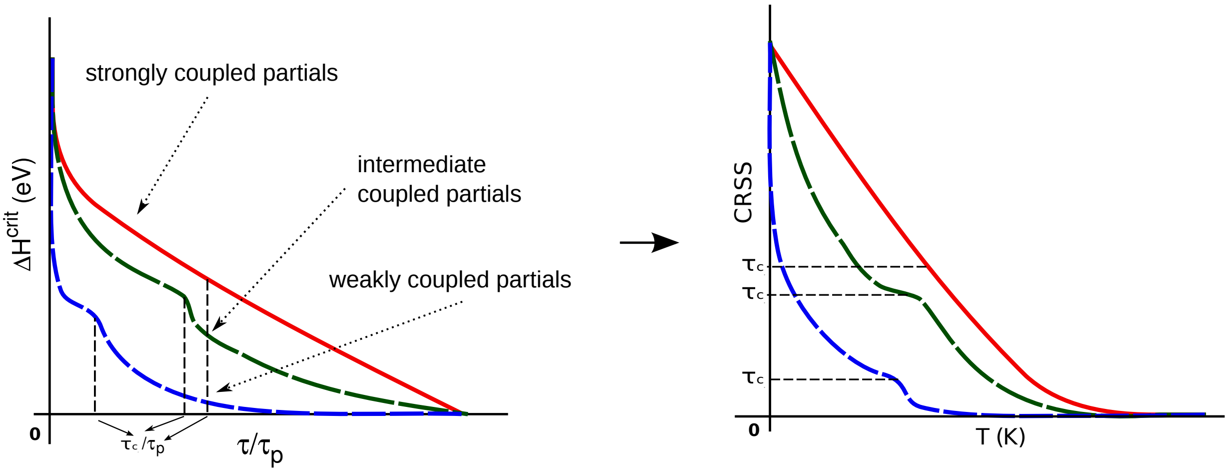

Figure 2.13: *Illustration of the evolution of the critical nucleation enthalpy* $\Delta H^{\mathrm{crit}}$ *as a function of* $\tau$ *normalized by the Peierls stress* $\tau_p$ *for three non-equivalent collinear dissociated dislocations each gliding into different planes in a fictive material. All dislocations are characterized the same Peierls stress (they experience the same intrinsic lattice friction) and the critical nucleation enthalpy* $\Delta H^{\mathrm{crit}}$ *at* $\tau \to 0$*. The first dislocation has strongly coupled partials with confined core structurs, the next intermediate coupled partials and the last one is characterized by weakly coupled partials which are extended into the glide plane. Finally, the relation is shown between the constitutive equations given as the* $T$*-dependence on the* $CRSS$ *and the* $\tau$*-dependent evolution of the critical nucleation enthalpies* $\Delta H^{\mathrm{crit}}$ *associated with thermally activated glide.*

### 2.3.5 Benchmark: $SrTiO_3$ perovskite

For the high pressure minerals that constitute the Earth's mantle, it is experimentally still impossible to obtain very accurate data of the $CRSS$ as a function of $T$ related to slip systems in single crystals. As such, there is no way to benchmark our elastic interaction model directly to mantle minerals. However, strontium titanate $SrTiO_3$, a cubic perovskite of space group $Pm3m$, is stable at ambient pressure conditions and can be considered as analogue of natural perovskites such as bridgmanite. Because of the ductility of strontium titanate at room temperature, numerous experimental studies have been performed on the intracrystalline plasticity of $SrTiO_3$ that provided accurate data related to dislocation mobility (Brunner 2001; Brunner 2006; Sigle *et al.* 2006; Castillo-Rodríguez and Sigle 2010; Hirel *et al.* 2012). At low temperature, below ~1000 $K$, plastic deformation is controlled by glide of the $\langle 110\rangle$ screw dislocations spreading into their $\{110\}$ glide planes (Brunner 2006; Castillo-Rodríguez and Sigle 2010).

| Dislocation | $b_p$ (Å) | $\mu$ (GPa) | $a'$ (Å) | $\xi^h$ (Å) | $d$ (Å) | $\nu$ (GPa) | $APB_\gamma$ ($J/m^2$) | $\tau_p$ (MPa) | $\rho$ (Å) |
|---|---|---|---|---|---|---|---|---|---|
| $\langle 110\rangle\{110\}$ | $b_{p_1}$=2.78 | 110 | 3.9 | $\xi_1^h$=3.5 | 30 | 0.25 | 0.45 | 500 | 0.56= |
| | $b_{p_2}$=2.78 | | | $\xi_2^h$=3.5 | | | | | $0.08\cdot 2\xi^h$ |

Table 2.2: *Parametrization of the core structures of the* $\langle 110\rangle\{110\}$ *screw dislocation and associated intrinsic lattice friction in* $SrTiO_3$*. The partial Burgers vector are given by* $b_p$*,* $\mu$ *is equal to the shear modulus,* $\nu$ *is the Poisson ratio,* $\xi^h$ *corresponds to the half width of each partial (*$2\xi^h$ *is the width of a partial),* $d$ *is equal to the equilibrium stacking fault width taken as the distance between the partials,* $APB_\gamma$ *is the apparent equilibrium stacking fault energy and* $\tau_p$ *is equal to the Peierls stress.*

In 2006, Brunner performed isothermal straining and isothermal straining temperature-lowering tests (IST's and ISTLP's) to quantify accurately the critical resolved shear stress $CRSS$ as a function of $T$ in $SrTiO_3$ single crystals. Polarized light microscopy revealed the dominance of $\langle 110\rangle$ $\{110\}$ screw dislocations until temperatures corresponding to 300 K. This is confirmed by weak-beam TEM characterization of the dominance of $\langle 110\rangle$ screw dislocations below 1000 K. The $\langle 110\rangle\,\{110\}$ screw dislocation is collinearly dissociated into two equivalent partials following the Burgers vector reaction: $\langle 110\rangle = {}^1\!/_2\langle 110\rangle + {}^1\!/_2\langle 110\rangle$ (Hirel *et al.* 2012). This has been supported by experimental observations (Castillo-Rodríguez and Sigle 2010).

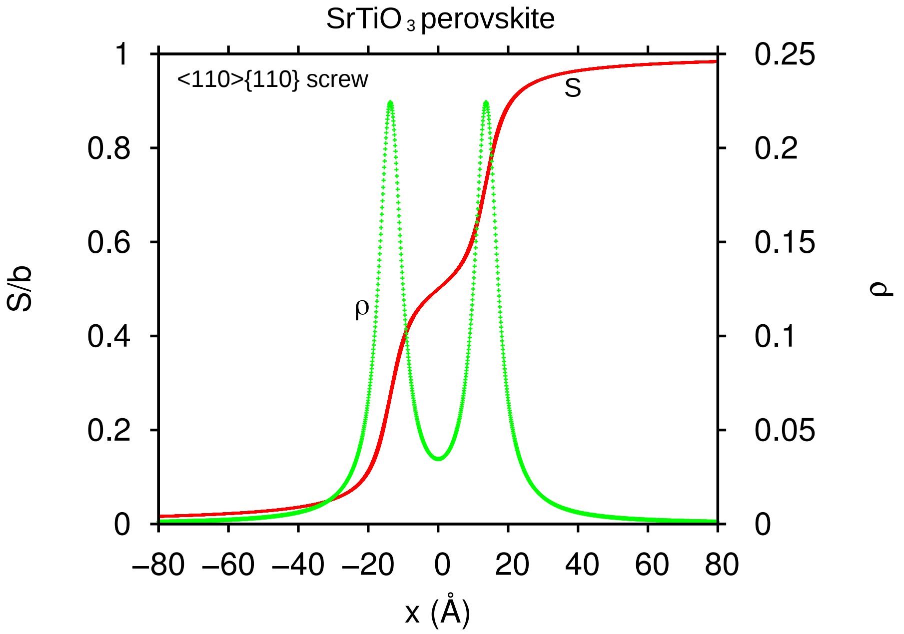

Figure 2.14: *Spread of the Burgers vector distribution or dislocation core structure in form of the disregistry (red continuous line) and its derivative, the local density of the Burgers vector (green dotted line) of the* $\langle 110\rangle\{110\}$ *screw dislocation in* $SrTiO_3$ *as inferred from the atomistic study of Hirel* et al. *(2012).*

We propose to benchmark our elastic interaction model adapted for dissociated dislocations by the thermal activation of $\langle 110\rangle\,\{110\}$ screw dislocations in the low temperature regime. The core structure of the glide-dissociated $\langle 110\rangle\,\{110\}$ screw dislocation has already been modelled using atomistic simulations by Hirel *et al.* (2012). The generalized stacking fault surface of the $\{110\}$ in $SrTiO_3$ has been calculated also by Hirel *et al.* (2010). We will use both the core structure and the $\gamma$-surface to calculate the intrinsic lattice friction of the $\langle 110\rangle\,\{110\}$ screw dislocation by the Peierls potential and the Peierls stress with which we will, in combination with the core structure as such, parametrize the elastic interaction model.

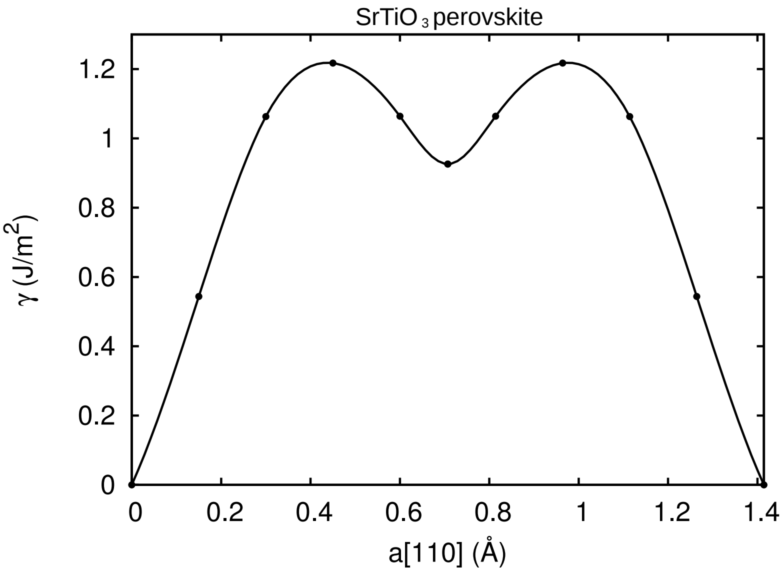

Figure 2.15: *$\gamma$-line in the direction of the $\langle 110\rangle$ screw dislocation in SrTiO$_3$ as calculated atomistically, using* ab initio *calculations, by Hirel* et al. *(2010).*

The model parameters used with respect to the core structure as inferred from Hirel *et al.* (2012) are listed in table 2.2. The use of the Thomas potential by Hirel *et al.* (2012) underestimates the dissociation width $d$ as they discuss, due to an overestimation of the equilibrium stacking fault energy of about 30%. We therefore rescale $d$ by 30% as input for our model, assuming that the overestimation can be translated to an underestimation of $d$ as suggested by Eq. 2.70. We choose to parametrize the disregistry $S(x)$ of the $\langle 110\rangle\{110\}$ screw dislocation by two arctangent functions (Eq. 2.41) as follows:

$$S(x) = \frac{b}{2} + \frac{b}{2\pi}\left[\arctan\left(\frac{x-d/2}{\xi_1^h}\right) + \arctan\left(\frac{x-d/2}{\xi_2^h}\right)\right] \tag{2.82}$$

The disregistry and its derivative, the local Burgers vector density can be seen in Fig. 2.14. The intrinsic lattice friction is quantified by the Peierls potential that is calculated by making use of the $\{110\}$ $\gamma$-surface according to Eq. 2.44, as described in chapter 2.2.4. The $\gamma$-surface of the $\{110\}$ plane has been obtained by the use *ab intio* calculations by Hirel *et al.* (2010), for which the $\gamma$-line in the Burgers vector direction is shown in Fig. 2.15. The resulting Peierls potential $V_p$ and the Peierls stress $\tau_p$, as derived from the Peierls force $\Sigma$=b$^{-1}$ $\nabla V_p$, are shown in Fig. 2.16. Results are as well listed in table 2.2.

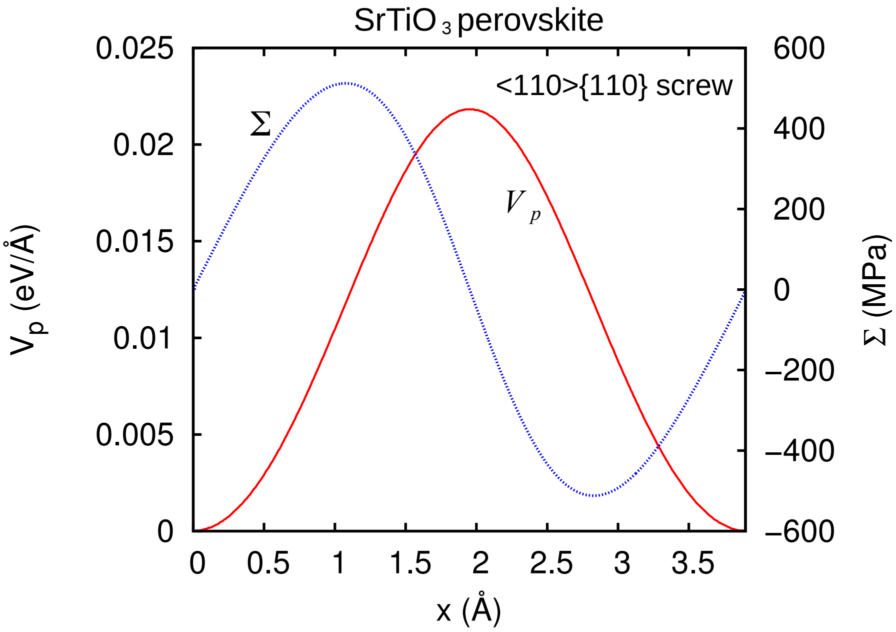

Figure 2.16: *Peierls potentials $V(p)$ and subsequent Peierls force $\Sigma = b^{-1}\ \nabla V(p)$ calculated using the PN model based on the dislocation structures for the $\langle 110\rangle\{110\}$ screw dislocations in SrTiO$_3$. The potentials give a pure mechanical measure of the lattice friction of both slip systems which will serve as input to calculate the thermally activated mobility the respective screw dislocations.*

The rescaled dissociation width $d$ as obtained by Hirel *et al.* (2012) are in good agreement with experimental observations (Castillo-Rodríguez and Sigle 2010). Since our model is based on linear elasticity, we will use the value of $d$ to calculate an apparent equilibrium stacking fault energy $APB_\gamma$ for the antiphase boundary by the use of elasticity theory (Eq. 2.70). The resulting value of $APB_\gamma$ is underestimated with respect to ∼0.9 $J/m^2$ from the $\gamma$-line in the $\langle 110\rangle$ direction, as shown in Fig. 2.15. A possible explanation of this discrepancy could lie in the imperfect ABP as the partials partially overlap, which can be seen in the Burgers vector density in Fig. 2.14 as it is not equal to 0 at the APB. The value of the apparent APB, $APB_\gamma$, as used in the model is given in table 2.2.

The cut-off radius $\rho$ is fixed such that the critical stress $\tau_p$ is about equal to the ∼100 MPa that is observed experimentally. This results in $\rho$=0.56 Å which is equal to 8% of a the width a partial $\xi_n$. This is in agreement with our initial choice of $\rho$=0.1×$\xi_n$ that is considered in the elastic interaction model (table 2.2).

The elastic interaction model adapted for collinear dissociated dislocations has been used to calculate the evolution of the $CRSS$ with $T$ related to thermally actived slip. The model is parametrized by the Peierls potential and the subsequent Peierls stress (Fig. 2.16) and the core structure of the $\langle 110\rangle\{110\}$ screw dislocation in $SrTiO_3$. All parameters are listed in table 2.2. The effective results of the critical activation enthalpies $\Delta H^{crit}$ are shown in Fig. 2.12e. These results can be converted into a constitutive equation as the $T$ dependence of the $CRSS$. The dislocation density $\rho$ has been parametrized by the Taylor relation to take into account the back stress of the (dislocation) forest:

$$\rho = \left(\frac{\tau_f}{C\mu b_p}\right)^2 \tag{2.83}$$

where $\tau_f$ is the back stress of the forest that has been measured experimentally (Castillo-Rodríguez and Sigle 2010) and $C \simeq 0.1$ is a constant. The effect of the forest on the plasticity is not included in our model. It is the most important in the low stress regime as the resolved shear stresses are too low to cut the dislocation forest. We therefore make the corrections in the low $CRSS$ regime as follows:

$$CRSS(T) = CRSS(T) + \left(\frac{T}{T_a} \times \tau_f\right) \tag{2.84}$$

where $T_a$ is equal to the athermal temperature. Figure 2.17 shows the final resuls of the $CRSS$ as a function of $T$ for the $\langle 110 \rangle \{110\}$ screw dislocation together with the experimental results obtained by Brunner (2006) and shown by the red dots.

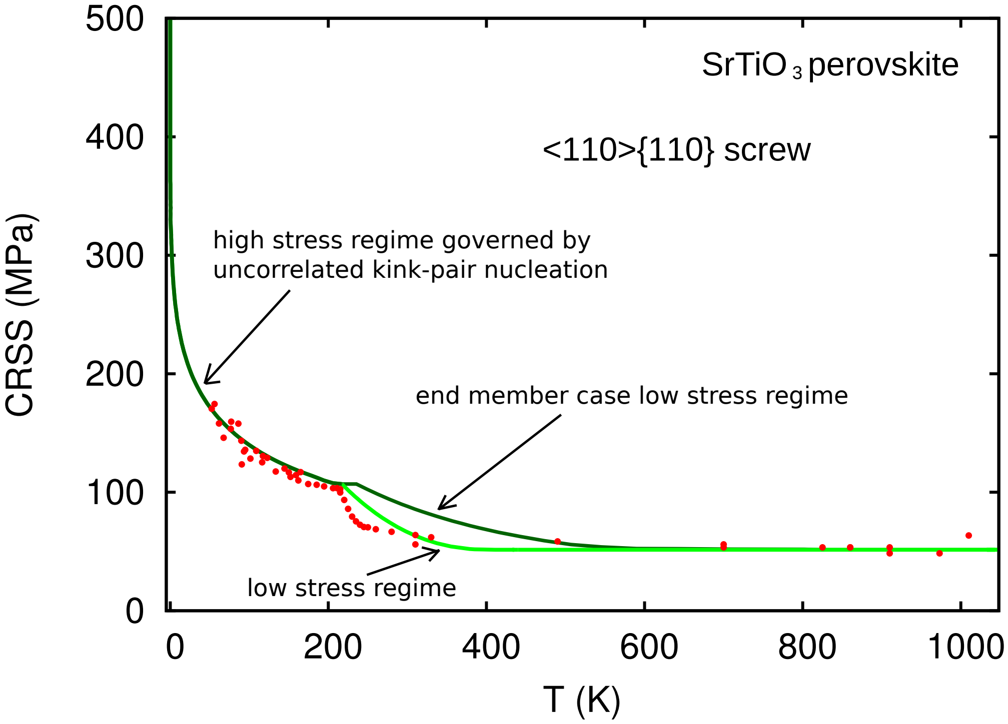

Figure 2.17: *Constitutive relation shown as the critical resolved shear stress ($CRSS$) versus temperature ($T$) at a fixed experimental strain rate of $\dot{\epsilon} = 10^{-5}\ s^{-1}$ for thermally actived glide of the rate controlling $\langle 110 \rangle \{110\}$ screw dislocations. The experimental values from Brunner (2006) are shown by the red dots.*

We can observe that there is an overall good agreement between the experimental values and the theoretical results from the elastic kink-pair model. The best fits are found in the low and high stress regime. The model shows that the non-monotonic behaviour of the $CRSS$ with $T$ can be explained by the transition from thermally activated glide by correlated nucleation of kink-pairs in the low stress regime to glide that is governed by uncorrelated nucleation of kink-pairs in the high stress regime. However, the model is not able to predict the exact curvature in the transition region. The elastic interaction model is based on the calculation of the critical nucleation enthalpy $\Delta H^{crit}$ related to a specific nucleation mechanism. The transition region between the different mechanisms is therefore not well described by the model. Nevertheless, Fig. 2.17 shows that the use of the model considering the end-member case at low stress produces less accurate results with respect to the low stress model. The latter takes explicitly into account the effect of the dissociation width on the mobility of the partials. Therefore, the weakness of the model lies in the description of the constitutive relations according to the transition between the low and high stress regime. However, the model seems to be capable of predicting the correct trends and the good order of magnitude of the constitutive equations related to thermally activated glide of the $\langle 110\rangle\{110\}$ dissociated dislocations in $SrTiO_3$ single crystals.

### 2.3.6 Conclusive summary

The modelling of thermally activated glide of dissociated dislocations is based on an elastic interaction model, intially proposed by Koizumi *et al.* (1993) for undissociated dislocations. In this work, it has been adapted to dissociated dislocations. In high lattice friction materials, the glide mobility is assumed to be controlled by the nucleation and propagation of unstable kink-pairs over the Peierls barrier assisted by the resolved shear stress (Kubin 2013). The rate of kink-pair formation is governed by the enthalpy variation $\Delta H$, as a function of the kink-pair geometry, required to nucleate a bulge from the initial dislocation line bowing out over the Peierls potential. The model is parameterized by the Peierls potential and the subsequent Peierls stress and the core structure of the rate limiting screw dislocation(s) in the respective material. The key features of the model are:

1. At low stress, correlated nucleation of kink-pairs along both partials is forced to govern the thermally activated glide motion of dissociated dislocations.

2. Above a critical stress $\tau_c$, uncorrelated nucleation of kink-pairs mostly account for the glide motion. This process is unable to occur below $\tau_c$.

3. The shift in kink-pair nucleation mechanism from purely correlated at low stress to uncorrelated governed kink-pair nucleation at higher stresses is characterized by a region of non-monotonic evolution of the $CRSS$ with $T$ in the framework of the elastic interaction model.

4. The effect of the dissociation on the dislocation mobility is strongly dependent on the dissociation width (equilibrium stacking fault width) between the partials.

5. The evolution of the $CRSS$ with $T$ in case of weakly coupled partials (*i.e.* large dissociation width) evolves more exponentially than in the case of strongly coupled partials.

The nature of the stacking fault between partials, and therefore the coupling mode between the partials, will have a determining influence on the mobility of dissociated dislocations.

# 3 Dislocation glide in $Mg_2SiO_4$ wadsleyite and ringwoodite

> *It is not possible to do much with only the results of a tensile test, because one does not know what they really mean. They are the outcome of a number of very complicated physical processes taking place during the test. The extension of a piece of metal is, in a sense, more complicated than the working of a pocket watch, and to hope to derive information about its mechanism from two or three data derived from measurements is perhaps as optimistic as would be the attempt to learn about the working of a pocket watch by determining its compressive strength.*
>
> Egon Orowan.
>
> (*The significance of tensile and other mechanical test properties of metals*, 1944.)

The aim of this chapter is to apply the multiscale modelling approach as presented in chapter 2 to $Mg_2SiO_4$ wadsleyite at 15 GPa and ringwoodite at 20 GPa. The purpose is to establish constitutive equations related to the glide mobility of the rate controlling dislocations that belong to the easiest slip systems. Our modelling approach is based on the glide mobility that is controlled by lattice friction: glide is the consequence of stress-assisted thermally activated motion of the (partial) dislocations through the nucleation and propagation of unstable kink-pairs by which the dislocation is able to overcome its lattice resistance. This means that dislocation motion in the form of glide is the result of the interaction between dislocations and the crystal lattice. This is the case below a critical temperature $T_a$ (commonly referred to as the athermal temperature) in a regime where the $CRSS$ is temperature dependent. At the same time, the model is able to determine the temperature threshold $T_a$ above which dislocation-dislocation interactions control the dislocation mobility.

The resulting constitutive equations have to be associated with single slip of the rate governing dislocations. Considering the appropriate conditions, they will be compared with the available data on plastic deformation of both wadsleyite and ringwoodite to be able to validate our modelling approach. Finally, single slip viscosities according to the relevant mantle conditions will be derived. The implications for the rheology of the transition zone are discussed in section 3.3 of this chapter and in chapter 4.

This chapter gave rise to the publication of the following articles:

- Ritterbex, S., Carrez, Ph., Gouriet, K., and Cordier, P. (2015) Modeling dislocation glide in $Mg_2SiO_4$ ringwoodite: Towards rheology under transition zone conditions. *Physics of the Earth and Planetary Interiors*, 248, 20-29.
- Ritterbex, S., Carrez, Ph., and Cordier, P. Modeling dislocation glide and lattice friction of $Mg_2SiO_4$ wadsleyite in conditions of the Earth's transition zone. *American Mineralogist*, in press, published in Sept. 2016.

## 3.1 Wadsleyite at 15 GPa

The dislocation core structures belonging to the easiest slip systems have already been calculated by Metsue *et al.* (2010) using the PNG model. They have taken into account the following slip systems: [100](010), [100](001), [010](100), [010](001), [001](010), $1/2\langle 111\rangle\,\{101\}$, for both the screw and edge dislocations. The calculations relied on the $\gamma$-surfaces of the potential slip planes, which were calculated using the so-called *THB1* empirical potential following the earlier work of Sanders *et al.* (1984) and Lewis and Catlow (1985). The easiest slip systems were found to be the $1/2\langle 111\rangle\,\{101\}$ and [100](010) which is supported by experimental observations (Thurel *et al.* 2003). Metsue *et al.* (2010) show that dislocation core structures of both slip systems are found to be more confined for the screw than for the edge dislocations. As a consequence, the mobility of the $1/2\langle 111\rangle\{101\}$ and the [100](010) screw dislocations will account for most of the plastic strain produced during deformation. In this work, we first have reevaluated the core structures of the $1/2\langle 111\rangle\{101\}$ and [100](010) screw dislocations. These results are used to model plastic deformation of $Mg_2SiO_4$ wadsleyite as a result of thermally activated dislocation glide.

### 3.1.1 $\gamma$-Surfaces

In order to validate the use of the *THB1* potential, Metsue *et al.* (2010) compared the $\gamma$-line in the [100] Burgers vector direction for the (010) plane obtained with explicit use of *ab initio* calculations. Apart from minor differences, the results were satisfying and the empirical potential was able to reproduce an equivalent shape and excess energy values as the line calculated using *ab initio* simulations. This exercise was not done for the {101}. Therefore, we calculate the $\gamma$-line of the {101} in the $1/2\langle 111\rangle$-direction. Calculations are perfomed with the *ab initio* based VASP code using the GGA approximation and the PAW pseudopontial method. Relaxation of the perfect crystal structure at 15 GPa leads to the lattice parameters $a = 5.6067$ Å $b = 11.2542$ Å $c = 8.0553$ Å comparable to the experimental values obtained at 18 GPa (Horiuchi and Sawamoto 1981).

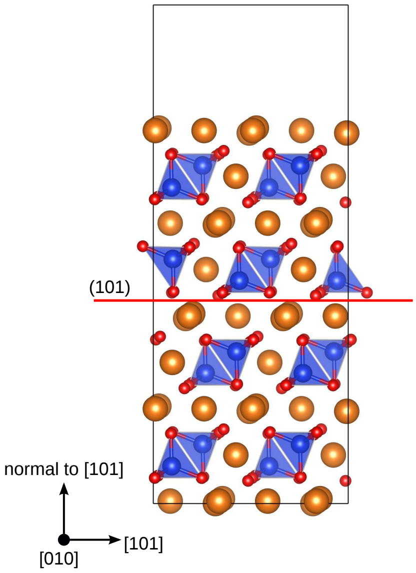

Figure 3.1: *Unsheared supercell configuration used to calculate the $\gamma$-lines in the* $^1/_2\langle 111\rangle$ *Burgers vector direction of the* $\{101\}$ *plane. The shear plane is presented by the red plane in the middle of the supercell. A vacuum layer of* 6 *Å at the top of the supercells avoids the effect of interaction between the stacking fault replicas due to periodic boundary conditions.*

A supercell was built in a Cartesian frame of reference defined by its normal and shear directions. The supercell is shown in Fig. 3.1. The stacking fault level in each of the three supercells is chosen in such a way as to avoid a cut of the strong Si-O bonds that leads to the definition of a unique choice of the cutting level with respect to the $\{101\}$ plane. See chapters 2.1.2 and 2.1.3 for more details about the construction of the supercells and the calculation of $\gamma$-surfaces. The resulting $\gamma$-line and the one calculated by Metsue *et al.* (2010) using the *THB1* potential are shown in Fig. 3.2a. Both the shape and the quantification of the excess energy related to $\gamma$-line from using the empirical potential are in relatively good agreement between the line obtained by our *ab initio* calculations. This validation enables us to use the full $\gamma$-surfaces of the (010) and $\{101\}$ as obtained by Metsue *et al.* (2010) from molecular statics (*THB1* potential). *Ab initio* calculations of the $\gamma$-lines of both potential (010) and {101} glide planes in their Burgers vector direction, [100] and $^1/_2\langle 111\rangle$ respectively, are shown in Fig. 3.2b. Both $\gamma$-lines exhibit a camel hump shape due to the existence of a metastable minimum, which forecasts the dissociation of the complete Burgers vector into partials. The complete $\gamma$-surfaces as used to parametrize the PNG model in order to calculate the core structures of the $^1/_2\langle 111\rangle\{101\}$ and the [100](010) screw dislocations are shown in Fig. 3.3. The lowest energy shear paths are indeed found along the [100] direction for the (010) plane and along the $^1/_2\langle 111\rangle$ direction for the {101} plane. These directions therefore correspond indeed to the Burgers vectors direction with respect to the (010) and {101} slip planes. From Fig. 3.2 and 3.3, it can be clearly observed that the energy values according to the {101} plane are signifantly lower than for the (010) plane which suggests the potential importance of the $^1/_2\langle 111\rangle\{101\}$ slip system.

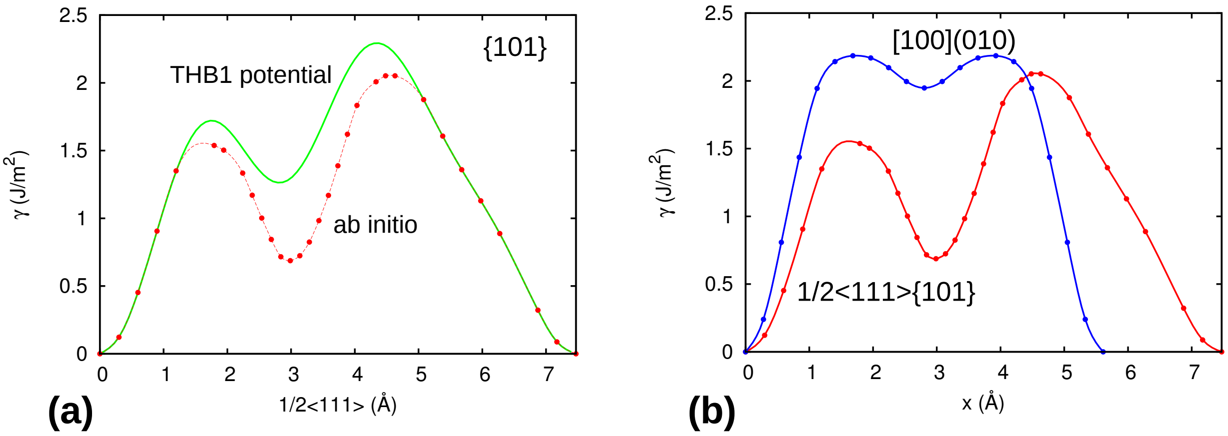

Figure 3.2: *$\gamma$-lines in the Burgers vector direction of the potential* (010) *and* {101} *slip planes at 15 GPa. a) Comparison between* ab initio *and molecular statics (*THB1 *potential used by Metsue* et al. *(2010)) based calculations of the $\gamma$-lines in the* $^1/_2\langle 111\rangle$ *Burgers vector direction of the* {101} *plane. b)* Ab initio *calculations of the $\gamma$-lines in the* [100] *and* $^1/_2\langle 111\rangle$ *Burgers vector direction of the potential* (010) *and* {101} *planes. The metastable energy minima are equal to the equilibrium stacking fault energies of the respective slip systems.*

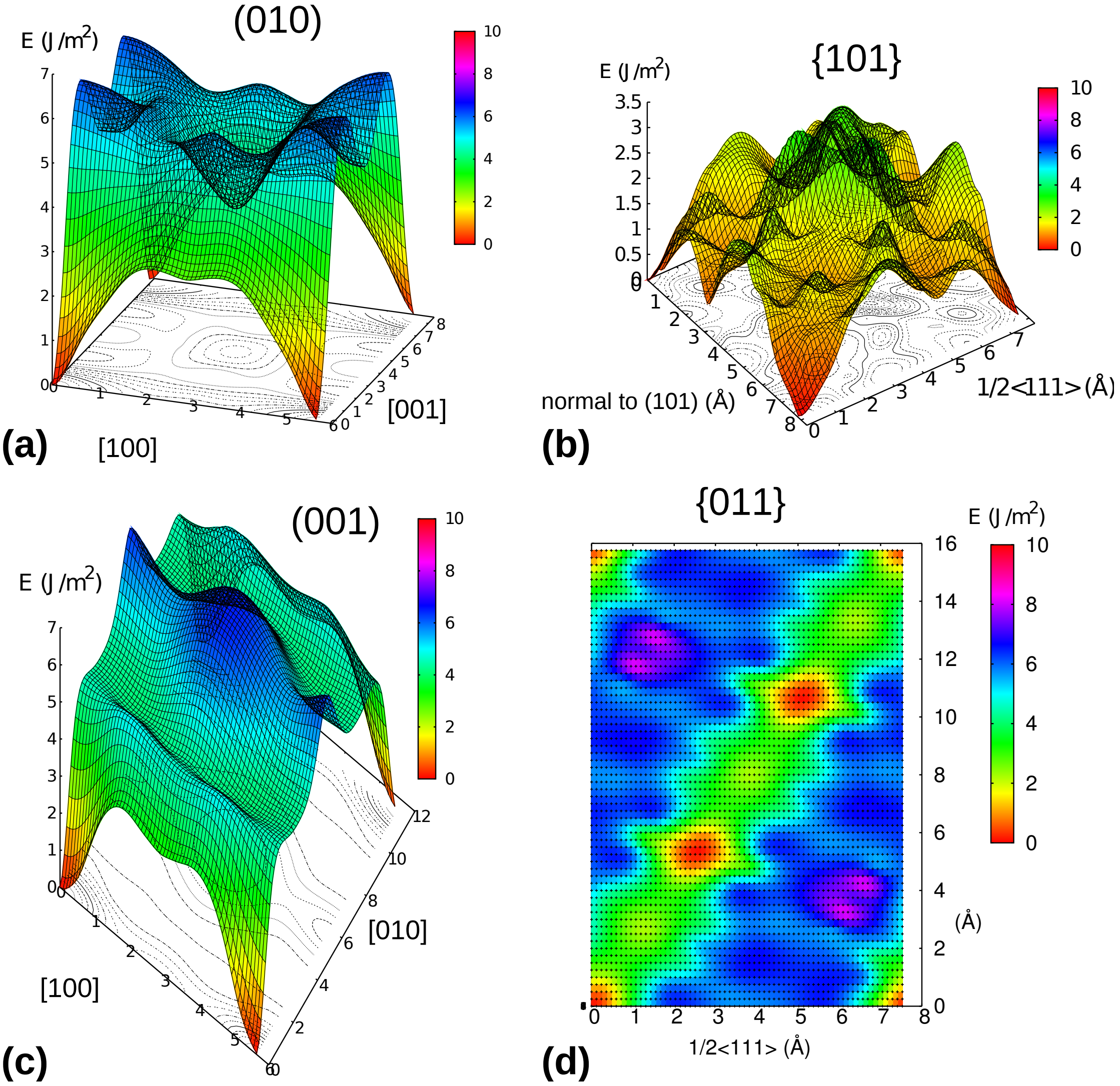

Figure 3.3: *γ-surfaces provided by Metsue* et al. *(2010) that were calculated using molecular statics based on the* THB1 *potential: a)* (010) *plane, b)* {101} *plane, c)* (001) *plane and d)*{011} *plane. The* (001) *and* {011} *planes are introduced into the PNG model to reconstruct the crystal structure of wadsleyite as explained in chapter 2.2. Both* {101} *and* {011} *surfaces are rotated in the appropriate way to introduce them into the mesh that will be used in the PNG model (see section 3.1.2).*

### 3.1.2 Core structures and lattice friction

The $\gamma$-surfaces are used as input for the PNG calculations in order to obtain the dislocation structures as described in chapter 2.2. Simulation cells are based on a nodal mesh constructed around the dislocation line which relies on the crystal structure by the introduction of families of planes corresponding to the potential glide planes. Two distinct mesh configurations were necessary to evaluate the core structures of the [100](010) and 1/2⟨111⟩{101} screw dislocation, as shown in Fig. 3.4 and 3.5. The planes (010) and (001) are considered with respect to the [100] Burgers vector and (101) and $(0\bar{1}1)$ are considered for the 1/2⟨111⟩ Burgers vector. A multiplicity of all planes have been used in the model to reproduce the periodic variation of the dislocation core energy in the crystal structure (Denoual 2007), as can be seen in Fig. 3.4 and 3.5. The simulation cells contain at least 20 unit cells of $Mg_2SiO_4$ wadsleyite with a node density of 18 nodes per Burgers vector. An increase in node density did not further affect the simulation results. A perfect Volterra dislocation is introduced in the center of the simulation box in such a way that it is allowed to spread into the families of planes introduced. As already shown by Metsue *et al.* (2010), the [100] Burgers vector distribution spreads entirely into the (010) and the Burgers vector distribution of the 1/2⟨111⟩ completely in the {101} plane.

| Dislocation | $b_p$ (Å) | K($\theta = 0°$) (GPa) | K($\theta = 90°$) (GPa) | $a'$ (Å) | $\xi$ (Å) | $d$ (Å) | $\tau_p$ (GPa) |
|---|---|---|---|---|---|---|---|
| [100](010) | 2.803 | 123 | 185 | 4.028 | 2.0 | 5.4 | 4.8 |
| 1/2⟨111⟩{101} | $b_{p_1}$=2.987<br>$b_{p_2}$=4.480 | 128 | 171 | 7.3 | $\xi_1$=8.4<br>$\xi_2$=12.5 | 35.8 | 3.5 |

Table 3.1: *Core structures of the* 1/2⟨111⟩{101} *and* [100](010) *screw dislocations with Peierls periodicity* $a'$ *and partial Burgers vectors* $b_p$. $K(\theta)$ *is equal to the anisotropic elastic parameter,* $\xi$ *corresponds to the width of each partial,* $d$ *is equal to the equilibrium stacking fault width taken as the distance between the partials and* $\tau_p$ *corresponds to the Peierls stress.*

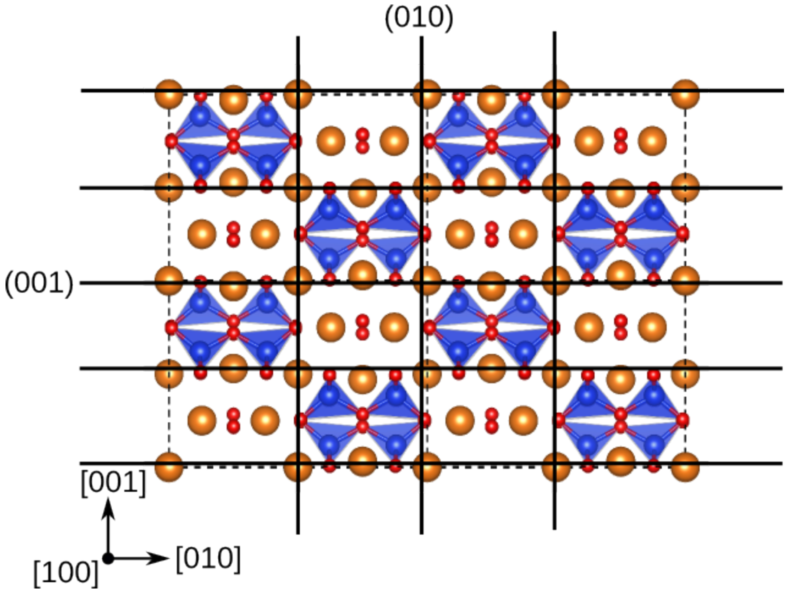

Figure 3.4: *Illustration of the mesh in the PNG model to calculate the core structure of the* [100](010) *screw dislocation: position of the* $\gamma$*-surfaces (solid lines) correspond to the location of the glide planes imposed on the actual crystal structure of* $Mg_2SiO_4$ *wadsleyite (yellow, red and blue atoms reflect the Mg, O and Si respectively). True unit cells shown by the dashed rectangular contours have been used to construct the simulation cell with orientations along* [100], [010] *and* [001] *directions.*

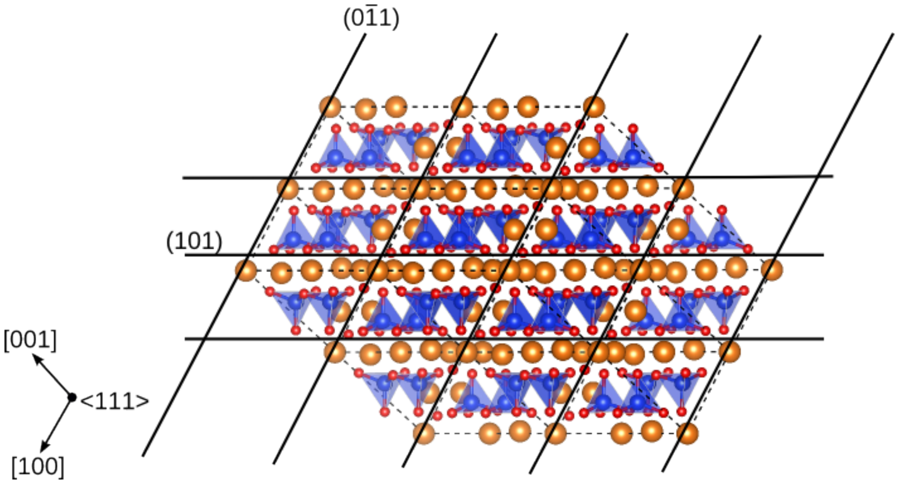

Figure 3.5: *Illustration of the mesh in the PNG-model to calculate the core structure of the* 1/2⟨111⟩{101} *screw dislocation comparable to Fig. (3.4). True unit cells shown by the dashed rectangular contours have been used to construct the simulation cell with orientations along the* [100] *and* [111] *directions and the direction normal to* [111] *with respect to the* (101) *plane.*

The resulting dislocation core structures are shown in Fig. 3.6 by the disregistry and its derivative, the local Burgers vector density. An illustration of the atomistic view of both the $1/2\langle 111\rangle\{101\}$ and $[100](010)$ screw dislocations are shown in Fig. 3.7 and 3.8, respectively. This shows the dissociation of both screw dislocations into two collinear partials. The Burgers vector reaction for the [100] screw in the {010} plane is $[100] = 1/2[100] + 1/2[100]$. This dissociation is collinear and both partials are strictly equivalent. The Burgers vector reaction for the $1/2\langle 111\rangle$ screw in the {101} plane is $1/2\langle 111\rangle = 2/10\langle 111\rangle + 3/10\langle 111\rangle$. Therefore, the collinear partials of the $1/2\langle 111\rangle$ screw dislocation are not equivalent. However, the asymmetry of the partials is small and is neglected throughout the calculations of the dislocation mobility. As a matter of fact, the core structure of this dislocation is widely spread with a large equilibrium stacking fault ($d$=35.8 Å). This significant core extension is confirmed by clear weak beam dark field observation (Fig. 3.9) of both partials of the $1/2\langle 111\rangle$ dislocation using TEM (Thurel and Cordier 2003). The effect of this low energy stacking fault on the mobility is more important than the small differences between both partials. So formally, we will assume both partials of the $1/2\langle 111\rangle$ screw dislocation to be equal to $1/4\langle 111\rangle$.

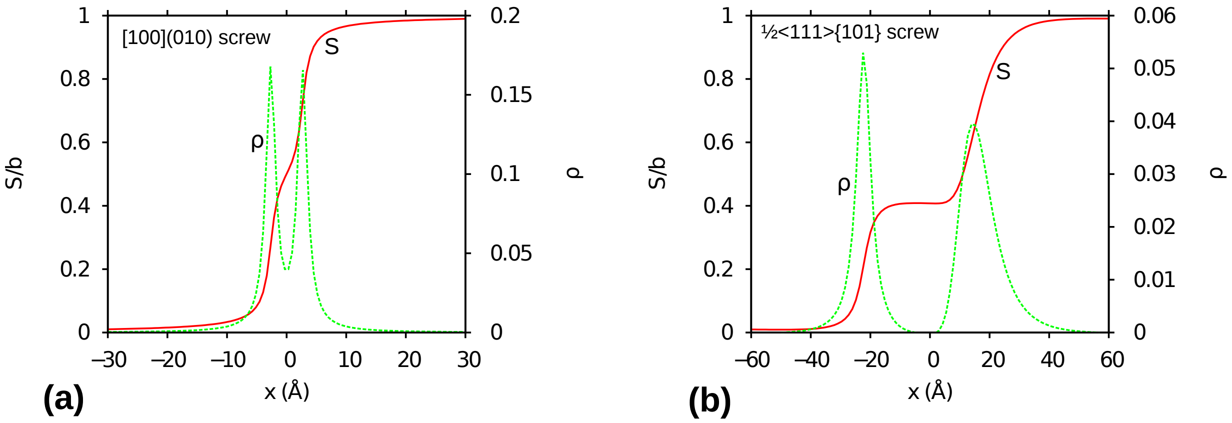

Figure 3.6: *Results of the PNG calculations in form of the disregistry (red continuous line) and its derivative, the local density of the Burgers vector (green dotted line) of the: a)* $1/2\langle 111\rangle\{101\}$ *screw dislocations and b)* $[100](010)$ *screw dislocations.*

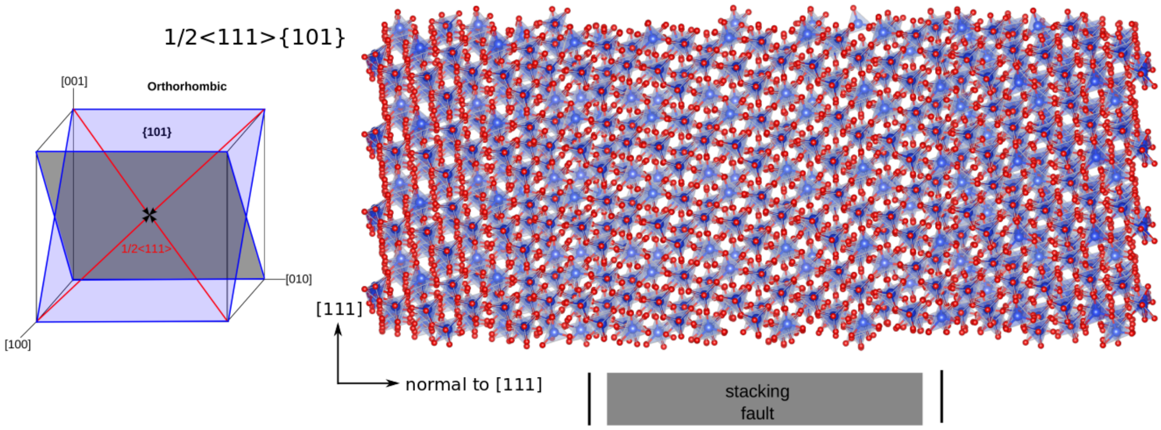

Figure 3.7: *Atomistic view of the core structure of the* $^1/_2\langle 111\rangle\{101\}$ *screw dislocation in wadsleyite, as inferred from the PNG results and shown in Fig. 3.6. The normal of the glide plane points out of the paper in the above figure which gives a top view on the glide plane. The dislocation core is visualized by atomic displacements according to the disregistry and dislocation density.*

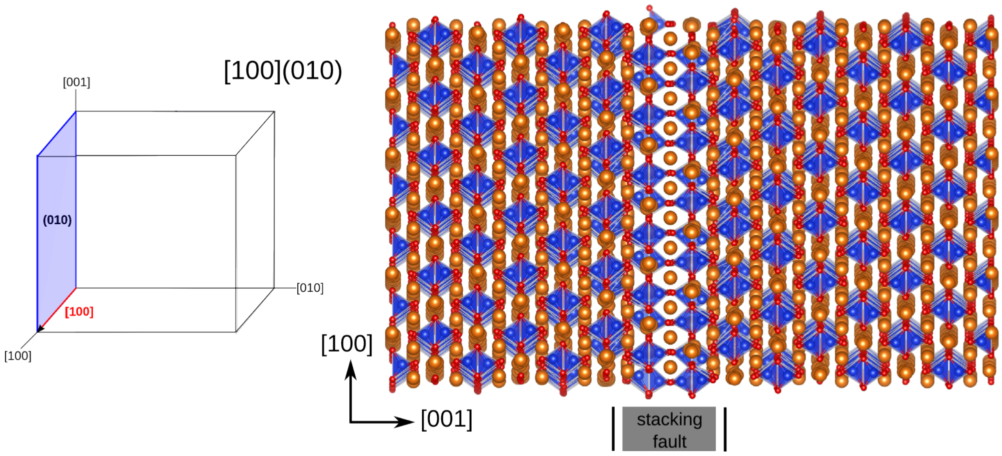

Figure 3.8: *Atomistic view of the core structure of the* $[100](010)$ *screw dislocation in wadsleyite, as inferred from the PNG results and shown in Fig. 3.6. The normal of the glide plane points out of the paper which gives a top view on the glide plane. The dislocation core is visualized by atomic displacements according to the disregistry and dislocation density.*

Finally, it is worth to mention that the equilibrium stacking fault width $d$ between the partials is always found to be equal to an integer multiple of the Peierls periodicity $a'$. This means that both partials occupy the minimum energy configuration in the crystal system under equilibrium conditions, so that both partials are well placed in the wells of the Peierls potential (Schoeck and Püschl 1994).

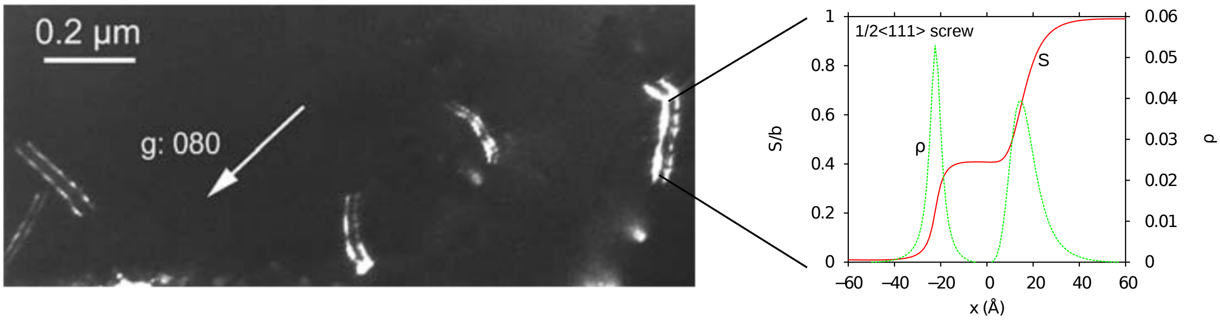

Figure 3.9: *Weak beam darm field image that shows the dissociation of the* $^1/_2\langle 111\rangle$ *dislocations into partials. The image is obtained by transmission electron microscopy (TEM) on a* $Mg_2SiO_4$ *wadsleyite polycrystal (Thurel and Cordier 2003). The dissociation width between the partials of the observed* $^1/_2\langle 111\rangle$ *dislocations are comparably large to the one inferred from core strutures of the* $^1/_2\langle 111\rangle$ *screw dislocation that glide in the* $\{101\}$ *plane calculated with the PNG model.*

Quantification of the intrinsic lattice friction of these $[100](010)$ and $^1/_2\langle 111\rangle\{101\}$ screw dislocations are obtained through explicit calculation of the Peierls potentials as derived according to Eq. 2.44. Table 3.1 shows the dislocation core properties as well as the Peierls stresses of both slip systems. Peierls potentials and their derivatives are shown in Fig. 3.10, respectively. Both slip systems have a value of $\tau_p/\mu \sim 3.5 \times 10^{-2}$. A comparison with $\tau_p/\mu \sim 1 \times 10^{-3}$ in MgO (Amodeo *et al.* 2011) at similar high pressure conditions indicates higher lattice friction in wadsleyite.

Although the core structures as calculated in this work are in good agreement with those previously obtained by Metsue *et al.* (2010), the Peierls stresses (PN-framework) are about one order of magnitude larger than the ones of Metsue *et al.* (2010) (PNG-

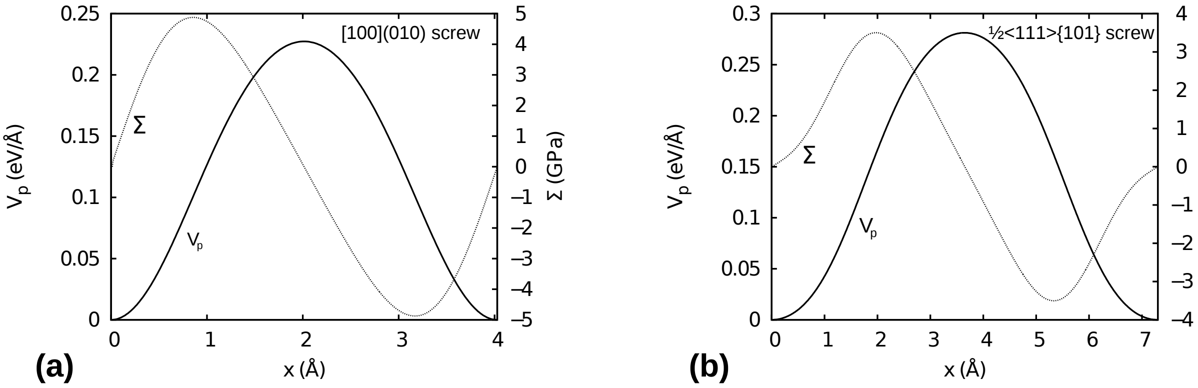

Figure 3.10: *Peierls potentials* $V_p$ *and subsequent Peierls force* $\Sigma = b^{-1}\ \nabla V_p$ *calculated using the PN model based on the core structures of the a)* [100](010) *and* 1/2⟨111⟩{101} *screw dislocations. The potentials give a pure mechanical measure of the lattice friction of both slip systems which will serve as input to calculate the thermally activated mobility of the respective screw dislocations.*

model). However, the relative differences between both screw dislocations are found to be equal. Nevertheless, the values of $\tau_p$ obtained in this study are more in line with what can be expected from experiments (Nishihara *et al.* 2008; Kawazoe *et al.* 2013; Hustoft *et al.* 2012; Farla *et al.* 2015).

### 3.1.3 Thermal activation of dislocation glide

Calculations of the critical kink-pair enthalpies are parametrized by the dislocation core structures (Fig. 3.6), the Peierls potentials (Fig. 3.10) and the associated Peierls stresses (Table 3.1) of the [100](010) and 1/2⟨111⟩{101} screw dislocations as calculated above. As the kink-pair model is based on linear elasticity, the shear modulus $\mu$ and Poisson ratio $\nu$ at 15 GPa have been deduced from the dislocation character dependent anisotropic elastic parameter $K(\theta)$. This is derived within the frame of the Stroh theory using the DisDi software (Douin 1987), where $K(0°) = \mu$ and $K(90°) = \mu/(1-\nu)$ for screw and edge type dislocation segments respectively (Table 3.1). The calculation relies on the elastic constants (at 15 GPa) as obtained with *ab initio* calculations (Table 3.2).

| | $C_{11}$ | $C_{22}$ | $C_{33}$ | $C_{44}$ | $C_{55}$ | $C_{66}$ | $C_{12}$ | $C_{13}$ | $C_{23}$ | (GPa) |
|---|---|---|---|---|---|---|---|---|---|---|
| *Ab initio* (15 GPa) | 439 | 431 | 350 | 116 | 126 | 120 | 116 | 130 | 140 | |
| Exp. Zha *et al.* (14.2 GPa) | 444 | 465 | 387 | 131 | 122 | 130 | 124 | 142 | 152 | |

Table 3.2: *Elastic constants of* $Mg_2SiO_4$ *wadsleyite at 15 GPa as obtained by* ab initio *calculations. A comparison is given with respect to the elastic constants inferred from experiments at* 14.2 *GPa as provided by Zha* et al. *(2000). The results are in good agreement. The shear modulus* $\mu$ *and Poisson ration* $\nu$ *for the different* $\boldsymbol{b}$ *are given in terms of the anisotropic elastic parameter* $K(\theta)$ *in table 3.1.*

The critical enthalpies related to kink-pair nucleation on the $1/2\langle 111\rangle\{101\}$ screw dislocation can be calculated as in the general case for dissociated dislocations, which is discussed in chapter 2.3. This means that correlated nucleation of kink-pairs is captured by the single critical activation enthalphy $\Delta H_c^{crit}$ (Fig. 3.11). However, two independent uncorrelated nucleation processes can be distinguished (Fig. 2.8). The process where the leading partial first starts to move outwards, described by $\Delta H_{u,l_1}^{crit}$, followed by the inward migration of the trailing partial, given by $\Delta H_{u,t_2}^{crit}$, is entirely governed by the first nucleation step: $\Delta H_{u,t_2}^{crit} \ll \Delta H_{u,l_1}^{crit} \approx \Delta H_c^{crit}$. Uncorrelated nucleation of kink-pairs is therefore essentially determined by $\Delta H_{u,l_2}^{crit}$ to which we will simply refer as $\Delta H_u^{crit}$, on the condition that uncorrelated nucleation of kink-pairs starting from the trailing partial is possible to occur.

This is not the case for the [100](010) screw dislocation since the equilibrium dissociation width $d$ is equal to a single period $a'$ of the Peierls potential (table 3.1): kink-pair nucleation that starts from the trailing partial is impossible to occur. The evolution of the critical nucleation enthalpy with stress for this slip system is therefore entirely given by $\Delta H_c^{crit}$, since $\Delta H_{u,l_1}^{crit} \approx \Delta H_c^{crit}$. Results of the critical nucleation enthalpies as a function of stress for both correlated ($\Delta H_c^{crit}$) and uncorrelated kink-pair nucleation ($\Delta H_u^{crit}$, $\Delta H_{u,l_1}^{crit}$) are presented in Fig. (3.11).

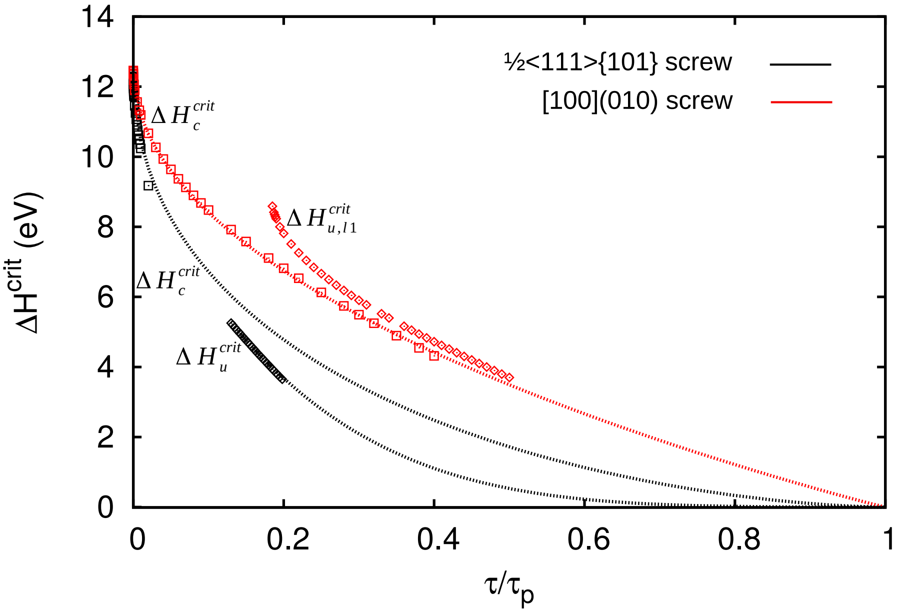

Figure 3.11: *Evolution of the critical kink-pair nucleation enthalpy as a function of the resolved shear stress (normalized by the Peierls stress) for the a)* $1/2\langle 111\rangle\{101\}$ *screw and b)* $[100](010)$ *screw dislocations. Results are shown for correlated nucleation and the relevant elementary steps of the uncorrelated nucleation processes.*

Because of the restriction of the elastic interaction model to the low and intermediate stress regime as mentioned by Caillard and Martin (2003), the critical nucleation enthalpy can be extrapolated up to the Peierls stress according to Eq. (2.64). The saddle point energies $\Delta H^{crit}$ (calculated at low stress) are used to fit $\Delta H_0$ and the empirical parameters $p$ and $q$. Fitting of the saddle point energies can be seen in Fig. (3.11) as dashed lines. Tables (3.3) and (3.4) show the parameterizations related to the two slip systems considered.

| Dislocation | $\tau_p$ (GPa) | $\Delta H_0$ (eV) | $p$ | $q$ |
|---|---|---|---|---|
| [100](010) | 4.8 | 12.5 | 0.5 | 1.03 |
| $1/2\langle 111\rangle\{101\}$ | 3.5 | 12.3 | 0.5 | 1.61 |

Table 3.3: *Key features and parameterization related to the glide as a result of correlated kink-pair nucleation of the governing screw dislocations.* $\Delta H_0$ *is the critical nucleation enthalpy at zero stress,* $a'$ *the Peierls periodicity,* $\tau_p$ *corresponds to the Peierls stress and* $p$ *and* $q$ *are together with* $\Delta H_0$ *the empirical fitting parameters of Eq. 2.64.*

| Dislocation | $\tau_p$ (GPa) | $\tau_c$ (GPa) | $\Delta H_0$ (eV) | $p$ | $q$ |
|---|---|---|---|---|---|
| [100](010) | 4.8 | 0.89 | 8.6 | $n/a$ | $n/a$ |
| $1/2\langle 111\rangle\{101\}$ | 3.5 | 0.455 | 5.3 | 1.0 | 5.0 |

Table 3.4: *Key features and parameterization related to the glide as a result of uncorrelated kink-pair nucleation of* $1/2\langle 111\rangle\{101\}$ *screw dislocation, where* $\Delta H_0$ *is the critical nucleation enthalpy at* $\tau = \tau_c$*. The remaining parameters are defined as in Table (3.3). The uncorrelated kink-pair nucleation of the* [100](010) *screws can be described as in Table (3.3) since they are constrained to kink-pair nucleation starting at the leading partial.*

### Kink-pair geometry

The saddle point $\Delta H^{crit}$ of the total enthalpy variation $\Delta H$ of kink-pair formation, as given in Fig. 3.11, is determined by the free variables that describe the kink-pair geometry: the critical width $w^{crit}$ and the critical height $h^{crit}$ of a metastable kink-pair. Figure (3.12) shows the evolution of the critical kink-pair geometry as a function of the applied stress of the [100](010) and $1/2\langle 111\rangle\{101\}$ screw dislocations. One can observe that the critical width $w^{crit}$ at low stresses (correlated nucleation) is on the order of $\sim 1000\times b_p$, whether at higher stress (uncorrelated nucleation) it converges rapidly to $\sim 10\times b_p$. The critical height $h^{crit}$ is about equal to the Peierls periodicity $a'$ at low stress and descreases with increasing stress. Figure 3.12a shows the kink-pair evolution as a function of stress $\tau$ with respect to the [100](010) screws. Kink-pair nucleation on this screw dislocation is essentially occuring in a correlated manner. The end-member case approach in the low stress regime is used to calculate the saddle point configuration of the total enthalpy variation $\Delta H_c$ (chapter 2.3.2.4). Figure 3.12b shows the kink-pair evolution as a function of stress $\tau$ with respect to the $1/2\langle 111\rangle\{101\}$ screws. The evolution of the kink-pair geometry with stress $\tau$ for both correlated and uncorrelated are presented. The low stress regime approach is used to calculate the saddle point configuration of the total enthalpy variation $\Delta H_{cc}$ (chapter 2.3.2.4) for correlated nucleation of kink-pairs at low stresses. As such, the effect of the large dissocation width on the kink-pair nucleation is taken into account. The critical height $h^{crit}$ is taken to be equal to the Peierls periodicity $a'$ at low stresses with the free variables being the widths $w_1$ and $w_2$ between the kink-pairs on each partial as described in chapter 2.3.2.4. The results for uncorrelated nucleation are equally shown in Fig. 3.12b. As correlated kink-pair nucleation mainly occurs in the low stress regime and is taken over by uncorrelated nucleation at higher stresses, one can clearly observe that there is a correlation between the values of the critical widths $w_2^{crit}$ and $w_u^{crit}$ of either nucleation processes as a function of stress.

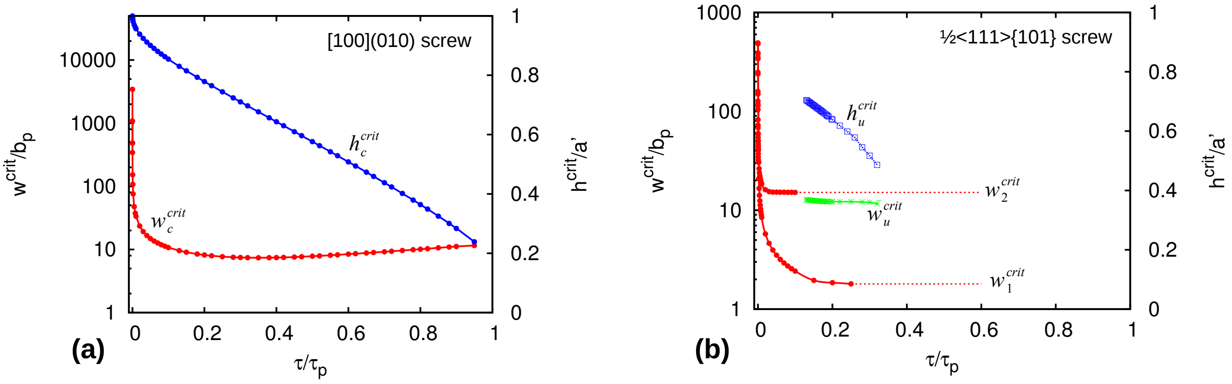

Figure 3.12: *Evolution of the critical kink-pair geometry* $h^{\mathrm{crit}}$ *and* $w^{\mathrm{crit}}$ *as a function of the resolved shear stress* $\tau$ *for the: a)* [100](010) *screw and b)* $1/2\langle 111\rangle\{101\}$ *screw dislocation.*

### 3.1.4 Dislocation mobility

Dislocation mobilities with respect to glide of the [100](010) and $1/2\langle 111\rangle\{101\}$ screw dislocations are parametrized by the critical nucleation enthalpies (Fig. 3.11) and calculated as described in chapter 2.3.3. The glide velocities obtained in this study rely on the assumption that kink-pair nucleation controls the overall mobility of the rate controlling screw dislocations. This implies that the second order Peierls potential, *i.e.* the potential which the individual edge kinks have to overcome to migrate along dislocation lines, is neglected (Joós and Zhou 2001). Nevertheless, since the edge kinks, after nucleation, are forced to lie over the Peierls potential, the energy associated with migration of the edge kinks is assumed to be less than the energy related to the nucleation process.

Dislocation velocity profiles as a function of the resolved shear stress for both $1/2\langle 111\rangle$ $\{101\}$ and [100](010) screw dislocations are shown in Fig. 3.13. The critical stress $\tau_c$ below which only correlated kink-pair nucleation can occur is equal to about 500 MPa and 900 MPa for the $1/2\langle 111\rangle\{101\}$ screw and [100](010) screw dislocations, respectively (table 3.4). Figure 3.13a shows the resolved shear stress dependence of the velocities for both screws at 1700 K in a logarithmic plot. This clearly shows that independent of the applied stress, the velocity of the $1/2\langle 111\rangle\{101\}$ screw is always larger than that of the [100](010) screw dislocation. The plot inserted in Fig. 3.13a shows the same velocity curves in a semi-log plot which gives a better insight into the velocity differences with stress between both screw dislocations. Here, we can observe that at high, but mainly at intermediate stress values, the velocity differences between both slip systems are relatively large and decrease with decreasing stress. At very low stress levels (what can be expected in mantle conditions), the dislocation velocities for both screw dislocations become more comparable. Typical laboratory strain rates of $\dot{\epsilon} = 10^{-5}$ s$^{-1}$ correspond to dislocation velocities of about $v = 2 \times 10^{-8}$ m/s. The stresses associated with these velocities are on the order of $0.5 - 2$ GPa. In constrast, dislocation velocities related to mantle strain rates of $\dot{\epsilon} = 10^{-16}$ s$^{-1}$ are about $v = 2 \times 10^{-15}$ m/s with stresses of $\sim 200 - 1000$ MPa. At room temperature, the velocity evolution with stress of the same screw dislocations are shown in Fig. 3.13b. To obtain physically relevant dislocation velocities, glide only takes place in the high stress regime where uncorrelated nucleation of kink-pairs governs the dislocation mobility. The overall trend of the velocity profiles at room temperature is comparable to the results at 1700 K. Stresses of about $1 - 4$ GPa are required to obtain dislocation velocities corresponding to typical laboratory strain rates at room temperature. Finally, one can observe in Fig. 3.13 that the dislocation velocities at the Peierls stress for each individual dislocation are strictly independent of temperature since this stress corresponds to the resolved shear stress required to move an infinite dislocation at the absolute zero. At the Peierls stress, the mobility of dislocations is governed by other mechanisms than the nucleation of kink-pairs and the results of $\lim_{\tau \to \tau_p} v(\tau)$ are considered to be unphysical.

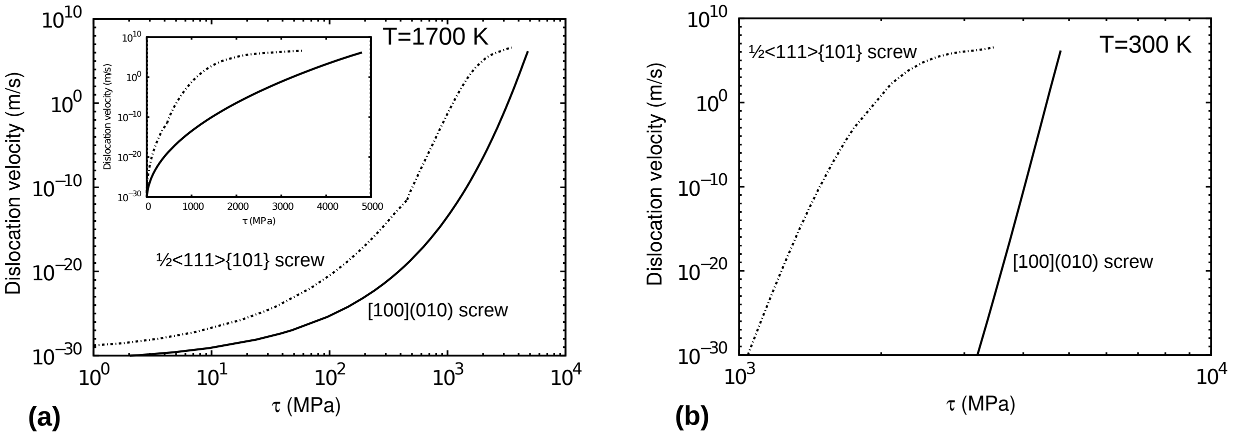

Figure 3.13: *Glide velocity of the* $1/2\langle 111\rangle\{101\}$ *and* $[100](010)$ *screw dislocations as a function of the resolved shear stress at: a)* 1700 *K and b)* 300 *K.*

The dislocation velocities as shown in Fig. 3.13 are parametrized by the critical kink-pair widths. This gives the stress dependency on the pre-exponential factor of the glide velocities. From Fig. 3.12, one can infer that the critical width $w^{crit}$ at low stresses (correlated nucleation) is on the order of $\sim 1000 \times b_p$, whereas at higher stress it converges rapidly to $\sim 10 \times b_p$. Figure 3.14 shows the glide mobility of the [100](010) screw dislocations as a function of the stress $\tau$ with accurate parametrization $w^{crit}(\tau)$ (red curve) and the fixed ones $w = 1000 \times b_p$ (blue curve) and $w = 10 \times b_p$ (green curve). Because the [100](010) screw dislocation is characterized by a single kink-pair nucleation mechanism, it is the best candidate to show the influence of $w^{crit}(\tau)$ on the resulting glide mobility. It can be seen in Fig. 3.14 that the evolution of the velocity with stress is comparable for all three curves. This shows that the stress dependence of the pre-exponential factor in the description of the velocity is of minor importance compared to the stress dependence of the critical activation enthalpies $\Delta H^{crit}$. Further, we can observe that the velocity curve with stress described by a fixed critical kink-pair width $w = 10 \times b_p$ follows the accurate velocity evolution with $w^{crit}(\tau)$ for velocities smaller than $10^{-25}$ m/s. The latter can be associated with unrealistic small mantle strain rates smaller than $10^{-26}$ $s^{-1}$. This implies that the stress dependence on the pre-expontential factor of the glide velocity as given in chapter 2.3.3 vanishes with respect to the importance of the large values of the stress dependent nucleation enthalpies $H^{crit}$ given in the exponential.

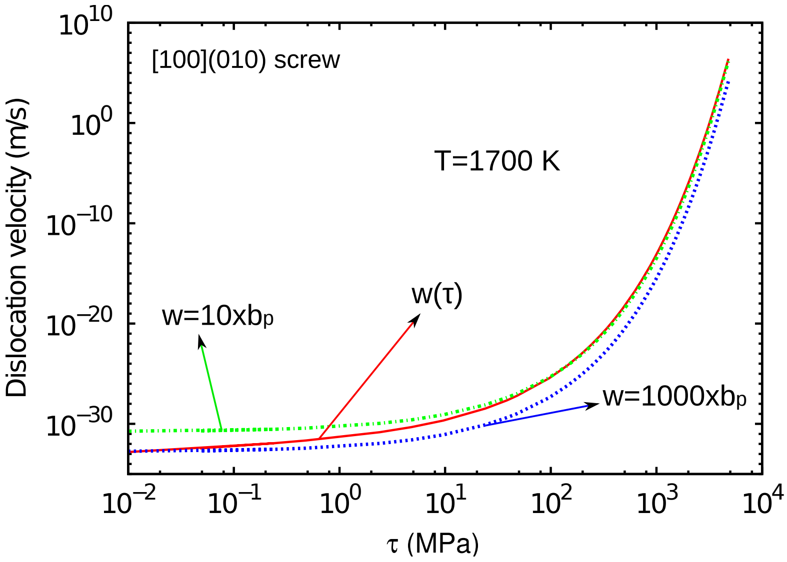

Figure 3.14: *Evolution of the glide velocity of the* [100](010) *screw dislocation with resolved shear stress* $\tau$ *at* 1700 *K for parameterizations of the critical kink-pair width* $w^{crit}(\tau)$ *(red curve) and the fixed widths* $w = 1000 \times b_p$ *(blue curve) and* $w = 10 \times b_p$ *(green curve).*

The dislocation velocities as shown in Fig. 3.13 are the result of the underlying kink-pair mechanism for the respective screw dislocations. Figure 3.13b shows that thermally activated glide of the [100](010) screw dislocation leads to pronounced differences in the velocity evolution with resolved shear stress with respect to the $1/2\langle 111\rangle\{101\}$ screw dislocation. These differences are directly related to the difference in evolution of $\Delta H^{crit}$

with stress as shown in Fig. 3.11. The latter, once more, is the consequence of the different core structures between the [100](010) and $1/2\langle 111\rangle\{101\}$ screws: [100](010) exhibits a narrow dissociation with a confined spreading of the partials, whether $1/2\langle 111\rangle\{101\}$ is characterized by an extended dissociation with a large spread of the partials as shown in Fig. 3.6. These features finally determine the velocity evolution of the dislocations as a function of the applied stress.

The results further show that correlated nucleation of kink-pairs which coincide along both partials is possible at every stress, whereas uncorrelated nucleation is only possible and becomes more favorable than correlated nucleation at $\tau \geq \tau_c$, due to the lower critical nucleation enthalpy. This implies that dislocation glide operating by the Peierls mechanism at low temperatures and high deviatoric stress (in most cases, laboratory conditions), will be mainly governed by uncorrelated nucleation of kink-pairs. However, at high temperatures and small deviatoric stresses (more likely to represent mantle conditions), glide will be predominantly controlled by correlated nucleation of kink-pairs on both partials.

### 3.1.5 Constitutive equations

As the plastic flow below the athermal temperature $T_a$ is directly controlled by the mobility of dislocations, the relation between the behaviour of individual dislocations and the collective macroscopic behaviour in this regime, as discussed in chapter 2.3.4, can be derived from Orowan's equation:

$$\dot{\epsilon} = \rho_m b v \tag{3.1}$$

where $\rho_m$ corresponds to the mobile dislocation density, $b$ is the modulus of the Burgers vector and $v$ is the average dislocation velocity. For any given constant strain rate $\dot{\epsilon}$, Eq. 3.1 can be solved for the temperature $T$ as function of the critical resolved shear stress $CRSS$.

$1/2\langle 111\rangle\{101\}$ **screw dislocation**:

- $0 < \tau \leq \tau_c$:

$$\dot{\epsilon}_c(\tau) = 2190\sqrt{\rho_m}\exp\left(-\frac{1.97\times 10^{-18}\left(1-\left(\frac{\tau}{\tau_p}\right)^{0.5}\right)^{1.6}}{k_b T}\right) \quad \text{in} \quad s^{-1}$$

- $\tau_c \leq \tau \leq \tau_p$:

$$\dot{\epsilon}_{c+u}(\tau) = \frac{1}{2}\rho_m b\left[v_c + v_u\right] = \frac{1}{2}\left[\dot{\epsilon}_c + \dot{\epsilon}_u\right] \quad \text{with}$$

$$\dot{\epsilon}_u = 4380\sqrt{\rho_m}\left(\frac{\tau-\tau_c}{\tau}\right)\exp\left(-\frac{8.49\times 10^{-19}\left(1-\left(\frac{\tau-\tau_c}{\tau_p}\right)^{1.0}\right)^{5.0}}{k_b T}\right) \quad \text{in} \quad s^{-1}$$

**[100](010) screw dislocation**:

- $0 < \tau \leq \tau_p$

$$\dot{\epsilon}_c(\tau) = 1208\sqrt{\rho_m}\exp\left(-\frac{2.0\times 10^{-18}\left(1-\left(\frac{\tau}{\tau_p}\right)^{0.5}\right)^{1.03}}{k_b T}\right) \quad \text{in} \quad s^{-1}$$

with $k_b$ equal to the Boltzmann constant, $T$ the temperature in $[K]$ and the dislocation density $\rho_m$ given in $\left[m^{-2}\right]$.

#### 3.1.5.1 Deformation under laboratory conditions

In order to compare the results of the above model with experimental data available on deformation of wadsleyite at around 15 GPa, we calculated the $CRSS$ over a broad temperature range for typical laboratory strain rates of $\dot{\epsilon} = 10^{-5}$ s$^{-1}$. The mobile dislocation density is set to $\rho_m = 10^{12}$ m$^{-2}$. Figure 3.15 shows the results for the slip of the rate govering $1/2\langle 111\rangle\{101\}$ and [100](010) screw dislocations. The transition of the curves to the dotted lines at 2500 K marks the onset of melting for the $Mg_2SiO_4$ system around 15 GPa. This demonstrates that dislocation glide in wadsleyite at laboratory strain rates always operates in the thermally-activated regime, since the athermal temperature would be higher than the melting temperature. It means that intracrystalline plasticity under laboratory conditions is mainly governed by the mobility of the rate controlling slip systems. The results show that for $0 < \tau \leq \tau_p$, slip of the $1/2\langle 111\rangle\{101\}$ screw dislocations is always easier than slip of the [100](010) screw dislocations. Furthermore, one can observe that the evolution of the $CRSS$ as a function of $T$ for both screw dislocations is significantly different. This is directly related to the difference in core structure between both screw dislocations and the subsequent difference in equilibrium stacking fault energies. Whereas the evolution at high $CRSS$ and low $T$ for [100](010) screw dislocations is roughly linear, the same evolution for the $1/2\langle 111\rangle\{101\}$ screws is highly exponential. At high $T$ where both curves converge towards each other, the difference in $CRSS$ are found to be the smallest.

Figure 3.15 shows a remarkably good agreement between the theoretical predictions and the available experimental data. It is worth mentioning that the deformation experiments used from Nishihara *et al.* (2008), Kawazoe *et al.* (2010), Kawazoe *et al.* (2013), Hustoft *et al.* (2013) and Farla *et al.* (2015) were performed on polycrystalline wadsleyite samples. The raw experimental data rather display the temperature dependence on the effective flow stress than on the $CRSS$ related to single slip systems as in

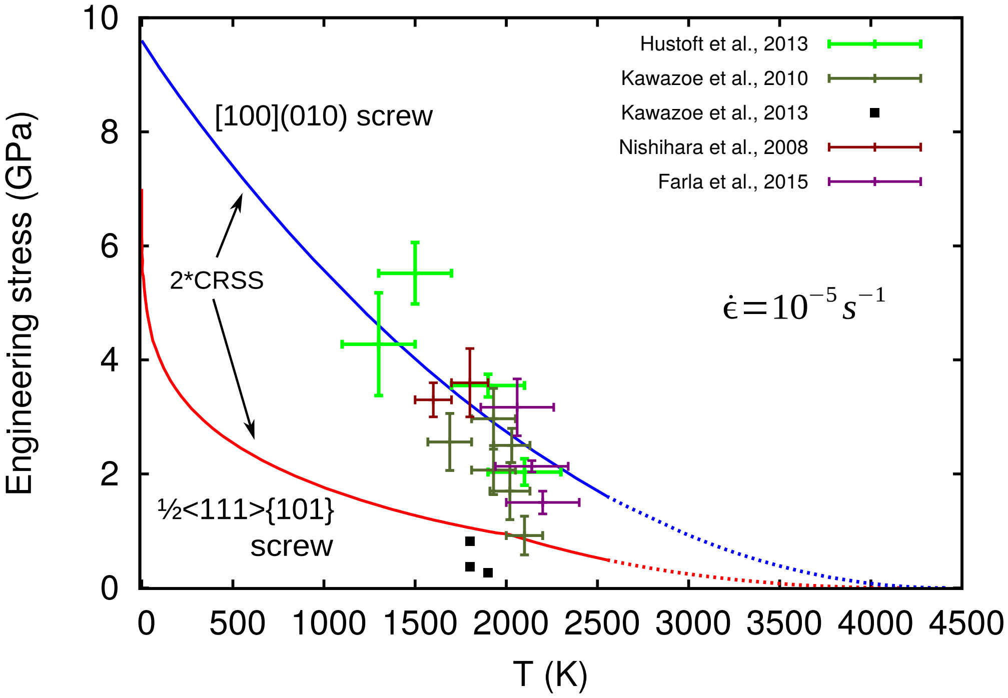

Figure 3.15: *Constitutive relation shown as the engineering stress versus temperature at a fixed strain rate of* $\dot{\epsilon} = 10^{-5}$ $s^{-1}$ *for thermally actived glide of the rate controlling* $1/2\langle 111\rangle\{101\}$ *and* [100](010) *screw dislocations. The mobile dislocation density is taken to be* $\rho_m = 10^{12}$ $m^{-2}$. *Single slip* $CRSS$ *as calculated are multiplied by two to be converted into apparent engineering stresses which allows for the comparison with the results from deformation experiments.*

our calculations. Only a fraction of the effective flow stress is resolved in the direction of dislocation motion within each single slip plane. The $CRSS(T)$ of the theoretical single slip results are therefore multiplied by two (corresponding to the maximum of the Schmid factor) in order to be compared with the experimental data in Fig. 3.15. The latter assumption may be too simple as more deformation mechanisms may be involved in the experiments and effects of grain boundaries and hardening have not been taken into account in our model. However, *a posteriori* TEM observations of deformed samples in some of the experimental studies (*e.g.* Hustoft *et al.* 2013; Farla *et al.* 2015) clearly reveal the potential contribution of dislocation glide to the overall deformation under laboratory conditions by the development of dense microstructures with high dislocation densities ($> 10^{12}$ m$^{-2}$). Furthermore, the agreement between the experimental data and the evolution of the *CRSS* with $T$ of the rate controlling dislocations shows that glide controls largely the mechanical behaviour in laboratory conditions.

#### 3.1.5.2 Deformation under transition zone conditions

Following the same approach as for laboratory strain rates, the *CRSS* as a function of $T$ for typical mantle strain rates of $\dot{\epsilon} = 10^{-16}$ s$^{-1}$ can be obtained. Wadsleyite is stable in the upper half of the transition zone from 410 to 520 km at a pressure range of $13 - 18$ GPa corresponding to temperatures of about 1700 K. The mobile dislocation density is taken to be $\rho_m = 10^8$ m$^{-2}$ to adjust to the low stress regime of the Earth's mantle. Results are shown in Fig. 3.16. One can observe that the minimum *CRSS*'s at 1700 K are on the order of 150 MPa for the easiest slip system, up to over 600 MPa for the more difficult slip system. The results show that glide in wadsleyite under mantle conditions still occurs in a regime where the *CRSS* is temperature dependent. This implies that plastic deformation by dislocation glide in wadsleyite under conditions of the upper transition zone would be governed by the average mobility of the rate governing screw dislocations. However, the athermal temperature is a function of the applied strain rate and the mobile dislocation density. Larger strain rates and smaller mobile dislocation densities would shift the athermal temperature to larger values and *vice versa.*

The constitutive relations as shown in Fig. 3.16 are used to calculate viscosities associated with single slip in wadsleyite at the conditions of the lower transition zone by

$$\eta = \frac{CRSS(T = 1700K)}{2\dot{\epsilon}} \tag{3.2}$$

A viscosity of $9 \times 10^{23}$ Pa s and $3 \times 10^{24}$ Pa s, with respect to glide, can be attributed to the $1/2\langle 111\rangle\{101\}$ and $[100](010)$ screw dislocations, respectively. These viscosity values

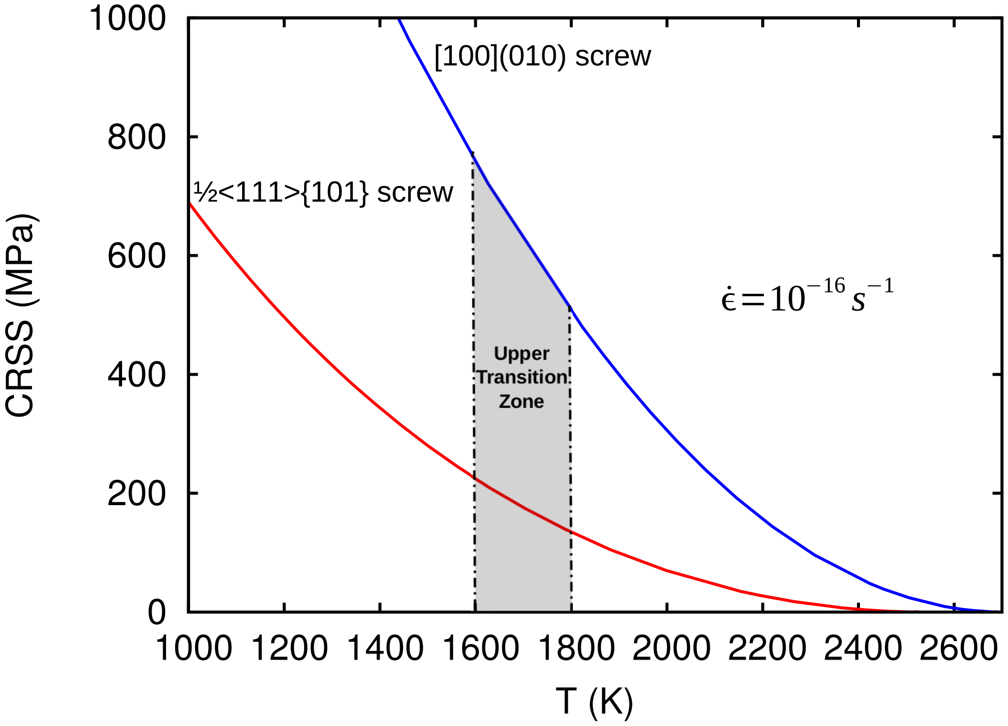

Figure 3.16: *Constitutive relations shown as the critical resolved shear stress (CRSS) versus temperature* $T$ *at a fixed strain rate of* $\dot{\epsilon} = 10^{-16}\ s^{-1}$ *for thermally actived glide of the rate controlling* 1/2⟨111⟩{101} *and* [100](010) *screw dislocations. The dislocation density is taken to be* $\rho_m$=$10^8\ m^{-2}$ *to adjust to the low stress regime in the Earth's mantle. The shaded area depicts the stability field of wadsleyite in the upper transition zone at* 15 *GPa.*

can be seen as lower bounds since they are related to the intrinsic glide resistance of single slip systems.

Dislocation core modelling shows that the intrinsic lattice resistance as defined by the Peierls stress is lower for 1/2⟨111⟩{101} than for the [100](010) screw dislocations. From our study, it follows that temperature and strain rate do not change this hierarchy since glide of the 1/2⟨111⟩{101} screw dislocations remains easier in the whole range of conditions considered here. Together with the fact that 1/2⟨111⟩{101} has more symmetrical variants than [100](010), we estimate that 1/2⟨110⟩{111} is the most important slip system in dislocation glide governed deformation of (poly)crystalline wadsleyite under both natural and laboratory conditions.

## 3.2 Ringwoodite at 20 GPa

As for wadsleyite, the aim of this section is to determine the constitutive equations according to the glide mobility of the rate controlling dislocations in $Mg_2SiO_4$ ringwoodite at 20 GPa. Previous studies (Karato *et al.* 1998; Thurel 2001; Carrez *et al.* 2006) suggest the importance of the activity of the following three main slip systems: $1/2\langle 110\rangle\{110\}$, $1/2\langle 110\rangle\{111\}$ and $1/2\langle 110\rangle\{001\}$. They involve dislocations dissociated into two collinear partials, according to the Burgers vector reaction: $1/2\langle 110\rangle \rightarrow 1/4\langle 110\rangle + 1/4\langle 110\rangle$. Our multiscale approach will be applied with respect to the aforementioned slip systems for which the $\gamma$-surfaces have been calculated. These are used in the next step of the model to calculate the core structures of the screw and edge dislocations belonging to the three main slip systems by using the PNG model. Finally, thermal activation of the rate controlling dislocations is calculated by the use of the elastic interaction model as adapted for dissociated dislocations. The constitutive equations are finally inferred from the stress dependence on the mobility of the rate controlling dislocations as obtained from the latter results.

### 3.2.1 $\gamma$-Surfaces

$\gamma$-surfaces have been calculated for the three potential $\{110\}$, $\{111\}$ and $\{001\}$ slip planes at 20 GPa using *ab initio* methods. Calculations are performed with the VASP code using the GGA approximation and the US pseudopotentials as described in chapter 2.1 (especially chapter 2.1.2.4). Relaxation of the perfect crystal structure at 20 GPa leads to a lattice parameter $a = 7.879$ Å and athermal elastic constants (stiffness tensor) of $C_{11} = 415$ GPa, $C_{12} = 160$ GPa and $C_{44} = 143$ GPa which are in agreement with previous work (Kiefer *et al.* 1997; Sinogeikin *et al.* 2001; Carrez *et al.* 2006) as listed in table 3.7.

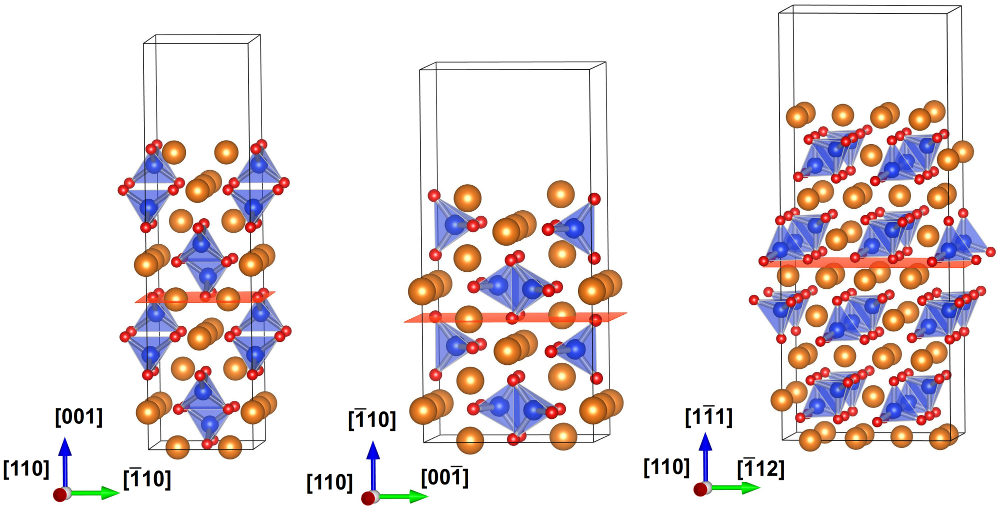

Figure 3.17: *Unsheared supercell configurations used to calculate the $\gamma$-surfaces associated with the following slip systems: a)* $1/2\langle110\rangle\{001\}$*, b)* $1/2\langle110\rangle\{110\}$ *and c)* $1/2\langle110\rangle\{111\}$*. The shear planes are presented in red in the middle of the supercells. A vacuum layer of* 6 *Å at the top of the supercells avoids the effect of interaction between the stacking fault replicas due to periodic boundary conditions.*

The unsheared supercells, according to the description in chapter 2.1, are shown in Fig. 3.17. All atoms, except those located near the external boundary layers were allowed to relax perpendicular to the shear plane in order to minimize the energy of the $\gamma$-surfaces. Finally, the stacking fault level in each of the three supercells is chosen in such a way as to avoid a cut of the strong Si-O bonds (Carrez *et al.* 2006), which leads to a unique choice of the cutting levels with respect to the {110} and {111} planes. Two cutting levels could be considered for the {001} plane: one in between a Mg-layer and a layer of $SiO_4$ tetrahedra and a one in between two $SiO_4$ tetrahedra layers. We choose to cut with respect to the Mg-layer, since this cutting level corresponds to the one with the largest interplanar distance and should as such reproduce the lowest stacking fault energies (Fig. 3.17).

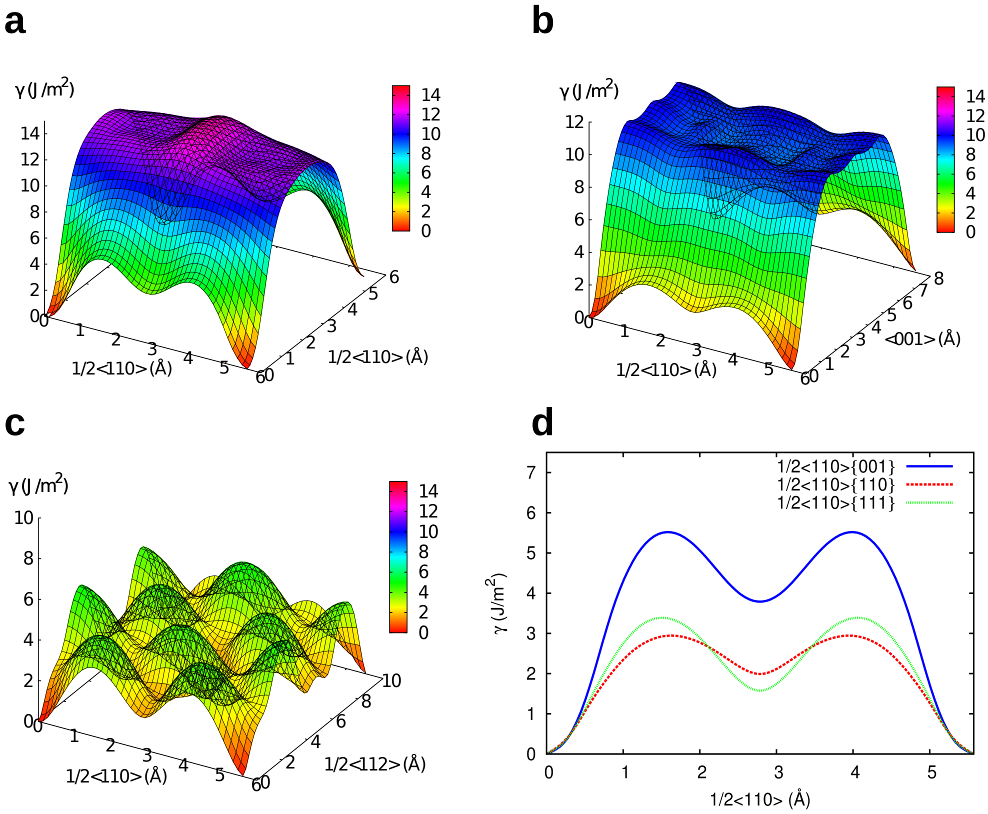

Figure 3.18: *$\gamma$-surfaces provided by first principles based density functional theory calculations (DFT) of the following planes at 20 GPa: a) $\{001\}$ plane, b) $\{110\}$ plane and c) $\{111\}$ plane. d) shows the $\gamma$-lines in the $1/2\langle 110\rangle$ Burgers vector direction for the $\{001\}$, $\{110\}$ and $\{111\}$ planes. The metastable energy minima are equal to the equilibrium stacking fault energies of the respective slip systems.*

The complete $\gamma$-surface calculations for the $\{001\}$, $\{110\}$ and $\{111\}$ slip planes are given in Fig. 3.18. This extends the results of Carrez *et al.* (2006), where only $\gamma$-lines were calculated along the $1/2\langle 110\rangle$ direction. However, it is confirmed that the lowest energy paths are found along the $1/2\langle 110\rangle$ direction, corresponding to the Burgers vector within the three potential slip planes. One can clearly observe in Fig. 3.18d that the energy excess of both $\gamma$-lines in the Burgers vector direction of the $\{110\}$ and $\{111\}$ planes are comparable and significantly smaller than those in the $\{001\}$ plane. The absolute values of the stacking fault energies are slightly larger than in the case of Carrez *et al.* (2006), due to difference in the degrees of freedom of the atomic relaxations. All $\gamma$-lines exhibit a camel hump shape due to the existence of a metastable energy minimum. This forecasts the dissociation of the Burgers vector into two equivalent partials separated by a stacking fault.

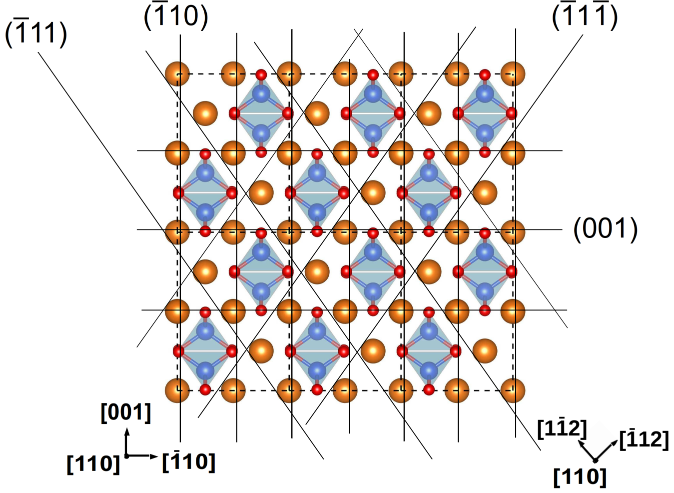

Figure 3.19: *Illustration of the mesh configuration as used to model the core structures of the* $1/2\langle 110\rangle$ *screw dislocations in the PN-model: position of the* $\gamma$*-surfaces (solid lines) correspond to the location of the glide planes imposed on the actual crystal structure of* $Mg_2SiO_4$ *ringwoodite (yellow, red and blue atoms reflect the Mg, O and Si respectively). True unit cells shown by the dashed rectanglar contours have been used to construct the simulation cells. Orientations along* $[\bar{1}10]$*,* $[110]$ *and* $[001]$ *directions have been used to construct a rectangular mesh. Orientations along the* $[\bar{1}12]$*,* $[1\bar{1}2]$ *and* $[110]$ *directions have been used to construct a quasi-hexagonal mesh configuration.*

### 3.2.2 Core structures and lattice friction

The $\gamma$-surfaces have been used as input for the PNG calculations of the dislocation structures. Simulation cells are based on a nodal mesh constructed around the dislocation line which relies on the crystal structure by the introduction of families of planes corresponding to the potential glide planes: $(\bar{1}10)$, $(001)$, $(\bar{1}11)$, $(\bar{1}1\bar{1})$ as considered for the $1/2\langle 110\rangle$ Burgers vector. The simulation cells contain at least 20 unit cells of $Mg_2SiO_4$ ringwoodite with a node density of 16 nodes per Burgers vector. An increase in node density did not further affect the simulation results.

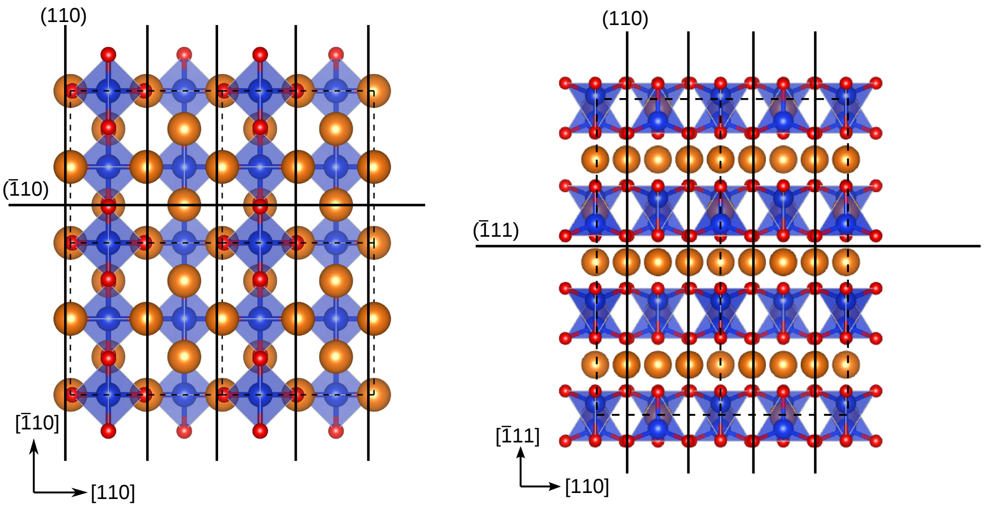

Figure 3.20: *Illustration of the meshes used to model the core structures of the* $^1/_2\langle 110\rangle$ *edge dislocations with the PNG model gliding in the a)* $\{110\}$ *and b)* $\{111\}$ *planes. Position of the* $\gamma$*-surfaces (solid lines) correspond to the location of the glide planes imposed on the actual crystal structure of* $Mg_2SiO_4$ *ringwoodite (yellow, red and blue atoms reflect the Mg, O and Si respectively). True unit cells shown by the dashed rectanglar contours have been used to construct the simulation cell with orientations along* $[\bar{1}10]$, $[110]$ *and* $[001]$ *directions.*

A rectangular mesh configuration with orientations along the $[\bar{1}10]$, $[110]$ and $[001]$ directions as illustrated in Fig. 3.19 is constructed to calculate the core structure of the $^1/_2\langle 110\rangle$ screw dislocation potentially spreading in the $(\bar{1}10)$, $(001)$, $(\bar{1}11)$, $(\bar{1}1\bar{1})$ planes. A Volterra screw dislocation is introduced in the center of the simulation box in such a way that it is able to spread in all possible families of planes. Introducing a $^1/_2\langle 110\rangle$ screw dislocation initially in $\{110\}$ or $\{001\}$ leads after relaxation to a complete spread into $\{110\}$. Due to the applied boundary conditions of the model, it is not possible to stabilize a core structure by introducing a $^1/_2\langle 110\rangle$ screw dislocation in $\{111\}$. To be able to investigate that possibility, a quasi-hexagonal mesh was constructed with orientations along the $[\bar{1}12]$, $[1\bar{1}2]$ and $[110]$ (Fig. 3.19). Introducing an initial $^1/_2\langle 110\rangle$ screw dislocation in the $\{111\}$ leads, after energy minimization, to a complete spread

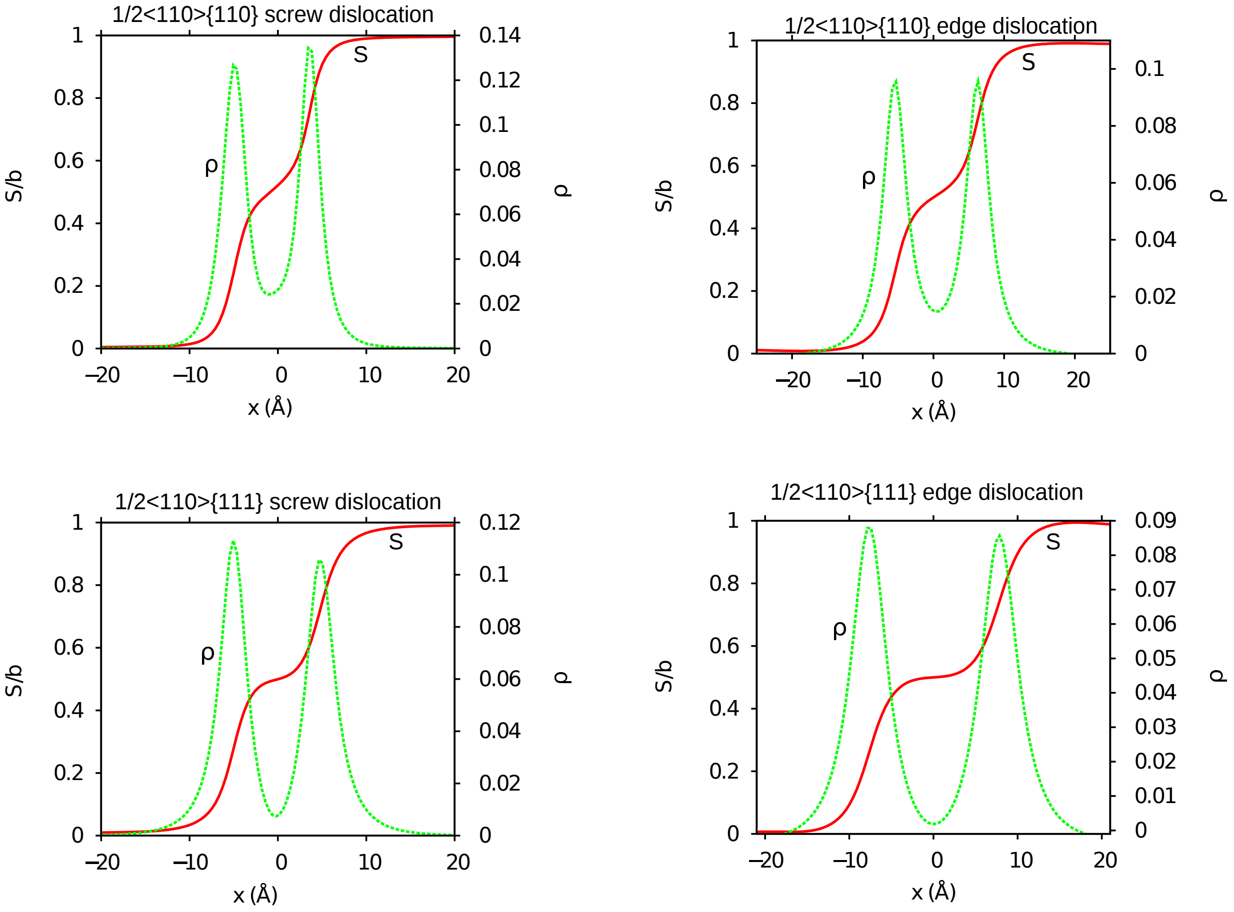

Figure 3.21: *Results of the PNG calculations in form of the disregistry (red continuous line) and its derivative, the local density of the Burgers vectors (green dotted line) of the* $^1/_2\langle 110\rangle$ *screw dislocation spreading into the* $\{110\}$ *and* $\{111\}$ *plane as presented in the first column and of the* $^1/_2\langle 110\rangle$ *edge dislocation spreading into the* $\{110\}$ *and* $\{111\}$ *plane presented in the second column.*

into $\{111\}$. The simulations performed with both mesh configurations showed that no significant Burgers vector distribution is found in the $\{001\}$ plane. However, we are not able to distinguish whether the $^1/_2\langle 110\rangle\{110\}$ or the $^1/_2\langle 110\rangle\{111\}$ screw dislocation exhibits the lowest energy configuration, due to the limitations of the boundary conditions of the PNG model. Consequently, we will take into account both $^1/_2\langle 110\rangle\{110\}$ and $^1/_2\langle 110\rangle\{111\}$ screw dislocations (Fig. 3.21).

A similar approach is used to calculate the structure of the edge dislocations except for the fact that they are confined into their plane of introduction as a consequence of the edge character. Since the stable $^1/_2\langle 110\rangle$ screw core configurations were found to spread in $\{110\}$ and $\{111\}$, we could constrain our calculations to the core structures of the $^1/_2\langle 110\rangle\{110\}$ edge and the $^1/_2\langle 110\rangle\{111\}$ edge dislocations. The PNG mesh configurations are constructed as shown in Fig. 3.20.

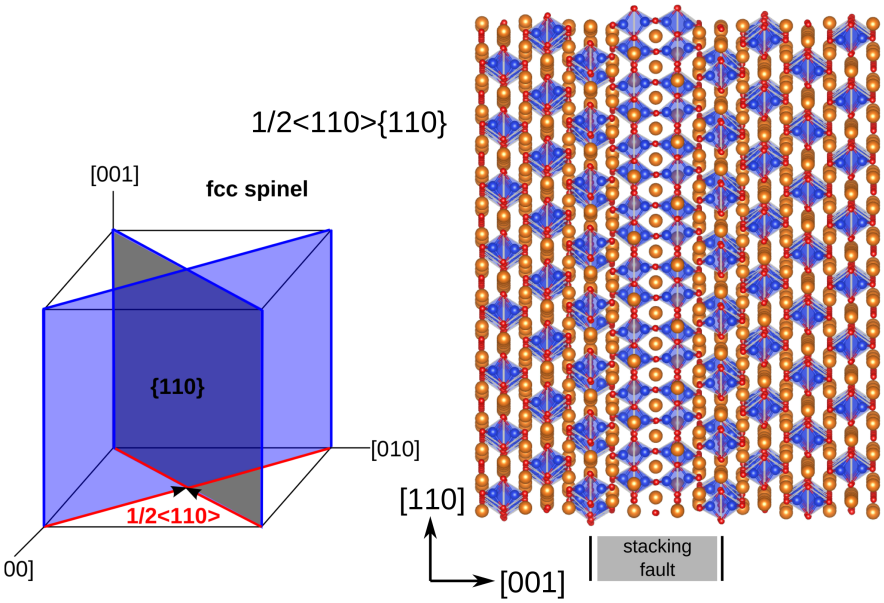

Figure 3.22: *Atomistic view of the core structure of the* $^1/_2\langle 110\rangle\{110\}$ *screw dislocation in wadsleyite, as inferred from the PNG results (Fig. 3.6). The normal of the glide plane points out of the paper. The dislocation core is visualized by atomic displacements according to the disregistry and local Burgers vector density.*

The resulting dislocation core structures of the $^1/_2\langle 110\rangle$ screw and edge dislocations spreading in $\{110\}$ and $\{111\}$ are shown in Fig. 3.21 by the disregistry and its derivative, the Burgers vector density. One can observe that the core structures of the $^1/_2\langle 110\rangle\{110\}$ and $^1/_2\langle 110\rangle\{111\}$ screw dislocations are very similar. It further shows clearly the collinear dissociation into two partials according to the Burgers vector reaction $^1/_2\langle 110\rangle = {}^1/_4\langle 110\rangle + {}^1/_4\langle 110\rangle$. Properties of all structures are shown in tables 3.5 and 3.6 for the $^1/_2\langle 110\rangle$ screw and edge dislocations respectively. It can be seen that all core structures of the screws are more confined and less extended into the glide plane

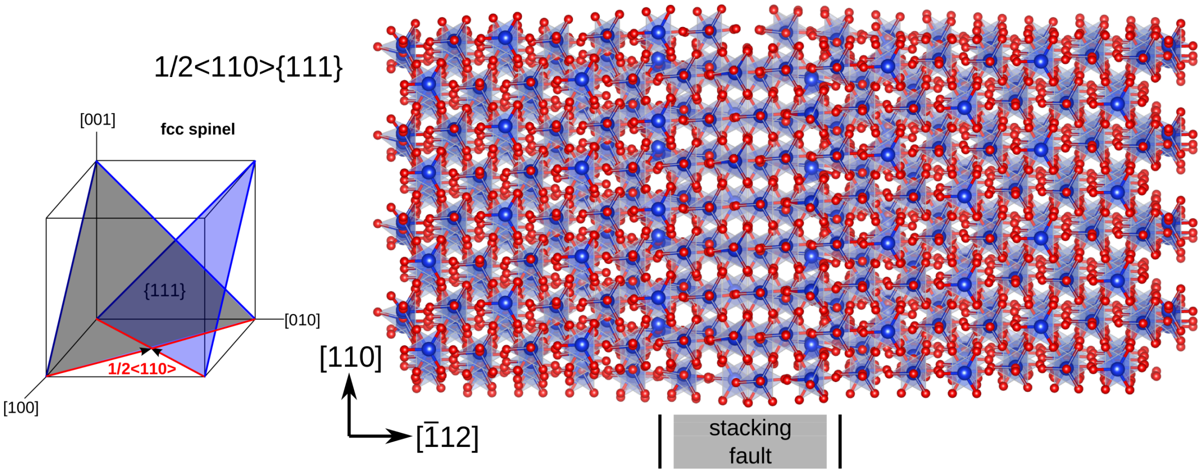

Figure 3.23: *Atomistic view of the core structure of the* ½⟨110⟩{111} *screw dislocation in wadsleyite, as inferred from the PNG results (Fig. 3.6). The normal of the glide plane points out of the paper in the above figure which gives a top view on the glide plane. The dislocation core is visualized by atomic displacements according to the disregistry and local Burgers vector density.*

than the edge characters. The equilibrium stacking fault width $d$ between the partials is always equal to an integer multiple of the lattice periodicity $a'$. This means that both partials occupy the minimum energy configuration in the crystal, and are therefore well placed into the wells of the Peierls potential, under equilibrium conditions. An illustration of the atomistic view of the ½⟨110⟩ screw dislocation spreading in the {110} and {111} planes are shown in Fig. 3.22 and 3.23.

| Dislocation | K($\theta = 0°$) (GPa) | $a'$ (Å) | $\xi$ (Å) | $d$ (Å) | $\tau_p$ (GPa) |
|---|---|---|---|---|---|
| ½⟨110⟩{110} | 135 | $a/2 \approx 3.940$ | 2.9 | 8.5 | 7 |
| ½⟨110⟩{111} | 135 | $a\sqrt{6}/4 \approx 4.825$ | 3.8 | 10 | 9 |

Table 3.5: *Core structures and quantification of the intrinsic lattice friction of the* ½⟨110⟩ *screw dislocations for a given periodicity* $a'$ *of the Peierls potential.* $K(\theta)$ *is equal to the anisotropic elastic parameter,* $\xi$ *corresponds to the width of each partial,* $d$ *is equal to the equilibrium stacking fault width taken as the distance between the partials comparable to an integer multiple of one lattice periodicity* $a'$ *and* $\tau_p$ *corresponds to the Peierls stress.*

| Dislocation | K($\theta = 90°$) (GPa) | $a'$(Å) | $\xi$ (Å) | $d$ (Å) | $\tau_p$ (GPa) |
|---|---|---|---|---|---|
| $1/2\langle 110\rangle\{110\}$ | 185 | $a\sqrt{2}/4 \approx 2.786$ | 4.5 | 12 | 1 |
| $1/2\langle 110\rangle\{111\}$ | 187 | | 5.5 | 14 | 2.5 |

Table 3.6: *Core structures and quantification of the intrinsic lattice friction for the* $1/2\langle 110\rangle$ *edge dislocations. All parameters are defined as in table 3.5.*

The dislocation core structures calculated in this study are in relatively good agreement with results previously obtained by Carrez *et al.* (2006). In both studies, all screw dislocations exhibit narrower core structures with respect to the edge dislocations. Nevertheless, all core structures here are found to be slightly more confined, so that the stacking fault widths, measured as the distance between the center of both partials in the spreading direction, are integer multiples of the corresponding Peierls periodicities. The only difference is that we show here that the $1/4\langle 110\rangle\{111\}$ partial screw dislocations exhibit minor edge components of 9% of the $1/2\langle 110\rangle$ Burgers vector. This may explain why spreading of the $1/2\langle 110\rangle$ screw dislocation is found in $\{111\}$ when initially introducing it in the same plane. This let us suggest that the $1/2\langle 110\rangle$ screw dislocation spreading in the $\{110\}$ may finally be the most stable dislocation core configuration in ringwoodite. Figure 3.24 shows the explicit Burgers vector path of a relaxed $1/2\langle 110\rangle\{111\}$ screw dislocation superimposed on a contourplot of the $\gamma$-surface of the $\{111\}$ plane. One can observe that the dislocation is dissociated into $1/4\langle 110\rangle\{111\}$ partials separated by a stacking fault, for which both partials are split into two smaller partials of large screw and small edge segments. However, this deviation from collinear dissociation is small and will therefore be neglected throughout the calculations of the dislocation mobility. So formally, we will assume the Burgers vector reaction for the $1/2\langle 110\rangle\{111\}$ screw dislocation to be $1/2\langle 110\rangle = 1/4\langle 110\rangle + 1/4\langle 110\rangle$. It is however worth to mention that exactly this type of core structure of the $1/2\langle 110\rangle\{111\}$ dislocation, as shown in Fig. 3.24, was proposed by Welsch *et al.* (1974) to exist in stoichiometric $MgAl_2O_4$ spinel after weak-beam TEM study. The dissociation of the $1/2\langle 110\rangle\{111\}$ dislocation into four partials has first been proposed by Hornstra in 1960.

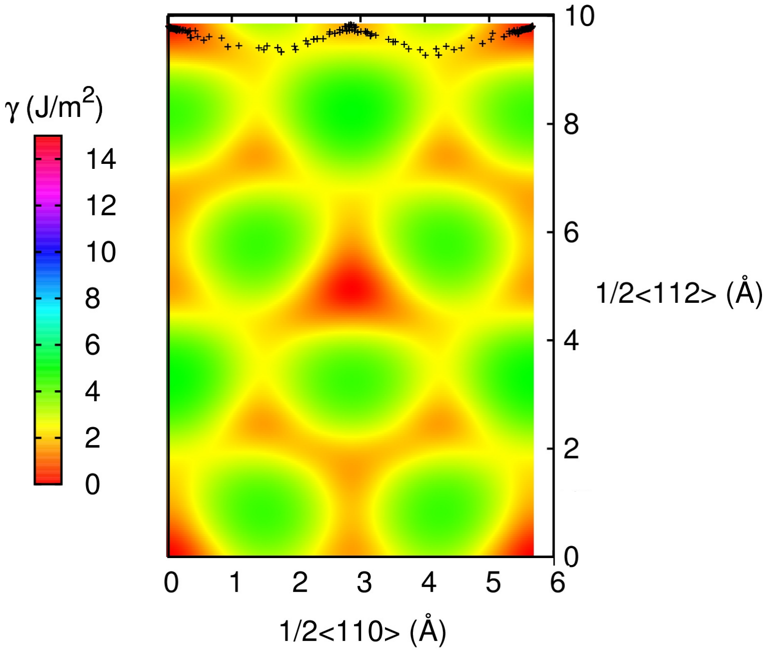

Figure 3.24: *Contourplot of the $\gamma$-surface of the {111} plane including the Burgers vector path for a relaxed* $^1\!/_2\langle 110\rangle\{111\}$ *dislocation initially introduced as purely screw using the PNG model. The metastable minimum at the top halfway along the* $^1\!/_2\langle 110\rangle$ *direction indicates the dissociation of the dislocation. It can be seen that both* $^1\!/_4\langle 110\rangle$ *partials exhibit small edge components of 9% of the* $^1\!/_2\langle 110\rangle$ *Burgers vector.*

Quantification of the intrinsic lattice friction of the $^1\!/_2\langle 110\rangle$ screw and edge dislocations is obtained through explicit calculation of the Peierls potentials according to Eq. 2.44 (chapter 2.2.4). Tables 3.5 and 3.6 give the Peierls stresses resulting from all dislocation structures. One can observe that the Peierls stresses for the edge dislocations are considerably lower than those for the screw dislocations. As the edge characters exhibit lower lattice friction, the mobility of the $^1\!/_2\langle 110\rangle$ screw dislocation gliding in the preferential {110} and {111} slip planes will account for most of the plastic strain produced during deformation (as plastic strain contributed by the faster edge segments is negligible). Peierls potentials of the most important $^1\!/_2\langle 110\rangle\{110\}$ and $^1\!/_2\langle 110\rangle\{111\}$ screw dislocations are shown in Fig. 3.25. Both slip systems have a value of $\tau_p/\mu \sim 5 \times 10^{-2}$. For comparison at similar high pressure conditions, $\tau_p/\mu \sim 1 \times 10^{-3}$ in MgO (Amodeo et al. 2011) and $\tau_p/\mu \sim 3.5 \times 10^{-2}$ in wadsleyite at 15 GPa with respect to the easiest slip systems.

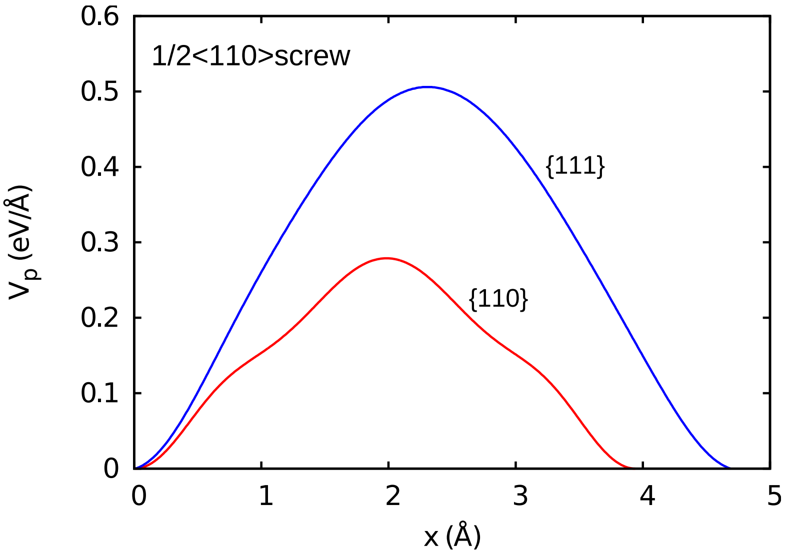

Figure 3.25: *Peierls potentials calculated using the PN model based on the dislocation structures for the* $1/2\langle 110\rangle$ *screw dislocations gliding in the* $\{110\}$ *and* $\{111\}$ *planes.*

### 3.2.3 Thermal activation of dislocation glide

Calculations of the critical kink-pair enthalpies are parametrized by the dislocation core structures (Fig. 3.6), the Peierls potentials (Fig. 3.10) and the associated Peierls stresses (Table 3.5) of the $1/2\langle 110\rangle\{110\}$ and $1/2\langle 110\rangle\{111\}$ screw dislocations as previously calculated. As the kink-pair model is based on linear elasticity, the shear modulus $\mu$ and Poisson ratio $\nu$ at 20 GPa have been deduced from the dislocation character dependent anisotropic elastic parameter $K(\theta)$ using the DisDi software (Douin, 1987) ($K(0°) = \mu$ and $K(90°) = \mu/(1-\nu)$ for screw and edge type dislocation segments respectively, see table 3.5 and 3.6). The calculations rely on the elastic constants at 20 GPa which are obtained with *ab initio* calculations (table 3.7), as discussed in section 2.1.4.

| | $C_{11}$ | $C_{44}$ | $C_{12}$ | (GPa) |
|---|---|---|---|---|
| *Ab initio* (this study) (GGA) (20 GPa) | 415 | 143 | 160 | |
| Exp. Sinogeikin *et al.* (15.8 GPa) | 427 | 142 | 161 | |
| *Ab initio* (Kiefer *et al.*) (LDA) (20 GPa) | 475 | 150 | 175 | |

Table 3.7: *Elastic constants of $Mg_2SiO_4$ ringwoodite at 20 GPa as obtained by* ab initio *calculations in this study. A comparison is given with respect to the elastic constants inferred from experiments at* 15.8 *GPa as provided by Sinogeikin* et al. *(2001) and with respect to* ab initio *calculation performed by Kiefer* et al. *(1997). The results are comparable.*

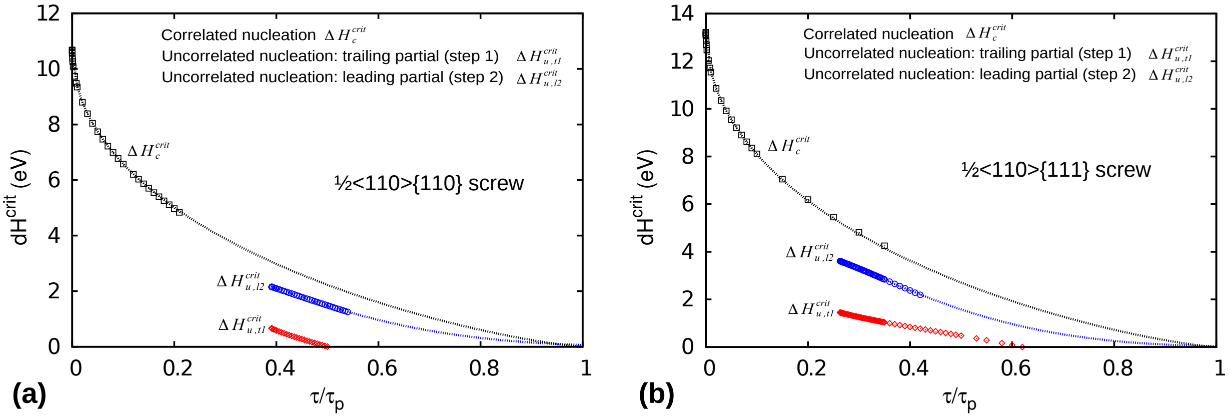

Figure 3.26: *Evolution of the critical kink-pair nucleation enthalpy as a function of the resolved shear stress (normalized by the Peierls stress) for the* ½⟨110⟩ *screw dislocation gliding in the a)* {110} *plane and b)* {111} *plane. Results are shown for correlated nucleation and both elementary steps of the uncorrelated nucleation process. It can be seen that the critical enthalpy related to step 2 of the uncorrelated nucleation of kink-pairs will govern this process since the corresponding mobility is described by an Arrhenius type of law as described in section 2.3.3.*

The critical enthalpies related to the nucleation of kink-pairs on the ½⟨110⟩{110} and ½⟨110⟩{111} screw dislocations are calculated as described in chapter 2.3. Kink-pair nucleation on both screw dislocations can be described as in the general case for dissociated dislocations. This means that correlated nucleation of kink-pairs is captured by the single critical activation enthalphy $\Delta H_c^{crit}$. On the other hand, uncorrelated kink-pair nucleation is essentially determined by the outward motion of the leading partial $\Delta H_{u,l_2}^{crit}$

(to which we will simply refer to as $\Delta H_u^{crit}$) associated with the nucleation process as shown in Fig. 2.8c in chapter 2.3. This means that both correlated and uncorrelated kink-pair nucleation can be described by the single critical activation enthalpies $\Delta H_c^{crit}$ and $\Delta H_u^{crit}$ respectively. Results of the critical nucleation enthalpies as a function of stress for both correlated ($\Delta H_c^{crit}$) and uncorrelated kink-pair nucleation ($\Delta H_{u,t_1}^{crit}$, $\Delta H_{u,l_2}^{crit}$) are presented in Fig. 3.26.

| Dislocation | $\tau_p$ (GPa) | $\Delta H_0$ (eV) | $p$ | $q$ |
|---|---|---|---|---|
| 1/2⟨110⟩{110} | 7 | 10.7 | 0.5 | 1.2 |
| 1/2⟨110⟩{111} | 9 | 13.2 | 0.5 | 1.1 |

Table 3.8: *Key features and parameterization related to the glide as a result of correlated kink-pair nucleation of the governing screw dislocations.* $\Delta H_0$ *is the critical nucleation enthalpy at zero stress,* $a'$ *is the periodicity of the Peierls potential,* $\tau_p$ *corresponds to the Peierls stress and* $p$ *and* $q$ *are together with* $\Delta H_0$ *the empirical fitting parameters of Eq. 2.64.*

| Dislocation | $\tau_p$ (GPa) | $\tau_c$ (GPa) | $\Delta H_0$ (eV) | $p$ | $q$ |
|---|---|---|---|---|---|
| 1/2⟨110⟩{110} | 7 | 2.7 | 2.2 | 1.0 | 2.9 |
| 1/2⟨110⟩{111} | 9 | 2.4 | 3.6 | 1.0 | 2.9 |

Table 3.9: *Key features and parameterization related to glide as a result of uncorrelated kink-pair nucleation of the governing screw dislocations, where* $\Delta H_0$ *is the critical nucleation enthalpy at* $\tau = \tau_c$. *The remaining parameters are defined as in table 3.8.*

As in the case of wadsleyite, the critical nucleation enthalpies can be extrapolated up to the Peierls stress according to Eq. 2.64. The saddle point energies $\Delta H^{crit}$ (as calculated at low stress) are used to fit $\Delta H_0$ and the empirical parameters $p$ and $q$. Fitting of the saddle point energies can be seen in Fig. 3.11 as dashed lines. Table 3.8 and 3.9 show the parameterizations related to the two slip systems considered.

### Kink-pair geometry

The saddle point configuration $\Delta H^{crit}$ of the total enthalpy variation $\Delta H$ of kink-pair nucleation as shown in Fig. 3.26 is determined by the free geometrical variables that define the kink-pair. The evolution of the critical kink-pair geometry as a function of the applied stress for both correlated and uncorrelated nucleation processes is shown in Fig. 3.27 with respect to the rate governing $^1/_2\langle 110\rangle\{110\}$ and $^1/_2\langle 110\rangle\{111\}$ screw dislocations. As mentionned before, under low stress conditions, the critical height $h^{crit}$ of a kink is about equal to the Peierls periodicity $a'$ and decreases with increasing stress. Further, one can observe that the critical width rapidly converges to finite values with increasing stress but diverges when the resolved shear stress goes to zero. Therefore, the critical kink-pair width has to be truncated at low stress with respect to the typical average length $L = 1/\sqrt{\rho_m}$ (where $\rho_m$ is equal to the dislocation density) of the partial dislocation lines.

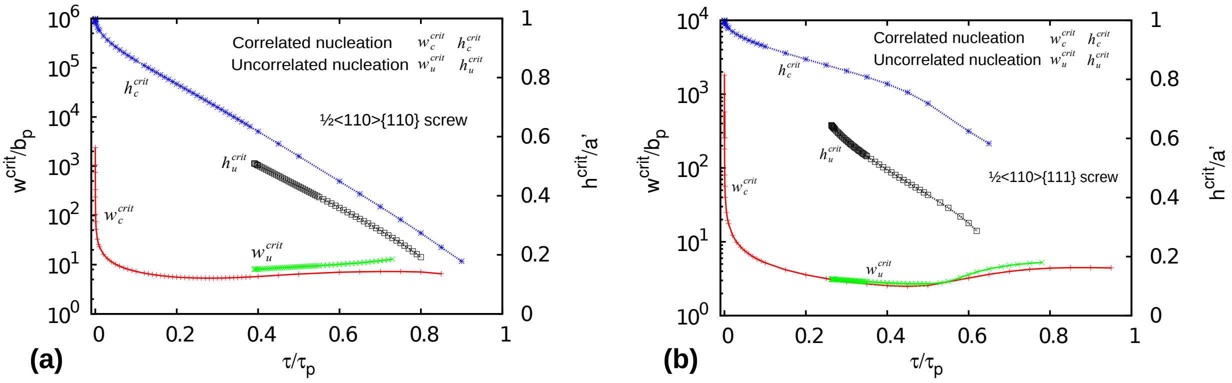

Figure 3.27: *Evolution of the critical kink-pair geometry* $h^{\text{crit}}$ *and* $w^{\text{crit}}$ *as a function of the resolved shear stress* $\tau$ *for* $^1/_2\langle 110\rangle$ *screw dislocation gliding in the a)* $\{110\}$ *and b)* $\{111\}$ *plane. It can be seen that the height of kink-pairs under negligible stress conditions is equal to the Peierls periodicity* $a'$ *and decreases with increasing stress. The width between the kink-pairs rapidly converge with increasing stress to almost constant values but diverges when the stress goes to zero.*

### 3.2.4 Dislocation mobility

Dislocation glide mobility of $1/2\langle 110\rangle$ screw dislocations in the $\{110\}$ and $\{111\}$ planes are parametrized by the critical nucleation enthalpies (Fig. 3.26) and calculated as described in chapter 2.3.3. The stress dependence of the pre-exponential factor in the description of the glide velocity, as discussed in section 2.3.3, can be neglected due to similar high values of the critical kink-pair nucleation enthalpies as for wadsleyite. The glide velocities obtained in this study rely on the assumption that kink-pair nucleation controls the overall mobility of the rate controlling screw dislocations as briefly discussed in section 3.1 on wadsleyite.

Dislocation velocity profiles as a function of the resolved shear stress for both $1/2\langle 110\rangle\{110\}$ and $1/2\langle 110\rangle\{111\}$ screw dislocations using a dislocation density of $\rho_m = 10^{12}$ m$^{-2}$ are shown in Fig. 3.28. At $T$=1800 K (Fig. 3.28a), the velocity difference between both slip systems remains fairly constant at low and intermediate stresses and decreases for high values approaching the Peierls stress $\tau_p$. The critical stress $\tau_c$ below which only correlated kink-pair nucleation can occur is equal to $\sim$ 2.5 GPa for both screw dislocations (table 3.9). Typical laboratory strain rates of $\dot{\epsilon} = 10^{-5}$ s$^{-1}$ correspond to dislocation velocities of about $v = 2 \times 10^{-8}$ m/s. The stresses associated with these velocities are $\sim$ 1 GPa. In constrast, the dislocation velocity related to mantle strain rates of $\dot{\epsilon} = 10^{-16}$ s$^{-1}$ is about $v = 2 \times 10^{-15}$ m/s. This demonstrates the intrinsic non-linearity of the velocity variation with resolved shear stress at fixed $T$. At room temperature, the dislocation velocity profiles for the same screw dislocations are shown in Fig. 3.28b. In this case, glide only takes place in the high stress regime where uncorrelated nucleation of kink-pairs governs the dislocation mobility. The overall trend of the velocity profile with stress at room temperature is comparable to the results at 1800 K. Stresses of about 4 GPa are required to obtain dislocation velocities corresponding to typical laboratory strain rates at room temperature.

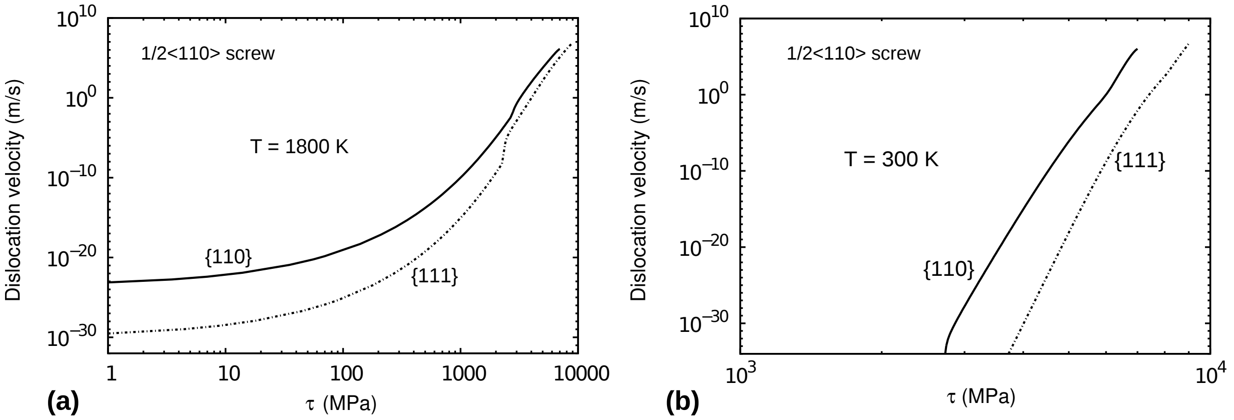

Figure 3.28: *Glide velocities of the* $1/2\langle 110\rangle\{110\}$ *and* $1/2\langle 110\rangle\{111\}$ *screw dislocations as a function of the resolved shear stress at: a)* 1800 *K and b)* 300 *K.*

The above results on the dislocation mobility show the same trends as in case of wadsleyite: dislocation glide operating by the Peierls mechanism at low temperatures and high deviatoric stress (in most cases, laboratory conditions), will be mainly governed by uncorrelated nucleation of kink-pairs. Whereas at high temperatures and small deviatoric stresses (more likely to represent mantle conditions), the glide will be predominantly controlled by correlated nucleation of kink-pairs on both partials. This is in agreement with what has been found on the mobility of collinearly dissociated dislocations in several intermetallic compounds and semiconducting crystals such as silicon (Si) and germanium (Ge) by Möller (1978) and Takeuchi (1995).

### 3.2.5 Constitutive equations

As the plastic flow below the athermal temperature is directly controlled by the mobility of dislocations, the relation between the behaviour of individual dislocations and the collective macroscopic behaviour in this regime, as discussed in chapter 2.3.4, can be derived from Orowan's equation:

$^1/_2\langle 110\rangle\{110\}$ **screw dislocation**:

- $0 < \tau \leq \tau_c$:

$$\dot{\epsilon}_c(\tau) = 3940\sqrt{\rho_m}\exp\left(-\frac{1.60\times 10^{-18}\left(1-\left(\frac{\tau}{\tau_p}\right)^{0.5}\right)^{1.2}}{k_bT}\right) \quad \text{in} \quad s^{-1}$$

- $\tau_c \leq \tau \leq \tau_p$:

$$\dot{\epsilon}_{c+u}(\tau) = \frac{1}{2}\rho_m b\left[v_c + v_u\right] = \frac{1}{2}\left[\dot{\epsilon}_c + \dot{\epsilon}_u\right] \quad \text{with}$$

$$\dot{\epsilon}_u = 7880\sqrt{\rho_m}\left(\frac{\tau-\tau_c}{\tau}\right)\exp\left(-\frac{3.52\times 10^{-19}\left(1-\left(\frac{\tau-\tau_c}{\tau_p}\right)^{1.0}\right)^{2.9}}{k_bT}\right) \quad \text{in} \quad s^{-1}$$

$^1/_2\langle 110\rangle\{111\}$ **screw dislocation**:

- $0 < \tau \leq \tau_c$:

$$\dot{\epsilon}_c(\tau) = 4800\sqrt{\rho_m}\exp\left(-\frac{2.0\times 10^{-18}\left(1-\left(\frac{\tau}{\tau_p}\right)^{0.5}\right)^{1.1}}{k_bT}\right) \quad \text{in} \quad s^{-1}$$

- $\tau_c \leq \tau \leq \tau_p$:

$$\dot{\epsilon}_{c+u}(\tau) = \frac{1}{2}\rho_m b\left[v_c + v_u\right] = \frac{1}{2}\left[\dot{\epsilon}_c + \dot{\epsilon}_u\right] \quad \text{with}$$

$$\dot{\epsilon}_u = 9600\sqrt{\rho_m}\left(\frac{\tau-\tau_c}{\tau}\right)\exp\left(-\frac{5.77\times 10^{-19}\left(1-\left(\frac{\tau-\tau_c}{\tau_p}\right)^{1.0}\right)^{2.9}}{k_bT}\right) \quad \text{in} \quad s^{-1}$$

with $k_b$ equal to the Boltzmann constant, $T$ the temperature in $[K]$ and the dislocation density $\rho_m$ given in $\left[m^{-2}\right]$.

### 3.2.5.1 Deformation under laboratory conditions

Single slip constitutive equations as a consequence of thermally actived glide of $1/2\langle 110\rangle\{110\}$ and $1/2\langle 110\rangle\{111\}$ screw dislocations can be inferred as described in chapter 2.3.4 and 3.1.5.

To compare the results of the constitutive equations obtained in our theoretical study with experimental data available on deformation of ringwoodite at 20 GPa, we calculated the $CRSS$ over a broad temperature range for typical laboratory strain rates of $\dot{\epsilon} = 10^{-5}$ s$^{-1}$. The mobile dislocation density is set to $\rho_m = 10^{12}$ m$^{-2}$. Figure 3.29 shows the results for the slip of the $1/2\langle 110\rangle\{110\}$ and $1/2\langle 110\rangle\{111\}$ screw dislocations. The transition from the solid to the thin lines at 2500 K marks the onset to melting for $Mg_2SiO_4$ ringwoodite at 20 GPa. This demonstrates that dislocation glide in ringwoodite at laboratory strain rates always operates in the thermally-activated regime, since the athermal temperature would be higher than the melting temperature. Slip of the $1/2\langle 110\rangle\{110\}$ screw dislocations is comparable, yet slightly softer than slip of the $1/2\langle 110\rangle\{111\}$ screw dislocations. Fig. 3.29 shows a remarkable agreement between our theoretical predictions and the experimental data available as it was the case in wadsleyite in section 3.1. As for wadsleyite (chapter 3.1), the deformation experiments on ringwoodite as used, from Meade and Jeanloz (1990), Kavner *et al.* (2001), Nishiyama *et al.* (2005), Hustoft *et al.* (2012) and Miyagi *et al.* (2013), were performed on polycrystalline samples. This means that only a fraction of the effective flow stress is resolved in the direction of dislocation motion within each single slip plane. The $CRSS(T)$ corresponding to our theoretical single slip results is therefore multiplied by two (corresponding to the maximum of the Schmid factor) in order to be compared with the experimental data in Fig. 3.29. The latter assumption may be too simple as more deformation mechanisms may be involved in the experiments and effects of impurities, grain boundaries and hardening have not been taken into account in our model. However, we are able to well reproduce the evolution of the $CRSS$ as a function of $T$ compared to the available experimental data in terms of dislocation activity for both wadsleyite at 15 GPa and ringwoodite at 20 GPa. This agreement suggest that dislocation glide controls the mechanical behaviour at laboratory conditions.

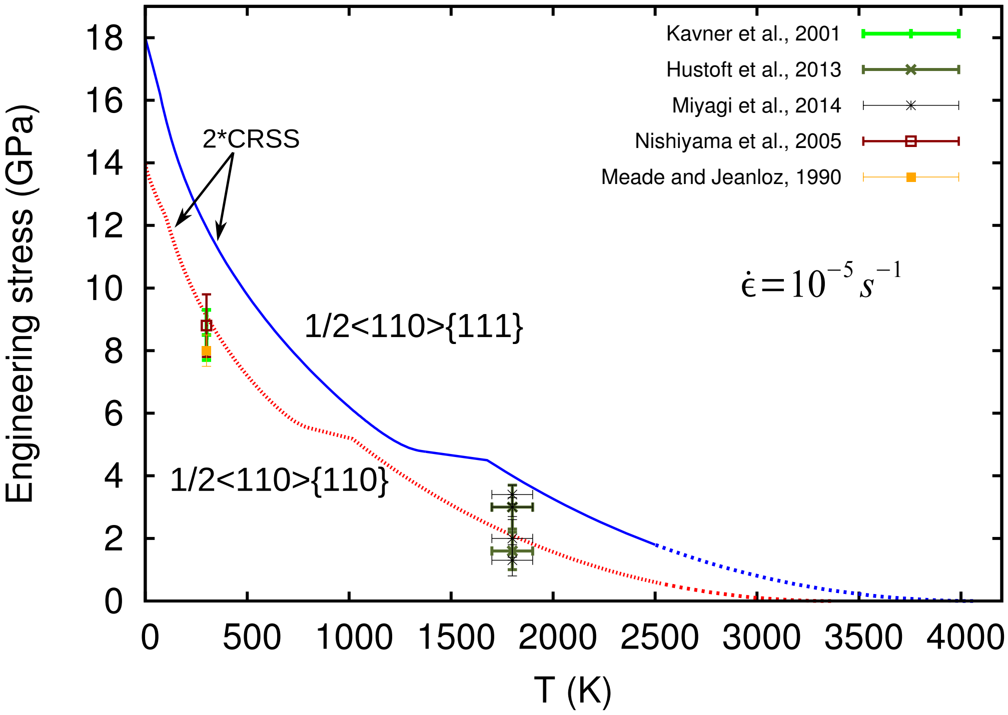

Figure 3.29: *Critical resolved shear stress* ($CRSS$) *versus temperature* ($T$) *at a fixed strain rate of* $\dot{\epsilon} = 10^{-5}\ s^{-1}$ *for thermally actived glide of the* $1/2\langle 110\rangle\{110\}$ *and* $1/2\langle 110\rangle\{111\}$ *screw dislocations. The mobile dislocation density is taken to be* $\rho_m = 10^{12}\ m^{-2}$. *The transition of correlated kink-pair nucleation towards both uncorrelated and correlated nucleation occurs around* $\tau_c \sim 2.5$ *GPa. Single slip* $CRSS$ *as calculated are multiplied by two to be converted into apparent engineering stresses which allows for the comparison with the results from deformation experiments.*

#### 3.2.5.2 Deformation under transition zone conditions

Following the same approach as for the laboratory strain rates, the *CRSS* can be obtained as a function of $T$ for typical mantle strain rates of $\dot{\epsilon} = 10^{-16}$ s$^{-1}$. Ringwoodite is stable in the lower half of the transition zone at a pressure around 20 GPa corresponding to a temperature of $\sim$ 1800 K. The mobile dislocation density is taken to be $\rho_m = 10^8$ m$^{-2}$ to adjust to the low stress regime of the Earth's mantle. The results are shown in Fig. 3.30. One can observe that the minimum *CRSS*'s are on the order of 100 MPa for the easiest slip system ($1/2\langle110\rangle\{110\}$ screw) up to over 500 MPa for the most difficult slip system ($1/2\langle110\rangle\{111\}$ screw) at 1800 K. The results show that dislocation glide in ringwoodite under mantle conditions operates in the thermally activated regime (where *CRSS* is a function of $T$), although near the boundary to the athermal regime above which dislocation-dislocation interactions would govern the dislocation mobility. However, the athermal temperature is a function of the applied strain rate and the mobile dislocation density. Smaller strain rates and larger mobile dislocation densities would shift the athermal temperatures to lower values and *vice versa.* We want to mention that the *CRSS* for both slip systems at the appropriate mantle conditions are significantly lower than the critical stress $\tau_c$, which means that the glide mobility is the result of correlated kink-pair nucleation under the relatively low stress and high $T$ conditions in the Earth's mantle.

Viscosities associated with single slip in ringwoodite are deduced from the constitutive relations as shown in Fig. 3.30 at the conditions of the lower transition zone by

$$\eta = \frac{CRSS(T = 1800K)}{2\dot{\epsilon}} \tag{3.3}$$

A viscosity of $8 \times 10^{23}$ Pa s and $3 \times 10^{24}$ Pa s with respect to glide can be attributed to the $1/2\langle110\rangle\{110\}$ and $1/2\langle110\rangle\{111\}$ screw dislocations, respectively. The viscosity

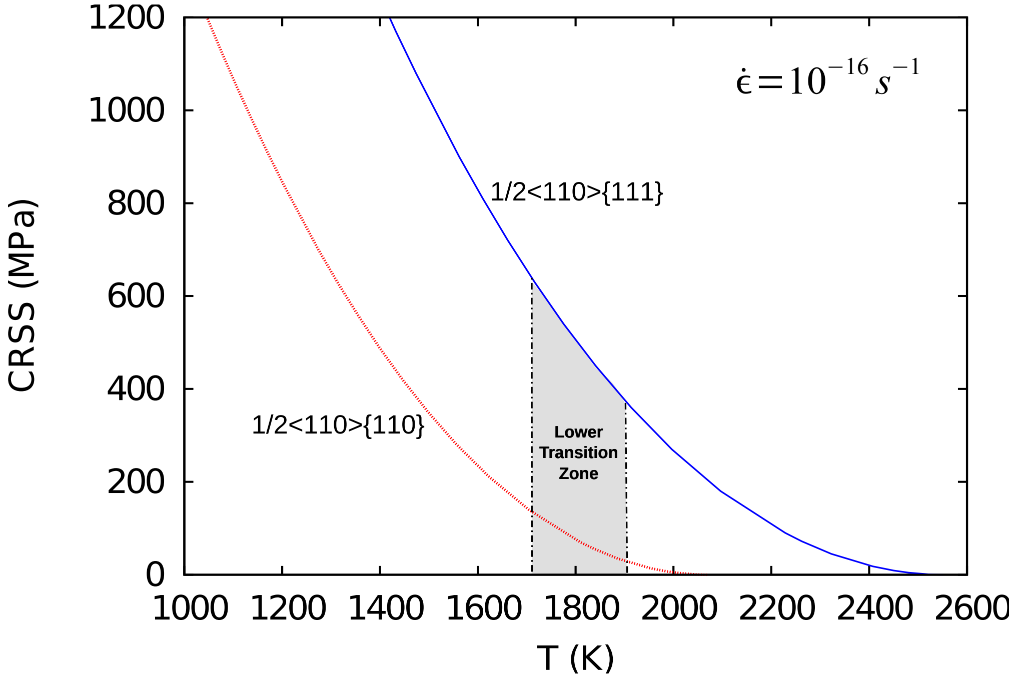

Figure 3.30: *Critical resolved shear stress (CRSS) versus temperature at a fixed strain rate of* $\dot{\epsilon} = 10^{-16}$ $s^{-1}$ *for thermally actived glide of the* $1/2\langle 110\rangle\{110\}$ *and* $1/2\langle 110\rangle\{111\}$ *screw dislocations. The dislocation density is taken to be* $\rho_m = 10^8$ $m^{-2}$. *The shaded area depicts the stability field of ringwoodite in the lower transition zone at* 20 *GPa.*

values as calculated can be seen as lower bounds since they are related to the intrinsic glide resistance of single slip systems.

Dislocation modelling shows that intrinsic lattice friction measured by the Peierls stress is lower for $1/2\langle 110\rangle\{110\}$ than for the $1/2\langle 110\rangle\{111\}$ screw dislocations. From our study, it follows that temperature and strain rate do not change this hierarchy since glide of the $1/2\langle 110\rangle\{110\}$ screw dislocations remains easier in the whole range of conditions considered here. This is in contrast with some experimental studies which emphasize the dominance of $1/2\langle 110\rangle\{111\}$ slip (Wenk *et al.* 2005; Miyagi *et al.* 2014). However, this conclusion is drawn from crystal preferred orientation measurements and viscoplastic self-consistent modelling (VPSC). As already noted by Carrez *et al.* (2006) and Miyagi *et al.* (2014), this may be due to the fact that $1/2\langle 110\rangle\{111\}$ has more symmetrical variants than the $1/2\langle 110\rangle\{110\}$ slip system and might therefore play an important role in the deformation despite its slightly more difficult slip.

## 3.3 On dislocation glide in wadsleyite and ringwoodite

Dislocation glide has been modeled using a multiphysics approach to investigate its potential contribution to the overall plastic deformation of $Mg_2SiO_4$ wadsleyite and ringwoodite in the Earth's transition zone. The multiscale model we have been using is extensively described in chapter 2, followed by the results regarding both $Mg_2SiO_4$ high-pressure polymorphs in chapter 3. Glide has been modelled in wadsleyite at 15 GPa and in ringwoodite at 20 GPa at finite temperatures at both laboratory and natural strain rates. Lattice friction that is opposed to glide motion of dislocations is quantified in the framework of the Peierls-Nabarro model, parametrized by atomic scale calculations of $\gamma$-surfaces, and used to model thermally activated glide of the rate controlling (screw) dislocations in wadsleyite and ringwoodite.

To move in both high-pressure polymorphs of olivine, dislocations have to overcome their intrinsic lattice friction. Plastic slip in this so called thermally-activated regime, is mainly governed by sluggish glide of long dislocation segments of screw character. If a dislocation bows-out in its glide plane, under the conjugate action of resolved shear stress and thermal activation, it activates non-screw segments that migrate rapidly and leave behind long straight slow moving screw segments, which in turn will account for most of the plastic strain produced. Our model is also able to determine the temperature threshold above which dislocation-dislocation interactions would govern the mobility of dislocations, *i.e.* the temperature threshold below which the glide mobility of dislocations is primarily dominated by the interaction between dislocations and the crystal lattice. As such, the model strongly relies on the intrinsic core properties of the rate governing (screw) dislocations: $1/2\langle 111\rangle\{101\}$ and $[100](010)$ screw dislocations in wadsleyite and the $1/2\langle 110\rangle$ screw dislocations gliding in the $\{110\}$ and $\{111\}$ planes in ringwoodite. A crucial feature of these rate controlling screw dislocations is the (collinear) dissociation into partials which determines their mobility. Thermal activation of these dissociated dislocations is then modelled in order to calculate the respective glide velocities. Deformation by dislocation glide is finally presented as the response of the $CRSS(T)$ to a constant applied strain rate at the grain scale.

We would like to focus on some points of the modelling approach and spend some time to discuss the possible effect on the final results in form of the glide mobilities, *i.e.* the constitutive equations. The glide mobilities of dislocations are derived by the use of the kink-pair model, which is based on linear elasticity. This model has been adopted and extended to describe the nucleation of kink-pairs on dissociated dislocations. The model is expected to be the most accurate in the low stress regime (correlated nucleation of kink-pairs). This implies that $CRSS(T)$ are found to be the most accurate at high $T$ and low stress conditions, which are the conditions of interest in the Earth's deep mantle. This also means that the values of the $CRSS(T)$, as determined by the kink-pair model, may be more uncertain at typical laboratory conditions of low $T$ and high stresses (uncorrelated nucleation of kink-pairs). However, the modelling approach has led to a good agreement with the constitutive relations at laboratory conditions in both wadsleyite and ringwoodite which exhibit high lattice friction. It has to be mentioned that the benchmark of our multiscale model on $SrTiO_3$ perovskite has shown that the model is capable of reproducing the constitutive equations related to glide in $SrTiO_3$ single crystals satisfactorily with respect to the initial assumptions which are used to model thermally activated glide in both transition zone minerals. The validations suggest that the model is able to capture the essential physics at all scales.

Secondly, we would like to spend a few lines on the fact that the contribution of the entropy change is neglected in the kink-pair model. In chapter 2, an estimation of this energy contibution was calculated to be lower than [0.2-1.2] eV at 1700 K. At these high temperatures, we are in the low-stress domain for the threshold of dislocation motion, which corresponds to high critical nucleation enthalpies $> 10$ eV for both wadsleyite and ringwoodite. As such, the entropy variation seems to be of minor importance on the energy contribution associated to kink-pair formation for both high-pressure polymorphs of olivine.

The modelling results show that glide in wadsleyite and ringwoodite under both laboratory and mantle conditions still occurs in a regime where the $CRSS$ is temperature dependent. This implies that plastic deformation by dislocation glide in both minerals under conditions of the transition zone is governed by the mobility of the rate governing screw dislocations. The constitutive equations related to glide at typical laboratory strain rates of $\dot{\epsilon} = 10^{-5}$ s$^{-1}$ show a good agreement with experimental data on plastic deformation of wadsleyite and ringwoodite. This suggests that glide may largely control the mechanical behaviour under laboratory conditions in both high-pressure $Mg_2SiO_4$ polymorphs. However, strain rate is one of the physical quantities that determine the potential contribution of a deformation mechanism to the overall plasticity. Taking into account the intrinsic strain rate dependency on the mobility of the defects, constitutive equations are derived with respect to typical mantle strain rates of $\dot{\epsilon} = 10^{-16}$ s$^{-1}$. This has been used to calculate single slip viscosities:

- $Mg_2SiO_4$ wadsleyite at 15 GPa
    1. $1/2\langle 111\rangle\{101\}$ screw - $\eta = 9 \times 10^{23}$ Pa s
    2. $[100](010)$ screw - $\eta = 3 \times 10^{24}$ Pa s

- $Mg_2SiO_4$ ringwoodite at 20 GPa
    1. $^1/_2\langle 110\rangle\{110\}$ screw - $\eta = 8 \times 10^{23}$ Pa s
    2. $^1/_2\langle 110\rangle\{111\}$ screw - $\eta = 3 \times 10^{24}$ Pa s

All viscosity values are on order of about $10^{24}$ Pa s. This shows that lattice friction of the transition zone minerals wadsleyite and ringwoodite cannot be neglected, even at the typical low strain rates expected in the Earth's mantle. The results suggest the inefficiency of dislocation glide as a strain producing deformation mechanism in the high-pressure polymorphs of olivine under transition zone conditions. Furthermore, difficult dislocation glide in the Mg-endmembers of wadsleyite and ringwoodite, under the conditions of the Earth's transition zone, is in contrast to glide in $(Mg,Fe)_2SiO_4$ olivine (Boioli *et al.* 2015) that seems to be much easier to activate. These results suggest that the sole contribution of dislocation glide is unlikely to account for the overall plasticity of $Mg_2SiO_4$ wadsleyite and ringwoodite under transition zone conditions.

It has to be mentionned that the single slip viscosities as obtained in our study are two orders of magnitude larger than what is expected ($10^{21} - 10^{22}$ Pa s) from global joint inversion (*e.g.* Ricard and Wuming 1991; Mitrovica and Forte 2004). It is essentially the evolution of the critical kink-pair nucleation enthalpies $\Delta H^{crit}(\tau)$ that determine the constitutive equations. Typical values of the critical nucleation enthalpies at low stress conditions of the mantle for the rate controlling dislocations in both high pressure polymorphs of olivine are found to be $\lim_{\tau \to 0} \Delta H^{crit} > 10$. This is what makes glide difficult to activate.

Large critical resolved shear stresses ($> 100$ MPa) regarding pure single slip dislocation glide would imply that other mechanisms may control the deformation of wadsleyite and ringwoodite in the Earth's transition zone.

# 4 Implications: which deformation mechanisms in the transition zone?

---

*I wish that they would softly creep ...*

William Wordsworth.

(*The Excursion: Being a portion of The Recluse, a poem* 1814.)

---

The above modelling of dislocation glide in $Mg_2SiO_4$ wadsleyite and ringwoodite confirms results from high $P$ and $T$ deformation experiments by obtaining comparable stress levels. This confirms that the glide motion of dislocations, despite the high plastic flow stresses required to produce plastic strain, largely controls the mechanical behavior under laboratory conditions. Moreover, by taking into account the intrinsic dependency of the strain rate on the dislocation velocity, we have shown that the lattice resistance for dislocations to glide in both high-pressure polymorphs of olivine remains relatively high for what can be expected under mantle conditions at very low strain rates of $10^{-16}$ $s^{-1}$. This implies that the sole contribution of dislocation glide to the overall plasticity in wadsleyite and ringwoodite cannot account for the plastic strain produced at low stress conditions of the Earth's deep mantle.

The glide of dislocations, as integral part of the dislocation creep deformation mechanism, is often seen as one of the efficient processes to produce intracrystalline plastic strain in minerals. This principle becomes questionable for wadsleyite and ringwoodite as a result of the high lattice friction under natural conditions. This suggests the need for deformation mechanisms other than dislocation glide to be responsible for the overall plasticity of both high-pressure polymorphs of olivine in the Earth's transition zone.

Beside dislocation glide, plastic deformation in (poly)crystalline materials can also be accomodated by the diffusion of point defects as present in the grains. Vacancy diffusion through the crystal bulk (Nabarro-Herring creep) or along grain boundaries (Coble creep) can both operate if vacancies are emitted or absorbed by the grain boundaries. Also dislocation creep may involve the diffusion of point defects through dislocation climb, where the core structure of the edge dislocations (instead of the grain boundaries) act as sources and sinks for vacancy diffusion. The nature of point defects (vacancies, interstitials, *etc.*), the diffusion process (single atomic diffusion, multicomponent diffusion, *etc.*) and the sources and sinks in relation to the interdiffusive distances determine for a large part the overall rate of deformation.

These diffusion based deformation mechanisms may provide a more efficient alternative to dislocation glide in the high-pressure phases of the Earth's transition zone. The next step therefore consists in comparing pure diffusion creep mechanisms with the dislocation creep involving both dislocation glide and vacancy diffusion (dislocation climb) by constructing deformation mechanism maps. The implications and constraints on the rheology of the transition zone will be discussed afterwards.

## 4.1 Deformation mechanisms: dislocation glide versus vacancy diffusion

In this section, we will introduce the underlying principles and physical description of the most important potential deformation mechanisms involving pure diffusion of vacancies versus the one involving both glide and vacancy diffusion: diffusion versus dislocation creep. The aim is to address the strain producing efficiency of these deformation mechanisms in wadsleyite and ringwoodite under transition zone conditions.

### 4.1.1 Diffusion creep

Diffusional flow in ionic and covalent bonded materials such as the silicates that constitute the Earth's mantle is governed by multicomponent diffusion of point defects (*i.e.* diffusion of multiple atomic species forming a structural unit ($Mg_2SiO_4$-unit in case of wadsleyite and ringwoodite)) so as for the minerals to remain charge neutral. This implies the migration of vacancies or interstitials. Although both types of defects can effectively contribute to the diffusion process, vacancies generally exhibit lower formation energies. We therefore assume that deformation by diffusional flow is controlled by the vacancy diffusion.

#### 4.1.1.1 Nabarro-Herring creep

An imposed stress field on a (poly)crystal causes a heterogeneous state of stress between grain surfaces with different orientations. This results in different vacancy concentrations between different surfaces which gives rise to a vacancy concentration gradient (hence a chemical potential gradient) between the boundaries of a grain that exhibits different orientations with respect to the imposed stress field. The resultant flux of vacancies through a grain then occurs from grain boundaries under tension to grain boundaries in compression, as is the opposite for the flux of matter (ions). This deformation mechanism, where plastic strain is produced by the conjugate and opposite transport of matter and vacancies through the crystal lattice is known as *Nabarro-Herring creep* (Nabarro 1948; Herring 1950). Figure 4.1a shows the principle of Nabarro-Herring creep caused by an applied engineering stress $\sigma$. The corresponding strain rate, under the assumption of equal distribution of matter and vacancies at the grain boundaries, can be described as:

$$\dot{\epsilon}_{NH} = \zeta \frac{D_{sd}\sigma\Omega}{d^2 k_b T} \tag{4.1}$$

where $\sigma$ corresponds to the applied engineering stress, $\Omega$ is the average molecular volume of vacancy formation and $d$ is the average grain size. The self-diffusion coefficient of one atomic species is given by $D_{sd}$ in $[m^2 s^{-1}]$ and $\zeta$ is a shape factor which after Poirier (1985) is taken to be equal to 16/3 for spherical grains and corresponding to the impossibility of grain boundary sliding (GBS).

#### 4.1.1.2 Coble creep

The diffusion of vacancies and matter as induced by concentration gradients of vacancies between crystal surfaces, become easier through grain boundaries than through the crystal lattice at intermediate temperatures and small grain sizes. This deformation mechanism is well known as *Coble creep* (Coble 1963). Figure 4.1b shows the principle of Coble creep under the assumption of spherical grains which form a polycrystal with sinusoidal grain boundaries (Ray and Ashby 1971). The strain rate induced by the engineering stress $\sigma$ (as boundaries locally experience compression and tension), under the assumption of equal distribution of matter and vacancies at the grain boundaries, can be described by the following equation:

$$\dot{\epsilon}_{C} = \zeta \frac{\pi\delta D_{gb}\sigma\Omega}{d^3 k_b T} \tag{4.2}$$

where $D_{gb}$ is the grain boundary self diffusion coefficient associated with one atomic species (slowest diffusing species) and $\delta$ is the grain boundary thickness. The remaining quantities are defined as in Eq. 4.1.

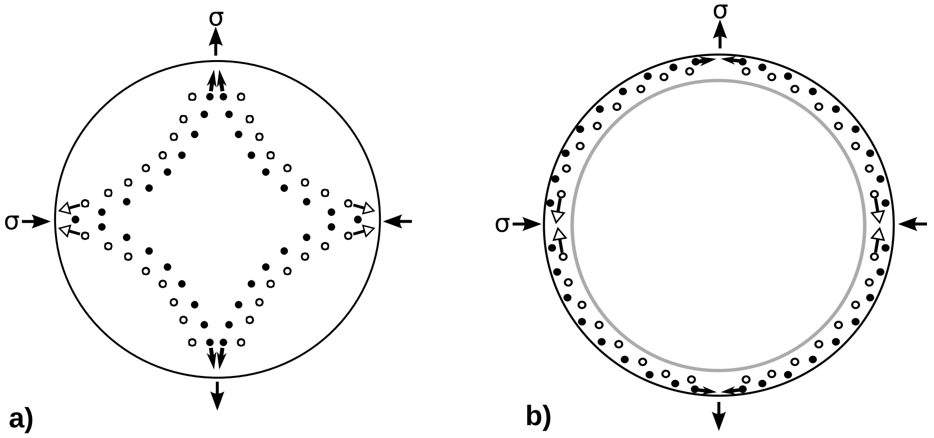

Figure 4.1: *The principle to produce plastic strain in a spherical grain by the following deformation mechanisms: a) Nabarro-Herring creep based on the conjugate bulk diffusion of vacancies (open dots) and matter (solid dots) through the crystal lattice in correspondence to the engineering stress $\sigma$. The arrows indicate the diffusion direction with respect to the engineering stress b) Coble creep that is based on conjugate diffusion of vacancies (open dots) and matter (solid dots) through grain boundaries in correspondence to an applied engineering stress $\sigma$.*

### 4.1.2 Dislocation creep

#### 4.1.2.1 Glide

The intrinsic resistance of the crystal lattice has to be overcome for dislocations to move by glide in high lattice friction silicates, such as the high-pressure phases of the mantle transition zone. Rather than moving as a straight line, a thermally activated dislocation nucleates so-called kink-pairs over the Peierls potential under the action of deviatoric stress. This initiates elementary displacements of dislocation segments after which the propagation of the kinks along the lines will trigger the motion of the complete segments. In case of high lattice friction, the dislocation mobility is mainly controlled by the resolved shear stress dependent enthalpy $\Delta H^{crit}(\tau)$ associated with a critical dislocation bow out over the Peierls potential (Kubin 2013). The relation between the resulting glide mobility and the macroscopic strain rate under steady state conditions as deduced from Orowan's equation equals

$$\dot{\epsilon} = \rho b v = \lambda\sqrt{\rho}\exp\left(-\frac{\Delta H^{crit}(\tau)}{k_b T}\right) \tag{4.3}$$

in which $\lambda$ in $[ms^{-1}]$ is slightly dependent on the resolved shear stress $\tau$, but can be considered as a constant in high lattice friction solids as this is negligible with respect to the stress dependent exponential term (chapter 2.3.4 and 3 and Ritterbex *et al.* 2015). Figure 4.2a shows the principle of dislocation glide by producing plastic strain through thermally activated nucleation of kink-pairs under applied stress.

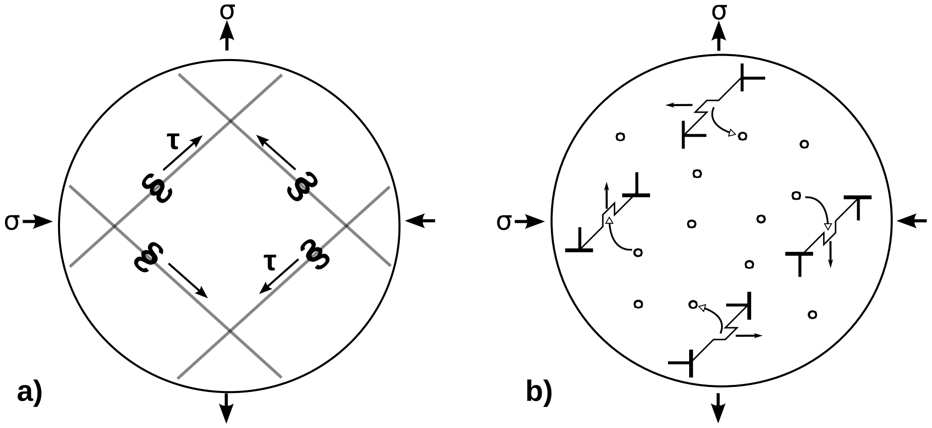

Figure 4.2: *The principle to produce plastic strain in a spherical grain by the following deformation mechanisms: a) glide of dislocations through thermally activated nucleation of kink-pairs under applied stress. Generally, the sluggish glide of screw dislocations will account for most of the plastic strain produced. Screw dislocations belonging to four slip systems are illustrated in one grain. The applied engineering stress is equal to $\sigma$ and $\tau$ corresponds to the resolved shear stress. b) pure climb creep as accomodated by bulk diffusion through the emission and absorption of vacancies (open dots) at jogs along dislocation lines. Pure shear strain can be produced by the coupled motion of edge dislocations belonging to quasi-perpendicular slip systems through the balanced emission and absorption of vacancies in response to an applied stress $\sigma$. The direction of climb with respect to $\sigma$ is indicated by arrows*

#### 4.1.2.2 Climb

Pure dislocation climb involves the conjugate diffusion of vacancies and matter through the crystal lattice, as in the case of Nabarro-Herring creep. Here, however, it is not the crystal surfaces which act as sources and sinks of vacancies but rather the dislocation cores in the bulk of the crystals. Pure dislocation climb is therefore assumed to be controlled by vacancy diffusion through the emission and absorption of vacancies at jogs along the line segments of edge dislocations (Nabarro 1967; Boioli *et al.* 2015). The climb velocity under steady-state conditions can be solved from the diffusion equation under the assumption that the dislocation lines with cylindrical symmetry are saturated with jogs:

$$v_{climb} = \frac{2\pi}{\ln\left(\frac{1}{2\sqrt{\rho}\xi}\right)} \frac{D_{sd}}{b} \left[\exp\left(\frac{\sigma\Omega}{k_b T}\right) - \frac{X_\infty}{X_v}\right] \tag{4.4}$$

where $\xi$ corresponds to the dislocation core width, $b$ is the modulus of the Burgers vector and $\rho$ is the dislocation density. The vacancy concentration far from the dislocation is defined as $X_\infty$ whether the equilibrium vacancy concentration in the crystal bulk is given by $X_v$. Figure 4.2b shows how pure shear strain can be produced by the coupled motion of edge dislocations belonging to quasi-perpendicular slip systems through the balanced emission and absorption of vacancies in response to a compressive and tensile stress respectively. The strain rate produced corresponding to this process under steady-state conditions, by assuming that dislocation multiplication (Bardeen-Herring climb sources) is balanced by a decrease in dislocation density $\rho$ through annihilation events, can thus be derived with the use of Orowan's equation as:

$$\dot{\epsilon}_{climb} = \frac{2\pi\rho}{\ln\left(\frac{1}{2\sqrt{\rho}\xi}\right)} D_{sd} \left[\exp\left(\frac{\sigma\Omega}{k_b T}\right) - 1\right] \tag{4.5}$$

Bardeen-Herring sources are the equivalent of Frank-read dislocation glide sources. In case of climb sources, dislocations are multiplicated through climb of edge dislocations in the presence of point defects around the dislocation core structures. Climb sources were initially proposed by Bardeen and Herring (1952) and later observed in silicon (Ravi 1972). Equation 4.5 corresponds to the condition that the equilibrium vacancy concentration in the crystal bulk is equal to the concentration far from the dislocation as is usually assumed in dislocation dynamics models.

As effective strain producing mechanism, pure climb creep is difficult to observe since dislocation glide is much easier in most cases, so that climb rather acts as recovery mechanism. However, evidence of pure dislocation climb governed deformation can be found in hexagonal crystals, when basal glide is inhibited by loading parallel to the $c$-axis (Edelin and Poirier 1973; Le Hazif *et al.* 1973). Further, pure climb creep is known to occur in quasi periodic crystals, which are complex alloys with an ordered but not periodic crystal lattice. Lattice friction is usually high in quasicrystals due to difficult shear along densely packed planes as a result of crystal symmetries that are forbidden for periodic crystals. Therefore, at high temperature, some quasicrystals deform plastically by pure climb creep since the glide mechanism is too difficult (Mompiou and Caillard 2008). The first natural occurrence of a quasicrystal has been discovered recently by Bindi *et al.* in 2011 and is known as $Al_{63}Cu_{24}Fe_{13}$ icosahedrite.

#### 4.1.2.3 Which dislocation creep mechanism in the transition zone

In contrast to diffusion creep mechanisms that rely purely on the diffusion of vacancies, dislocation creep involves both glide and diffusion controlled climb processes. Dislocation creep at high temperatures was first formulated by Weertman (1955; 1957) and is often referred to as recovery-controlled or climb-controlled dislocation creep (Fig. 4.3). In this framework, plastic strain is considered to be produced by the glide of dislocations that are free to move. Due to glide and hence the activation of dislocation sources, dislocations may interact with each other. Edge dislocations can free themselves by climbing out of their glide planes by the emission or absorption of vacancies at jogs along the lines to be able to produce strain again by glide. The climb process in this case can be seen as a recovery mechanism necessary to maintain steady-state deformation. As screw dislocations cannot move out of their glide planes, they may continue gliding by cross-slip which allows them to change glide planes without the interaction with point defects.

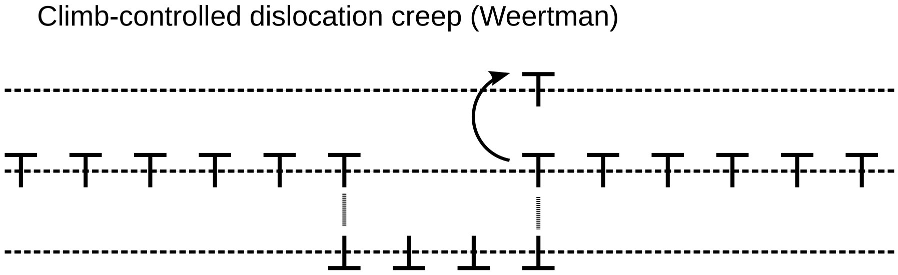

Figure 4.3: *Illustration of the principle of high temperature recovery controlled dislocation creep as introduced by Weertman (1955; 1957). Dislocation glide is activated under the conjugate action of stress and thermal activation that is responsible for the production of plastic strain. The activation of dislocation sources however leads to the multiplication of dislocations interacting with each other that leads to the formation of a mircrostructure, illustrated in this figure by some dipole-dipole interactions. Dislocations are able to free themselves by climbing out of their glide plane by the emission or absorption of vacancies at jogs along the dislocation lines to become mobile. This recovery mechanism enables the freed dislocations to further produce plastic strain by glide to maintain steady-state deformation.*

This recovery-controlled creep mechanism corresponds well to dislocation creep in olivine as shown by Boioli *et al.* (2015). Figure 4.4 shows the ratio of the glide ($\mathrm{v}_{glide}$) versus climb ($\mathrm{v}_{climb}$) velocity in olivine at ambient pressure conditions as a function of engineering stress ($\sigma$) and temperature ($T$). It can be seen that $v_{glide} \gg v_{climb}$ in the complete $\sigma$-$T$ domain. It is therefore the fast glide mechanism that is responsible for producing the plastic strain whereas the slower climb mechanism effectively controls the rate of deformation under steady-state conditions as described by Weertman (1955).

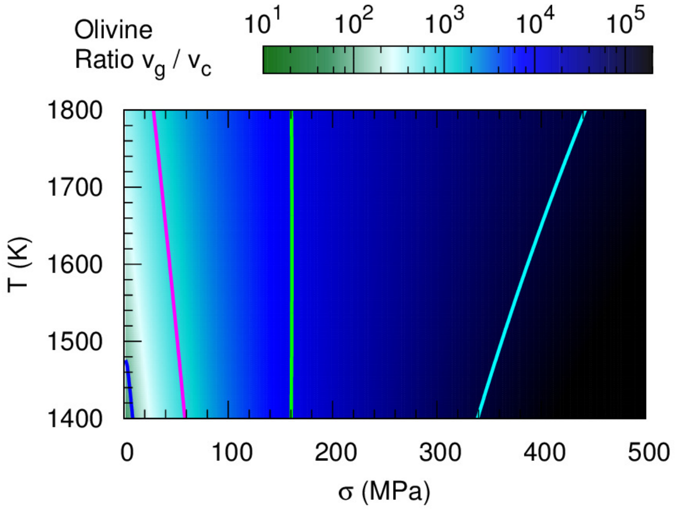

Figure 4.4: *The ratio of the glide versus the climb velocity* $v_{glide}/v_{climb}$ *as function of engineering stress* $\sigma$ *and temperature* $T$ *for olivine under ambient pressure conditions. The glide and climb mobilities are calculated with respect to the* [100](010) *slip system (Boioli* et al. *(2015).*

Coming back to the transition zone minerals, the ratio between the glide and climb velocities $\mathrm{v}_{glide}/\mathrm{v}_{climb}$ for the easiest slip sytems in wadsleyite at 15 GPa and ringwoodite at 20 GPa has been mapped out as a function of engineering stress $\sigma$ and $T$ in a similar way as in olivine by using the 2.5-D dislocation dynamics code as in Boioli *et al.* (2015). The Si self-diffusion coefficients $D_{sd}$ are taken from Shimojuku *et al.* (2009) for ringwoodite and from Shimojuku *et al.* (2010) for wadsleyite (tables 4.1 and 4.2). It can be seen in Fig. 4.5, that the $\mathrm{v}_{glide}/\mathrm{v}_{climb}$ ratio in both high-pressure polymorphs of olivine are completely opposite to those in olivine itself: the climb velocity is always significantly larger than the glide velocity ($v_{glide} \ll v_{climb}$) in the $\sigma$-$T$ domain appropriate to mantle conditions. This demonstrates the efficiency of the climb mechanism to produce plastic strain with respect to the glide mechanism in wadsleyite and ringwoodite under transition zone conditions. The main reason is the high lattice friction necessary to overcome for the dislocation to move by the nucleation of kink-pairs at conditions of the transition zone. This implies that the coupled interaction between the glide and climb mechanism in recovery-controlled dislocation creep as formulated by Weertman (1955) is not valid anymore. Both glide and climb processes will be decoupled in wadsleyite and ringwoodite. We suggest that dislocation glide is not likely to operate in the high-pressure polymorphs of olivine under the conditions of the transition zone. Instead, dislocation climb would be the main strain producing mechanism and has to be considered as an effective deformation mechanism rather than a recovery process: pure climb creep.

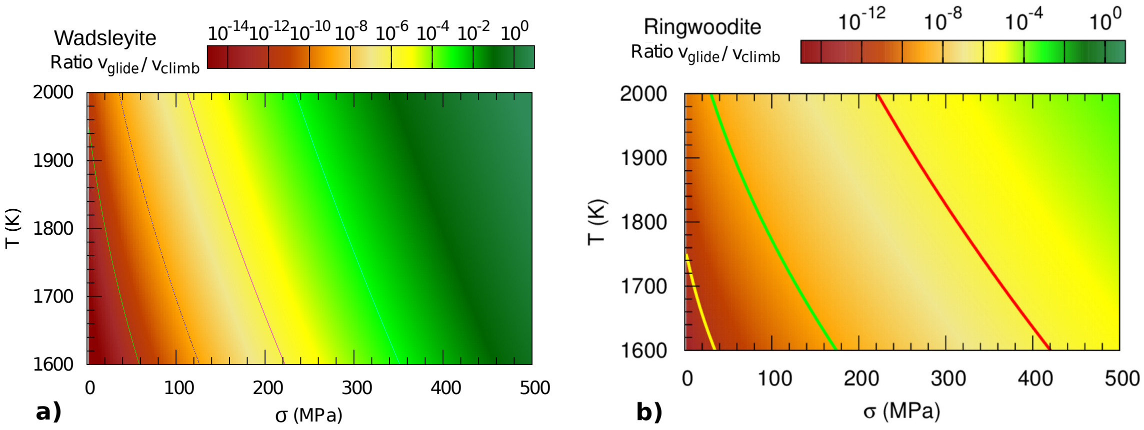

Figure 4.5: *The ratio of the glide versus climb velocity* $v_{glide}/v_{climb}$ *as a function of enineering stress* $\sigma$ *and temperature* $T$ *for: a) wadsleyite at* 15 *GPa. The glide and climb mobilities are calculated with respect to the easiest to the* $^1/_2\langle 111\rangle\{101\}$ *slip system and b) ringwoodite at* 20 *GPa. The glide and climb mobilities are calculated with respect to the easiest to the* $^1/_2\langle 110\rangle\{110\}$ *slip system.*

## 4.2 Deformation mechanism maps

### 4.2.1 How to build a deformation mechanism map?

Deformation mechanism maps are typically drawn in 2-D space that spans the stress ($\sigma$), temperature ($T$) and grain size ($d$) to map the predominance of different deformation mechanisms considered (*i.e.* the ones operating under the lowest stress) under steady-state flow conditions at constant strain rates.

Having the constitutive equations in terms of the $\sigma$-$\dot{\epsilon}$ relations of the different potential deformation mechanisms, the minimum stress contours in a for example $\sigma$-$d$ or $\sigma$-$T$ space identify which mechanism provides the largest contribution to the strain rate (*i.e.* the lowest stress necessary to produce plastic deformation by a given steady-state strain rate).

In this section, deformation mechanism maps for the transition zone minerals will be constructed in a $\sigma$-$d$ space showing isothermal contours since the temperature range over which the minerals in the transition zone are stable is very constrained. The deformation mechanisms that are considered involve diffusion creep versus dislocation creep as has been discussed above: Nabarro-Herring and Coble creep will be considered for the pure diffusional mechanisms as well as dislocation glide and climb which can be associated with dislocation creep.

### 4.2.2 Diffusion coefficients

Both Nabarro-Herring creep and pure climb creep are assumed to be activated at high temperature and therefore potentially important in plastic deformation of wadsleyite and ringwoodite in the transition zone. Both deformation mechanisms involve the diffusion of vacancies and matter through the crystal lattice. Coble creep may play a role in case of small grain sizes (*e.g* nucleation of new grains during phase transformation). A description of the strain rate produced by those mechanisms depends on the self-diffusion coefficients (Eq. 4.1, 4.2 and 4.5):

$$D = D_v X_v = D_0 \exp\left(-\frac{\Delta E}{k_b T}\right) \tag{4.6}$$

where $D$ is the diffusion coefficient (*e.g.* self-diffusion or grain boundary self-diffusion coefficient), $D_0$ is a pre-exponential factor, $\Delta E$ is the activation enthalpy barrier to overcome during diffusion, $k_b$ is the Boltzmann constant and $T$ is the absolute temperature. The vacancy diffusion coefficient is given by $D_v = \exp(-\Delta H_m/k_b T)$ which depends on the migration enthalpy of vacancy diffusion $\Delta H_m$.

Vacancy diffusion in high-pressure silicates involves different ionic species. Experimental studies at high pressure and temperature (Shimojuku *et al.* 2004; Shimojoku *et al.* 2009; Shimojuku *et al.* 2010; Zhang *et al.* 2011 and Holzapfel *et al.* 2009) have shown that Si is the slowest diffusion species in wadsleyite and ringwoodite. The self-diffusion coefficients of Fe-Mg interdiffusion are not shown as they are found to be much larger than those for Si and O (*e.g.* Holzapfel *et al.* 2009). As such, Fig. 4.6 incorporates all relevant data available on the atomic self-diffusion in ringwoodite and wadsleyite. Apart from the fact that Si is the slowest diffusion species at transition zone temperatures between 1600-1900 K, more interesting is the similarity between the self-diffusion coefficients $\mathrm{D}_{sd}$ for the different species in the different phases under those temperature conditions as being the result of different experiments, given the dependency of the equilibrium bulk vacancy concentration $\mathrm{X}_v$ on $D$ (Eq. 4.6). Grain boundary self-diffusion coefficients in wadsleyite and ringwoodite are found to be smallest for the Si species as well (table 4.1). Tables 4.1 and 4.2 give an overview of the available experimental data on the diffusion coefficients of Si and O species in wadsleyite and ringwoodite. Given the latter results, we will assume that diffusion processes in wadsleyite and ringwoodite will be controlled by the migration of Si as slowest diffusing species. The available data further suggests that the rate limiting diffusivities in wadsleyite and ringwoodite are comparable without much variation under the appropriate temperature conditions.

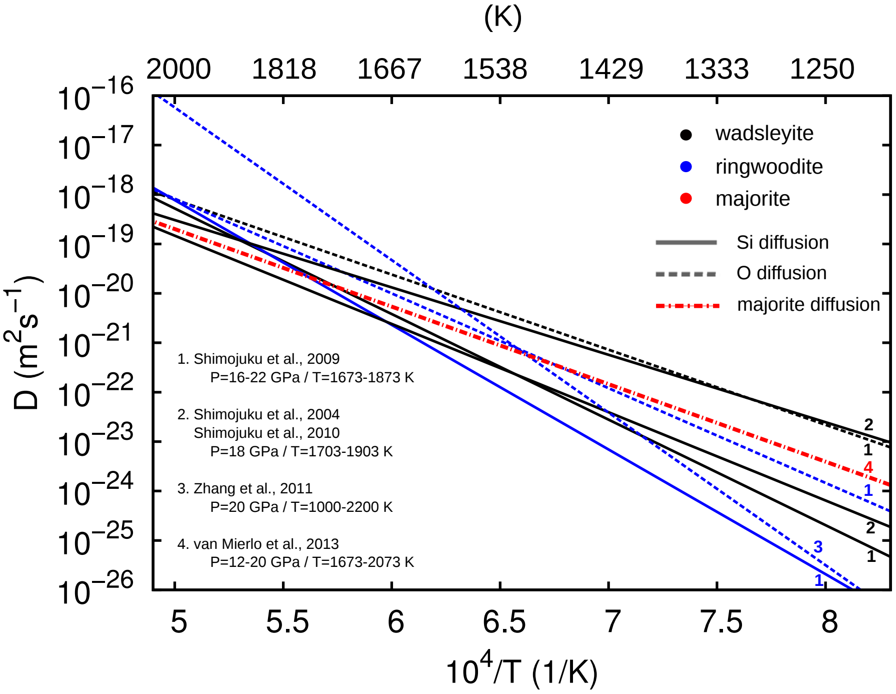

Figure 4.6: *Arrhenius plot showing the self-diffusion coefficients* $D_{sd}$ *of Si, O and* $Mg_4Si_4O_{12}$ *majorite in wadsleyite, ringwoodite and a majorite-pyrope diffusion couple. Colors indicate the different mineral phases. Different line characters (solid, dotted) indicate the different diffusing species.*

| Species/phase | $D_{0,sd}$ $(m^2/s)$ | E $(KJ/mol)$ |
|---|---|---|
| Si<br>wadsleyite<br>1673-1873 K<br>16 GPa<br>Shimojuku et al. 2009 | 2.51 $10^{-8}$ | 409 |
| Si<br>wadsleyite<br>1703-1903 K<br>18 GPa<br>Shimojuku et al. 2010 (2004) | 2.00 $10^{-12}$ | 261 |
| Si<br>wadsleyite<br>1673-1873 K<br>18 GPa<br>Shimojuku et al. 2010 | 1.26 $10^{-10}$ | 342 |
| O<br>wadsleyite<br>1673-1873 K<br>16 GPa<br>Shimojuku et al. 2009 | 3.16 $10^{-11}$ | 291 |
| Si<br>ringwoodite<br>1673-1873 K<br>22 GPa<br>Shimojuku et al. 2009 | 3.16 $10^{-6}$ | 483 |
| O<br>ringwoodite<br>1673-1873 K<br>22 GPa<br>Shimojuku et al. 2010 (2004) | 3.16 $10^{-9}$ | 367 |
| $Mg_4Si_4O_{12}$ component<br>majorite<br>1673-2073 K<br>12-20 GPa<br>van Mierlo et al. 2013 | 1.4 $10^{-11}$ | 214 (15 GPa)<br>300 (18 GPa) |

Table 4.1: *Comparison between experimental data available of the self-diffusion coefficients* $D_{sd}$ *of Si, O and* $Mg_4Si_4O_{12}$ *diffusion in wadsleyite, ringwoodite and a pyrope-majorite diffusion couple at different pressure and temperature conditions.*

| Species/phase | $\delta D_{0,gb}$ $(m^3/s)$ | E $(KJ/mol)$ |
|---|---|---|
| Si<br>wadsleyite<br>1673-1873 K<br>16 GPa<br>Shimojuku et al. 2009 | 1.26 $10^{-15}$ | 327 |
| Si<br>wadsleyite<br>1703-1903 K<br>18 GPa<br>Shimojuku et al. 2010 (2004) | 1.58 $10^{-17}$ | 257 |
| Si<br>wadsleyite<br>1673-1873 K<br>18 GPa<br>Shimojuku et al. 2010 | 1.00 $10^{-20}$ | 159 |
| O<br>wadsleyite<br>1673-1873 K<br>16 GPa<br>Shimojuku et al. 2009 | 1.58 $10^{-17}$ | 244 |
| Si<br>ringwoodite<br>1673-1873 K<br>22 GPa<br>Shimojuku et al. 2009 | 6.31 $10^{-14}$ | 402 |
| O<br>ringwoodite<br>1673-1873 K<br>22 GPa<br>Shimojuku et al. 2009 | 7.94 $10^{-18}$ | 246 |

Table 4.2: *Comparison between experimental data available of the grain boundary self-diffusion coefficients $D_{gb}$ of Si and O diffusion in wadsleyite and ringwoodite at different pressure and temperature conditions.*

### 4.2.3 Deformation mechanism maps: wadsleyite and ringwoodite

Based on the available Si diffusion coefficients in wadsleyite and ringwoodite, we are able to construct deformation mechanism maps regarding Nabarro-Herring creep, Coble creep and pure climb creep according to Eq. 4.1, 4.2 and 4.5. The average vacancy formation volume $\Omega$ associated with a complete structural defect unit is about 60 $\text{Å}^3$ for $Mg_2SiO_4$ wadsleyite and ringwoodite as calculated from their unitcells at transition zone pressures.

The plastic contribution of dislocation glide as modelled in this work (chapter 3) will be used. Equation 4.3 relates the plastic strain rate to the resolved shear stress $\tau$ with respect to dislocations belonging to single slip systems. We therefore consider, as already mentionned in chapter 3, $\sigma = 2\tau$ (maximum of the Schmid factor) to account for the fact that only a fraction of (engineering) stress is resolved in the direction of dislocation motion (Fig 4.2a). The constitutive relations associated with dislocation motion (Eq. 4.3 and 4.5) depend on the engineering stress $\sigma$ and the dislocation density $\rho$. To have a self-consistent set of equations, we assume the dislocation density $\rho$ to be a function of the yield stress $\sigma$ to activate a dislocation source (Knight and Burton 1989; Mordehai *et al.* 2008; Hirth and Lothe 1992):

$$\sigma = \frac{\mu b}{L} = \mu b \sqrt{\rho} \rightarrow \rho = \left(\frac{\sigma}{\mu b}\right)^2 \tag{4.7}$$

where $\mu$ corresponds to the shear modulus, $\rho$ to the dislocation density and $L$ to the length of the dislocation lines $L = 1/\sqrt{\rho}$. In the high-pressure silicates of the transition zone for which $\mu \sim$150 GPa and $b \simeq 5$ Å, Eq. (4.7) leads to the following relation between dislocation density and the engineering stress: $\rho \simeq 10^{-4}\sigma^2$.

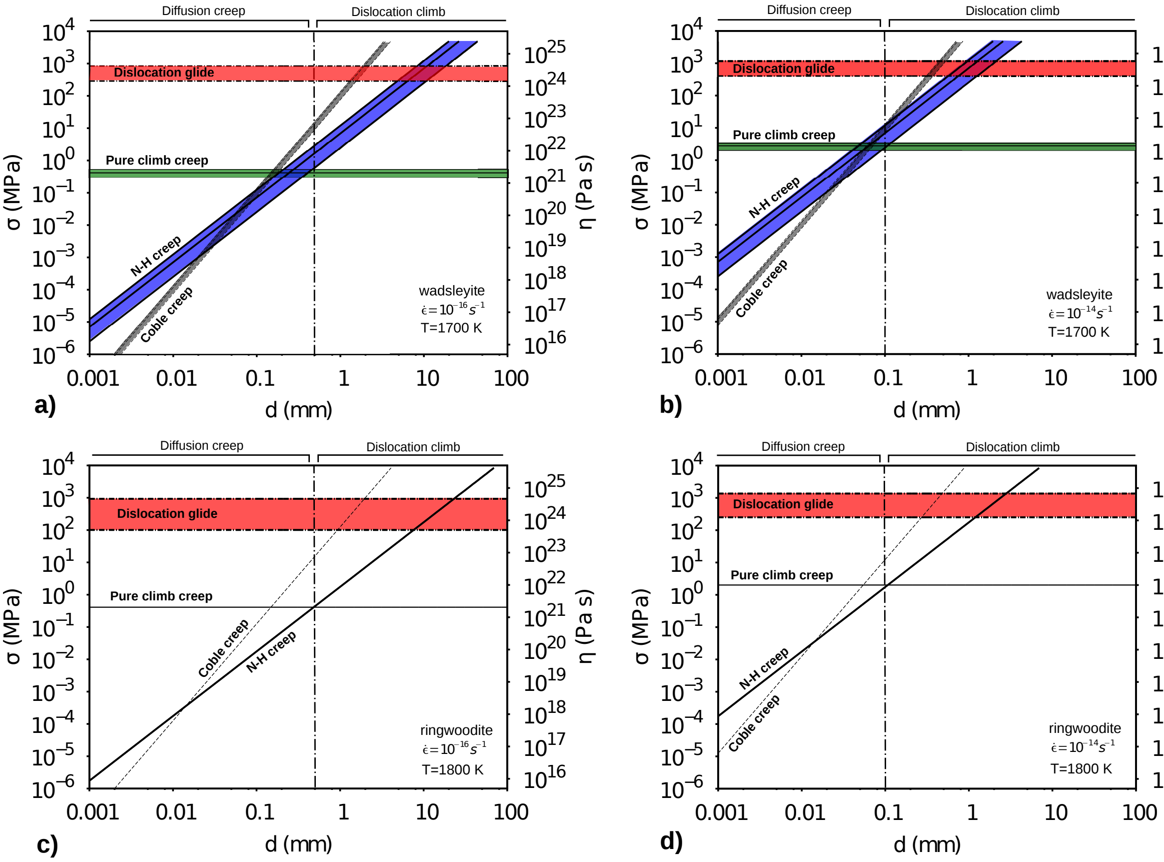

Figure 4.7: *Deformation mechanism maps associated with steady state deformation in: a) Wadsleyite at* 1700 *K with* $\dot{\epsilon} = 10^{-16}$ $s^{-1}$. *Pure dislocation glide is parametrized by single slip of the rate controlling* $\frac{1}{2}\langle 111\rangle\{101\}$ *and* $[100](010)$ *screw dislocations. The diffusion based accomodated mechanisms are parametrized with respect to three Si diffusion coefficients D (Eq. 4.6) available from experimental data (table 1 and 2). The engineering stress and resolved shear stress are given by* $\sigma$ *and* $\tau$ *respectively, where* $\sigma = 2\tau$ *is considered (maximum of the Schmid factor) to account for the fact that only a fraction of principle stress is resolved in the direction of dislocation motion. Viscosity* $\eta$ *has been calculated as* $\sigma/2\dot{\epsilon}$ *and d corresponds to the mean grain size. b) Wadsleyite at* 1700 *K with* $\dot{\epsilon} = 10^{-14}$ $s^{-1}$. *c) Ringwoodite at 1800 K at* $\dot{\epsilon} = 10^{-16}$ $s^{-1}$. *Pure dislocation glide is parametrized by single slip of the rate controlling* $\frac{1}{2}\langle 110\rangle\{110\}$ *and* $\frac{1}{2}\langle 110\rangle\{111\}$ *screw dislocations. The diffusion based accomodated mechanisms are parametrized with respect to the Si diffusion coefficients D available from experimental data (table 4.1 and 4.2). d) Ringwoodite at* 1700 *K with* $\dot{\epsilon} = 10^{-14}$ $s^{-1}$.

Figure 4.7 a and c shows the deformation mechanism maps for wadsleyite (at 15 GPa) at 1700 K and ringwoodite (at 20 GPa) at 1800 K under steady-state strain rate conditions of $\dot{\epsilon} = 10^{-16}$ $s^{-1}$. The different band widths in relation to the diffusion dependent deformation mechanisms are constrained by the data of Si self- and grain boundary self-diffusion coefficients as given in table 4.1 and 4.2. The band widths shown in relation to pure dislocation glide are the result of different single slip constitutive equations with respect to the rate controlling dislocations: $^1/_2\langle 111\rangle\{101\}$ and [100](010) screw dislocations in wadsleyite (chapter 3.1) and the $^1/_2\langle 110\rangle\{110\}$ and $^1/_2\langle 110\rangle\{111\}$ screw dislocations in ringwoodite (chapter 3.2). It has to be mentioned that the constitutive equations (Eq. 4.3 and 4.5) at high stress $\sigma$ become insensitive to the dislocation density $\rho$, as is the case for dislocation glide. The results for glide as shown in Fig. 4.7 have therefore to be understood as lower bounds. From the ratio of the glide velocity versus the climb velocity ($\mathrm{v}_{glide}/\mathrm{v}_{climb}$) in both high-pressure polymorphs of olivine, we already inferred the inefficiency of the glide mechanism to produce plastic strain in comparison to the climb mechanism. The deformation mechanism maps as shown in Fig. 4.7 confirm the latter by a significant difference in the stress contours between the climb and the glide mechanism (even as lower stress bound): $<1\%$ of $\sigma$ necessary to reach steady-state deformation at $\dot{\epsilon} = 10^{-16}\ s^{-1}$ by pure dislocation glide is already sufficient to produce the same plasticity by pure dislocation climb. This again underlines the inefficiency of dislocation glide with respect to the climb mechanism. This implies that dislocation creep in wadsleyite and ringwoodite under transition zone conditions is likely to be governed by the climb mechanism: pure climb creep.

One can observe that if the grain size $d < 0.5$ mm, diffusion creep processes will slowly take over as primary deformation mechanisms, where Coble creep at very small grain sizes will become dominant over Nabarro-Herring creep. Nevertheless, for $d > 0.5$ mm, we suggest that pure climb creep will be the dominant deformation mechanism in wadsleyite and ringwoodite under the appropriate mantle conditions. We would like to mention the striking similarity between the efficiency of the strain producing mechanisms and their grain size dependency for wadsleyite and ringwoodite with respect to the available data.

Figure 4.7b and d show the deformation mechanism maps for wadsleyite and ringwoodite (as in Fig. 4.7a and c), but under enhanced steady-state strain rate conditions of $\dot{\epsilon} = 10^{-14}\ s^{-1}$. One may think of its importance around the ongoing subduction of slabs that penetrate through the transition zone. It can be seen that the main features as discussed with respect to $\dot{\epsilon} = 10^{-16}\ s^{-1}$ remain the same: 1) similarity between the deformation mechanism maps at conditions of $\dot{\epsilon} = 10^{-14}\ s^{-1}$. 2) Decoupling between dislocation glide and climb mechanisms. The threshold grain size $d$ above which pure dislocation climb is the most dominant mechanism shifts to slightly lower values ($d > 0.1$ mm) in both phases. For both dislocation glide and pure climb creep, larger stresses correspond to lower viscosities than at a rate of $\dot{\epsilon} = 10^{-16}\ s^{-1}$. Because of the stress dependence of the line segments $L$ via the dislocation density $\rho(\sigma)$, dislocation climb is not purely Newtonian, even at low stresses. Nevertheless, the same orders of magnitude of stress and viscosities are found in comparison to Fig. 4.7a and c for both the glide and climb mechanisms.

### 4.2.4 Extension to majorite garnets

#### 4.2.4.1 Plastic deformation experiments

Wadsleyite and ringwoodite are estimated to represent the largest volume fraction of the transition zone in the order of about 60%. However, majorite garnet is another major mineral phase that is assumed to represent the bulk remaining 40% of volume fraction of the transition zone.

A handful of studies are available on deformation experiments of garnets, in particular on majorite garnet, to investigate its mechanical behaviour at high pressure conditions. In 2000, Kavner *et al.* performed compression experiments using the diamond anvil cell (DAC) at ambient temperature conditions. They show that majorite was able to support shear stresses of at least $2-3$ GPa at pressure conditions between $7-11$ GPa. Further measurements on grossular garnet deformed in the DAC at ambient temperatures indicate engineering stresses of 4.1 GPa at a pressure of 15.7 GPa (Kavner 2007) under typical laboratory strain rates ($\sim 10^{-5}$ s$^{-1}$). The latter results would be in agreement by extrapolation of the stress measurements as obtained by Kavner *et al.* (2000) at pressures between $7-11$ GPa (under which condition the same results are obtained on grossular garnet) to pressures of $15-19$ GPa at ambient temperatures. Karato *et al.* (1995) performed hot indentation tests for which the extrapolation in homologous temperature of the collected data down to 0 K led to a stress $\sigma_p = 14.8$ GPa. By using the same extrapolation as Karato *et al.* (1995), Kavner *et al.* (2000) have estimated a stress of $\sigma_p = 9.5-10.7$ GPa for majorite at a pressure of $\sim 9$ GPa at 0 K. Stress-relaxation experiments on a pyrope-majorite solid solution by Hunt *et al.* (2010) using the D-DIA and T-cup show initial stresses of 2.5 GPa at a pressure of 12.9 GPa at $T = 900$ K. This result at low temperature is in relatively good agreement with results obtained at ambient temperature conditions as inferred form the DAC-studies. Weidner *et al.* (2001) performed further stress-relaxation experiments using a multi-anvil high pressure apparatus and suggest that the relative strength of majorite-rich garnet is comparable to the relative strength of wadsleyite at $T = 900$ K (and slightly softer than ringwoodite) and decreases at higher temperatures. The stress of majorite-rich garnet at this temperature is estimated to be 3 GPa. Unfortunately, no deformation experiments (RDA, D-DIA, DAC) were performed on majorite garnet at transition zone conditions of a pressure around 18 GPa and temperatures of 1800 K to determine its mechanical behaviour. However, the low-$T$ results of the stress-relaxation experiments support the stress measurements from both real deformation experiments at ambient temperature on majorite and grossular garnet of Kavner *et al.* (2000) and Kavner (2007) respectively. A comparison of a stress of $\sigma_{maj} = 4$ GPa ($P = 15$ GPa) at ambient temperature (300 K) with experimental data and our results obtained for ringwoodite (Fig. 3.29)

($\sigma_{ring} \simeq 10$ GPa) implies that majorite would be significantly softer at those conditions. Nevertheless, comparing those results to wadsleyite (Fig. 3.15) ($\sigma_{wad} \simeq 5.5$ GPa, as a mean value of both slip systems) suggest more comparable plastic behaviour associated with dislocation glide (as favored under these conditions) from our theoretical results at typical laboratory strain rates ($\sim 10^{-5}$ s$^{-1}$). By taking into account $\tau_p = \sigma_p/2$, the Peierls stress as estimated by Kavner *et al.* (2000) would be equal to $\tau_p = 5$ GPa for dislocation slip in majorite garnet at pressure conditions of the Earth's transition zone. This is similar to Peierls stresses calculated for the easiest slip systems in wadsleyite: 3.5 GPa for [100](010) and 4.8 GPa for the more difficult $1/2\langle 111\rangle\{101\}$ screw dislocations. Since high lattice friction in wadsleyite extends to the appropriate conditions of the transition zone, we propose the Ansatz that lattice friction in majorite garnet may be comparably high under those conditions.

Despite the lack of constitutive relations for the rate controlling dislocations in majorite, evidence of high resistance to dislocation glide has also been observed in transmission electron microscope (TEM) characterizations of microstructures developed in majorite garnet during high pressure and temperature deformation using the multi-anvil apparatus (Couvy *et al.* 2011). They suggest the activation of $1/2\langle 111\rangle$ and $\langle 100\rangle$ dislocations and the importance of dislocation climb under transition zone conditions due to the appearance of subgrain boundaries. Other work on plastic deformation of silicate garnets (Cordier *et al.* 1996; $^a$Voegelé *et al.* 1998; $^b$Voegelé *et al.* 1998) and shock veins in majorite garnet (Voegelé *et al.* 2000) support the main conclusion of Couvy *et al.* (2011) by large scale observations of dislocation junctions and subgrain boundaries. Latter observations indicate the evidence for activation of dislocation climb in majorite garnet, even under laboratory conditions ($< 1700$ K). This is in line with theoretical results that demonstrate high lattice friction as opposed to glide in high-pressure silicates of the Earth's mantle as shown in this and other related work (Ritterbex *et al.* 2015;

Ritterbex *et al.* (in press); Kraych *et al.* 2016). We therefore postulate the likelihood of high lattice friction in majorite garnet under natural conditions, comparable to the high-pressure polymorphs of olivine. In that case, a decoupling between the glide and climb mechanism in the framework of dislocation activity can be expected in majorite. Under this hypothesis, the contribution of pure climb creep to the overall plasticity of majorite in conditions of the Earth's transition zone would become of interest to quantify.

#### 4.2.4.2 Deformation mechanism maps: majorite garnet

Based on the $Mg_4Si_4O_{12}$ majorite self-diffusion in a pyrope-majorite diffusion couple studied by van Mierlo *et al.* (2013), the $Mg_4Si_4O_{12}$ self-diffusion coefficient $D_{sd}$ as a function of the inverse temperature $T$ is shown in Fig. 4.6. This has been used to construct the deformation mechanism maps regarding Nabarro-Herring creep and pure climb creep according to Eq. 4.1 and 4.5. The average vacancy formation volume $\Omega$ associated with a complete structural defect unit is equal to 70 $Å^3$ in $Mg_4Si_4O_{12}$ majorite as calculated from its unitcell at 18 GPa.

Figure 4.8 shows the deformation mechanism maps for majorite ($P$=18 GPa) at 1800 K under both steady-state strain rate conditions of $\dot{\epsilon} = 10^{-16}\ s^{-1}$ and $\dot{\epsilon} = 10^{-14}\ s^{-1}$. We would like to note the striking similarities between the deformation mechanism maps of majorite and those of the high-pressure polymorphs of olivine. These analogous findings support once more the potential decoupling between the glide and climb mechanisms in majorite garnet under natural conditions. The potential importance of pure climb creep can be seen above an average grain size of $d > 0.5$ mm at $\dot{\epsilon} = 10^{-16}\ s^{-1}$, which may shift gradually towards diffusional creep at lower grain sizes. The enhanced strain rate of $\dot{\epsilon} = 10^{-14}\ s^{-1}$ leads to a smaller grain size threshold $d > 0.1$ mm above which pure climb creep becomes a potential important deformation mechanism in majorite under conditions of the transition zone.

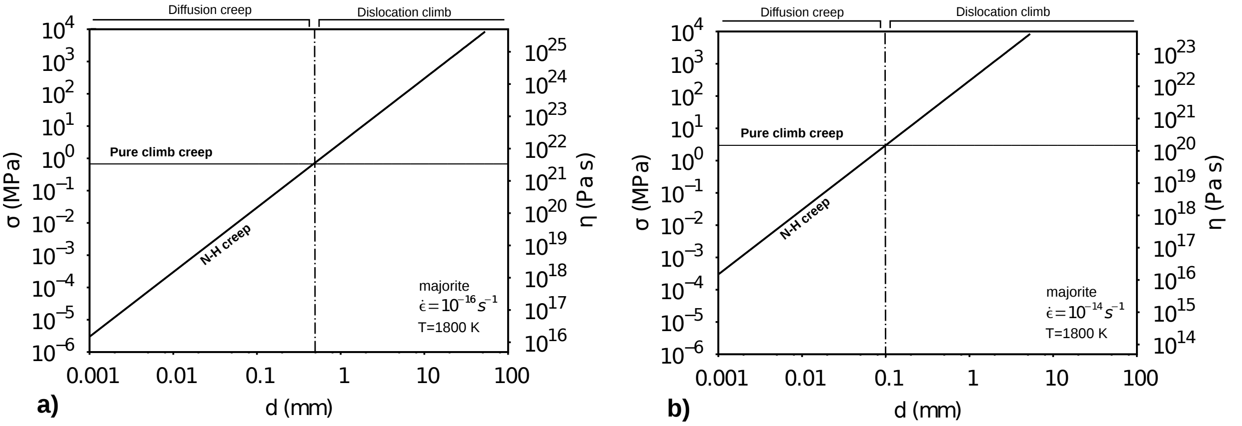

Figure 4.8: *Deformation mechanism maps associated with steady state deformation in majorite at 1800 K at: a)* $\dot{\epsilon} = 10^{-16}$ $s^{-1}$ *and b)* $\dot{\epsilon} = 10^{-14}$ $s^{-1}$*. The diffusion based accomodated mechanisms are parametrized with respect to the* $Mg_4Si_4O_{12}$ *self diffusion coefficient in a pyrope-majorite diffusion couple provided by van Mierlo* et al. *(2013) (table 4.1).*

## 4.3 Discussion

High values of the $CRSS(T)$ regarding pure single slip dislocation glide in wadsleyite and ringwoodite under natural conditions as inferred from the main study of this work, suggest that other mechanisms may control the deformation of minerals in the Earth's transition zone. By taking into account vacancy diffusion related deformation mechanisms, we finally have produced deformation mechanism maps for wadsleyite and ringwoodite regarding the strain producing efficiency of dislocation creep versus diffusion creep under natural conditions. Based on the appropriate defect mobilities, the maps clearly show a decoupling of dislocation glide and climb in wadsleyite and ringwoodite, suggesting the importance of pure climb creep as a potential dominant deformation mechanism for average grain sizes of $d > 0.5$ mm under typical steady state mantle strain rate conditions of $\dot{\epsilon} = 10^{-16}$ $s^{-1}$. An enhancement of the creep rate shows an insignificant reduction in the threshold grain size ($d > 0.1$ mm) above which pure climb creep is a potential dominant deformation mechanism. Below this grain size, the dominant deformation mechanism will gradually shift towards diffusional creep processes as may be important in relation to the nucleation of new grains during phase transformations as present in the Earth's transition zone (apart from any other deformation mechanisms that have not been included so far). The work has been extended to incorporate majorite garnet based on results of experimental studies. From these studies we propose that high lattice friction, opposed to dislocation glide, could be expected under natural conditions. The deformation mechanism maps for majorite are comparable to what has been found for wadsleyite and ringwoodite, which suggests the importance of pure climb creep under transition zone conditions.

### 4.3.1 Limitations of the model

Constitutive equations of the diffusion dependent deformation mechanisms (Nabarro-Herring creep, Coble creep, dislocation climb) depend on the diffusivity of the rate controlling species. This in turn, is sensitive to the crystal chemistry (*e.g.* presence of $Fe^{3+}$, Al, H, *etc.*) regarding the Mg end-members of wadsleyite and ringwoodite as well as for majorite. This may be important since both high-pressure polymorphs of olivine, and certainly wadsleyite, are besides the general presence of "impurities", potentially able to bear significant volume fractions of water (Inoui *et al.* 1995; Chen *et al.* 1998; Huang *et al.* 2005; Pearson *et al.* 2014). Yet, so far, the effect of hydrogen and iron concentrations on the diffusion coefficients of wadsleyite and ringwoodite is expected to be limited within one order of magnitude (Fig. 4.6) at the appropriate temperatures as inferred from experiments (Shimojuku *et al.* 2009; Shimojuku *et al.* 2010). We further want to emphasize the fact that even the diffusion coefficients related to different atomic species within the different phases as experimentally determined (Fig. 4.6 and table 4.1 and 4.2) do not show large variations. It nevertheless has to be mentioned that the number of studies and method approaches are too limited to draw any strong conclusive constraints on the influence of impurities on the diffusion coefficients of diffusing species.

At the same time, the diffusion of point defects in mantle silicates depend strongly on the mechanism of point defect diffusion (*i.e.* the effective diffusion paths associated with diffusing a complete structural unit. The latter once more depends on the local atomic scale electrostatics as well as on elasticity and their mutual influence). The constitutive equations used to construct the deformation mechanism maps are based upon simple effective mobility laws. All together, this suggests that the results obtained regarding the diffusional mechanisms therefore have to be interpreted in terms of orders of magnitude.

The situation is different regarding the effect of impurities on dislocation glide based plasticity. Here, the first point to address is whether or not the presence of impurities may significantly influence the mobility (*i.e.* kink-pair nucleation processes) of the rate controlling dislocations in $Mg_2SiO_4$ wadsleyite and ringwoodite. In other words, it remains questionable whether there may or may not be an influence of the presence of impurities on the nucleation and propagation of kink-pairs in or in the vicinity of the dislocation cores at the atomic scale. If this would be the case, it is not clear how this (local) effect translates to the overall (macroscopic) plasticity due to thermally activated glide, given the relatively large critical enthalpies for kink-pair nucleation $\Delta H^{crit} > 10$ eV as determined at low stress conditions in both high-pressure polymorphs of olivine. It is namely the stress dependence of these nucleation enthalpies that determines the average dislocation mobilities as discussed in chapter 2 and 3. These fundamental questions however are beyond the scope of our study. Nevertheless, given the significant critical enthalpies ($\Delta H^{crit} > 10$ eV) inferred for kink-pair nucleation at low stress in $Mg_2SiO_4$ wadsleyite and ringwoodite at natural conditions, we suggest that dislocation glide is likely to be largely inhibited in wadsleyite and ringwoodite in the Earth's transition zone. Experimental study on deformation of silicate garnets, as discussed above, let us suggest that this may be equally the case in majorite.

### 4.3.2 Implications on the rheology of the transition zone

The Earth's transition zone is characterized by a number of phase transitions. These phase transitions will occur over a certain depth range depending on the nature and kinetics of the phase tranformations (mainly olivine → wadsleyite, wadsleyite → ringwoodite and pyroxene → majorite). The average grain size $d$ in these "transformation regions" can be lower than for the rest of the transition zone region (grain size reduction due to nucleation of new grains), which because of the high temperature conditions, cannot be expected to be extremely small. We therefore suggest that pure climb creep is a potentially important plastic deformation mechanism in the transition zone away from those transformation regions. As inferred from Fig. 4.7 and 4.8, this would result in an average viscosity expected around $1 \times 10^{21}$ Pa s, depending on the strain rate, which is comparable to the early Haskell mantle estimate of $10^{21}$ Pa s (Haskell 1937). Nevertheless, we want to note that this value depends on the self-diffusion coefficients $D_{sd}$ as inferred from experiments which may vary due to water content and chemical heterogeneities in the Earth's mantle: $D_{sd}$ depends on the bulk vacancy concentration $X_v$ (Eq. 4.6) which, in an extrinsic regime, is related to the chemistry (*e.g.* the redox state of the mantle, *etc.*) of the transition zone.

A strong depth dependence of the rheology of the Earth's transition zone apart from the transformation regions cannot be expected based on the similarity of plastic behaviour of wadsleyite, ringwoodite and what can be expected for majorite under natural conditions regarding the mechanisms taken into account. Nevertheless, local variations in the transition zone's rheology cannot be completely excluded especially given the presence of the phase transformations. Grain size dependent Nabarro-Herring and Coble creep tend to become progressively important for $d < 0.5$ mm in all high pressure silicates considered. Grain boundary related deformation mechanisms as for instance disclination activity (Cordier *et al.* 2014) or grain boundary sliding (GBS) may under these conditions become active as well. Besides, also water weakening processes may occur due to the water bearing capacity of wadsleyite and ringwoodite (Chen *et al.* 1998; Huang *et al.* 2005) associated with diffusion accomodated deformation mechanisms. All this can lead to various radial and/or lateral low viscosity regions depending on the average grain size $d$ to expect.

In addition, the presence of phase tranformations may also give rise to another deformation mechanism in the transformation regions: transformation plasticity, also sometimes referred to as transformational superplasticity (Greenwood and Johnson 1964; Poirier 1982; Paterson 1983). Nevertheless, it can be expected that grain growth processes are favored under high temperature and low strain rate conditions of the transition zone. We like to mention that pure climb creep in the high-pressure transition zone silicates would still be the dominant deformation mechanism for average grain sizes of $d \simeq 0.5$ mm. Therefore, as can be seen from Fig. 4.7 and 4.8, it is not expected that diffusion creep accomodated deformation in the transformation regions would lead to anomalously large viscosity contrasts with respect to the average of $1 \times 10^{21}$ Pa s at $d > 0.5$ mm.

### 4.3.3 Comparison to observables

The above implications show that the average viscosity of the transition zone is not expected to exceed $> 10^{22}$ Pa s. This corresponds well with respect to the order of magnitude ($10^{21}$-$10^{22}$ Pa s) expected as calculated from global joint inversion by Ricard and Wuming (1991) and Mitrovica and Forte (2004). Phase transformations may even lead to regions that exhibit lower viscosities (grain size reduction, water weakening, grain boundary related mechanisms, transformation plasticity). From this study, no significant upwards viscosity jump is therefore predicted to occur from the lower upper mantle to the transition zone, nor over the complete transition zone itself. Yet, the potential existence of a viscosity jump in the Earth's mid mantle has been suggested by geoid inversion analysis (Rudolph *et al.* 2015), mineral physics (Marquardt and Miyagi 2015) and implied by some studies of seismic tomography (van der Hilst *et al.* 1991; van der Hilst *et al.* 1997; Grand 2002; Zhao 2004; Fukao *et al.* 2013; Fukao and Obayashi, 2013) from observations of slab stagnation of laterally deflecting lithosphere and from shape changes of upwelling mantle plumes (French and Romanowicz, 2015). Our work suggests that this potential viscosity jump has to be placed either at the top or further down into the lower mantle at for instance 1000 km depth, where some slabs seem to stagnate and changes in the shape of mantle plumes are observed. In fact, the deformation mechanism maps (Fig. 4.7 and 4.8) show that the transition zone, according to the diffusion based deformation mechanisms, is well able to accomodate slab deflection (as revealed by the aforementioned studies of seismic tomography) by plastic deformation of wadsleyite and ringwoodite, as can also be expected for majorite.

It nevertheless may be noteworthy that in case atomic diffusion processes are locally inhibited, high lattice friction as opposed to dislocation glide in the transition zone silicates is able to increase the resistance to plastic flow in the transition zone significantly by more than up to two orders of magnitude (Fig. 4.7 and 4.8). It therefore has to be taken into account that local slab stagnation in the transition zone, from a rheological point of view, could be related to high lattice resistance associated with plastic slip in wadsleyite and ringwoodite, and that can also be expected in majorite.

The relative efficiency (presence) and inefficiency (absence) of dislocation glide activity in the upper mantle and the transition zone respectively, is expected to lead to distinct seismic signals. This is due to the fact that dislocation glide accomodated deformation is able to develop the formation of lattice preferred orientations (LPO) in minerals, apart from other sources of seismic anisotropy (*e.g.* shape preferred orientations (SPO) and layered structures) in contrast to pure climb. Pure climb creep is not able to produce LPO's and can as such not be the primary cause of seismic anisotropy (*e.g.* shear wave splitting). Yet, seismic studies (Trampert and van Heijst 2002; Vinnik *et al.* 1998; Tong *et al.* 1994; Fouch and Fischer 1996; Fischer and Wiens 1996) suggest seismic anisotropy to exist in the mantle transition zone, but only locally and significantly less pronounced than observed in the upper mantle (where olivine can be expected to deform by Weertman creep). It nevertheless has to be taken into account that the transition zone is a structural boundary layer and contains rock fabric of subducted lithosphere. In this light, the above seismic studies correspond reasonably well to the rheology of the transition zone as inferred from this study.

# 5 Conclusion and perspectives

## 5.1 Conclusion

The heart of this work has been dedicated to investigate the potential contribution of dislocation glide to the plasticity of wadsleyite and ringwoodite under transition zone conditions by modelling thermally activated glide in $Mg_2SiO_4$ wadsleyite at 15 GPa and $Mg_2SiO_4$ ringwoodite at 20 GPa. Modelling is based on a multiscale computational mineral physics approach to study plastic deformation of the high-pressure phases of the Earth's interior (Amodeo *et al.* 2011; Cordier *et al.* 2012). It allows us to calculate the constitutive equations associated with single slip for a wide range of temperatures and strain rates typical for the laboratory and the Earth's mantle. The model relies on the core structures of the rate governing dislocations belonging to the easiest slip systems. A crucial feature of these dislocations in wadsleyite and ringwoodite is their dissociation into collinear partials which determines their mobility. The intrinsic resistance of the crystal lattice as opposed to dislocation glide has been quantified and used to model thermal activation of these dissociated dislocations in order to calculate the glide mobilities. Steady-state flow due to plastic slip is described by relating the glide velocity to the macroscopic strain rate by solving Orowan's equation. A good agreement between our results at typical laboratory strain rates and the available experimental data on plastic deformation of wadsleyite and ringwoodite demonstrates that dislocation glide largely controls the mechanical behaviour at laboratory conditions. After this validation, constitutive equations related to dislocation glide are calculated for typical mantle strain rates taking into account the intrinsic strain rate dependency on the mobility of the defects. Critical resolved shear stresses $> 100$ MPa regarding pure single slip suggest that deformation of wadsleyite and ringwoodite under natural conditions may be controlled by other deformation mechanisms, since the sole contribution of dislocation glide to the overall plasticity in wadsleyite and ringwoodite cannot account for the plastic strain produced at low stress conditions of the Earth's deep mantle.

Diffusion based deformation mechanisms may provide a more efficient alternative to dislocation glide in the high-pressure phases of the Earth's transition zone. By making use of the available experimental data of self-diffusion coefficients in the high-pressure polymorphs of olivine, we have computed dislocation glide versus climb velocities for the rate controlling dislocations. It is shown that the climb velocity is always significantly larger than the glide velocity in the $\sigma$-$T$ domain appropriate to mantle conditions. This implies the breakdown of the coupled interaction between the glide and climb mechanisms in dislocation creep as formulated by Weertman (1950) (recovery-controlled dislocation creep). Both glide and climb processes are completely decoupled in the case of wadsleyite and ringwoodite under natural conditions. This means that dislocation climb becomes a main strain producing mechanism in both high-pressure polymorphs of olivine and has to be considered as an effective deformation mechanism rather than a recovery process: pure climb creep.

Although no quantification of the glide mobility of dislocations in majorite garnet exists, the decoupling between both glide and climb velocity under natural conditions may as well be expected based on the few deformation experiments available. The latter is supported by TEM observation of the activation of climb related processes (even at low temperatures).

To finally compare the relative importance of the pure climb creep mechanism to grain size dependent Nabarro-Herring creep (bulk diffusion) and Coble creep (grain boundary diffusion) under natural conditions, we have been constructing deformation mechanism maps for wadsleyite, ringwoodite and majorite based on the appropriate defect mobilities. Besides the decoupling between dislocation glide and climb in wadsleyite and ringwoodite, the maps suggest the relative importance of pure climb creep as a potential dominant deformation mechanism above average grain sizes of 0.5 mm, under typical steady state mantle strain rate conditions of $\dot{\epsilon} = 10^{-16}\ s^{-1}$ in wadsleyite and ringwoodite as also expected in majorite. Below this grain size, this dominance will gradually shift towards diffusional creep processes as may be important in relation to the nucleation of new grains during phase transformations as present in the Earth's transition zone (apart from other mechanisms such as grain boundary related disclination activity and grain boundary sliding or water weakening, *etc.*).

It is noteworthy to mention that the resistance to plastic flow in the transition zone is able to increase significantly by up to two orders of magnitude if dislocation glide is the only active deformation mechanism, for instance in case when atomic diffusion processes may be locally inhibited. As such, from a rheological point of view, local slab stagnation could be related to high lattice resistance associated with plastic slip in the transition zone minerals.

The rheology of the transition zone as discussed forms merely the starting point for a better understanding of plastic deformation and associated solid-state flow in this boundary layer that separates the upper from the lower mantle. All together, this work suggests the potential importance of point defect diffusion and especially of pure climb creep as an efficient strain producing mechanism in wadsleyite and ringwoodite, and also likely in majorite under natural conditions. This is what makes the transition zone, apart from the phase tranformations, rheologically distinct from the upper mantle.

## 5.2 Perspectives

One of essential key stones in modelling thermally activated dislocation glide is the use of the kink-pair model to be able to derive dislocation glide mobilities at elevated temperatures and at low stress conditions. Although the model is based on linear elasticity, it was shown to be able to predict the constitutive relations at laboratory conditions for both wadsleyite and ringwoodite. The model however is not able to describe the mechanism of kink-pair nucleation at the transition between correlated and uncorrelated kink-pair nucleation on dissociated dislocations (chapter 2.3.2.3 and 2.3.2.4). Given the significantly large values of the critical kink-pair nucleation enthalpies $\Delta H^{crit}$ obtained in wadsleyite and ringwoodite, it is not expected that a fine tuning of the kink-pair model will change the order of magnitude of the $CRSS(T)$ in case of these high lattice friction materials. Together with the fact the kink-pair model is expected to be the most accurate under the conditions of the Earth's deep mantle (high $T$, low stress), we consider the effort to use a more detailed modelling approach of kink-pair nucleation (*e.g.* kinetic Monte Carlo approach), in the context of geophysics, not to be of primary importance since it is not considered to change the fact that the glide mechanism is unlikely to operate in the high pressure silicates of the transition zone.

Our work reveals the potential importance of diffusion based deformation mechanisms, especially pure climb creep, which is expected to become an efficient strain producing mechanism at grain sizes above 0.5 mm in wadsleyite and ringwoodite and as is presumably the case in majorite. It is important to notice that these results depend strongly on the self-diffusion coefficients which have been taken from the relatively poor amount of experimental data available. It is therefore essential to investigate in more detail the mechanisms of diffusion in wadsleyite, ringwoodite and majorite to be able to better constrain their intrinsic transport properties which determine their plastic behaviour.

The self-diffusion coefficient can be written as $D_{sd} = XD$, where $D$ is the point defect diffusion coefficient given by $D = \exp(-\Delta H_m/k_bT)$. The latter is governed by the point defect migration enthalphy $\Delta H_m$ which is determined by the effective atomic diffusion paths of the atomic species involved. Besides the need in further studying the atomic scale diffusion mechanisms, the nature and concentration $X$ of point defects, as crystal vacancies, may be largely controlled by the presence of chemical heterogeneities (*e.g.* $Fe^{3+}$, H, Al, etc.) in an extrinsic regime. In this light, it may be relevant to study the effect of impurity concentrations on the thermodynamic and transport properties of wadsleyite, ringwoodite and majorite to be able to relate the effect of the crystal chemistry to point defect accomodated plastic deformation mechanisms such as pure climb creep. The latter however additionally requires the explicit study of the atomic interaction between point defects and the dislocation core structures to be able to capture and describe the (rate) controlling mechanism at the atomic scale. The related energy barriers for this mechanism may then be brought to the next scale to model the coupled absorption and emission of point defects between dislocations in the bulk of the crystal with for instance a dislocation dynamics code.

The transition zone is characterized by a number of phase transformations. The deformation mechanisms operating in the local regions where the transformations occur may deviate with respect to the rest of the transition zone. Besides the potential importance of Nabarro-Herring and Coble creep as a result of grain size reduction processes in the transformation regions, other mechanisms such as grain boundary related mechanisms (GBS, disclination activity) as well as transformation plasticity could play an important role in the transition zone. The physics of the latter mechanism has not been well understood so far, although it might be of importance in the transition zone. It lies in the hands of future studies to attack the problem of transformation plasticity in the main phases of the mantle transition zone.

The merit of this work is having gained the insight of the inefficiency of dislocation glide to produce plastic strain with respect to the climb mechanism in the main high-pressure phases of the Earth's transition zone. In the context of dislocation activity, this leads to a breakdown of the conventional concept of dislocation creep (Weertman 1950) in these phases and suggest the importance of pure climb creep as an active deformation mechanism operating in the transition zone. This however only defines the beginning of a more complete quantification of the potential deformation mechanisms operating in parallel in the high-pressure phases of the Earth's transition zone. These future studies would, together with results of the present work contribute to a better understanding of the effective solid-state flow in the Earth's transition zone and its effect on the dynamics of the Earth's interior.

# 6 References

Agee, C.B. (1998) Phase transformations and seismic structure in the upper mantle and transition zone. *In: Ultrahigh-Pressure Mineralogy: Physics and Chemistry of the Earth's Deep Interior, Reviews in Mineralogy*, 37, ed: R.J. Hemley, Mineralogical Society of America.

Amodeo, J., Carrez, Ph., Devincre, B., and Cordier, P. (2011) Multiscale modelling of MgO plasticity. *Acta Materialia* 59, 2291-2301.

Amodeo, J., Carrez, Ph., and Cordier, P. (2012) Modelling the effect of pressure on the critical shear stress of MgO single crystals. *Philisophical Magazine*, 92, 1523-1541.

Akimoto, S., and Sato, Y. (1968) High pressure transformation in $Co_2SiO_4$ olivine and some geophysical implications. *Physics of the Earth and Planetary Interiors*, 1, 498-504.

Amodeo, J., Carrez, Ph., Devincre, B., and Cordier, P. (2011) Multiscale modelling of MgO plasticity. *Acta Materialia*, 59, 2291-2301.

Anderson, O. (1982) The Earth's core and the phase diagram of iron. *Philosophical Transactions of the Royal Society of London. Series A, Mathematical and Physical Sciences*, 306(1492), 21-35.

Bardeen, J., and Herring, C. (1952) Imperfections in Nearly Perfect Crystals. Ed.: W. Shockley, page 261, John Wiley and Sons, Inc., New York.

Bernal, J.D. (1936) Geophysical discussion. *Observatory*, 59, 258.

Bina, C.R., Stein, S., Marton, F.C., and Van Ark, E.M. (2001) Implications of slab mineralogy for subduction dynamics. *Physics of the Earth and Planetary Interiors*, 127, 51-66.

Bindi, L., Steinhardt, P.J., Yao, N., and Lu, P.J. (2011) Icosahedrite, $Al_{63}Cu_{24}Fe_{13}$, the first natural quasicrystal. *American Mineralogist*, 96, 928-931.

Binns, R.A., Davis, R.J., and Reed, S.J.B. (1969) Ringwoodite, natural $(Mg,Fe)_2SiO_4$ spinel in the Tenham meteorite. *Nature*, 221, 943.

Birch, F. (1952) Elasticity and Constitution of the Earth's Interior. *Journal of Geophysical Research*, 57(2), 227-286.

Blöchl, P.E. (1964) Projector augmented-wave method. *Physical Review B*, 50, 17953-17979.

Boioli, F., Carrez, Ph., Cordier, P., Devincre, B., and Marquille, M. (2015) Modeling the creep properties of olivine by 2.5-dimensional dislocation dynamics simulations. *Physical Review B*, 92, 014115.

Born, M., and Oppenheimer, R. (1927) Zur Quantentheorie der Molekeln. *Annalen der Physik*, 289, 457-484 (in German).

Brunner, D., Taeri-Baghbadrani, S., Sigle, W., and Rühle, M. (2001) Surprising results of a study on the plasticity in strontium titanate. *Journal of the American Ceramic Society*, 84(5), 1161-1163.

Brunner, D. (2006) Low-temperature plasticity and flow-stress behaviour of strontium titanate single crystals. *Acta Materialia*, 54, 4999-5011.

Bullen, K.E. (1950) An Earth Model Based on a Compressibility-Pressure Hypothesis. *Geophysical Journal International*, 6(6), 50-59.

Bunge, H.-P., Richards, M.A., and Baumgardner, J.R. (1996) Effect of depth-dependent viscosity on the planform of mantle convection. *Nature*, 379, 436-438.

Bunge, H.-P., Richards, M.A., and Baumgardner, J.R. (1997) A sensitivity study of three-dimensional spherical mantle convection at 108 Rayleigh number: Effects of depth-dependent viscosity, heating mode, and an endothermic phase change. *Journal of Geophysical Research*, 102 (B6), 11991-12007.

Caillard, D., and Martin, J.L. (2003) Thermally activated mechanisms in crystal plasticity. Pergamon Materials Series, Amsterdam.

Carrez, Ph., Cordier, P., Mainprice, D., and Tomassi, A. (2006) Slip systems and plastic shear anisotropy in $Mg_2SiO_4$ ringwoodite: insights from numerical modelling. *European Journal of Mineralogy*, 18, 149-160.

Carrez, Ph., Ferré, D., and Cordier, P. (2007) Peierls-Nabarro model for dislocations in $MgSiO_3$ post-perovskite calculated at 120 GPa from first principles. *Philosophical Magazine A*, 87, 3229-3247.

Carrez, Ph., Walker, A.M., Metsue, A., and Cordier, P. (2008) Evidence from numerical modelling for 3D spreading of [001] screw dislocations in $Mg_2SiO_4$ forsterite. *Philosophical Magazine*, 88, 2477-2485.

Carrez, Ph., Ferré, D., and Cordier, P. (2009) Thermal activation of dislocation glide in MgO based on an Elastic-Interaction model of kink-pair nucleation. *In: IOP Conference Series: Materials Science and Engineering*, 3, 1-9.

Carrez, Ph., Ferré, D., and Cordier, P. (2009) Peierls-Nabarro modelling of dislocations in MgO from ambient pressure to 100 GPa. *Modelling and Simulation in Materials Science and Engineering*, 17, 035010.

Castillo-Rodríguez, M., and Sigle, W. (2011) The kink-pair mechanism and low-temperature flow-stress behaviour of strontium titanate single crystals. *Scripta Materialia*, 64, 241-244.

Celli, V., Kabler, T., Ninomiya, T., and Thomson, R. (1963) Theory of dislocation mobility in semiconductors. *Physical Review*, 131, 58-72.

Chen, J., Inoue, T, Weidner, D.J., Wu, Y., and Vaughan, M.T. (1998) Strength and water weakening of mantle minerals, olivine, wadsleyite and ringwoodite. *Geophysical Research Letters*, 25, 575-578.

Christian, J.W., and Vítek, V. (1970) Dislocations and stacking faults. *Reports on Progress in Physics*, 33, 307-411.

Coble, R.L. (1963) A model for boundary-diffusion controlled creep in polycrystalline materials. *Journal of Applied Physics*, 34, 1679-1682.

Cordier, P., Raterron, P., and Wang, Y. (1996) TEM investigation of dislocation microstructure of experimentally deformed silicate garnet. *Physics of the Earth and Planetary Interiors*, 97, 121-131.

Cordier, P., and Rubie, D.C. (2001) Plastic deformation of minerals uder extreme pressure using a multi-anvil apparatus. *Materials Science and Engineering*, A309-310, 38-43.

Cordier, P. (2002) Dislocation and slip systems of mantle minerals. *In: Plastic deformation of minerals and rocks, Reviews in Minerology*, 41, Mineralogical Society of America (Ed).

Cordier, P., Thurel, E., and Rabier, J. (2002) Stress determination in multianvil deformation experiments based on dislocation curvatures measurements: Application to wadsleyite and ringwoodite. *Geophysical Research Letters*, 29, 1029.

Cordier, P., Amodeo, J., and Carrez, Ph. (2012) Modelling the rheology of MgO under Earth's mantle pressure, temperature and strain-rates. *Nature*, 481, 177-181.

Cordier, P., Demouchy, S., Beausir, B., Taupin, V., Barou, F., and Fressengeas, C. (2014) Disclinations provide the missing mechanism for deforming olivine-rich rocks in the mantle. *Nature*, 507, 51-56.

Couvy, H., Cordier, P., and Chen, J. (2011) Dislocation microstructures in majorite garnet experimentally deformed in the multi-anvil apparatus. *American Mineralogist*, 96, 549-552.

Davies, G.F. (1995) Penetration of plates and plumes through the mantle transition zone. *Earth and Planetary Science Letters*, 133, 507-516.

Denoual, C. (2004) Dynamic dislocation modeling by combining Peierls Nabarro and Galerkin methods. *Physical Review B*, 70, 024106.

Denoual, C. (2007) Modeling dislocation by coupling Peierls-Nabarro and element-free Galerkin methods. *Computer Methods in Applied Mechanics and Engineering*, 196, 1915-1923.

Dorn, J.E., and Rajnak, S. (1964) Nucleation of kink pairs and the Peierls' mechanism of plastic deformation. *Transactions of the Metallurgical Society of AIME*, 230, 1052-1064.

Douin, J. (1987) Structure fine des dislocations et plasticit dans $Ni_3Al$, Ph.D. thesis, University of Poitiers, France (in French).

Duclos, R. (1981) High-temperature deformation of MgO·1.8$Al_2O_3$ spinel single crystals of ⟨111⟩ axial orientation. *Journal of Physics (Paris)*, 42, 49-58.

Dupas, C., Doukhan, N., Doukhan, J.C., Green II, H.W., and Young, T.E. (1994) Analytical electron microscopy of a synthetic peridotite experimentally deformed in the $\beta$ olivine stability field. *Journal of Geophysical Research*, 99, 15821-15832.

Dupas-Bruzek, C., Sharp. T., Rubie, D., and Durham, W. (1998) Mechanisms of transformation and deformation in $Mg_{1.8}Fe_0.2SiO_4$ olivine and wadsleyite under non-hydrostatic stress. *Physics of the Earth and Planetary Interiors*, 108, 33-48.

Durinck, J., Carrez, Ph., and Cordier, P. (2007) Application of the Peierls-Nabarro model to dislocations in forsterite. *European Journal of Mineralogy*, 19, 631-639.

Dziewonski, A.M., and Anderson, D.L. (1981) Preliminary reference Earth model. *Physics of the Earth and Planetary Interiors*, 25(4), 297-356.

Edelin, G., and Poirier, J.P. (1973) Étude de la montée des dislocations au moyen d'expérience de fluage par diffusion dans le magnésium. I. Mécanisme de déformation. *Philosophical Magazine*, 28, 1203-1210 (in French).

Eshelby, J.D. (1949) LXXXII. Edge dislocations in anisotropic materials. *Philosophical Magazine*, 7, 903-912.

Farla, R., Amulele, G., Girard, J., Miyajima, N., and Karato, S.-I. (2015) High-pressure and high-temperature deformation experiments on polycrystalline wadsleyite using the rotational Drickamer apparatus. *Physics and Chemistry of Minerals*, 42(7), 541-558.

Fei, Y., Saxena, S.K., and Navrosky, A. (1990) Internally constituent thermodynamic data and equilibrium phase relations for compounds in the system MgO-$SiO_2$ at high pressure and high temperature. *Journal of Geophysical Research*, 95, 6915-5928.

Ferré, D., Carrez, Ph., and Cordier, P. (2007) First principles determination of dislocation properties of $MgSiO_3$ perovskite at 30 GPa based on the Peierls-Nabarro model. *Physics of the Earth and Planetary Interiors*, 163, 283-291.

Ferré, D., Carrez, Ph., and Cordier, P. (2009) Dislocation modeling in calcium silicate perovskite based on the Peierls-Nabarro model. *American Mineralogist*, 94, 135-142.

Fischer, K., and Wiens, D. (1996) The depth distribution of mantle anisotropy beneath the Tonga subduction zone. *Earth and Planetary Science Letters*, 142, 253-260.

Forte, A.M., and Mitrovica, J.X. (1996) New inferences of mantle viscosity from joint inversion of long-wavelength mantle convection and post-glacial rebound data. *Geophysical Research Letters*, 23, 1147-1150.

Fouch, M.J., and Fischer, K.M. (1996) Mantle anisotropy beneath northwest Pacific subduction zone. *Journal of Geophysical Research*, 101, 15987-16002.

French, S.W., and Romanowicz, B. (2015) Broad plumes rooted at the base of the Earth's mantle beneath major hotspots. *Nature*, 525, 95-99.

Friedel, J. (1964) Dislocations. Pergamon Press.

Fukao, Y., Widiyantoro, S., and Obayashi, M. (2001) Stagnant slabs in the upper and lower mantle transition region. *Reviews of Geophysics*, 39, 291-323.

Fukao, Y., and Obayashi, M. (2013) Subducted slabs stagnant above, penetrating through, and trapped below the 660 km discontinuity. *Journal of Geophysical Research: Solid Earth*, 118, 5920-5938.

Goldschmidt, V.M. (1931) Zur Kristallchemie des germaniums. *Nachrichten von der Gesellschaft der Wissenschaften zu Gttingen, Mathematisch-Physikalische Klasse*, 1931, 184-190 (in German).

Gouriet, K., Carrez, Ph., and Cordier, P. (2014) Modelling [100] and [010] screw dislocations in $MgSiO_3$ perovskite based on the Peierls-Nabarro-Galerkin model. *Modelling and Simulations in Materials Science and Engineering*, 22, 025020.

Grand, S.P., van der Hilst, R.D., and Widiyantoro, S. (1997) Global seismic tomography: A snapshot of convection in the Earth. *Geological Society of America Today*, 7 (4), 1-7.

Grand, S.P. (2002) Mantle shear-wave tomography and the fate of subducted slabs. *Philosophical Transactions: Mathematical, Physical and Engineering Sciences*, 360, 2475-2491.

Greenwood, G.W., and Johnson, R.H. (1965) The deformation of metals under small stresses during phase transformations. *Proceedings of the Royal Society A*, 283, 403-422.

Guyot, P., and Dorn, J.E. (1967) A critical review of the Peierls mechanism. *Canadian Journal of Physics*, 45, 983-1016.

Haskell, N.A. (1937) The viscosity of the asthenosphere. *American Journal of Science*, 38, 22-28.

Herring, C. (1950) Diffusional Viscosity of a Polycrystalline Solid. *Journal of Applied Physics*, 21, 437.

Hirel, P., Marton, P., Mrovec, M., and Elsässer, C. (2010) Theoretical study of {110} generalized stacking faults and their influence on dislocation properties in perovskite oxides. *Acta Materialia*, 58, 6072-6079.

Hirel, P., Mrovec, M., and Elsässer, C. (2012) Atomistic simulation study of ⟨110⟩ dislocations in strontium titanate. *Acta Materialia*, 60, 329-338.

Hirel, P., Kraych, A., Carrez, Ph., and Cordier, P. (2014) Atomic core structure and mobility of [100](010) and [010](100) dislocations in $MgSiO_3$ perovskite. *Acta Materialia*, 79, 117-125.

Hirth, J.P., and Lothe, J. (1982) Theory of dislocations. John Wiley & Sons, Inc, New York.

Hohenberg, P., and Kohn, W. (1964) Inhomogeneous Electron Gas. *Physical Review*, 136(3b), 864-871.

Holzapfel, C., Chakraborty, S., Rubie, D.C., and Frost, D.J. (2009) Fe-Mg interdiffusion in wadsleyite: The role of pressure, temperature and composition and the magnitude of jump in diffusion rates at 410 km discontinuity. *Physics of the Earth and Planetary Interiors*, 172, 28-33.

Horiuchi, H., and Sawamoto, H. (1981) $\beta$-$Mg_2SiO_4$: single-crystal X-ray diffraction study. *American Mineralogist*, 66, 568-575.

Hornstra, J. (1960) Dislocations, stacking faults and twins in the spinel structure. *Journal of Physics and Chemistry of Solids*, 15, 311-323.

Huang, X., Xu, Y., and Karato, S.-I. (2005) Water content in the transition zone from electrical conductivity of wadsleyite and ringwoodite. *Nature*, 434, 746-749.

Hunt, S.A., Dobson, D.P., Li, L., Weidner, D.J., and Brodholt, J.P. (2010) Relative strength of the pyrope-majorite solid solution and the flow-law of majorite containing garnets. *Physics of the Earth and Planetary Interiors*, 179, 87-95.

Hustoft, J., Amulele, G., Ando, J.-I., Otsuka, K., Du, Z., Jing, Z., and Karato, S.-I. (2013) Plastic deformation experiments to high strain on mantle transition zone minerals wadsleyite and ringwoodite in the rotational Drickamer apparatus. *Earth and Planetary Science Letters*, 361, 7-15.

Inoue, T., Yurimoto, H., and Kudoh, Y. (1995) Hydrous modified spinel, $Mg_{1.75}SiH_{0.5}O_4$: A new water reservoir in the mantle transition region. *Geophysical Research Letters*, 22, 117-120.

Irifune, T., and Ringwood, A.E. (1987) Phase transformations in primitive MORB and pyrolite compositions to 25 GPa and some geophysical implications. *In: M.H. Manghnani and Y. Syono, Eds., High-Pressure Research in Mineral Physics.* American Geophysical Union, Washington, DC, 231-242.

Jaupart, C., Labrosse, S., and Mareschal, J.-C. (2007) Temperature, Heat and Energy in the Mantle of the Earth. *In: Bercovici, D., Schubert, G. (eds.) Treatise on Geophysics, vol. 7, Mantle dynamics, Chapter 7.06.* Elsevier, Amsterdam, 253-303.

Joós, B., Ben, Q., and Duesbery, M.S. (1994) Peierls-Nabarro model of dislocations in silicon with generalized stacking-fault restoring forces. *Physical Review B*, 50, 5890-5898.

Joós, B., and Duesbery, M.S. (1997) The Peierls Stress of Dislocations: An Analytic Formula. *Physical Review Letters*, 78(2), 266-269.

Joós, B., and Zhou, J. (2001) The Peierls-Nabarro model and the mobility of the dislocation line. *Philosophical Magazine A*, 81(5), 1329-1340.

Kárason, H., and van der Hilst, R.D. (2000) Constraints on mantle convection from seismic tomography. *In: M.R. Richards, R. Gordon and R.D. van der Hilst, Eds., The History and Dynamics of Global Plate Motion, Geophysical Monograph*, 121, p. 277-288. American Geophysical Union, Washington, DC.

Karato, S.-I., Wang, Z., Liu, B., and Fujino, K. (1995) Plastic deformation of garnets: Systematics and implications for the rheology of the mantle transition zone. *Earth and Planetary Science Letters*, 130, 13-30.

Karato, S.-I., Dupas-Bruzek, C., and Rubie, D.C. (1998) Plastic deformation of silicate spinel under the transition-zone conditions of the Earth's mantle. *Nature*, 395, 266-296.

Karato, S.-I., Reidel, M.R., and Yuen, D.A. (2001) Rheological structure and deformation of subducted slabs in the mantle transition zone: implications for mantle circulation and deep earthquakes. *Physics of the Earth and Planetary Interiors*, 127, 83-108.

Kavner, A., Sinogeikin, S.V., Jeanloz, R., and Bass, J.D. (2000) Equation of state and strength of natural majorite. *Journal of Geophysical Research*, 105, 5963-5971.

Kavner, A., and Duffy., T.S. (2001) Strength and elasticity of ringwoodite at upper mantle pressures. *Geophysical Research Letters*, 28, 2691-2694.

Kavner, A. (2007) Garnet yield strength at high pressure and implications for upper mantle and transition zone rheology. *Journal of Geophysical Research*, 112, B12207.

Kawazoe, T., Karato, S.-I., Otsuka, K., Jing, Z., and Mookherjee, M. (2009) Shear deformation of dry polycrystalline olivine under deep upper mantle conditions using a rotational Drickamer apparatus (RDA). *Physics of the Earth and Planetary Interiors*, 174(1-4), 128-137.

Kawazoe, T., Ohuchi, T., Nishiyama, N., Nishihara, Y., and Irifune, T. (2010) Preliminary deformation experiment of ringwoodite at 20 GPa and 1700 K using a D-DIA apparatus. *Journal of Earth Science*, 21 (5), 517-522.

Kawazoe, T., Karato, S.-I., Ando, J., Jing, Z., Otsuka, K., and Hustoft, J.W. (2010) Shear deformation of polycrystalline wadsleyite up to 2100 K at 14-17 GPa using a rotational Drickamer apparatus (RDA). *Journal of Geophysical Research*, 115, 1-11.

Kawazoe, T., Ohuchi, T., Nishihara, Y., Nishiyama, N., Fujino, K., and Irifune, T. (2013) Seismic anisotropy in the mantle transition zone induced by shear deformation of wadsleyite. *Physics of the Earth and Planetary Interiors*, 216, 91-98.

Kiefer, B., Stixrude, L., and Wentzcovitch, R.M. (1997) Calculated elastic constants and anisotropy of $Mg_2SiO_4$ spinel at high pressure. *Geophysical Research Letters*, 24, 1963-1966.

Knight, D.T., and Burton, B. (1989) The climb behaviour of a dislocation which is pinned at two points. *Philosophical Magazine*, 59(5), 1027-1044.

Kocks, U.F., Argon, A.S., and Ashby, M.F. (1975) Thermodynamics and kinetics of slip. Pergamon Press.

Kohn, W., and Sham, L.J. (1965) Self-Consistent Equations Including Exchange and Correlation Effects. *Physical Review*, 140(4a), 1133-1139.

Koizumi, H., Kirchner, H.O.K., and Suzuki, T. (1993) Kink pair nucleation and critical shear stress. *Acta Metallurgica et Materialia*, 41, 3483-3493.

Koizumi, H., Kirchner, H.O.K., and Suzuki, T. (1994) Nucleation of trapezoidal kink pairs on a Peierls potential. *Philosophical Magazine A*, 69, 805-820.

Kraych, A., Carrez, Ph., Hirel, P., Clouet, E., and Cordier, P. (2016) Peierls potential and kink-pair mechanism in high-pressure $MgSiO_3$ perovskite: an atomic scale study. *Physical Review B*, 93, 014103.

Kresse, G., and Hafner, J. (1993) Ab initio molecular dynamics for liquid metals. *Physical Review B*, 47, 558.

Kresse, G., and Hafner, J., 1994. Norm-conserving and ultrasoft pseudopotentials for first-row and transition elements. *Journal of Physics: Condensed Matter*, 6, 8245.

Kresse, G., and Furthmüller, J (1996) Efficiency of ab-initio total energy calculations for metals and semiconductors using a planewave basis set. *Computational Materials Science*, 6, 15-50.

Kubin, L.P. (2013) Dislocations, mesoscale simulations and plastic flow. Oxford University Press, UK.

Le Hazif, R., Edelin, G., and Dupouy, J.M. (1973) Diffusion Creep by Dislocation Climb in Beryllium and Be-Cu Single Crystals. *Metallurgical Transactions*, 4, 1275-1281.

Lewis, G., and Catlow, C. (1985) Potential models for ionic oxides. *Journal of Physics C: Solid Sate Physics*, 18, 1149-1161.

Marquardt, H., and Miyagi, L. (2015) Slab stagnation in the shallow lower mantle linked to an increase in mantle viscosity. *Nature Geoschience*, 8, 311-314.

Meade, C., and Jeanloz, R. (1990) The strength of mantle silicates at high pressure and room temperature: implications for the viscosity of the mantle. *Nature*, 348, 533-535.

Meng, Y., Fei, Y., Weidner, D., Gwanmesia, G.D., and Hu, J. (1994) Hydrostatic compression of $\gamma$-$Mg_2SiO_4$ to mantle pressures and 700 K: thermal equation of state and related thermodynamic properties. *Physics and Chemistry of Minerals*, 21, 407-412.

Metsue, A., Carrez, Ph., Denoual, C., Mainprice, D., and Cordier, P. (2010) Plastic deformation of wadsleyite: IV Dislocation core modelling based on the Peierls-Nabarro-Galerkin model. *Acta Materialia*, 58, 14671478.

$^a$Metsue, A., Carrez, Ph., Denoual, C., Mainprice, D., and Cordier, P. (2010) Peierls-Nabarro modelling of dislocations in diopside. *Physics and Chemistry of Minerals*, 37, 711-720.

Miranda, C.R., and Scandolo, S. (2005) Computational materials science meets geophysics: dislocations and slip planes of MgO. *Computer Physics Communications*, 169, 24-27.

Mitchell, T.E., Hwang, L., and Heuer, A.H. (1976) Deformation in spinel. *Journal of Materials Science*, 11, 264-271.

Mitchell, T.E. (1999) Dislocations and mechanical properties of MgO-$Al_2O_3$ spinel single crystals. *Journal of American Ceramic Society*, 82, 3305-3316.

Mitchell, T.E., Anderson, P.M., Baskes, M.I., Chen, S.P., Hoagland, R.G., and Misra, A. (2003) Nucleation of kink-pairs on partial dislocations: A new model for solution hardening and softening. *Philosophical Magazine*, 83(11), 1329-1346.

Mitrovica, J.X., and Forte, A.M. (2004) A new inference of mantle viscosity based upon joint inversion of convection and glacial isostatic adjustment data. *Earth and Planetary Science Letters*, 225, 177-189.

Miyagi, L., Amulele, G., Otsuka, K., Du, Z., Farla, R., and Karato, S.-I. (2014) Plastic anisotropy and slip systems in ringwoodite deformed to high shear strain in the Rotational Drickamer Apparatus. *Physics of the Earth and Planetary Interiors*, 2014, 244-253.

Möller, H.-J. (1978) The movement of dissociated dislocations in the diamond-cubic structure. *Acta Metallurgica*, 26, 963-973.

Mompiou, F., and Caillard, D. (2008) Dislocation-climb plasticity: Modelling and comparison with the mechanical properties of icosahedral AlPdMn. *Acta Materialia*, 56, 2262-2271.

Monkhorst, H.J., and Pack, J.D. (1976) Special points for Brillouin-zone intergrations. *Physical Review B*, 23, 5188-5192.

Mordehai, D., Clouet, E., Fivel, M., and Verdier, M. (2008) Introducing dislocation climb by bulk diffusion in discrete dislocaction dynamics. *Philosophical Magazine*, 88(6), 899-925.

Mosenfelder, J.L., Connolly, J.A.D., Rubie, D.C., and Liu, M. (2000) Strength of $(Mg,Fe)_2SiO_4$ wadsleyite determined by relaxation of transformation stress. *Physics of the Earth and Planetary Interiors*, 120, 63-78.

Nabarro, F. R. N. (1947) Dislocations in a simple cubic lattice. *Proceedings of the Physical Society*, 59, 256-272.

Nabarro, F.R.N. (1948) Report of a Conference on Strength of Solids. *Physical Society of London*, 75-90.

Nabarro, F.R.N. (1967) Steady-state diffusional creep. *Philosophical Magazine*, 16, 231-237.

Nishihara, Y., Tinker, D., Kawazoe, T., Xu, Y., Jing, Z., Matsukage, K.N., and Karato, S.-I. (2008) Plastic deformation of wadsleyite and olivine at high-pressure and high-temperature using a rotational Drickamer apparatus (RDA). *Physics of the Earth and Planetary Interiors*, 170, 156-169.

Nishiyama, N., Wang, Y., Uchida, T., Irifune, T., Rivers, M.L., and Sutton., S.R. (2005) Pressure and strain dependence of the strength of sintered polycrystalline $Mg_2SiO_4$ ringwoodite. *Geophysical Research Letters*, 32, L04307.

Ono, S. (2008) Experimental constraints on the temperature profile in the lower mantle. *Physics of the Earth and Planetary Interiors*, 170(3-4), 267-273.

Paterson, M.S. (1983) Creep in transforming polycrystalline materials. *Mechanics of Materials*, 2, 103-109.

Pearson, D.G., Brenker, F.E., Nestola, F., McNeill, J., Nasdala, L., Hutchison, M.T., Matveev, S., Mather, K., Silversmit, G., Schmitz, S., Vekemans, B., and Vincze, L. (2014) Hydrous mantle transition zone indicated by ringwoodite included within diamond. *Nature*, 507, 221-224.

Peierls, R.E. (1940) The size of a dislocation. *Proceedings of the Physical Society*, 52, 34-37.

Perdew, J.P., Burke, K., and Ernzerhof, M. (1996) Generalized Gradient Approximation Made Simple. *Physical Review Letters*, 77, 3865.

Philibert, J. (1979) *In: Dislocations et Déformations Plastique, Eds. Groh, P., Kubin, L.P., Martin, J.-L., CNRS Ecole d'été d'Yvrals* (in French).

Poirier, J.P. (1982) On transformation plasticity. *Journal of Geophysical Research*, 87, 6791-6797.

Poirier, J.P. (1985) Creep of crystals. Cambridge University Press.

Price, G.D., Putnis, A., and Smith, D.G.W. (1982) A mechanism for the spinel to $\beta$ phase transformation in the $(Mg,Fe)_2SiO_4$ system. *Nature*, 296, 729-731.

Price, G.D. (1983) The nature and significance of stacking faults in wadsleyite, natural $\beta$-$(Mg,Fe)_2SiO_4$ from the Peace River meteorite. *Physics of the Earth and Planetary Interiors*, 33, 137-147.

Putnis, A., and Price, G.D. (1979) High-pressure $(Mg,Fe)_2SiO_4$ phases in the Tenham chondrite meteorite. *Nature*, 280, 217-218.

Ravi, K.V. (1972) On the Observation of Bardeen-Herring Sources in Silicon. *Metallurgical Transactions*, 3, 1311-1313.

Ricard, Y., and Wuming, B. (1991) Inferring the viscosity and the 3-D density structure of the mantle from geoid, topography and plate velocities. *Geophysical Journal International*, 105, 561-571.

Richards, M.A., and Hager, B.H. (1988) The earth's geoid and the large-scale structure of mantle convection. *In: Runcorn, S.K. (Ed.), The Physics of Planets*, Wiley, 247-272.

Ringwood, A.E. (1962) A model for the upper mantle. *Journal of Geophysical Research*, 67, 4473-4477.

Ringwood, A.E., and Major, A. (1966) Synthesis of $Mg_2SiO_4$-$Fe_2SiO_4$ spinel solid solutions. *Earth and Planetary Science Letters*, 1, 241-245.

Ringwood, A.E., and Major, A. (1970) The system $Mg_2SiO_4$-$Fe_2SiO_4$ at high pressures and temperatures. *Physics of the Earth and Planetary Interiors*, 3, 89-108.

Ringwood, A.E. (1975) Composition and Petrology of the Earth's Mantle. McGraw-Hill, New York.

Ritterbex, S., Carrez, Ph., Gouriet, K., and Cordier, P. (2015) Modeling dislocation glide in Mg2SiO4 ringwoodite: Towards rheology under transition zone conditions. *Physics of the Earth and Planetary Interiors*, 248, 20-29.

Ritterbex, S., Carrez, Ph., and Cordier, P. Modeling dislocation glide and lattice friction of $Mg_2SiO_4$ wadsleyite in conditions of the Earth's transition zone. *American Mineralogist*, in press.

Rudolph, M.L., Lekić , V., and Lithgow-Bertelloni, C. (2015) Viscosity jump in the Earth's mid-mantle. *Science*, 350, 1349-1352.

Sanders, M., Leslie, M., and Catlow, C. (1984) Interatomic potentials for $SiO_2$. *Journal of the Chemical Society, Chemical communications*, 1271-1273.

Schoeck, G., and Püschl, W. (1994) Dissociated dislocations in the Peierls potential. *Materials Science and Engineering: A*, 189, 61-67.

Schoeck, G. (1999) The Peierls energy revisited. *Philosophical Magazine A*, 79(11), 2629-2636.

Schoeck, G. (2005) The Peierls model: progress and limitations. *Materials Science and Engineering A*, 400-401, 7-17.

Schoeck, G. (2006) The core structure of dislocations: Peierls model vs. atomic calculations. *Acta Materialia*, 54, 4865-4870.

Seeger, A., and Schiller P. (1962) The formation and diffusion of kinks as the fundamental process of dislocation movement in internal friction measurements. *Acta Metallurgica*, 10, 348-357.

Sharp, T., Bussod, G., and Katsura, T. (1994) Microstructures in $\beta$-$Mg_1.8Fe_0.2SiO_4$ experimentally deformed at transition-zone conditions. *Physics of the Earth and Planetary Interiors*, 86, 69-83.

Shimojuku, A., Kubo, T., Ohtani, E., and Yurimoto, H. (2004) Silicon self-diffusion in wadsleyite: Implications for the rheology of the mantle transition zone and subducting plates. *Geophysical Research Letters*, 31, L13606.

Shimojuku, Al, Kubo, T., Ohtani, E., Nakamura, T., Okazaki, R., Dohmen, R., and Chakraborty, S. (2009) Si and O diffusion in $(Mg,Fe)_2SiO_4$ wadsleyite and ringwoodite and its implications for the rheology of the mantle transition zone. *Earth and Planetary Science Letters*, 284, 103-112.

Shimojuku, A., Kubo, T., Ohtani, E., Nakamura, T., and Okazaki, R. (2010) Effects of hydrogen and iron on the silicon diffusivity of wadsleyite. *Physics of the Earth and Planetary Interiors*, 183, 175-182.

Sigle, S., Sarbu, C., Brunner, D., and Rühle, M. (2006) Dislocations in plastically deformed $SrTiO_3$. *Philosophical Magazine*, 86, 4809-4821.

Sinogeikin, S.V., Bass, J.D., and Katsura, T. (2001) Single-crystal elasticity of $\gamma$-$(Mg_{0.91}Fe_{0.09})_2SiO_4$ to high pressures and to high temperatures. *Geophysical Research Letters*, 28, 4335-4338.

Tackley, P.J. (2000) Mantle convection and plate tectonics: Towards an integrated physical and chemical theory. *Science*, 288, 2002-2007.

Tajima, F., and Grand, S.P. (1995) Evidence of high velocity anomalies in the transition zone associated with southern Kurile subduction zone. *Geophysical Research Letters*, 22, 3139-3142.

Takeuchi, S. (1995) Glide of interacting partial dislocations in the Peierls mechanism. *Philosophical Magazine A*, 71(6), 1255-1263.

Thurel, E. (2001) Etude par microscopie électronique en transmission des mécanismes de déformation de la wadsleyite et de la ringwoodite. Ph.D. thesis, University Lille 1 Science and Technology, France (in French).

Thurel, E., and Cordier, P. (2003) Plastic deformation of wadsleyite: I High-pressure deformation in compression. *Physics and Chemistry of Minerals*, 30(5), 256-266.

Thurel, E., Cordier, P., Frost, D., and Karato, S.-I. (2003) Plastic deformation of wadsleyite: II High-pressure deformation in shear. *Physics and Chemistry of Minerals*, 30(5), 267-270.

Thurel, E., Douin, J., and Cordier, P. 2003. Plastic deformation of wadsleyite: III. Interpretation of dislocations and slip systems. *Physics and Chemistry of Minerals*, 30(5), 271-279.

Tong, C., Gudmundsson, O., and Kennett, B.L.N. (1994) Shear wave splitting in refracted waves returned from the upper mantle transition zone beneath northern Australia. *Journal of Geophysical Review*, 99, 15783-15797.

Trampert, J., and van Heijst, H.J. (2002) Global Azimuthal Anisotropy in the Transition Zone. *Science*, 296, 1297-1299.

Vanderbilt, D. (1990) Soft self-consistent pseudopotentials in a generalized eigenvalue formalism. *Physical Review B*, 41, 7892-7895.

van der Hilst, R.D., Engdahl, R., Spakman, W., and Nolet, G. (1991) Tomographic imaging of subducted lithosphere below northwest Pacific island arcs. *Nature*, 353, 37-43.

van der Hilst, R.D., Widyantoro, S., and Engdahl, E.R. (1997) Evidence for deep mantle circulation from global tomography. *Nature*, 386, 578-584.

van Mierlo, W.L., Langenhorst, F., Frost, D.J., and Rubie, D.C. (2013) Stagnation of subducting slabs in the transition zone due to slow diffusion in majorite garnet. *Nature Geoscience*, 6, 400-403.

Vaughan, P.J., and Kohlstedt, D.L. (1981) Cation stacking faults in magnesium germanate spinel. *Physics and Chemistry of Minerals*, 7, 241-245.

Vinnik, L.P., Chevrot, S., and Montagner, J.-P. (1998) Seismic evidence of flow at the base of the upper mantle. *Geophysical Research Letters*, 25, 1995-1998.

Vítek, V. (1968) Intrinsic stacking faults in body-centred cubic crystals. *Philosophical magazine*, 18(154), 773-768.

$^a$Voegelé, V., Ando, J.I., Cordier, P., and Liebermann, R.C. (1998) Plastic deformation of silicate garnets. I. High-pressure experiments. *Physics of the Earth and Planetary Interiors*, 108, 305-318.

$^b$Voegelé, V., Cordier, P., Sautter, V., Sharp, T.G., Lardeaux, J.M., and Marques, F.O. (1998) Plastic deformation of silicate garnets. II. Deformation microstructures in natural samples. *Physics of the Earth and Planetary Interiors*, 108, 319-338.

Voegelé, V., Cordier, P., Langenhorst, F., and Heinemann, S. (2000) Dislocations in meteoritic and synthetic majorite garnet. *European Journal of Mineralogy*, 12, 695-702.

Walker, A.M., Slater, B., Gale, J.D., and Wright, K. (2004) Predicting the structure of screw dislocations in nanoporous materials. *Nature Materials*, 3(10), 715-720.

$^a$Walker, A.M., Slater, B., Gale, J.D., and Wright, K. (2005) Atomic scale modelling of the cores of dislocations in complex materials part 1: methodology. *Physical Chemistry Chemical Physics*, 7, 3227-3234.

$^b$Walker, A.M., Slater, B., Gale, J.D., and Wright, K. (2005) Atomic scale modelling of the cores of dislocations in complex materials part 2: applications. *Physical Chemistry Chemical Physics*, 7, 3235-3242.

Walker, A.M. (2010) Simulation of screw dislocations in wadsleyite. *Physics and Chemistry of Minerals*, 37(5), 301-310.

Wang, Y., Durham, W.B., Getting, I.C., and Weidner, D.J. (2003) The deformation-DIA: A new apparatus for high temperature triaxial deformation to pressures up to 15 Gpa. *Review of Scientific Instruments*, 74, 3002-3011.

Wang, Shao-Feng (2006) Dislocation energy and Peierls stress: a rigorous calculation from lattice theory. *Chinese Physical Society*, 15(6), 1301-1309.

Weidner, D.J., Vaughan, M.T., Ko, J., Wang, Y., Liu, X., Yeganeh-Haeri, A., Pacalo, R.E., and Zhao, Y. (1992) Characterization of stress, pressure and temperature in SAM85, a DIA type high pressure apparatus. *In: Y. Syono, M.H. Manghnani (eds) High-Pressure Research: Application to Earth and Planetary Sciences, Geophysical Monograph Series*, 67, 13-17. Terra Scientific Publishing Co and American Geophysical Union, Tokyo and Washington DC.

Weidner, D.J., Chen, J., Xu, Y., Wu, Y., Vaughan, M.T., and Li, L. (2000) Subduction zone rheology. *Physics of the Earth and Planetary Interiors*, 127, 67-81.

Welsch, G., Hwang, L., Heuer, A.H., and Mitchell, T.E. (1974) Dislocation dissociation in stoichiometric $MgAl_2O_4$ spinel observed by weak-beam electron microscopy. *Philosophical Magazine*, 29(6), 1371-1379.

Wenk, H.-R, Lonardelli, I., Pehl, J., Devine, J., Prakapenka, V., Shen, G., and Mao, H.-K. (2004) In situ observation of texture development in olivine, ringwoodite, magesiowstite and silicate perovskite at high pressure. *Earth and Planetary Science Letters*, 226, 507-519.

Wenk, H.-R., Ischia, G., Nishiyama, N., Wang, Y., and Uchida, T. (2005) Texture development and deformation mechanisms in ringwoodite. *Physics of the Earth and Planetary Interiors*, 152, 191-199.

Woo, C.H., and Püls, M.P. (1977) The Peierls Mechanism in MgO. *Philosophical Magazine*, 35(6), 1641-1652.

Xu, Y., Weidner, D.J., Chen, J., Vaughan, M.T., Wang, Y., and Uchida, T. (2003) Flow-law for ringwoodite at subduction zone conditions. *Physics of the Earth and Planetary Interiors*, 136, 3-9.

Yamazaki, D., and Karato, S.-I. (2001) High-pressure rotational deformation apparatus to 15 GPa. *Review of Scientific Instruments*, 72(11), 4207-4211.

Yang, L.H., Söderlind, P., and Moriarty, J.A. (2001) Atomistic simulation of pressure-dependent screw dislocation properties in bcc tantalum. *Materials Science and Engineering*, A309-310, 102-107.

Zhang, B., Wu, X., and Zhou, R. (2011) Calculation of oxygen self-diffusion coefficients in $Mg_2SiO_4$ polymorphs and $MgSiO_3$ perovskite based on the compensation law. *Solid State Ionics*, 186, 20-28.

Zhao, D. (2004) Global tomographic images of manlte plumes and subducting slabs: Insight into deep Earth dynamics. *Physics of the Earth and Planetary Interiors*, 146, 3-34.